Du sillage des insectes aux gaz de Fermi ultra-froids : dynamique des fluides classiques et quantiques

Frédéric Chevy

DÉPARTEMENT DE PHYSIQUE
DE L'ÉCOLE NORMALE SUPÉRIEURE

LABORATOIRE KASTLER BROSSEL

HABILITATION À DIRIGER LES RECHERCHES DE L'UNIVERSITÉ PARIS VI
spécialité : Physique Quantique

présentée par
Frédéric Chevy

Sujet du mémoire :

Du sillage des insectes aux gaz de Fermi ultra-froids : dynamique des fluides classiques et quantiques

Soutenue le 24 novembre 2008 devant le jury composé de :

S. Balibar
J.-F. Joanny
R. Kaiser
M. Lewenstein
J. Walraven

Table des matières

Remerciements

Le travail qui suit résumé l'essentiel de mes travaux de recherches effectués à la suite de ma thèse. À l'issue de cette période passionante pour laquelle je suis redevable de l'encadrement toujours stimulant et attentionné de Jean Dalibard, j'avais décidé d'aller explorer un autre domaine de la physique à l'occasion de mon postdoc. Profitant d'un contrat d'agrégé-préparateur en cours, j'ai frappé à la porte des laboratoires de matière molle parisien et je remercie tout particulièrement Élie Raphaël, David Quéré et Pierre-Gilles de Gennes de ne pas avoir été effrayé par ce physicien atomiste ne connaissant pas grand-chose à l'hydrodynamique qui prétendait néanmoins rejoindre leur groupe au Collège de France. Les deux années passées au laboratoire de la Matière condensée comptent probablement parmi les plus enrichissantes de ma carrière. J'y ai en effet découvert une façon complètement différente de faire de la physique, très loin de l'esprit régnant dans les laboratoires de physique atomique où dominent les expériences "lourdes" nécessitant des équipes de plusieurs étudiants et chercheurs. Cette période n'aurait pas été aussi passionnante sans l'ambiance unique qui régnait au laboratoire, et plus particulièrement dans le groupe dit des "Quérettes". Je remercie donc tout particulièrement pour tous les bons moments que nous avons passés ensemble Pascale Aussilous, Damien Baigl, Ashod Aradian, José Bico, Anne-Laure Biance (que je m'excuse encore d'avoir fait lever aux aurores pour ne pas voir tomber la pluie), Aurélie Lafuma, Elise Lorenceau-Bossy, Etienne et Mathilde Reyssat, Frédéric Restagno, Florent Saulnier. Je leur souhaite à tous bonne chance dans leurs carrières respectives, ainsi qu'à la prochaine génération qui est déjà bien avancée.

Suite à cette période centrée sur la physique macroscopique, je suis retourné au monde du $\hbar$ en intégrant le groupe fermions ultra-froids au Labortoiire Kastler Brossel. Un grand merci à Christophe Salomon pour m'avoir accueilli dans son groupe. Je lui suis gré de son enthousiasme permanent m'avoir fait partager ses vastes connaissances en optique et en physique atomique. Je le remercie de sa confiance et de m'avoir laissé une grande latitude

dans la conception et la réalisation de la future expérience Fermix qui ne devrait pas tarder à voir le jour. Du fait de leur complexité, les expériences d'atomes froids ne pourraient produire de résultats sans des étudiants doctorants et postdoctorants en connaissant toutes les arcanes. Un grand merci à Julien Cubizolles, Thomas Bourdel, Lev Khaykovich, Martin Teichmann, Jing Zhang, Leticia Tarruell, Grainne Duffy, Jason McKeever, Sylvain Nascimbène, Nir Navon et Kaijun Jiang qui beau ou gros temps ont toujours réussi à surmonter les caprices de l'expérience lithium pour en faire un montage performant malgré son âge avancé. De même, l'expérience Fermix ne pourrait progresser sans le travail de Kilvia Magalaes, Armin Ridinger, Thomas Salez, Ulrich Eismann et Saptarishi Chaudhuri, qui déploient toute leur énergie pour qu'un mélange de lithium et de potassium dégénéré puissent voir le jour à Paris. ainsi que tous les étudiants et chercheurs permanents du groupe atomes-froids hantant le sous-sol et la mezzanine, ainsi qu'à tous les personnels techniques et administratifs du LKB, Francis Hulin-Hubard, Christophe Bonnet, Bernard Trégon, Lionel Pérenes, Jean-Michel Isac, Saysavanh Souramasing, Richard Pescari, Christophe Bernard, Linda Krikorian, Thierry Tardieu, Françoise Tarquis et Viviane Tia pour leur aide et leur patience vis à vis de nos demandes parfois trop empressées.

J'ai pu me frotter au monde de la théorie en travaillant avec nos théoriciens maisons Christophe Mora, Roland Combescot, Yvan Castin, Xavier Leyronas et Félix Werner, mais aussi avec le très réputé groupe de Trento en Italie, où j'ai pu collaborer avec Sandro Stringari, Franco Dalfovo, Stefano Giorgini, Alessio Recati, Chiara Menotti et Carlos Lobo lors de mes quelques visites italiennes.

Bien que la plupart du temps plongé dans le monde des atomes froids, il m'arrive encore de pouvoir travailler sur les problèmes d'hydrodynamique qui avaient occupé mon postdoc. En ces quelques occasions, j'ai pu côtoyer Alexei Chepelianskii, Christophe Clanet (ex-sudiste qui durant ma période au Collège de France m'avait accueilli à Marseille pour profiter de sa caméra rapide), Marie Le Merrer et Guillaume Lagubeau avec qui j'ai plaisir à retrouver des sujets aussi variés que les gouttes, les vagues, les insectes ou les ballons de foot.

Les travaux réalisés durant ces quelques années sont brièvement résumés dans les pages qui suivent. Je remercie Sébastien Balibar, Jean-François Joanny, Robin Kaiser, Maciej Lewenstein et Jook Walraven d'avoir accepté de participer au jury de la soutenance d'Habilitation et de s'être confrontés à cet étrange mélange de physique microscopique et macroscopique qui a été l'objet de mon attention.

Je conçois difficilement faire de la recherche sans enseigner, qui est une

occasion d'enrichir ses connaissances auprès d'autres enseignants, mais aussi par le contact avec les étudiants qui imposent une remise en question permanente. Je suis ainsi tout particulièrement redevable des discussions que j'ai pu avoir avec Gwendal Fève, Jean-marc Berroir, Claude Aslangul, Édouard Brézin, Adrien Mahé, Hélène Perrin, Jean-François Joanny, Jean-François Allemand, Stephan Fauve et toute l'équipe de la FIP. Durant la période où j'ai eu la responsabilité du L3 de physique et du M2 de physique quantique, j'ai eu à perturber dans leur travail France Lamette, Anne-France Seyer, Françoise David et Mascia Reato et je leur remercie de m'avoir toujours porté secours malgré leur emploi du temps chargé.

Et pour finir un grand merci à mes amis, ma famille et surtout Sandrine et Ariane qui m'a confirmé que je n'étais vraiment, vraiment pas du matin !

Introduction

Ce manuscrit résume les travaux auxquels j'ai participé durant mon séjour postdoctoral au Laboratoire de physique de la matière condensée au Collège de France, puis dans le groupe Atomes froids du Laboratoire Kastler Brossel. Les thèmes qui seront abordés vont de l'hydrodynamique macroscopique de gouttes d'eau en impact sur des surfaces non-mouillantes à l'étude des superfluides fermioniques partiellement polarisés, des thèmes qui pourraient *a priori* paraître éloignés les un des autres, et pourtant ! Considérons par exemple le cas de la marche des insectes à la surface de l'eau, un problème auquel je me suis intéressé avec Élie Raphaël. Une question encore ouverte, et qui sera partiellement discutée au premier chapitre de cette habilitation, concerne la force propulsive responsable de la progression de ces animaux, pour laquelle deux scénarios concurrents existent. Tout d'abord, un mécanisme de type "rayonnement de freinage", dans lequel c'est la génération d'ondes de surface par le mouvement des pattes de l'animal qui le fait avancer. Par opposition, le mécanisme concurrent suppose que les tourbillons générés dans le sillage de la patte sont les vrais responsables. Bien que ces tourbillons aient été effectivement observés par le groupe de J. Bush au MIT (Fig. 1, référence [1]), les contributions relatives des deux effets restent encore discutées. Dans le cadre des atomes ultra-froids, un problème en tous points similaires se pose lorsque l'on s'intéresse au mouvement d'un obstacle dans un superfluide. En effet, un objet se déplace sans friction dans un condensat de Bose-Einstein si sa vitesse est inférieure à une certaine vitesse critique pouvant posséder là aussi deux origines : tout d'abord le mécanisme de Landau, dans lequel l'objet dissipe de l'énergie par émission d'ondes acoustiques. Comme pour les insectes, le second mécanisme, suggéré par Y. Pomeau et S. Ricca, implique l'émission d'un sillage tourbillonaire, effectivement observé au MIT [2, 4].

Au delà de cet exemple particulièrement emblématique, le travail qui suit montre nombre d'autres connexions entre l'hydrodynamique classique et la physique des gaz ultra-froids : ainsi, ce sont les même modes de vibrations

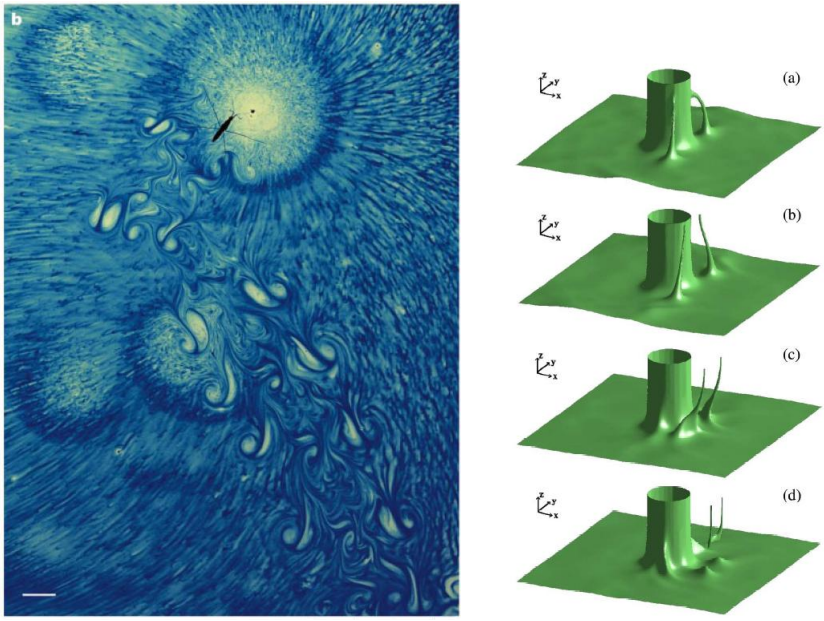

FIG. 1 – Gauche : Photos de l'allée de tourbillons générés à l'arrière d'un insecte à la surface de l'eau [1]. Droite : décrochement de ligne de vorticité lors de l'écoulement d'un superfluide autour d'un obstacle (courbes iso-densités extraites de [3]). Dans les deux cas, la dissipation résulte de la compétition entre émission de vortex et une traînée induite par l'émission d'ondes (ondes de surface pour l'insecte ou ondes acoustiques pour le condensat).

quadrupolaires qui participent à l'entretien du rebond d'une goutte sur une plaque chaude et permettent de mesurer le moment cinétique d'un condensat de Bose-Einstein en vibration, ou d'exciter les ondulations d'une ligne de vortex quantique ; c'est la tension de surface qui régit la marche des insectes et explique la forme du cœur superfluide d'un gaz de fermions de spin 1/2 dont on a déséquilibré les populations de spins ; enfin, les mêmes lois d'échelles et les raisonnements aux dimensions qui permettent d'appréhender simplement les phénomènes hydrodynamiques complexes et nous donnent accès au comportement macroscopique des gaz quantiques dans le régime d'interaction forte.

Le manuscrit est divisé en deux parties : dans les deux premiers chapitres nous aborderons tout d'abord mes contributions à l'hydrodynamique interfaciale. Le premier chapitre, de nature essentiellement théorique, rassemble un certain nombre de résultats obtenus en compagnie d'Elie Raphaël puis d'Alexei Chepelianskii sur le problème de la résistance de vague subie par un objet en mouvement à l'interface entre deux fluides. Comme mentionné précédemment, la motivation essentielle de ce travail était la compréhension du mécanisme de propulsion des insectes, mais nous cherchions aussi à résoudre le différent qui opposaient les résultats de deux groupes expérimentaux. Ce travail sur les ondes de surface m'a ensuite amené a travailler avec Elise Lorenceau-Bossy sur les problèmes d'entraînement d'air par des jets liquides. Une extension du formalisme développé pour l'étude de la marche des insectes au cas d'interfaces cylindriques a ainsi permis de mieux comprendre les mécanismes d'instabilité à l'origine de la forme caractéristique des jets après impact.

Le deuxième chapitre d'hydrodynamique classique est plus expérimental, et concerne le problème de l'impact de gouttes sur des surfaces non mouillantes, un travail réalisé dans le groupe de David Quéré, en compagnie d'Anne-Laure Biance, Etienne Reyssat, Christophe Clanet et Guillaume Lagubeau. Nous y verrons que lorsqu'une goutte tombe sur une surface super-hydrophobe, elle rebondit avec un coefficient de restitution proche de l'unité, et peut ainsi réaliser un nombre impressionnant de rebonds successifs. Nous verrons comment la plupart des résultats peuvent être compris en décrivant les déformations de la goutte par un ressort linéaire et nous conclurons en dévoilant certaines connexions entre situation de mouillage nul et la taille des gouttes de pluie.

La deuxième partie, sur les superfluides, s'ouvre sur un chapitre consacré à la dynamique des condensats de Bose-Einstein en rotation servant de lien entre les aspects classique et quantique de mes travaux. En effet, il montre que sous bien des aspects, et malgré la nature éminemment quantique des

mécanismes de mise en rotation d'un condensat *via* la nucléation de vortex quantifiés, la dynamique de ces systèmes peut être comprise en utilisant l'équation d'Euler d'écrivant l'hydrodynamique classique d'un fluide inviscide. Ce travail, qui faisait directement suite et prolonge mon travail de thèse sur les condensats de Bose-Einstein en rotation a été réalisé en collaboration avec Sandro Stringari à l'Université de Trento, et le groupe de Jean Dalibard à l'ENS : Vincent Bretin, Sabine Stock et Peter Rosenbusch. Nous présenterons une étude des modes de "haute" énergie pour lesquelles la structure singulière du champ de vorticité d'un condensat en rotation peut être omise et rendant ainsi applicable l'hydrodynamique classique. Nous verrons aussi que pour les modes de plus basse énergie (modes de Kelvin d'une ligne isolée de vorticité ou modes de torsions d'un réseau de vortex), les aspects quantiques doivent être pris en compte. Dans le cas des condensats en rotation rapide, la dynamique du système possède des analogies avec celle d'un gel, puisque celle-ci résulte de l'interaction entre l'écoulement hydrodynamique du superfluide et l'élasticité du réseau d'Abrikosov sous-jacent réticulant le superfluide.

Avec l'étude des superfluides fermioniques, les deux derniers chapitres abordent les aspects plus fondamentalement quantiques de ce manuscrit. Le premier de ces deux chapitres synthétise les travaux réalisés aux LKB sur l'expérience de lithium fermionique ultra-froid, en compagnie de Christophe Salomon, Thomas Bourdel, Jing Zhang, Leticia Tarruell, Martin Teichmann, Jason McKeever et Grainne Duffy. Nous verrons comment cette expérience nous a permis d'étudier la superfluidité des gaz de fermions et d'explorer le lien entre condensation de Bose-Einstein et superfluidité BCS (du nom de Bardeen-Cooper-Schrieffer) caractéristique des systèmes de fermions faiblement attractifs à basse température. Nous présenterons des résultats préliminaires sur la possibilité d'observer un appariement anisotrope et conclurons sur les perspectives des expériences de nouvelle génération en cours de développement dans notre groupe.

Le dernier chapitre est de nature théorique et s'intéresse à l'analyse de données expérimentales contradictoires obtenues à Rice et MIT sur la superfluidité des gaz de fermions en présence d'un déséquilibre des populations de spin. Nous montrerons que ces expériences peuvent être interprétées quantitativement par des modèles théoriques relativement simples. En particulier, le nombre de phases du système peut être déterminé rigoureusement par l'analyse variationnelle du problème d'une impureté immergée dans une mer de Fermi. Ce travail, réalisé en collaboration avec Alessio Reccatti et Carlos Lobo à Trento et Roland Combescot au Laboratoire de Physique Statistique de l'ENS, aboutit à un modèle analytique simple donnant des résultats très

proches des calculs Monte-Carlo exacts réalisés par la suite et concordant exceptionnellement bien avec les données expérimentales.

Bibliographie

[1] D. L. Hu, B. Chan, et J. W. M. Bush, Nature **424**, 663 (2003).

[2] T. Frisch, Y. Pomeau et S. Rica, Phys. Rev. Lett. **69**, 1644 (1992).

[3] A. Aftalion, Q. Du et Y. Pomeau, Phys. Rev. Lett. **91**, 090407 (2003)

[4] S. Inouye, S. Gupta, T. Rosenband, A.P. Chikkatur, A. Görlitz, T.L. Gustavson, A.E. Leanhardt, D.E. Pritchard et W. Ketterle, Phys. Rev. Lett. **87**, 080402 (2001).

Première partie

Fluides classiques

Chapitre 1

Ondes de capillarité-gravité, résistance de vague et entraînements de films d'air.

La mer fait des vagues à saute mouton
La mer fait des blagues aux poissons.
Anne Sylvestre : la mer fait des vagues

1.1 Introduction : de la vitesse des sous-marins nucléaires à la marche des insectes

Pour les amateurs de détails insolites, un rapide voyage sur internet permet de relever un fait intriguant : un sous-marin nucléaire se déplace plus vite en plongée qu'en surface[1], contrairement à l'intuition qui nous ferait penser que la traînée visqueuse ou turbulente devrait augmenter en immersion puisque la surface de contact entre la coque et l'eau y est la plus grande.

La réponse a ce paradoxe est cependant bien connue des spécialistes d'architecture navale. On sait en effet depuis le dix-neuvième siècle qu'une source importante de traînée pour les navires est la résistance de vague, c'est-à-dire la perte d'énergie par émission de sillage à longue distance, un équivalent aquatique du rayonnement de freinage bien connu en électromagnétisme.

[1]Ceci n'est vrai que pour des sous marins à propulsion nucléaire dont la puissance motrice est indépendante de la quantité d'oxygène disponible. Pour les sous-marins diesel, la vitesse en immersion est plus faible.

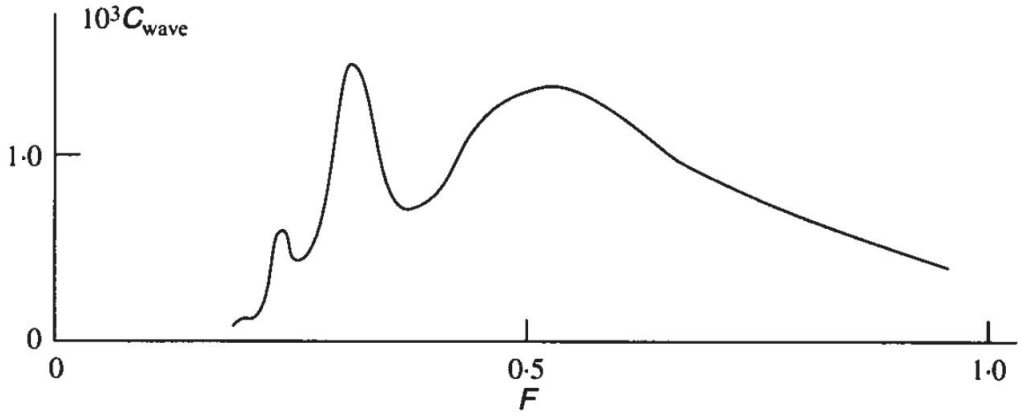

FIG. 1.1 – Résistance de vague R en fonction de la vitesse V d'une péniche de longueur L. $F = V/\sqrt{Lg}$ est le nombre de Froude, et $c_{wave} = 2R/\rho A V^2$, où A est l'aire de la péniche en contact avec l'eau. Données extraites de [1]

Une des contraintes sur la forme des coques de navires est ainsi de s'assurer que le sillage émis à la proue et à la poupe interfèrent destructivement de façon à minimiser l'amplitude des vagues émises à l'infini (Fig. 1.1). L'existence de cette résistance de vague explique donc naturellement le comportement des sous-marins : en plongée, le navire ne perturbe pas la surface de l'eau, et n'émet donc pas de sillage, ce qui réduit sa résistance de vague.

Le critère général d'apparition d'une dissipation par émission d'onde est relativement simple et très générale. En effet, un objet en mouvement rectiligne et uniforme dans un milieu pouvant propager des ondes de relation de dispersion $\omega(k)$ dissipera de l'énergie par sillage si sa vitesse dépasse une vitesse limite V_c donnée par la vitesse de phase minimale, à savoir

$$V_c = \min_k \frac{\omega(k)}{k}. \tag{1.1}$$

En effet, dans le référentiel de l'objet le sillage est stationnaire et possède donc une fréquence $\omega' = \omega - \boldsymbol{k} \cdot \boldsymbol{V}$ nulle. Cette condition sélection donc les modes satisfaisant la relation $\omega(\boldsymbol{k}) = \boldsymbol{k} \cdot \boldsymbol{V}$ et on trouve alors la relation (1.1) en notant que $\boldsymbol{k} \cdot \boldsymbol{V} < kV$.

Dans le cas d'un milieu non dispersif, V_c est simplement la vitesse de propagation des ondes, ce qui redonne par exemple le critère d'apparition du rayonnement Cerenkov [2] dans le cas des ondes électromagnétiques, ou, lorsque les excitations sont les phonons d'un superfluide, le critère de super-

fluidité de Landau [3]. Dans le cas des vagues de grande longueur d'onde à la surface de l'eau, on peut négliger les effets capillaires et les ondes de surface sont dominées par la gravité. La relation de dispersion en eau profonde[2] est alors $\omega(k) = \sqrt{gk}$ [4], qui possède une vitesse de phase minimale nulle. Un gros objet tel qu'un navire émettra donc toujours un sillage à longue distance et subira toujours une résistance de vague. Dans le cas de petits objets, tels qu'un insecte se déplaçant à la surface d'un étang, les effets capillaires ne peuvent plus être négligés[3]. Si ρ est la densité du liquide et γ la tension de surface, la nouvelle relation de dispersion est

$$\omega^2(k) = gk + \frac{\gamma k^3}{\rho}.$$

Or, cette forme particulière de relation de dispersion possède une vitesse de phase minimale valant

$$V_c^2 = 2\sqrt{\frac{g\gamma}{\rho}},$$

soit, dans le cas de l'eau pour laquelle $\gamma = 72$ mN/m, $V_c = 23$ cm/s. L'existence de cette vitesse limite pose un problème pour la locomotion des insectes. En effet, le déplacement de l'insecte n'est possible que si la surface de l'eau exerce une force de réaction à son mouvement. Un scénario envisagé est de supposer que c'est la résistance de vague qui exerce cette force, mais comme M. W. Denny l'a fait remarquer, ceci implique que les insectes doivent tous se déplacer à des vitesses supérieures à 23 cm/s, en général trop rapide pour les jeunes spécimens [5].

Ce *paradoxe de Denny* a suscité un grand intérêt pour l'étude de la résistance de vague dans le régime de capillarité-gravité : Citons par exemple les travaux théoriques d'E. Raphaël et P.G. de Gennes sur le calcul analytique de la résistance de vague [6], les expériences de Burghelea *et al.* [7] et J. Browaeys *et al.* [8] visant à mesurer directement la résistance de vague sur un objet millimétrique, ou encore les travaux de J. Bush sur la propulsion des insectes [9]. Dans ce contexte, le chapitre qui suit est consacré à une série de travaux théoriques et expérimentaux portant sur ces problèmes d'onde de capillarité-gravité. Dans un premier paragraphe, nous verrons que les résultats expérimentaux obtenus dans [7] et [8] aboutissent à des conclusion apparemment opposées l'une avec l'autre, et partiellement en contradiction avec les modèles théoriques. Nous montrerons cependant que le traitement de

[2] C'est-à-dire lorsque la profondeur est grande devant la longueur d'onde.

[3] C'est d'ailleurs la tension de surface qui leur permet de tenir à la surface de l'eau.

Raphaël *et al.* peut être adapté de façon à lever cette difficulté. Nous poursuivrons ensuite en montrant que l'accélération de l'insecte peut avoir un grand rôle dans l'existence d'une résistance de vague puisque dans l'exemple d'un mouvement circulaire, il n'y a plus de vitesse limite d'apparition du sillage. Enfin, nous quitterons les considérations de résistance de vague proprement dite et nous appliquerons ces questions de propagation d'onde capillaires au phénomène d'entraînement d'air par les liquides.

1.2 Résistance de vague pour les ondes de capillarité-gravité

Bien que l'effet de la résistance de vague sur des gros objets tels que des navires ou des sous-marins ait été depuis plusieurs siècles bien connu des architectes navals, depuis notamment les travaux de Froude, l'effet des forces capillaires n'a réellement commencé à être étudié qu'au cours des années 90. Une première étude théorique de la force de résistance de vague exercée sur un objet de petite taille (plus petite que la longueur capillaire) a été entreprise par E. Raphaël et P.G. de Gennes [6]. Dans ce calcul, on simplifie la situation physique en remplaçant l'objet mobile par un champ de pression extérieur. Cette approche à l'avantage de ne pas avoir à faire intervenir efforts visqueux à la surface du liquide et permet de séparer les effets de résistance de vague de ceux de traînée hydrodynamique plus classiques. Par ailleurs, l'absence de ligne de contact élimine les inévitables effets d'hystérésis qui lui sont associés. Tout calcul fait, ce modèle retrouve bien l'effet de seuil prédit plus haut et montre que la résistance de vague passe discontinument de 0 à R_c avec

$$R_c = \frac{F^2 \kappa}{2^{3/2}\gamma} \tag{1.2}$$

lorsque l'on passe au dessus de V_c (ici, F est la force vertical exercée par le champ de pression et $\kappa^{-1} = \sqrt{\rho g/\gamma}$ est la longueur capillaire, valant à peu près 3 mm pour l'eau).

À la suite de ces travaux théoriques, deux expériences ont été réalisées, l'une à Paris dans le groupe de J.C. Bacri [8], et l'autre en Israël dans celui de V. Steinberg [7]. Ces deux groupes confirmèrent effectivement l'existence d'un seuil en vitesse à partir duquel la résistance de vague commence à se manifester, mais n'obtinrent en revanche pas la même dépendance en fonction de la vitesse : alors que le groupe de Paris observait la discontinuité prédite

par le modèle d'E. Raphaël et P.G. de Gennes, l'expérience israëlienne aboutissait à un comportement continu, en désaccord apparent avec la théorie. Après une longue polémique, la cause de ce désaccord semble résider dans les techniques de mesure utilisées par les deux groupes pour évaluer la résistance de vague. Dans [8], l'objet immergé est une tige élastique maintenue par un support rigide. La résistance de vague courbe alors la tige et la force est obtenue par mesure de la déflexion élastique. En revanche, dans le dispositif expérimental décrit dans [7], l'objet est une bille magnétique maintenue fixe par un champ magnétique extérieur : la valeur de la résistance de vague peut donc être obtenue par la mesure du champ magnétique nécessaire pour ramener la bille à sa position d'équilibre. Cette seconde expérience étant plus simple à analyser et montrant les plus importantes déviations avec les prédictions de [6], c'est sur elle que nous avons porté notre attention. À cette occasion, nous avons remarqué que dans le modèle théorique le champ de pression extérieur, et donc la force verticale, est constante. En revanche, dans l'expérience de Steinberg, c'est la profondeur d'immersion de l'objet qui est maintenue fixe par le système de rétroaction magnétique. Nous avons donc repris l'analyse de [6] en ajustant la force verticale F de façon à maintenir constant le tirant d'eau. Ces travaux, présentés dans *Capillary gravity waves : A "fixed-depth" analysis* [10] ont montré que F s'annule à la vitesse critique. Selon l'équation (1.2), la force de résistance de vague est proportionnelle à F et on s'attend donc à un passage continu de $R = 0$ pour $V \leq V_c$ à $R \geq 0$ pour $V \geq V_c$ en accord qualitatif avec les données expérimentales de [7].

Afin de confirmer ce scénario, nous avons procédé à une mesure de la force verticale exercée sur une pointe immergée dans un écoulement à vitesse variable. Le dispositif expérimental est inspiré de celui utilisé par Browaeys et al. Une pointe d'acier de 1 mm de diamètre est immergée dans un canal circulaire de largeur 1 cm. Le canal est mis en rotation autour de son axe à une vitesse angulaire variable. L'aiguille est suspendue à un capteur de force permettant la mesure de la force verticale en fonction de la vitesse d'écoulement de l'eau dans le canal. Le résultat de l'expérience est présenté sur la figure 1.2. Ces données confirment l'importance des variations de la force verticale au voisinage du seuil d'apparition de la résistance de vague. Les effets de déplacement de la ligne de contact n'ont cependant pas permis une comparaison quantitative avec notre modèle - ainsi, au-delà de $V/V_c \sim 1.4$, le ménisque se détache de la pointe.

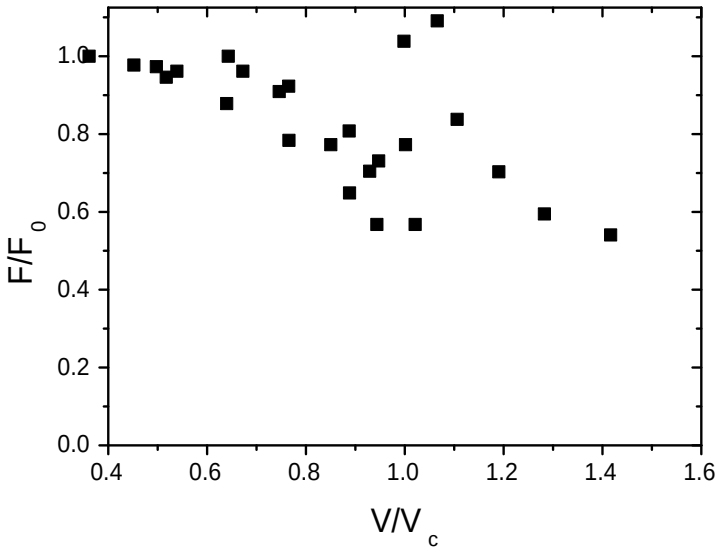

FIG. 1.2 – Mesure de la force verticale exercée sur une pointe immergé dans un écoulement de vitesse V variable. F_0 désigne la force à vitesse nulle et $V_c = 23$ cm/s est la vitesse théorique d'apparition de la résistance de vague.

1.3 Résistance de vague pour un mouvement accéléré

Le paradoxe de Denny mentionné dans l'introduction se fonde sur l'existence d'une vitesse critique d'apparition de la résistance de vague pour un mobile en mouvement rectiligne uniforme. Cependant, lorsque la patte d'un insecte frappe l'eau, son mouvement est accéléré, et on est donc légitimement amené à se poser la question de la pertinence de l'argument de Denny dans une situation réaliste. En effet, si l'on se fonde sur l'analogie avec l'électromagnétisme, la résistance de vague est l'équivalent du rayonnement de freinage - ou rayonnement Cerenkov - émis par une particule chargé se déplaçant plus vite que la lumière dans son milieu de propagation. Or, malgré ce seuil dans le cas d'un mouvement rectiligne, on sait qu'il n'est en général pas nécessaire d'atteindre le domaine relativiste pour émettre une onde électromagnétique. En effet, il suffit que le mouvement soit accéléré (par exemple un mouvement sinusoïdal dans le cas du très classique dipôle oscillant) pour qu'apparaisse une dissipation par réaction de rayonnement. De la même façon, on s'attend donc à ce qu'un sillage soit émis par un objet accéléré à la surface d'un liquide, et ce même lorsque sa vitesse est en dessous de la vitesse critique V_c. Dans *On capillary-gravity waves generated by a slow moving object*, nous avons étendu le formalisme de [6] au cas des mouvements accélérés, et plus particulièrement du mouvement circulaire uniforme. Ce choix de mouvement est guidé par l'étude des gyrins, des insectes vivant à la surface des cours d'eau et dont le nom provient de leur tendance à se déplacer en cercle. Ces insectes sont étudiés de façon approfondie par l'équipe de Jérôme Casas à l'Université de Tours avec qui nous collaborons sur le rôle éventuel joué par la forme de leurs trajectoires sur l'émission des vagues qu'ils utilisent pour l'écholocation.

Dans ce cadre, nous avons ainsi montré qu'en parfaite analogie ave l'électromagnétisme classique, une résistance de vague, était effectivement attendue lorsque la vitesse linéaire de l'objet était inférieure à V_c [11]. Deux obstacles se sont opposées à la vérification expérimentale de notre prédiction théorique : d'une part, l'expérience acquise après la polémique entre les groupes de J.C. Bacri et V. Steinberg nous a montré l'extrême sensibilité des mesures aux conditions de réalisation des expériences. En particulier, bien que les aspects qualitatifs de ces deux expériences soient à présent compris, leur étude quantitative est encore loin d'être accessible à l'analyse théorique. D'autre part, il est délicat de séparer les effets de friction visqueuse et de résistance de vague[4]. Nous nous sommes par conséquent contentés d'étudier

[4]Les expériences de Bacri et Steinberg mesurent elles aussi la traînée totale (vis-

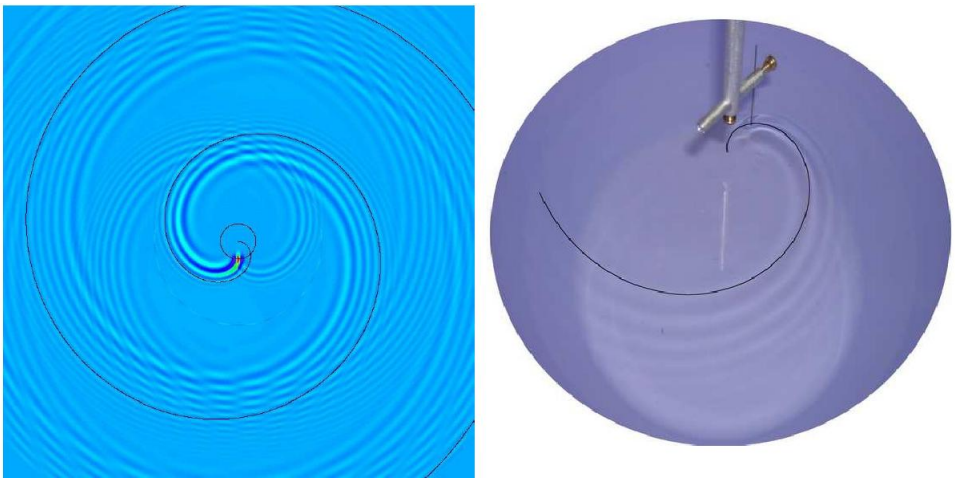

FIG. 1.3 – Sillage théorique (gauche) et expérimental (droite) émis par une pointe se déplaçant sur une trajectoire circulaire à la surface de l'eau. Dans les deux cas, les lignes noires correspondent à une spirale d'Archimède décrivant les lignes d'équiphase dont le pas est donné par l'équation (1.3).

l'existence et l'allure du sillage en fonction de la vitesse. Nous avons pu observer la génération d'ondes spirales pour des vitesses aussi basses que $V/V_c \sim 0.6$. Pour $V/V_c \gtrsim 0.8$ nous avons pu étudier l'allure du sillage par des photographies directes de celui-ci, qui ont montré un très bon accord avec notre modèle théorique (Fig. 1.3). Pour $0.8 \gtrsim V/V_c \gtrsim 0.6$, l'amplitude des ondes de surfaces est trop faible pour être décelable sur les photos. Nous avons alors étudié les déformations de la surface en mesurant la déflexion d'un faisceau laser réfléchi sur la surface liquide. La forme de ces ondes spirales est une spirale d'Archimède, dont l'équation en coordonnées polaires (r, ϕ) centrées sur le centre de la trajectoire est $r = a\phi + b$, où b repère l'origine des angles, et $2\pi a$ est le pas de l'hélice. Nous avons montré analytiquement que pour un objet se déplaçant à la vitesse V sur une trajectoire circulaire de rayon $\mathcal{R}$, a était donné par

queuse+résistance de vague). Pour éliminer la composante visqueuse, ils fittent par un polynôme la traînée pour $V < V_c$, faisant l'hypothèse que la résistance de vague est nulle dans ce régime. Pour $V < V_c$, ils soustraient alors à la traînée totale l'extrapolation du polynôme trouvé pour $V < V_c$. Puisque nous essayons ici de mettre en évidence une résistance de vague en dessous de la vitesse critique, cette technique n'est bien entendu plus applicable.

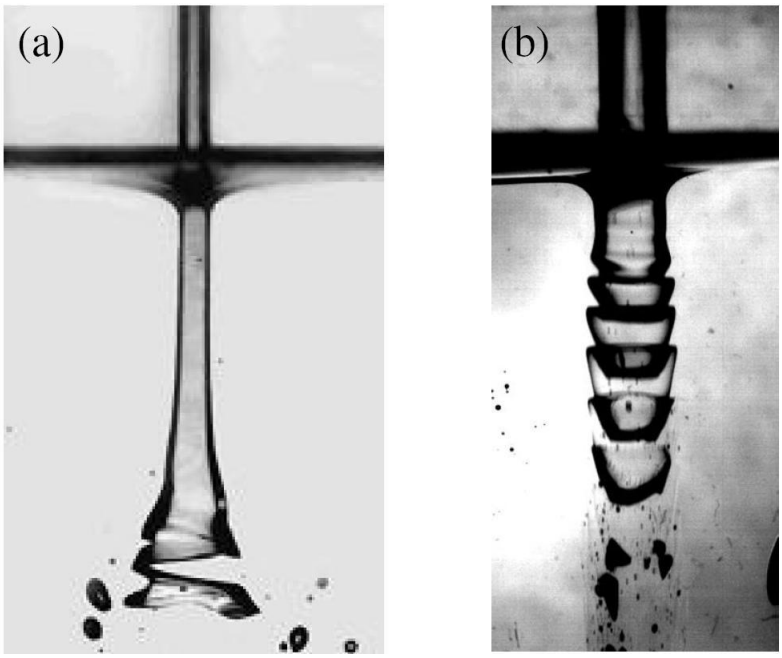

FIG. 1.4 – Expérience d'entraînement d'air lors de l'impact d'un jet dans un bain du même liquide. Pour des vitesses d'impacts identiques, les liquides visqueux s'évasent en pavillon de trompette (Fig. a, viscosité dynamique $\eta = 970$ mPa.s), alors que pour les liquides moins visqueux le film d'air s'écrase en accordéon (Fig. b, $\eta = 100$ mPa.s).

$$a \sim \frac{\kappa \mathcal{R}}{k(\omega = \kappa V)}, \tag{1.3}$$

où $k(\omega)$ désigne l'inverse de la relation de dispersion $\omega(k)$ des ondes de gravité-capillarité et κ^{-1} désigne la longueur capillaire. Comme on le constate sur la figure 1.3, cette prédiction est relativement bien vérifiée expérimentalement, ce qui justifie donc les aspects cinématiques de notre modèle.

1.4 Ondes capillaires en géométrie cylindrique : instabilité des films d'entraînement

L'étude théorique de la résistance de vague se fonde sur les propriétés des ondes de faible amplitude se propageant à l'interface plane entre deux fluides. Nous avons utilisé des techniques très similaires dans une étude

portant sur l'interprétation d'expériences réalisées par Élise Lorenceau dans le cadre de ses travaux de thèse sur l'entraînement de films d'air (*Trumpet and accordion instabilities of a viscous jet*, non publié).

Ces travaux consistaient à étudier l'impact d'un liquide dans un bain de liquide identique. Lorsque la vitesse du jet est suffisamment grande, le ménisque se rompt et un film d'air est entraîné dans le bain jusqu'à une profondeur critique où il se brise en une multitude de bulles (Fig. 1.4). Le problème de l'entraînement des films a un grand intérêt industriel, puisque les bulles d'airs nuisent notamment aux qualités d'un moulage. L'examen de la figure 1.4 montre l'existence de deux régimes qualitativement différents suivant la viscosité du liquide. Pour les fluides les plus visqueux, le film prend une forme de trompette due au ralentissement du jet par friction visqueuse avec le bain immobile (1.4.a). À faible viscosité, la trompette se déforme en accordéon (1.4.b). Cette forme caractéristique peut être expliquée par une instabilité linéaire de l'interface entre le jet et le bain, mêlant des mécanismes de Rayleigh-Plateau[5] et Kelvin-Helmholtz[6]. Pris indépendamment, ces deux mécanismes ne sélectionnent pas de longueur caractéristiques : en effet, pour un fluide de viscosité η les instabilités de Rayleigh-Plateau et de Kelvin-Helmholtz possèdent des taux de divergence donnés par $\Gamma_{\mathrm{KH}}(k) \sim \Gamma_{\mathrm{RP}}(0) - \gamma k/2\eta$, avec $\Gamma_{\mathrm{RP}} > 0$ et $\Gamma_{\mathrm{KH}}(k) \sim V_0 k/2$ qui sélectionnent respectivement des longueurs d'ondes arbitrairement petites et grandes respectivement[7]. Cependant, on peut montrer que la combinaison des deux mécanismes sélectionne la longueur d'onde telle que $\Gamma_{\mathrm{KH}} \sim \Gamma_{\mathrm{KH}}$, soit $\lambda_{\max} \propto \eta/\rho RV$. Cette prédiction, ainsi que la vitesse de phase de propagation des ondes de surface se compare favorablement aux données expérimentales (fig. 1.5). Le seuil d'éclatement du film d'air est l'aspect le moins connu du modèle, puisqu'il se produit dans le régime non-linéaire où l'instabilité s'est développée et l'amplitude des ondes de surface a saturé sous l'effet des non-linéarités.

[5]Instabilité d'un cylindre liquide responsable notamment de l'éclatement du filet d'eau sortant d'un robinet, ou du perlage de la rosée sur un fil d'araignée.

[6]Instabilité de l'interface entre deux liquides en cisaillement, responsable notamment de l'apparition des vagues à la surface de l'eau ou les ondes à la surface des champs de blé.

[7]En pratique, des longueurs d'ondes finies sont sélectionnées lorsqu'on affine le modèle de façon à le rendre plus réaliste. Ainsi, dans l'instabilité de Kelvin-Helmhtoltz, la longueur d'onde de l'instabilité est fixée par l'épaisseur de la couche de cisaillement.

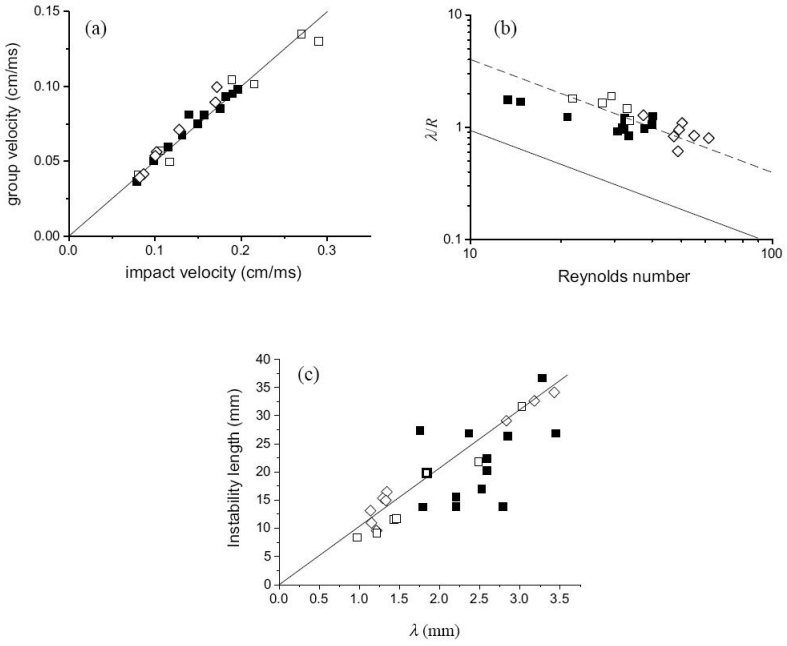

FIG. 1.5 – Comparaison entre les données expérimentales et le modèle de compétition Kelvin-Helmholtz/Rayleigh-Taylor. a) Vitesse de groupe de la déformation du film. b) Longueur d'onde λ sélectionnée - les courbes correspondent à des lois en 1/Re, cf. article. c) Longueur totale du film avant sa déstabilisation.

1.5 Conclusion

Si les travaux présentés dans les pages qui précèdent montrent que le paradoxe de Denny sur la marche des insectes n'a en réalité pas réellement lieu d'être, la nature physique de la force propulsive des insectes reste encore à élucider. En effet, suite aux travaux expérimentaux de John Bush au MIT [9], il semble à peu près clair que le déplacement de l'animal génère une traînée de tourbillons dans son sillage qui contribue elle aussi à réaction de la surface de l'eau. La part relative de ces deux effets (résistance de vague et traînée tourbillonaire) reste en revanche à préciser. Des travaux théoriques récents [12] suggèrent par exemple un facteur 2 entre les deux effets, mais qui reste à vérifier expérimentalement.

Du point de vue expérimental, nous avons vu que la vérification du modèle Raphaël-de Gennes se heurtait, aussi bien dans les expérience de J.C. Bacri et V. Steinberg, à la méconnaissance de la force verticale exercée sur les objets immergés. Une alternative séduisante a été suggérée récemment par C. Clanet et D. Quéré dans le cadre de leur travaux sur les gouttes caléfiés (cf. Chapitre 2). Dans ces expériences, on dépose une goutte d'azote liquide sur un bain d'eau à température ambiante. L'important écart de température entre l'azote et l'eau provoque l'apparition d'un film de vapeur entre les surface de l'eau et de l'azote qui permet de ralentir la vaporisation de celui-ci et forme un coussin d'air sur laquelle la goutte flotte quasi-librement. Dans cette configuration expérimentale, la force verticale est bien connue et est donnée par le poids de la goutte, et l'on retrouve la situation de la théorie Raphaël-de Gennes d'une dynamique à force verticale fixée.

Pour finir, la dernière partie de ce chapitre a montré l'intérêt de l'étude des ondes de surface se propageant sur des interfaces non planes (cylindrique dans le cas des entraînements de films d'air). Dans le cas d'une interface sphérique, un problème très similaire à la résistance de vague est le rebond d'une goutte liquide sur une surface non mouillante. Comme nous le verrons au chapitre suivant, le contact entre la goutte et le substrat génère des ondes de surfaces (essentiellement capillaires dans le cas des gouttes millimétriques utilisés en général dans les expériences) qui durant le rebond absorbent puis restituent l'énergie cinétique du centre de masse et conditionnent par conséquent le coefficient de restitution de la goutte. Dans la limité des faibles vitesses d'impact où les déformations restent faibles, la théorie linéaire des ondes capillaires devrait par conséquent être suffisante pour décrire la dynamique du rebond.

Bibliographie

[1] T. E. Faber, *Fluid dynamics for physicists* (Cambridge University Press, Cambridge 1995).

[2] P. A. Cherenkov, C. R. Acad. Sci. URSS 8, 451 (1934).

[3] L. P. Pitaievskii et S. Stringari *Bose-Einstein Condensation* (Oxford University Press, Oxford 2004).

[4] E. Guyon, J.-P. Hulin et L. Petit, *Hydrodynamique physique* (CNRS Éditions, EDP Science, 2001).

[5] M. W. Denny, *Air and Water*, (Princeton University Press, Princeton 1993).

[6] E. Raphaël et P.-G. de Gennes Phys. Rev. E, **53** 3448 (1996).

[7] T. Burghelea et V. Steinberg, Phys. Rev. Lett. **86**, 2557 (2001) et Phys. Rev. E 66, 051204 (2002).

[8] J. Browaeys, J.-C. Bacri, R. Perzynski et M. Shliomis, Europhys. Lett. 53, 209 (2001).

[9] D. L. Hu, B. Chan, et J. W. M. Bush, Nature **424**, 663 (2003).

[10] F. Chevy et E. Raphaël, Europhys. Lett., **61** 796 (2003).

[11] A. D. Chepelianskii, F. Chevy et E. Raphaël, Phys. Rev. Lett. **100**, 074504 (2008).

[12] O. Bühler, J. Fluid Mech. **573**, 211 (2007).

Capillary gravity waves : A "fixed-depth" analysis

EUROPHYSICS LETTERS 15 March 2003

Europhys. Lett., **61** (6), pp. 796–802 (2003)

Capillary gravity waves: A "fixed-depth" analysis

F. Chevy and E. Raphaël

Laboratoire de Physique de la Matière Condensée
UMR CNRS 7125 and FR CNRS 2438
Collège de France, 75231 Paris Cedex 05, France

(received 7 October 2002; accepted in final form 10 January 2003)

PACS. 68.03.Kn – Dynamics (capillary waves).

Abstract. – We study the onset of the wave resistance due to the generation of capillary gravity waves by a partially immersed moving object in the case where the object is held at a fixed immersion depth. We show that, in this case, the wave resistance varies continuously with the velocity, in qualitative accordance with recent experiments by Burghelea *et al.* (*Phys. Rev. Lett.*, **86** (2001) 2557).

Introduction. – The dispersive properties of capillary gravity waves are responsible for the complicated wave pattern generated at the free surface of a still liquid by a disturbance moving with a velocity V greater than the minimum phase speed $V_c = (4g\gamma/\rho)^{1/4}$, where g is the gravity, γ is the surface tension and ρ the density of the fluid [1]. The disturbance may be produced by a small object partially immersed in the liquid or by the application of an external surface pressure distribution [2]. The waves generated by the moving perturbation propagate momentum to infinity and, consequently, the disturbance experiences a drag $\boldsymbol{R}$ called the wave resistance [3]. For $V < V_c$, the wave resistance is equal to zero since, in this case, no propagating long-range waves are generated by the disturbance [4].

A few years ago, it was predicted that the wave resistance corresponding to a surface pressure distribution symmetrical about a point should be discontinuous at $V = V_c$ [5]. More precisely, if F_0 is the total vertical force exerted on the fluid surface, the wave resistance is expected to reach a finite value $R_c > 0$ for $V \to V_c^+$. For an object much smaller than the capillary length $\kappa^{-1} = \sqrt{\gamma/\rho g}$, the discontinuity R_c is given by

$$R_c = \frac{F_0^2}{2\sqrt{2}} \frac{\kappa}{\gamma}. \tag{1}$$

Experimentally, the onset of the wave resistance due to the generation of capillary gravity waves by a partially immersed moving object was studied recently by two independent groups [6, 7]. While Browaeys *et al.* [6] used a flexible wire and found a discontinuous behaviour of the wave resistance at $V = V_c$ [8], Burghelea *et al.* [7] used a bead immersed at a fixed depth and observed a smooth transition.

The discrepancy between the theoretical analysis of [5] and the experimental results of [7] might be due to the fact that the experimental setup of Burghelea *et al.* uses a feedback

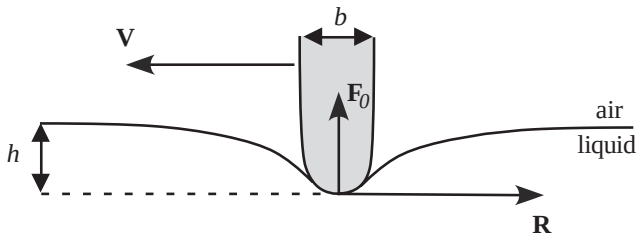

Fig. 1 – We study the behavior of a hydrophobic moving object of characteristic size b immersed at a depth h. The velocity of the object is V. We decompose the force exerted by the fluid on the object in a component orthogonal to the free surface (F_0) and a component parallel to it (R).

loop to keep the object at a constant depth while the analysis of [5] assumes that the vertical component F_0 of the force exerted by the disturbance on the fluid does not depend on the velocity V (we might call such an analysis a "fixed force" analysis). In order to check this proposition, we perform in this letter a "fixed-depth" calculation of the wave drag close to the onset threshold. A somewhat similar analysis was performed in the large velocity limit by Sun and Keller [9]. We will show that such a calculation indeed yields a cancellation of the vertical force at $V = V_c$, *i.e.* according to eq. (1), a smoothing of the discontinuity.

Model. – We take the (x, y)-plane as the equilibrium surface of the fluid. The immersed object exerts a stress at the fluid surface that can be considered equivalent to a pressure field p [10] that travels over the surface with a velocity V in the x-direction (fig. 1). We assume $\hat{p}$ (the Fourier transform of p) to be of the form

$$\hat{p}(k_x, k_y) = F_0 \hat{\phi}(k), \tag{2}$$

where $k = \sqrt{k_x^2 + k_y^2}$ and $\hat{\phi}(0) = 1$. In this case, $\hat{p}$ is isotropic [11] and F_0 is the total vertical force exerted on the fluid.

Within the framework of Rayleigh's linearized theory of capillary gravity waves, the Fourier transform $\hat{\xi}(\boldsymbol{k})$ of the free surface displacement $\xi(\boldsymbol{r})$ is related to the pressure field through [12]

$$\hat{\xi}(k_x, k_y) = -F_0 \frac{k}{\rho} \left(\frac{\hat{\phi}(k)}{\omega_0^2(k) - 4\nu^2 k^3 q + (2\nu k^2 - i\boldsymbol{V}\cdot\boldsymbol{k})^2} \right), \tag{3}$$

where $\omega_0^2(k) = gk + \gamma k^3/\rho$ is the free dispersion relation, $q^2 = k^2 - i\boldsymbol{k}\cdot\boldsymbol{V}/\nu$ and $\nu = \eta/\rho$ is the kinematic viscosity of the fluid.

Let us suppose that the object is located at the origin of the moving frame. If h is its depth, the free surface displacement ξ must be $-h$ under the pinpoint (here we suppose the object sufficiently hydrophobic and h not to large so that the pinpoint does not pierce the surface). This leads to the following normalization condition:

$$\xi(\boldsymbol{0}) = \int \frac{\mathrm{d}^2 k}{(2\pi)^2}\, \hat{\xi}(\boldsymbol{k}) = -h. \tag{4}$$

The value of h as a function of F_0 can be readily calculated using eqs. (3) and (4):

$$h = \Xi(V) F_0, \tag{5}$$

with

$$\Xi(V) = \int \frac{\mathrm{d}^2k}{(2\pi)^2}\frac{k}{\rho}\left(\frac{\hat{\phi}(k)}{\omega_0^2(k) - 4\nu^2k^3q^2 + (2\nu k^2 - i\boldsymbol{V}\cdot\boldsymbol{k})^2}\right). \tag{6}$$

Finally, the drag-force $\boldsymbol{R}$ is calculated by simply integrating the pressure force over the free surface [13],

$$\boldsymbol{R} = -\int \mathrm{d}^2r\, p(\boldsymbol{r})\boldsymbol{\nabla}\xi(\boldsymbol{r}) = -\int \frac{\mathrm{d}^2k}{(2\pi)^2}\, i\boldsymbol{k}\hat{p}^*(\boldsymbol{k})\hat{\xi}(\boldsymbol{k}). \tag{7}$$

This yields, using the explicit expression (3) for $\hat{\xi}$,

$$\boldsymbol{R} = F_0^2\boldsymbol{\Lambda}(V), \tag{8}$$

with

$$\boldsymbol{\Lambda}(V) = \int \frac{\mathrm{d}^2k}{(2\pi)^2\rho}\left(\frac{ik\boldsymbol{k}|\hat{\phi}(k)|^2}{\omega_0^2(k) - 4\nu^2k^3q^2 + (2\nu k^2 - i\boldsymbol{V}\cdot\boldsymbol{k})^2}\right). \tag{9}$$

According to eq. (8), the integral $\boldsymbol{\Lambda}$ describes the fixed-force behaviour of the wave resistance. Due to the symmetry of $\hat{\phi}$, $\boldsymbol{\Lambda}$ is parallel to $\boldsymbol{V}$ and we shall henceforth set $\boldsymbol{\Lambda} = \Lambda\boldsymbol{u}$, where $\boldsymbol{u} = \boldsymbol{V}/V$ is the unit vector parallel to the velocity of the object. The authors of [5] studied the properties of Λ in the case of a non-viscous fluid for which they showed that

a) $\Lambda = 0$ for $V < V_\mathrm{c}$;

b) Λ is discontinuous for $V \to V_\mathrm{c}^+$, with

$$\lim_{V\to V_\mathrm{c}^+}\Lambda = \Lambda_\mathrm{c} = \frac{1}{2\sqrt{2}}\frac{\kappa}{\gamma}; \tag{10}$$

c) in the large velocity limit

$$\Lambda \sim \frac{2\rho V^2}{3\pi\gamma^2}. \tag{11}$$

In the case of a fixed depth analysis, F_0 becomes a function of V. Using eqs. (5), we can rewrite the wave resistance as

$$\boldsymbol{R} = h^2\frac{\boldsymbol{\Lambda}(V)}{\Xi^2(V)}. \tag{12}$$

In general, we have to rely on numerics to calculate the integrals Ξ and Λ. Typical results are presented in fig. 2 for an object of size 0.1 mm immersed in water, and for a step-like function $\hat{\phi}$ equal to 1 for $k < 1/b$ and 0 otherwise. We first observe in fig. 2(a) that Ξ increases sharply near the threshold. This leads to two rather different behaviours for Λ and R as shown in fig. 2(b): while Λ exhibits a discontinuity close to $V = V_\mathrm{c}$ [14], the fixed-depth wave drag $R = \Lambda/\Xi^2$ cancels smoothly at the critical velocity.

Inviscid flow. – The characteristic features displayed by the plots of fig. 2 can be captured by a zero-viscosity analysis. Setting $\nu = 0$, eq. (6) can be simplified as

$$\Xi = \mathcal{P}\int \frac{\mathrm{d}^2k}{(2\pi)^2}\frac{k}{\rho}\left(\frac{\hat{\phi}(k)}{\omega_0^2(k) - (\boldsymbol{k}\cdot\boldsymbol{V})^2}\right), \tag{13}$$

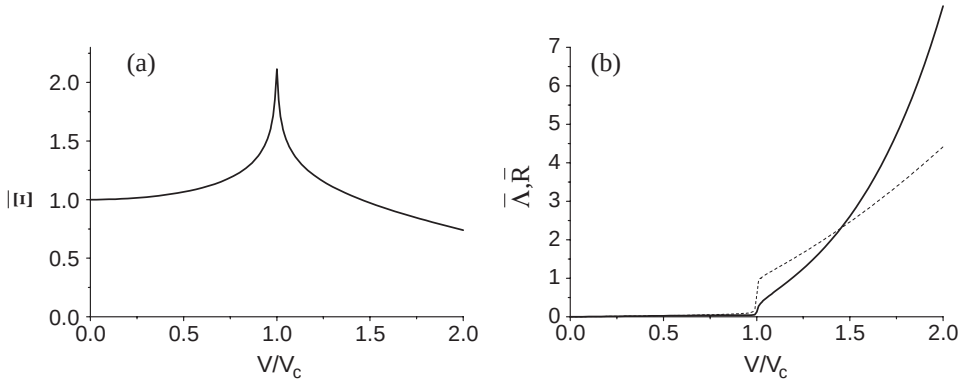

Fig. 2 – (a) Numerical calculation of the dimensionless integral $\bar{\Xi} = \Xi(V)/\Xi(0)$. (b) Comparison of $\bar{\Lambda}(V) = \Lambda(V)/\Lambda_c$ (dashed line) and $\bar{R} = \bar{\Lambda}/\bar{\Xi}^2$ (full line) describing, respectively, the fixed-force and fixed-depth behaviour of the wave resistance. We clearly see that contrary to the fixed-force analysis, the fixed-depth calculation does not yield any discontinuity at the threshold. Here $\nu = 10^{-6}$ m^2 s^{-1}, $\gamma = 72$ mN m^{-1}, $\rho = 1000$ kg m^{-3} and $b = 0.1$ mm.

where $\mathcal{P}$ denotes the Cauchy principal value of the integral. The integral is calculated in polar coordinates (k, θ), where θ is the angle of $\boldsymbol{k}$ with respect to $\boldsymbol{V}$. Introducing the function G defined by

$$G(k) = \mathcal{P} \int_0^{2\pi} \frac{\mathrm{d}\theta}{2\pi} \left(\frac{1}{m_k^2 - 2\mathcal{M}^2 \cos^2(\theta)} \right), \tag{14}$$

where $m_k^2 = k/\kappa + \kappa/k$ and $\mathcal{M} = V/V_c$ is the "Mach" number, eq. (13) can then be rewritten as

$$\Xi = \frac{1}{\gamma\kappa} \int_0^{\infty} \frac{\mathrm{d}k}{2\pi} \hat{\phi}(k) G(k). \tag{15}$$

Using the residue theorem [15], we get

$$G(k) = \frac{1}{\sqrt{m_k^2(m_k^2 - 2\mathcal{M}^2)}}\, \Theta(m_k^2 - 2\mathcal{M}^2), \tag{16}$$

where Θ is the Heaviside step function. The variations of m_k^2 with k are plotted in fig. 3: m_k^2 reaches its minimum value $(m_k^2)_{\min} = 2$ for $k = \kappa$. It shows that the equation $2\mathcal{M}^2 - m_k^2 = 0$ has two solutions, k_1 and k_2, with $k_1 < \kappa < k_2$, if V is larger than the critical velocity V_c, and none if $V < V_c$.

For $V > V_c$, Ξ evaluates to

$$\Xi = \frac{1}{\gamma\kappa} \left[\int_0^{k_1} \frac{\mathrm{d}k}{2\pi} \frac{\hat{\phi}(k)}{\sqrt{m_k^2(m_k^2 - 2\mathcal{M}^2)}} + \int_{k_2}^{\infty} \frac{\mathrm{d}k}{2\pi} \frac{\hat{\phi}(k)}{\sqrt{m_k^2(m_k^2 - 2\mathcal{M}^2)}} \right]. \tag{17}$$

The above integrals can be calculated in the two limiting cases $\mathcal{M} \approx 1$ (*i.e.* $V \approx V_c$) and $\mathcal{M} \gg 1$ (*i.e.* $V \gg V_c$).

For large $\mathcal{M}$, the integrals are restricted to either large or small values of k. If $\hat{\phi}$ vanishes faster than $1/k$ for large k, we can show that the small-k contribution dominates. In this region, the dispersion relation is dominated by gravity waves, so that we can approximate m_k^2 by k/κ. A straightforward calculation then yields the following asymptotic expansion for Ξ:

$$\Xi \sim \frac{1}{6\pi\gamma} \left(\frac{V_c}{V} \right)^4. \tag{18}$$

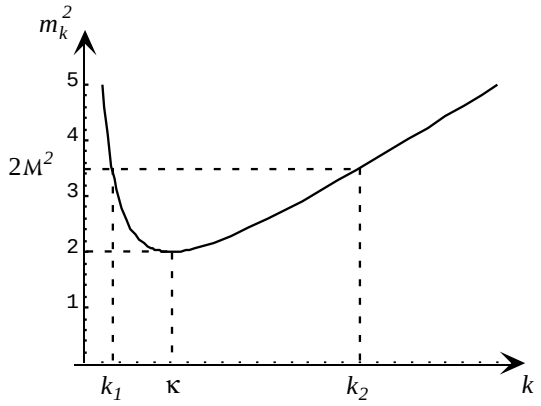

Fig. 3 – Variations of m_k^2 (see text) with k. Since m_k^2 reaches a minimum for $k = \kappa$ with $m_\kappa^2 = 2$, the equation $m_k^2 = 2\mathcal{M}^2$ presents solutions for $\mathcal{M} > 1$. In this case, there are two possible values, k_1 and k_2 with $k_1 < \kappa < k_2$.

Combining this result with (11) and 12, we get

$$R \sim 12\pi\rho h^2 \frac{V^{10}}{V_{\mathrm{c}}^8}.$$

Let us now focus on the case V close to V_{c}. We set

$$\widetilde{\Xi}_1 = \int_0^{k_1} \frac{\mathrm{d}k}{2\pi} \frac{\hat{\phi}(k)}{\sqrt{m_k^2(m_k^2 - 2\mathcal{M}^2)}},$$

and

$$\widetilde{\Xi}_2 = \int_{k_2}^{\infty} \frac{\mathrm{d}k}{2\pi} \frac{\hat{\phi}(k)}{\sqrt{m_k^2(m_k^2 - 2\mathcal{M}^2)}}.$$

Using the fact that k_1 and k_2 are the roots of $m_k^2 = 2\mathcal{M}^2$, we can rewrite $\widetilde{\Xi}_1$ as

$$\widetilde{\Xi}_1 = \int_0^{k_1} \frac{\mathrm{d}k}{2\pi} \frac{k\hat{\phi}(k)}{\sqrt{(k^2/\kappa^2)(k-k_1)(k-k_2)}}.$$

When $V \to V_{\mathrm{c}}$, the $(k-k_1)(k-k_2)$ term cancels in $k = \kappa$. Since all other terms are regular, we can write at the leading order

$$\widetilde{\Xi}_1 \sim \kappa \frac{\hat{\phi}(\kappa)}{\sqrt{2}} \int_0^{k_1} \frac{\mathrm{d}k}{2\pi} \frac{1}{\sqrt{(k-k_1)(k-k_2)}}.$$

This latter integral is readily calculated and gets a very simple form in the limit $V \to V_{\mathrm{c}}$:

$$\widetilde{\Xi}_1 \sim \kappa \frac{\hat{\phi}(\kappa)}{\sqrt{2}} \ln(k_2 - k_1) \sim \kappa \frac{\hat{\phi}(\kappa)}{2\sqrt{2}} \ln(\mathcal{M} - 1).$$

Since m_k^2 is invariant by the transformation $k/\kappa \to \kappa/k$, Ξ_1 and Ξ_2 have the same asymptotic behaviour for $V \to V_{\mathrm{c}}$. In this limit $\Xi = \left(\widetilde{\Xi}_1 + \widetilde{\Xi}_2\right)/\gamma\kappa \approx 2\widetilde{\Xi}_1/\gamma\kappa$, hence

$$\Xi \sim \frac{1}{2\pi\sqrt{2}\gamma} \hat{\phi}(\kappa) \ln(\mathcal{M} - 1). \tag{19}$$

For an object of size b, the width of $\hat{\phi}$ is about $1/b$. If we choose $b \ll \kappa^{-1}$, we can approximate $\hat{\phi}(\kappa)$ by $\hat{\phi}(0) = 1$. Equation (19) then takes the following form [16]:

$$\Xi \sim \frac{1}{2\pi\sqrt{2}\gamma} \ln\left(\mathcal{M} - 1\right) \sim \frac{1}{2\pi\sqrt{2}\gamma} \ln\left(\frac{V - V_{\mathrm{c}}}{V_{\mathrm{c}}}\right). \tag{20}$$

Combining eqs. (10) and (20), we see that slightly above the threshold, the wave resistance behaves like

$$R \sim \frac{4\pi^2}{\sqrt{2}} \left(\frac{\gamma\kappa h^2}{\ln^2\left(V/V_{\mathrm{c}} - 1\right)}\right). \tag{21}$$

Equation (21) constitutes the main result of this paper. First, we notice that for small objects this relation is independent of the shape of the pressure field. Second, and more important, it shows that the wave resistance R cancels out at $V = V_{\mathrm{c}}$. This smearing is due to the cancellation of the vertical force F_0 near the threshold that we get from the behaviour of Ξ.

Comparison with experiments. – Comparison of eq. (21) and the result of [5] proves that the behaviour of the wave resistance is strongly dependent on the conditions in which the experiments are performed and suggests that a full test of Raphaël and de Gennes' model requires a measurement of both R and F_0.

The model proposed here roughly reproduces the conditions of Burghelea's setup. It leads indeed to a smooth cancellation of the drag at the threshold but accordance remains only qualitative. Indeed, authors of [17] find the following scaling for the wave drag:

$$R_{\mathrm{exp}} \sim F_{\mathrm{c}}\rho\left(gh\right)^{3/2} \frac{b^2}{\nu\gamma} f(V/V_{\mathrm{c}}),$$

where F_{c} is the Stockes drag at threshold and h the width of the channel. Assuming the simple law $F_{\mathrm{c}} \sim \rho\nu b V_{\mathrm{c}}$, we get

$$R_{\mathrm{exp}} \sim \left(\frac{\rho^7 g^7}{\gamma^3}\right)^{1/4} h^{3/2} b^3 f(V/V_{\mathrm{c}}), \tag{22}$$

which differs from the scaling of eq. (21). It should be emphasized that (22) involves finite-size effects (due to the presence of the width h of the channel) and is hence beyond the scope of our model which assumes an infinite geometry.

In this respect comparison with [6] is more involved and would require further theoretical studies to be fully understood. Indeed, due to the setup design (an immersed wire, wetted by the liquid and the deflection of which measures the wave resistance), it cannot be described by any of the two simple types of models presented here (constant depth or constant force).

Conclusion. – In this paper we have shown that in a fixed-depth situation the discontinuity of the drag force calculated in [5] vanishes and is replaced by a smooth variation, in accordance with the experimental results found in [7]. A quantitative comparison between the present analysis and the data of ref. [7] is however more involved, since experiments from [7] were performed in narrow channel geometry [17] and would require the description of the reflections of the waves on the walls of the channel. Further study would also be required to understand the role of wetting of the liquid on the object in the variation of the wave drag. The present calculation suggests nevertheless that to fully test relation (1), experiments need to be devised that would measure both R and F_0.

* * *

We wish to thank J. Browaeys, P.-G. de Gennes and D. Richard for very helpful discussions, as well as V. Steinberg for sending us his experimental data prior to publication.

REFERENCES

[1] Lighthill J., in *Waves in Fluids* (Cambridge University Press) 1978.
[2] Lord Kelvin, *Proc. R. Soc. London, Ser. A*, **42** (1887) 80.
[3] See, *e.g.*, Debnath L., in *Nonlinear Water Waves* (Academic Press Inc., San Diego) 1994.
[4] Note that for a viscous fluid, the moving perturbation is also subjected to the usual Stokes drag, for both $V < V_c$ and $V > V_c$.
[5] Raphaël E. and de Gennes P. G., *Phys. Rev. E*, **53** (1996) 3448.
[6] Browaeys J., Bacri J.-C., Perzynski R. and Shliomis M., *Europhys. Lett.*, **53** (2001) 209.
[7] Burghelea T. and Steinberg V., *Phys. Rev. Lett.*, **86** (2001) 2557.
[8] We shall see later that the comparison of the data from [6] and the theoretical prediction requires some care, and the experimental observation of a discontinuous behaviour of the wave-resistance is not a proof of the validity of eq. (1).
[9] Sun Shu-Ming and Keller J., *Phys. Fluids*, **13** (2001) 2146.
[10] Not that this assumption is not entirely correct in the presence of viscosity since it leads to a slip of the object with respect to the fluid surface. In this case, a force field parallel to the free surface should also be added. However, this new term leads to the usual Stokes drag, that is subtracted from experimental results, and so can be omitted in our analysis.
[11] This latter hypothesis is not too restrictive in the case of very small object.
[12] This generalizes the 2D result of Richard D. and Raphaël E., *Europhys. Lett.*, **48** (1999) 53.
[13] Havelock T. H., *Proc. R. Soc. London, Ser. A*, **95** (1918) 354.
[14] For an inviscid fluid, this increase is actually a discontinuity. For high viscosities, we have observed no noticeable accident of $\mathbf{\Lambda}$ for V close to V_c.
[15] See, *e.g.*, Riley K. F., Hobson M. P. and Bence S. J., in *Mathematical Methods for Physics and Engineering* (Cambridge University Press) 1998.
[16] A more precise evaluation of the validity range would require to know the actual shape of $\hat{\phi}$ and its evolution with the object velocity.
[17] Burghelea T. and Steinberg V., *Phys. Rev. E*, **66** (2002) 051204.

On capillary-gravity waves generated by a slow moving object

Capillary-Gravity Waves Generated by a Slow Moving Object

A. D. Chepelianskii,[1,2] F. Chevy,[3] and E. Raphaël[1,*]

[1]Laboratoire Physico-Chimie Théorique, UMR CNRS Gulliver 7083, ESPCI, 10 rue Vauquelin, 75005 Paris, France
[2]Laboratoire de Physique des Solides, UMR CNRS 8502, Bâtiment 510, Université Paris-Sud, 91405 Orsay, France
[3]Laboratoire Kastler Brossel, ENS, Université Paris 6, CNRS, 24 rue Lhomond, 75005 Paris, France

(Received 30 April 2007; published 21 February 2008)

We investigate theoretically and experimentally the capillary-gravity waves created by a small object moving steadily at the water-air interface along a circular trajectory. It is well established that, for straight uniform motion, no steady waves appear at velocities below the minimum phase velocity $c_{\min} = 23\ \mathrm{cm\,s^{-1}}$. We demonstrate that no such velocity threshold exists for a steady circular motion, for which, even for small velocities, a finite wave drag is experienced by the object. This wave drag originates from the emission of a spiral-like wave pattern. Our results are in good agreement with direct experimental observations of the wave pattern created by a circularly moving needle in contact with water. Our study leads to new insights into the problem of animal locomotion at the water-air interface.

DOI: 10.1103/PhysRevLett.100.074504 PACS numbers: 47.35.−i, 68.03.−g

Capillary-gravity waves propagating at the free surface of a liquid are driven by a balance between the liquid inertia and its tendency, under the action of gravity and surface tension, to return to a state of stable equilibrium [1]. For an inviscid liquid of infinite depth, the dispersion relation relating the angular frequency ω to the wave number k is given by $\omega^2 = gk + \gamma k^3/\rho$, where ρ is the liquid density, γ the liquid-air surface tension, and g the acceleration due to gravity [2]. This equation may also be written as a dependence of the wave velocity $c(k) = \omega(k)/k$ on wave number: $c(k) = (g/k + \gamma k/\rho)^{1/2}$. The dispersive nature of capillary-gravity waves is responsible for the complicated wave pattern generated at the surface of a liquid by a moving disturbance such as a partially immersed object (e.g., a boat or an insect) or an external pressure source [2–6]. Since the disturbance expends a power to generate these waves, it will experience a drag R_w called the wave resistance [3]. In the case of boats or ships, this drag is known to be a major source of resistance and important efforts have been devoted to the design of hulls minimizing it [7]. The case of objects small relative to the capillary length $\kappa^{-1} = (\gamma/(\rho g)^{1/2}$ has only recently been considered [8–11].

In the case of a disturbance moving at constant velocity $\boldsymbol{V}$, the wave resistance R_w cancels out for $V < c_{\min}$ where V stands for the magnitude of the velocity, and $c_{\min} = (4g\gamma/\rho)^{1/4}$ is the minimum of the wave velocity $c(k)$ for capillarity gravity waves [3,4,8]. For water with $\gamma = 73\ \mathrm{mN\,m^{-1}}$ and $\rho = 10^3\ \mathrm{kg\,m^{-3}}$, one has $c_{\min} = 0.23\ \mathrm{m\,s^{-1}}$ (room temperature). This striking behavior of R_w around $c_{\min}$ is similar to the well-known Cherenkov radiation emitted by a charged particle [12], and has been recently studied experimentally [13,14]. In this Letter, we demonstrate that just like accelerated charged particles radiate electromagnetic waves even while moving slower than the speed of light [15], an accelerated disturbance experiences a nonzero wave resistance R_w even when propagating below $c_{\min}$. We consider the special case of a uniform circular trajectory, a situation of particular importance for the study of whirligig beetles (*Gyrinidae*, [16]) whose characteristic circular motion might facilitate the emission of surface waves that they are thought to be used for echolocation [17,18]. This Letter is therefore restricted to the effect of a wake stationary in the rotating frame, and does not consider time dependent contributions, like vortex shedding [19,20].

We consider the case of an incompressible infinitely deep liquid whose free surface is unlimited. In the absence of external perturbation, the free surface is flat and each of its points can be described by a radius vector $\boldsymbol{r} = (x, y)$ in the horizontal plane. The motion of a small object along the free surface disturbs the equilibrium position of the fluid, and each point of the free surface acquires a finite vertical displacement $\zeta(\boldsymbol{r})$. Rather than solving the complex hydrodynamic problem of finding the flow around a moving object, we consider the displacement of an external pressure source $P_{\mathrm{ext}}(\boldsymbol{r}, t)$ [5,6]. The equations of motion can then be linearized in the limit of small wave amplitudes [21].

In the frame of this linear-response theory, it is convenient to introduce the Fourier transforms of the pressure source $\hat{P}_{\mathrm{ext}}(\boldsymbol{k}, t)$ and of the vertical displacement $\hat{\zeta}(\boldsymbol{k}, t)$ [22]. It can be shown that, in the limit of small kinematic viscosity ν, the relation between $\hat{\zeta}(\boldsymbol{k}, t)$ and $\hat{P}_{\mathrm{ext}}(\boldsymbol{k}, t)$ is given by [9]

$$\frac{\partial^2 \hat{\zeta}}{\partial t^2} + 4\nu k^2 \frac{\partial \hat{\zeta}}{\partial t} + \omega^2(k)\hat{\zeta} = -\frac{k\hat{P}_{\mathrm{ext}}(\boldsymbol{k}, t)}{\rho}. \qquad (1)$$

In this Letter we assume that the pressure source has radial symmetry and that the trajectory $\boldsymbol{r}_0(t)$ of the object is circular: namely, $\boldsymbol{r}_0(t) = \mathcal{R}(\cos(\Omega t), \sin(\Omega t))$. Here $\mathcal{R}$ is the circle radius, and Ω is the angular frequency. The linear

velocity of the object is then given by $V = \mathcal{R}\Omega$. With these assumptions, the external pressure field is $P_{\text{ext}}(\boldsymbol{r}, t) = P_{\text{ext}}(|\boldsymbol{r} - \boldsymbol{r}_0(t)|)$, yielding in Fourier space $\hat{P}_{\text{ext}}(\boldsymbol{k}, t) = \hat{P}_{\text{ext}}(k)e^{-i\boldsymbol{k}.\boldsymbol{r}_0(t)}$. Since the right hand side of Eq. (1) is periodic with frequency Ω, it is possible to find its steady state solution by expanding the right hand side into Fourier series. The problem then becomes equivalent to the response of a damped oscillator to a sum of periodic forces with frequencies $n\Omega$, where n is an integer. The vertical deformation at any time t can then be reconstructed by evaluating the inverse Fourier transform. For the particular case of uniform circular motion, the time dependence is rather simple. Indeed, in steady state, the deformation profile rotates with the same frequency Ω as the disturbance. Therefore, in the rotating frame, ζ depends on the position $\boldsymbol{r}$ only. The analytical expression of $\zeta(\boldsymbol{r})$ in cylindrical coordinates $(x, y) = r(\cos\phi, \sin\phi)$ is given by

$$\zeta(r, \phi) = \sum_{n=-\infty}^{\infty} e^{\text{in}\phi} \int \frac{k^2 dk}{2\pi\rho} \frac{\hat{P}_{\text{ext}}(k) J_n(kr) J_n(k\mathcal{R})}{n^2\Omega^2 - \omega^2(k) + 4\text{in}\nu k^2\Omega} \tag{2}$$

where J_n is nth order Bessel function of the first kind. The summation index n is directly related to the nth Fourier harmonic of the periodic function $e^{-i\boldsymbol{k}.\boldsymbol{r}_0(t)}$ and, since the problem is linear, the contributions of all the harmonics add together.

The knowledge of the exact structure of the wave pattern is precious, but a quantitative measurement of the wave resistance is needed in order to understand, for example, the forces developed by small animals moving at the surface of water. In the case of the circular motion under study, the wave resistance R_w can be calculated from its average power $P_w = -\int d^2r \langle P_{\text{ext}}(\boldsymbol{r}, t) \frac{\partial\zeta(\boldsymbol{r},t)}{\partial t} \rangle$ by $R_w = P_w/V$. Using the Fourier expansion of ζ, one then obtains in the limit $\nu\kappa/c_{\min} \to 0$ (for water, $\nu\kappa/c_{\min} \sim 10^{-3}$):

$$R_w(V, \mathcal{R}) = \sum_{n>0} \frac{n}{\rho\mathcal{R}} \frac{(k_n J_n(k_n\mathcal{R})\hat{P}_{\text{ext}}(k_n))^2}{(\frac{d\omega^2}{dk})_{k_n}}, \tag{3}$$

where k_n is the unique solution of the equation $\omega(k_n) = n\Omega$ [the notation $R_w(V, \mathcal{R})$ stresses the dependence of R_w on the velocity magnitude and on the trajectory radius]. Equation (3) shows that the wave resistance R_w takes the form of a sum $R_w = \sum_{n>0} A_n$, where the A_n are positive numbers that measure the contribution of each Fourier mode of the external pressure source (with frequency $n\Omega$) to the wave resistance.

A numerical calculation of the wave resistance is presented in Fig. 1 for a pressure source $\hat{P}_{\text{ext}}(k) = p_0 \exp(-kb)$, where p_0 is the total force exerted on the surface and b is the typical object size [23]. As observed, Eq. (3) differs significantly from the original prediction on the wave drag in the case of a straight uniform motion with velocity V [8,11] given by

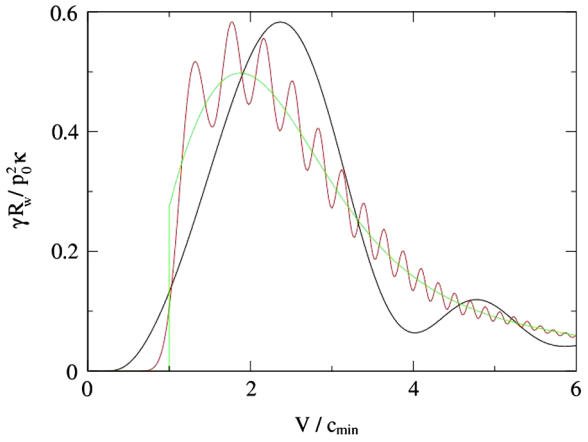

FIG. 1 (color online). Plot of the wave resistance R_w in units of $p_0^2\kappa/\gamma$, as a function the reduced velocity $V/c_{\min} = \mathcal{R}\Omega/c_{\min}$ for different ratios between the trajectory radius $\mathcal{R}$, and the object size b, as predicted by Eq. (3). The red or gray curve (presenting many oscillations) corresponds to $\mathcal{R}/b = 100$, while the black one (with fewer oscillations) corresponds to $\mathcal{R}/b = 10$. The green or light gray curve displaying a typical discontinuity at $V = c_{\min}$ is the wave drag for a straight uniform motion with velocity V [8]. The object size b was set to $b = 0.1\kappa^{-1}$.

$$R_{w,l}(V) = \int_0^{\infty} \frac{kdk}{2\pi\rho} \frac{\hat{P}_{\text{ext}}^2(k)\theta(V - c(k))}{V^2\sqrt{1 - (c(k)/V)^2}}, \tag{4}$$

where $\theta(.)$ is the Heaviside function and $c(k) = \omega(k)/k$ is the phase velocity. Most notably, the wave drag for a circular motion is nonzero for all velocities, even for $V < c_{\min}$ where wave resistance vanishes exactly in the case of a linear motion and this effect is far from negligible: for $\mathcal{R}/b = 10$ and at velocities as slow as $V/c_{\min} \sim 0.6$, the wave drag is still one fifth of that applied to an object moving linearly at $V/c_{\min} = 1$. The radiation of waves by an accelerated particle should not be surprising and is a very general phenomenon that is observed, for instance, in electromagnetism (bremsstrahlung) or in general relativity (Zeldovich-Starobinsky effect [24]). Mathematically, the fact that, for a circular motion, the wave resistance is finite even below $c_{\min}$ can be understood as follows. In the case of uniform motion, all the wave numbers such as $c(k) < V$ contribute to the wave drag, whereas for circular motion this is the case for only a discrete set of wave numbers k_n. While the condition $c(k) < V$ can be satisfied only when $V > c_{\min}$, the equations for the wave number k_n, $\omega(k_n) = nV/\mathcal{R}$, have positive solutions for any velocity V. These wave numbers k_n create finite contributions $A_n > 0$ to the wave drag. Therefore for a circular trajectory a finite wave drag exists at any velocity $V > 0$; for the same reasons R_w is also continuous at $V = c_{\min}$. Moreover, the wave resistance develops a small oscillating component as a function of the velocity V. It originates from the oscillatory behavior of Bessel functions and will be analyzed more thoroughly in a future publication. Finally, we note that

despite these striking differences Eq. (3) and (4) should coincide in the limit of a large trajectory radius. We confirmed this behavior by checking both analytically [25] and numerically that in the limit $\mathcal{R} \to \infty$, $R_w(V, \mathcal{R}) \to R_{w,l}(V)$. However, even if the circular wave drag $R_w(V, \mathcal{R})$ is close to $R_{w,l}(V)$ starting from $\mathcal{R}/b \sim 10$, important differences remain even up to very large values of $\mathcal{R}/b$ such as $\mathcal{R}/b \sim 100$.

Figure 2 represents the wave crest pattern [computed numerically form Eq. (2)] at the origin of this finite wave drag. It exhibits characteristic concentric Archimedean spirals (also known as arithmetic spirals) of the form $r = a\phi + r_0$. This can be understood from our theoretical results as follows. In a first estimation, one can assume that the integrals in Eq. (2) are dominated by the contribution of the poles at $k = k_n$. Thus $\zeta(\boldsymbol{r})$ can be written as $\zeta(\boldsymbol{r}) \sim (1/\sqrt{r})\sum_n B_n e^{i(n\phi - k_n r)}$, where we have used the asymptotic development of $J_n(k_n r)$ at large distances r and B_n are complex coefficients that do not depend on the position $\boldsymbol{r} = r(\cos\phi, \sin\phi)$. By separating the contribution of the different modes in the relation $\boldsymbol{F}(t) = -\int d^2 r P_{\text{ext}}(\boldsymbol{r}, t)\boldsymbol{\nabla}\zeta(\boldsymbol{r}, t)$, one finds that B_n is proportional to A_n (where, as defined earlier, the positive coefficients A_n measure the contribution of each Fourier mode to the wave drag: $R_w = \sum_{n>0} A_n$). One can show that in the regime of small object sizes $\kappa b \ll 1$, the proportionality constant between B_n and A_n depends only weakly on the Fourier mode number n; thus, one has $\zeta(\boldsymbol{r}) \propto (1/\sqrt{r}) \times \sum_n A_n e^{i(n\phi - k_n r)}$. We have checked numerically that in the regime $V < c_{\min}$, the distribution of the coefficients A_n is usually peaked around $n \sim \kappa\mathcal{R}$. For example, for $\kappa\mathcal{R} = 10$ and $\kappa b = 0.1$, A_n is peaked around $n = 10$ for velocities V in the interval $(c_{\min}/2, c_{\min})$. The wave crests are given by the lines of constant phase $n\phi - k_n r = \text{const}$ of the dominant mode $n = \kappa\mathcal{R}$, leading to the following expression for a:

$$a \approx \frac{\kappa\mathcal{R}}{k(\omega = \kappa V)}, \tag{5}$$

where $k(\omega)$ is the inverse function of $\omega(k)$. An interesting special case of the formula Eq. (5) corresponds to $V = c_{\min}$, for which one obtains $a \approx \mathcal{R}$. The spiral predicted by Eq. (5) is in very good agreement with the exact numerical results [Eq. (2)], as can be seen in Fig. 2.

We have also compared our theoretical approach with experimental results obtained using a 1 mm wide stainless steel needle immersed in a 38 cm wide water bucket. The needle was rotated on circular trajectories of various radii and angular velocities. Since direct measurement of wave drag, and, in particular, comparison with theory, is nontrivial even for a linear motion [13,14], we restricted ourselves to the study of the wake itself. A typical wave pattern obtained by this method is shown in Fig. 3 for $\mathcal{R} \approx 2.7$ cm and $\Omega \approx 2\pi \times 1.2$ Hz (corresponding to $V/c_{\min} \approx 0.9$) and unambiguously demonstrates the existence of a wake at velocities smaller than $c_{\min}$. The wave pattern is in remarkable agreement with the theoretical prediction $r = a\phi + b$ with a given by Eq. (5) and r_0 a free parameter corresponding to an overall rotation of the spiral [26]. For $V/c_{\min}$ lower than 0.8, no wake was observed by the naked eye. At lower rotation velocities, we probed the surface deformation by measuring the deflexion of a laser beam reflected by the air-water interface at a distance $r = 11$ cm from the rotation axis.

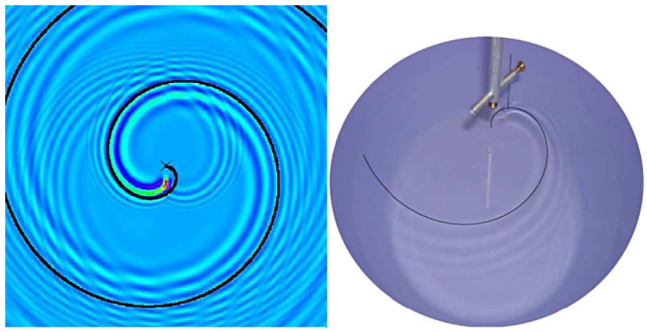

FIG. 2 (color online). Wave radiation for $V \approx 21$ cm/s $\approx 0.9 c_{\min}$ with a radius $\mathcal{R} \approx 2.7$ cm $\approx 9\kappa^{-1}$ Left: Color or shaded diagram of the surface deformation $\zeta(\mathbf{r})$ computed numerically from Eq. (2). This image represents a square region of size $400\kappa^{-1}$ around the center of rotation, red or gray color corresponds to maximal $\zeta(\mathbf{r})$ values, while green or light gray corresponds to minimal values of $\zeta(\mathbf{r})$. The cross indicates the center of the trajectory and the moving object is located in the region of highest deformation. Right: Photography of the wave crests generated on a water surface by a needle rotating at a velocity. On both pictures, the black curve represents the Archimedean spiral of radius given by Eq. (5).

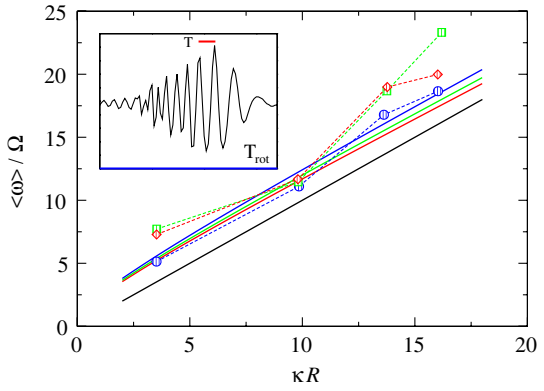

FIG. 3 (color online). Inset: typical time dependence of the laser deflection angle (arbitrary units) during a rotation period $T_{\text{rot}} = 2\pi/\Omega$, the fast oscillation frequency is given by $\langle\omega\rangle = 2\pi/T$. Main figure: Dependence of the ratio $\langle\omega\rangle/\Omega$ on $\kappa\mathcal{R}$ for different needle velocities. The dashed curves represent experimental results, while the continuous curve display the numerical results of our model. Red or gray, green or light gray, and blue or dark gray curves (diamonds, squares, and circles, respectively) correspond to $V/c_{\min} = 0.69$, 0.76, and 0.84. The black curve correspond to the analytical estimate $\langle\omega\rangle/\Omega = \kappa\mathcal{R}$.

Using this scheme, we have established the existence of waves down to $V/c_{\min} \approx 0.6$, and verified quantitatively that the wave packet spectrum is peaked around $\langle\omega\rangle \sim \kappa\mathcal{R}\Omega$ (see Fig. 3). Experimentally, the frequency $\langle\omega\rangle$ corresponds to the period of the fast temporal oscillations of the laser deflection angle (see Fig. 3, inset). In order to compare our experimental results with our model, we note that the deflection of the laser at a point $\mathbf{r}$ is proportional to the derivatives $\frac{1}{r}\frac{\partial\zeta(\mathbf{r},t)}{\partial\phi}$ and $\frac{\partial\zeta(\mathbf{r},t)}{\partial r}$. For simplicity, we will mainly consider the angular derivative, but we have checked numerically that our result do not depend on this choice. Using Eq. (2) the angular derivative can be decomposed into Fourier series: $\frac{\partial\zeta(\mathbf{r},t)}{\partial\phi} = \sum_n C_n e^{\mathrm{i}n(\phi-\Omega t)-ik_n r}$. The coefficients C_n are proportional to the contribution of the frequency $n\Omega$ to the wave packet spectrum and we can thus calculate the mean wave packet frequency using the expression: $\langle\omega\rangle = \Omega\sum_{n>0} n|C_n|/\sum_{n>0}|C_n|$. As shown in Fig. 3, our model is consistent with good accuracy with the experimental data without any adjustable parameters.

Below $V/c_{\min} \approx 0.6$, the signal-to-noise ratio of the experiment becomes too small to observe the laser deflection. Note that this value is in qualitative agreement with Fig. 1 where the wave resistance (hence the wave amplitude) has also significantly decreased with respect to its maximum value for $V/c_{\min} \lesssim 0.5$.

To summarize, we have shown theoretically that a disturbance moving along a circular trajectory experienced a wave drag even at angular velocities corresponding to $V < c_{\min}$, where $c_{\min}$ is the minimum phase velocity of capillary-gravity waves. Our prediction is supported by experimental observation of a long distance wake for $V/c_{\min}$ as low as 0.6. For $V/c_{\min} > 0.8$, we observed by naked eye Archimedean spiral shaped crests, in good agreement with theory. These results are directly related to the accelerated nature of the circular motion, and thus do not contradict the commonly accepted threshold $V = c_{\min}$ that is only valid for a rectilinear uniform motion, an assumption often overlooked in the literature. It would be very interesting to know if whirligig beetles can take advantage of such spirals for echolocation purposes. Although restricted to stationary wakes and thus excluded effects such as vortex shedding, the results presented in this Letter should be important for a better understanding of the propulsion of water-walking insects [19,20,27,28] where accelerated motions frequently occurs (e.g., when hunting a prey or escaping a predator [29]). Even in the case where the insect motion is rectilinear and uniform, one has to keep in mind that the rapid leg strokes are accelerated and might produce a wave drag even below $c_{\min}$.

We are grateful to J. Bico, J. Casas, M. W. Denny, and J. B. Keller for fruitful discussions. F. C. acknowledges support from Région Ile de France (IFRAF) and A. C. acknowledges support from Ecole Normale Supérieure Paris.

*Corresponding author.
elie.raphael@espci.fr

[1] L. D. Landau and E. M. Lifshitz, *Fluid Mechanics* (Pergamon Press, New York, 1987), 2nd ed.
[2] D. J. Acheson, *Elementary Fluid Dynamics* (Clarendon Press, Oxford, 1990).
[3] J. Lighthill, *Waves in Fluids* (Cambridge University Press, Cambridge, 1979), 6th ed.; T. H. Havelock, Proc. R. Soc. A **95**, 354 (1918).
[4] H. Lamb, *Hydrodynamics* (Cambridge University Press, Cambridge, 1993), 6th ed.
[5] Lord Rayleigh, Proc. London Math. Soc. **s1-15**, 69 (1883).
[6] Lord Kelvin, Proc. London Math. Soc. A **15**, 80 (1887).
[7] J. H. Milgram, Annu. Rev. Fluid Mech. **30**, 613 (1998).
[8] E. Raphaël and P.-G. de Gennes, Phys. Rev. E **53**, 3448 (1996).
[9] D. Richard and E. Raphaël, Europhys. Lett. **48**, 53 (1999).
[10] S.-M. Sun and J. Keller, Phys. Fluids **13**, 2146 (2001).
[11] F. Chevy and E. Raphaël, Europhys. Lett. **61**, 796 (2003).
[12] P. A. Cherenkov, C. R. Acad. Sci. URSS **8**, 451 (1934).
[13] J. Browaeys, J.-C. Bacri, R. Perzynski, and M. Shliomis, Europhys. Lett. **53**, 209 (2001).
[14] T. Burghelea and V. Steinberg, Phys. Rev. Lett. **86**, 2557 (2001); Phys. Rev. E **66**, 051204 (2002).
[15] J. D. Jackson, *Classical Electrodynamics* (Wiley, New York, 1998), 3rd ed.
[16] W. Nachtigall, in *The Physiology of Insecta* (Academic Press, New York, 1965).
[17] V. A. Tucker, Science **166**, 897 (1969).
[18] M. W. Denny, *Air and Water* (Princeton University Press, Princeton, 1993).
[19] J. W. Bush and D. L. Hu, Annu. Rev. Fluid Mech. **38**, 339 (2006).
[20] O. Buhler, J. Fluid Mech. **573**, 211 (2007).
[21] For nonlinear effects, see F. Dias and C. Kharif, Annu. Rev. Fluid Mech. **31**, 301 (1999).
[22] The Fourier transform $\hat{f}(\boldsymbol{k}, t)$ is related with the function $f(\boldsymbol{r}, t)$ through $f(\boldsymbol{r}, t) = \int \frac{d^2k}{(2\pi)^2} e^{i\boldsymbol{k}.\boldsymbol{r}} \hat{f}(\boldsymbol{k}, t)$.
[23] While all the data shown in this Letter are obtained with this expression for $P_{\text{ext}}(r)$, we have verified that other distributions (Gaussian, step function, ...) lead qualitatively to the same results.
[24] Ya. B. Zeldovich, JETP Lett. **14**, 180 (1971); A. A. Starobinsky, JETP **37**, 28 (1973).
[25] J. B. Keller (private communication).
[26] Note that we also observed on some pictures the weaker spiral seen in Fig. 2 and propagating in the opposite direction with respect to the main wake. However, this "advanced" wake could only be observed at high velocities ($V/c_{\min} \sim 2$) because of its small relative amplitude.
[27] R. McNeill Alexander, *Principle of Animal Locomotion* (Princeton University Press, Princeton, 2002).
[28] M. W. Denny, J. Exp. Biol. **207**, 1601 (2004); F. Fish and A. Nicastro, J. Exp. Biol. **206**, 1649 (2003)
[29] H. Bendele, J. Comp. Physiol. A **158**, 405 (1986).

Trumpet and accordion instabilities of a viscous jet.

Trumpet and accordion instabilities of a viscous jet.

Frederic Chevy [1], Elise Lorenceau [2]

[1] *Laboratoire Kastler Brossel, École Normale Supérieure, Paris, France*
[2] *DEAS, Harvard University, Cambridge 02138 USA*

Abstract

In this paper, we describe the profile of the air film entrained by a liquid jet impinging a bath of the same liquid. We show both experimentally and theoretically that depending on the viscosity of the liquid two regimes can be observed: for high viscosity the air film is similar to the bell of a trumpet while in the low viscosity regime, the jet crumples up through an instability mixing Rayleigh-Plateau and Kelvin-Helmholtz mechanisms.

1 Introduction

Although the entrainment of air bubbles in a liquid bath is a commonly observed phenomenon that leads for instance to the formation of foam in breaking waves, it can prove undesirable in many industrial situations such as the pouring of a viscous liquid (typically a polymer or a molten metal) in a mould . The production of bubbles can then be severely detrimental to the quality of the moulding. In some other cases, gas entrainment might be useful, as for example in the aeration of rivers or some water treatment processes where bubbles, entrained by jets or waterfalls and then dispersed into water, play a major role [1].

Several studies have recently tried to understand the mechanism of air-entrainment in the simple configuration of a liquid jet impinging a bath of the same liquid [1, 2, 3]. In the case of viscous liquids, it has been shown in particular that after penetrating the bath the jet is isolated from the quiescent liquid by a thin ($\sim$ 10 μm) air film [1]. However, this air film is not stable and breaks up into bubbles as observed in Fig. 3. Hereafter, we shall present a complementary study focusing on the stability of the gaseous film that might provide a first step towards a better understanding of the break-up mechanism of the entrained film. In what follow, we shall first describe the experimental setup and results for liquids of different viscosities, then present the theoretical analysis of this problem and finally, we shall compare our theoretical predictions with our experimental observations.

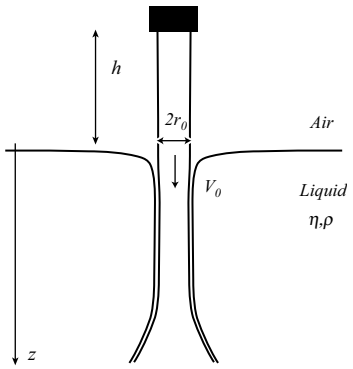

Figure 1: Experimental setup : a jet of viscous liquid of radius R falls from a height h in a bath of the same liquid. When the impact velocity is high enough, a thin air film is entrained inside the bath and wraps the jet.

2 Experimental setup

We consider a plunging jet falling from a nozzle located at a distance h above a pool filled up with the same liquid (Fig. 1). The dimensions of the pool are large enough to consider it as infinite [4]. The liquid is a silicon oil of density ρ. Its dynamical viscosity η ranges from 100 to 1000 mPa.s and was chosen to ensure the formation of an air-wrapping. Finally, the interfacial tension between air and silicon oil is denoted as $\gamma \sim 20$ mN/m. The velocity of the impinging jet is controlled by the distance h (larger than 10 cm) and is in the range of 1-3 m/s. The radius r_0 of the impinging jet before the impact varies from 1 to 3 mm. The mean velocity V_0 of the jet before the impact is evaluated by following the motion of small air bubbles located in the jet with a fast camera. Both these quantities were measured for each experiment. When the jet impinges the pool with a velocity V_0 large enough, it entrains with it a thin sheet of air [1]. This film of air isolates the liquid jet from the rest of the bath for several centimeters, after which the air film breaks up as observed on Fig. 2.

3 Experimental observations : the two "instruments"

Depending on the viscosity of the liquid, the jet takes different shapes as can be seen on Fig. 2. When the viscosity of the liquid is larger than 0.8 Pa.s, it widens like the bell of a trumpet. In this regime, the shape of the jet profile is a simple consequence of the viscous deceleration. Indeed, for high viscosities, we expect the liquid to strongly decelerate after penetrating the bath: due to mass conservation this leads to an increase of the radius and thus to the trumpet shaped jet observed on Fig 2.a). Let us denote respectively as $r(z)$, $V(z)$ and $Q(z) = \pi r(z)^2 V(z)$ the radius, the velocity and the flow rate of the jet at depth

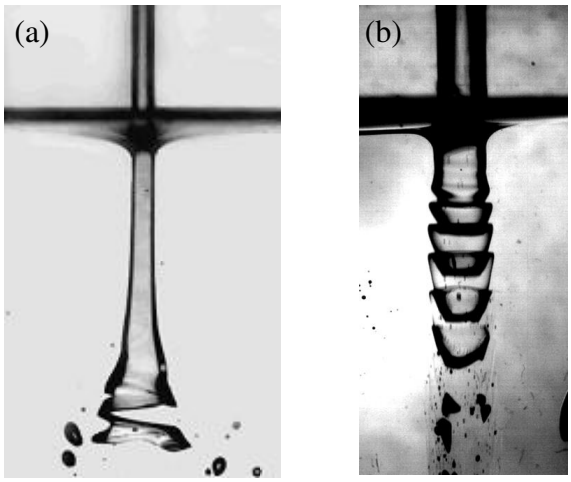

Figure 2: Shape of a liquid jet entraining an air film. (a) For a liquid of high viscosity (dynamical viscosity $\eta = 970$ mPa.s), the jet opens like the bell of a trumpet. (b) For intermediate viscosities ($\eta = 100$ mPa.s) the jet crumples-up like an accordion.

z (see Figure 1). On Fig. 3 the following physical quantities as a function of the depth z: the measured speed (open squares), the flow rate $Q(z)$ (black lozenge) and the speed $V' = \overline{Q}/\pi r(z)^2$ deduced from the analysis of the shape of the trumpet and from the measured mass flow $\overline{Q}$ (continuous line) . The results clearly indicate that along z, Q is indeed constant and confirms that the trumpet bell shape can be explained by the simple mass-conservation argument.

For low enough viscosities, the velocity does not decrease significantly along the jet and the break-up mechanism involves a more dramatic behavior of the air film that crumples up like an accordion as observed on Fig. 2.b). The characteristic wavelength of the perturbation, denoted henceforth as λ, is here of the order of the radius of the jet (~ 2 mm wide). We might imagine two simple scenarios for this instability of the interface, based either on the Rayleigh-Plateau (instability of a cylinder under capillary forces) or the Kelvin-Helmholtz mechanisms (instability of a sheared interface). The Kelvin-Helmholtz mechanism is known to select wavelengths of the order of the shearing distance, that is the air film thickness, here ten micrometers [5]. The observed wavelength of the disturbance being of the order of several millimeters, this scenario is therefore unlikely to be responsible for the crumpling observed here. The case of the viscous Rayleigh-Plateau instability with inner and outer fluids of same viscosities was studied by Tomotika [6, 7, 8] who showed that the most instable wavelength was of the order of the jet length. Once more, this contradict our experimental observations, that show that that λ is actually much smaller than the jet length.

To summarize, neither Kelvin-Helmholtz nor viscous Rayleigh-Plateau instabilities seem to provide the correct value for the wavelength of the instability

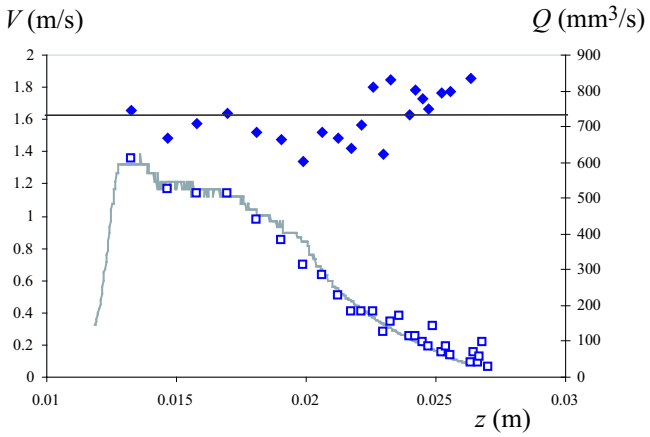

Figure 3: Conservation of the mass flow in the trumpet. □: measured velocity. ♦: mass flow Q. Black line: flow rate mean value $\overline{Q}$. Grey line: velocity $V'(z) = \overline{Q}/\pi r(z)^2$ calculated from the jet profile assuming a constant mass flow $\overline{Q}$.

observed experimentally. However, in the next section, we shall show that mixing them two can lead to a model capturing most of the experimental results.

4 Theoretical analysis

We model the jet as an infinite cylinder of radius R entraining an air film in a bath, infinite in all three dimensions. We shall call region 1 and region 2 respectively the inside and the outside of the jet. γ is the air/liquid surface tension, η the liquid viscosity of the fluid and ρ its density.

The main assumption of the model is that the viscosity of the air is so small with respect to that of the liquid that we can suppose the only role of the air film is to allow the velocity discontinuity at the interface between the jet and the bath without any shear stress. This assumption is confirmed by the study of the shape of the inverted meniscus at the impact spot [9] where it was proved that the observed meniscus is static, the quiescent liquid bath being totally isolated from the falling jet by the air film.

When the jet interface is unperturbed, we write the velocity field in region $i = 1, 2$ of liquid as V_i^0 with:

$$\mathbf{V}_1^0 = V_0 \mathbf{u}_z \quad (1)$$

$$\mathbf{V}_2^0 = \mathbf{0}, \quad (2)$$

where $\mathbf{u}_z$ is the unit vector pointing downwards in the z (vertical) direction. Let us stress once more that the slip at the interface between region 1 and 2 is

permitted by the presence of the air film, even though the liquid is supposed to be viscous.

The static pressure field P_j^0 is given by Archimedes law that is:

$$\begin{aligned} P_1^0 &= C_1 + \rho g z \\ P_2^0 &= C_2 + \rho g z, \end{aligned}$$

where C_1 and C_2 are two integration constants, related through Laplace law $C_1 - C_2 = 2\gamma/R$ (note the factor 2 due to the two air liquid interfaces that need to be crossed to go from region 1 to region 2).

Let us now perturb the velocity field $\mathbf{V}_j$ in region j that now reads $\mathbf{V}_j = \mathbf{V}_j^0 + \mathbf{w}_j$ with $w_j \ll V_0$. Linearizing the hydrodynamics equations for an incompressible fluid, we get for $\mathbf{w}_j$:

$$\nabla \cdot \mathbf{w}_j = 0 \tag{3}$$

$$\rho \left(\partial_t + \mathbf{V}_j^0 \cdot \nabla\right) \mathbf{w}_j = -\nabla p_j + \eta \nabla^2 \mathbf{w}_j, \tag{4}$$

where the perturbed pressure field P_j in region j reads $P_j = P_j^0 + p_j$.

From (3), we know that the velocity field perturbation $\mathbf{w}_j$ can be written as the curl of a vector potential $\mathbf{A}_j$. From Fig. 2.b), we notice that the jet profile is isotropic in the transverse plane. We shall then write in the cylindrical coordinates system (r, θ, z):

$$\mathbf{A}_j(r, \theta, z) = \psi_j(r) e^{i(kz - \omega t)} \mathbf{u}_\theta,$$

where ψ_j is the stream-function in region j and $\mathbf{u}_\theta$ is the unit orthoradial vector associated with the polar angle θ. In this case, the cylindrical components of the velocity field $\mathbf{w}_j$ are related to ψ_j through:

$$\mathbf{w}_j = \begin{pmatrix} -ik\psi_j \\ 0 \\ \partial_r \psi_j + \psi_j / r \end{pmatrix} e^{i(kz - \omega t)} \tag{5}$$

Taking the curl of the linearized Navier-Stockes equation (4) and noting that $\mathbf{A}_j$ satisfies the Coulomb gauge condition $\nabla \cdot \mathbf{A}_j = 0$, we see that ψ_j is solution of the following linear equation:

$$\left(D - k^2\right)\left(D - q_j^2\right)\psi_j = 0, \tag{6}$$

where D is the differential operator defined by $D\psi = \partial_r^2 \psi + \partial_r(r^{-1}\psi)$ and $q_j = \sqrt{k^2 - i(\omega - kV_j^0)}$ with $\mathrm{Re}(q_j) > 0$.

The solutions of the differential equation (6) can be expressed in terms of the modified Bessel functions of first and second kinds I_1 and K_1 [10]. Using the boundary conditions $\psi_j(r)$ finite for $r \to 0$ and $r \to \infty$, we get:

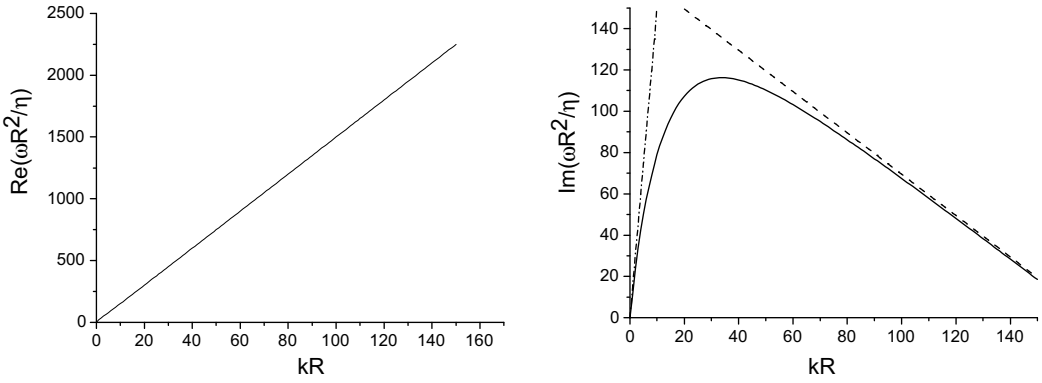

Figure 4: Dispersion relation $\omega(k)$ for $\gamma = 20$ mN/m, $\eta = 0.1$ Pa.s, $\rho = 1000$ kg/m^3, $R = 1$ mm and $V_0 = 3$ m/s. Analytical expansion for large (dashed line) and small (dash-dotted lines) k's.

$$\left\{ \begin{array}{rcl} \psi_1 & = & \alpha_1 I_1(kr) + \beta_1 I_1(q_1 r) \\ \psi_2 & = & \alpha_2 K_1(kr) + \beta_2 K_1(q_2 r) \end{array} \right. \tag{7}$$

After a calculation presented in appendix of this paper, the non penetration condition of the two liquid regions as well as the stress continuity in $r = R$ yield a linear system of four equations in α_j and β_j that possess non trivial solution if its determinant Δ is zero, that is if k and ω satisfy the dispersion relation:

$$\Delta(k, \omega(k)) = 0, \tag{8}$$

As usual, the instability criterion is given by the sign of the imaginary part of $\omega(k)$: the interface is unstable for $\sigma(k) = \mathrm{Im}(\omega(\mathrm{k})) > 0$ and the mode of wavevector $k_{\max}$ with the highest σ is the most likely to develop. Moreover, since the wave propagates at a group velocity $v_g = d\mathrm{Re}(\omega)/dk$, the length L_c other which the instability grows is given by:

$$L_c = \frac{v_g}{\sigma(k_{\max})}.$$

Fig. (4) presents a numerical solution of Eqn. (8) for typical experimental parameters. Let us first notice that, by contrast with the viscous Kelvin-Helmholtz scenario, we see that our model yields a most instable mode for a finite k (here $k_{\max} R \sim 35$). Also note that the most unstable mode of a cylindrical thread surrounded by a liquid of the same viscosity (which is an extension of the Rayleigh Plateau instability) was found to be equal to $k_{\max} R \sim 0.56$ [7]. Hence, the presence of the film of air allow the system to select smaller wavelengths of disruption. To get a better insight on this dispersion relation we performed asymptotic expansions for low and large wavevectors.

On the one hand, we get for $k \gg k_{\max}$:

$$\omega_{\mathrm{RP}} = (V_0 - i\gamma/\eta)k/2 + 3\rho i(V_0^2 + \gamma^2/\eta^2)/16\eta, \tag{9}$$

which is reminiscent of the high k Rayleigh-Plateau behavior for a viscous fluid [8].

On the other hand, for $k \ll k_{\max}$ (but with $kR \gg 1$ nevertheless), our expansion yields:

$$\omega_{\mathrm{KH}} = (i+1)kV_0/2, \tag{10}$$

which is the Kelvin-Helmholtz dispersion relation [8].

Both asymptotic expansions fit well with the exact numerical result (see Fig. 4) and lead to the following physical consequences:

- The relation $\mathrm{Re}(\omega) = V_0 k/2$ is valid in both regimes and yields for the wave group velocity

$$v_g = V_0/2 \tag{11}$$

- $k_{\max}$ is given by the cross-over between the Rayleigh-Plateau and Kelvin-Helmholtz behaviors, that is $\omega_{\mathrm{RP}} \sim \omega_{\mathrm{KH}}$. For large capillary numbers $\mathrm{Ca} = V_0\eta/\gamma$, this condition reads:

$$k_{\max} R \sim \mathrm{Re}, \tag{12}$$

  where $\mathrm{Re} = \rho V_0 R/\eta$ is the Reynolds number of the jet.

  Beyond this mere scaling law, an exact calculation can be performed that yields in the limit of large Re:

$$k_{\max} R \sim \frac{26}{35}\mathrm{Re}. \tag{13}$$

- Finally according to Eqn. (11) and (12) the instability length scales like:

$$L_{\mathrm{c}} \sim \frac{R}{\mathrm{Re}} \sim \frac{1}{k_{\max}}. \tag{14}$$

  In other words, L_{c} scales like the wavelength $\lambda_{\max} = 2\pi/k_{\max}$ of the most instable mode.

5 Comparison with the experiment

We checked equations (11), (12) and (14) by comparing them to experimental data obtained with silicon oils of viscosities $\eta \sim 100, 160$ and 350 mPa.s for which accordion instabilities could be observed. These results are summarized on Fig. (5) and show a nice agreement between theory and experiments.

- We first compared the jet velocity to that of the waves propagating at the interface. Data from Fig. 5.a) show that the experimental result follow accurately the behavior predicted by Eqn. (11).

- Although the scaling law (9) looks satisfied, the prefactor obtained experimentally is different from that predicted by a factor about 4. One explanation for this discrepancy might be that, as observed on fig. (2.b), the wavelength of the perturbations increases when propagating along the jet, probably because some non linear effects. Since our linear stability calculation is performed in the weak perturbation limit, the measured wavelength is necessarily larger than that expected theoretically.

- We used the length of the jet as an estimation of the instability length L_c: indeed, the faster the accordion instability develops and the faster the jet breaks up. We observe experimentally a linear variation of L_c versus wavelength in agreement with the scaling law (14). Let us note that the measurement of L_c is not very precise due to large temporal fluctuations of the end of the jet.

6 Conclusion

We have studied the dstabilisation of a viscous-jet falling into a pool of the same liquid but isolated from it by a thin sheet of air. We found that the jet, as a jet falling from a nozzle into air, is submitted to the Rayleigh-Plateau instability. Moreover, as the film of air is strongly sheared by the two liquid media (the moving jet and the quiescent bath) it undergoes the so-called Kelvin-Helmholtz instability. The observed wavelength of the disturbance of the jet is in good agreement with a model mixing this two instabilities. However, lot of works remain to be done especially in the trumpet-like regime, where a quantitative analysis of the velocity of the jet should be performed. Moreover, we have not focused so far on the cross-over between the trumpet and accordion regimes.

We wish to thank E. Raphaël, C. Clanet and D. Quéré for helpful and simulating discussions.

A Hydrodynamics

We present in this appendix some details of the calculation leading to the analytical expression of Δ (Eqn. 8). The analysis is based on the boundary conditions of the system at the air/liquid interface.

Non penetration: When the system is perturbed, the interface between regions 1 and 2 is no longer cylindrical but is now characterized by the local radius $r(z) = R + \xi(z,t)$ with our new unit system. The displacement ξ is the related to the velocity field at interface by the relation:

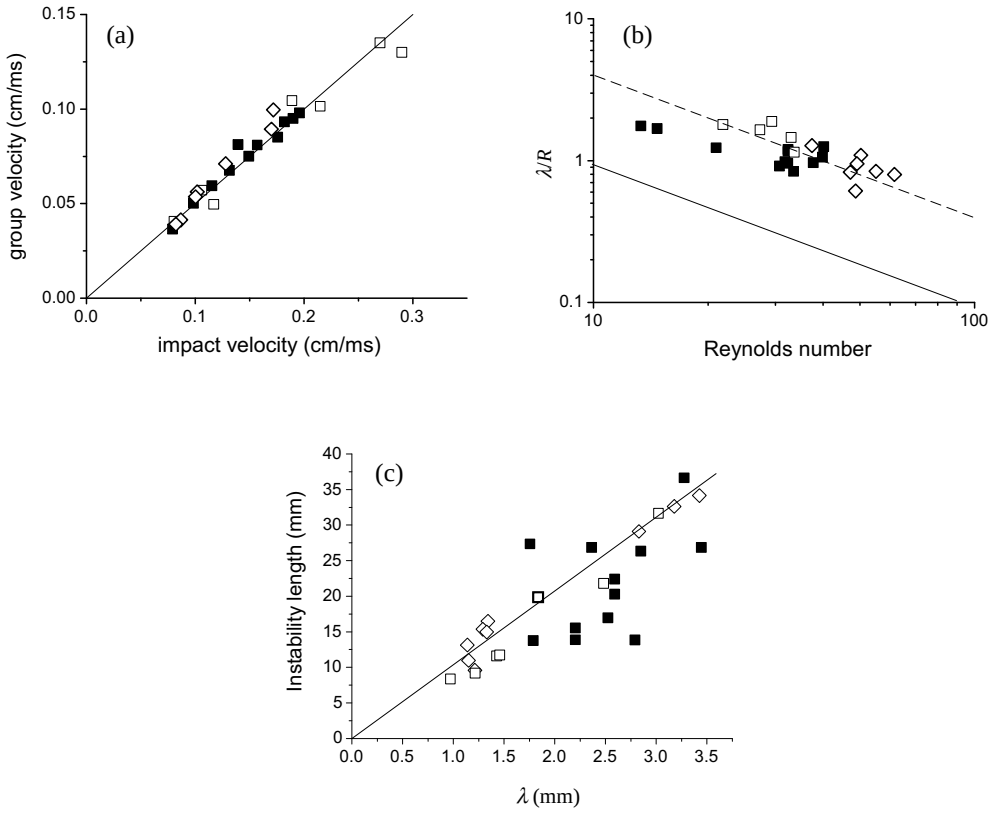

Figure 5: Comparison between theoretical predictions and experimental results for various silicon oils (■: $\eta = 100$ mPa.s; □: $\eta = 160$ mPa.s; ◊: $\eta = 350$ mPa.s). (a) Measured group velocity v_g of the perturbation vs. jet velocity. The straight ligne is the theoretical prediction $v_g = V_0/2$. (b) Evolution of the instable wavelength $\lambda_{\max}$ vs the Reynolds number Re=$\rho V_0 R/\eta$. Experimental data are compared to the prediction of Eqn 13 (full line) as well as the best-fitting law $\lambda/R \sim 33/\mathrm{Re}$ (dashed line). (c) Length of the trumpet vs. unstable wavelength λ. Full line: best fitting linear behavior.

$$\frac{D\xi}{Dt} = \mathbf{v}_1(r = R^-) \cdot \mathbf{u}_r = \mathbf{v}_2(r = R^+) \cdot \mathbf{u}_r,$$

where D/Dt is the Lagrangian time derivative operator. Using Eqn. (5), we get at the leading order in the perturbation :

$$(-i\omega + ikv_j^0)\xi = -ik\psi_j, \tag{15}$$

with $j = 1, 2$. Using the explicit expression (7) for $\psi_{1,2}$ we get the first equation for the α_j and β_j:

$$\frac{I_1(kR)}{\omega - kV_0}\alpha_1 + \frac{I_1(q_1R)}{\omega - kV_0}\beta_1 - \frac{K_1(kR)}{\omega}\alpha_2 - \frac{K_1(q_2R)}{\omega}\beta_2 = 0. \tag{16}$$

Shear stress: we have seen above that the main effect of the air film was to cancel shear stress at the interface between the jet and the bath. In other word, it imposes the boundary conditions $\sigma_\parallel(r = R^+) = \sigma_\parallel(r = R^+) = 0$, where $\sigma_\parallel$ is the stress component tangent to the interface.

Since $\sigma_\parallel = \eta(\partial_z w_{j,r} + \partial_r w_{j,z})$, we get after some algebra:

$$(k^2 + D)\psi_j = 0,$$

where D is the differential operator introduced at Eqn. (6). In terms of α_j and β_j, the previous equation reads:

$$2k^2 I_1(kR)\alpha_1 + (k^2 + q_1^2)I_1(q_1R)\beta_1 = 0 \tag{17}$$

$$2k^2 K_1(kR)\beta_1 + (k^2 + q_2^2)K_1(q_2R)\beta_2 = 0 \tag{18}$$

Normal stress: the last equation is given by the Laplace law relation normal stresses $\sigma_\perp$ on the sides of the interface. We have indeed:

$$\sigma_\perp(r = R^+) - \sigma_\perp(r = R^-) = 2\gamma C,$$

where C is the mean curvature of the interface. Let us also note the factor 2 in the right hand side of the equation which is due to the two air/liquid interfaces that need be crossed to go from region 1 to region 2.

At the first order in the perturbation, C is related to the surface deformation ξ by :

$$C = \frac{1}{R} - \partial_{zz}\xi - \frac{\xi}{R^2} = \frac{1}{R} + (k^2R^2 - 1)\frac{\xi}{R^2}.$$

Using (15) for $j = 1$, C can be expressed in terms of ψ_1 since we have:

$$C = \frac{1}{R} + (k^2R^2 - 1)\frac{k}{\omega - kV_0}\frac{\psi_1(R)}{R^2}.$$

The normal stress reads in region j :

$$\sigma_{\perp,j} = 2\eta\partial_r w_{j,r} - p_j,$$

that is in terms of vector potential :

$$\sigma_{\perp,j} = -2ik\eta\partial_r\psi_j - p_j.$$

The pressure field p_j is calculated using the z component of the linearized Navier-Stockes equation (4), that is:

$$p_j = \frac{\eta}{ik}\nabla^2 w_{j,z} + \frac{\rho}{k}\left(\omega - kV_j^0\right) w_{j,z}.$$

In terms of α_j and β_j, this is also:

$$\begin{aligned} p_1 &= (\omega - kV_0)\frac{\rho}{k}\alpha_1(kI_1'(kR) + I_1(kR)/R) \\ p_2 &= \omega\frac{\rho}{k}\alpha_2(kK_1'(kR) + K_1(kR)/R) \end{aligned}$$

General result. Combining the previous equations, we finally get for Δ :

$$\begin{vmatrix} \frac{I_1(kR)}{\omega - kV_0} & \frac{I_1(q_1R)}{\omega - kV_0} & -\frac{K_1(kR)}{\omega} & -\frac{K_1(q_2R)}{\omega} \\ 2k^2 I_1(kR) & (k^2+q_1^2)I_1(q_1R) & 0 & 0 \\ 0 & 0 & 2k^2K_1(kR) & (k^2+q_2^2)K_1(q_2R) \\ F_1(k,\omega) & F_2(k,\omega) & F_3(k,\omega) & -2ik^2q_2R^3K_1'(q_2R) \end{vmatrix},$$

with:

$$\begin{aligned} F_1 &= 2ik^3R^3I_1'(kR) - 2\frac{\gamma R}{\eta}\frac{k^2(k^2R^2-1)}{\omega - kV_0}I_1(kR) + \frac{\rho R^2(\omega - kV_0)}{\eta}(kRI_1'(kR) + I_1(kR)) \\ F_2 &= 2ik^2q_1R^3I_1'(q_1R) - 2\frac{\gamma R}{\eta}\frac{k^2(k^2R^2-1)}{\omega + kV_0}I_1(q_1R) \\ F_3 &= \left(-kR(\rho R^2\omega/\eta + 2ik^2R^2)K_1'(kR) - \rho\omega R^2K_1(kR)/\eta\right) \end{aligned}$$

Large wavevector approximation. In the limit $kR \gg 1$ which is relevant for experiments, Δ can be simplified using the asymptotic expansion of Bessel function. It is known indeed that for $x \to +\infty$ [10]:

$$\begin{aligned} I_1'(x) &\sim I_1(x)(1 - 1/2x + 3/8x^2 + ...) \\ K_1'(x) &\sim -K_1(x)(1 + 1/2x + 3/8x^2 + ...). \end{aligned}$$

Equations (10) and (9) are derived in this approximation by assuming $\omega(k) = a_0 + a_1k + ...$ and expanding Δ for low and large wavevectors.

References

[1] A. K. Bin, Chem. Eng. Sci. **48**, 3585 (1993).

[2] C. Clanet and J.C. Lasheras, Phys. Fluids **9**, 1864, 1997

[3] C. D. Ohl, H. N. Oguz, A. Prosperetti, Phys. Fluids **12**, 1710, 2000

[4] We checked in particular that the results presented here were independent of the shape or the size of our recipient.

[5] E. Lorenceau, F. Restagno and D. Quéré, Phys. Rev. Lett. **90**, 184501, 2003.

[6] Lord Rayleigh, Phil. Mag. **34**, 145, 1892

[7] S. Tomotika, Proc. Roy. Soc. London A **150**, 322, 1935

[8] S. Chandrasekar, *Hydrodynamic and hydromagnetic stability*, Oxford University Press, Oxford (1961).

[9] E. Lorenceau, J. Eggers and D. Quéré, to be published.

[10] M. Abrahamowitz and I.A. Stegun, *Handbook of mathematical functions*, Dover Publications, New York (1972).

Chapitre 2

Avatars d'une goutte de pluie : instabilité et impact en mouillage nul.

La pluie c'est flic floc
La pluie c'est plic ploc
La pluie c'est flitch flatch floutch
Bloub chclouf
Et il fait beau Anne Sylvestre : la pluie c'est Flic Floc

2.1 Introduction

Depuis sa naissance dans les nuages jusqu'à sa chute et son impact avec le sol, une goutte de pluie passe par plusieurs étapes dont la compréhension est fondamentale à la prévision des précipitations en météorologie. Dans ce chapitre, nous aborderons tout d'abord la question de la taille des gouttes de pluie : Il est en effet notable que, bien que les plus gros grêlons fassent plusieurs centimètres de diamètres, les gouttes de pluie sont elles toujours millimétriques. En étudiant la chute de gouttelettes d'eau dans l'air, nous avons montré que cette taille maximale provenait d'une instabilité hydrodynamique déstabilisant les grosses gouttes. Plus les gouttes sont grosses, plus leur chute est rapide et plus la friction avec l'air les déforme, jusqu'à l'explosion (cf. *Shape and instability of free-falling liquid globules*).

Lorsque la goutte touche le sol, la dynamique de l'impact dépend très fortement des propriétés de mouillage du liquide sur l'interface. Alors que dans la plupart des cas, la goutte ne redécolle pas après l'impact, dans cer-

taines conditions très particulières, la goutte peut se comporter comme une balle élastique et rebondir sur la surface. En effet, si l'impact est suffisamment bref, l'air entre la goutte et la surface n'a pas le temps d'être évacué et il se forme un matelas d'air sur lequel la goutte rebondit pratiquement élastiquement[1] (Fig. 2.1). L'étude du rebond sur une surface parfaitement non-mouillante (on parle aussi de *super-hydrophobie*) a d'importantes implications pratiques : ainsi le développement de nouvelles générations de pare-brise ou de revêtements de salle de bain exige de développer des procédés industriels de traitements rendant les surfaces parfaitement hydrophobes de façon à empêcher l'adhésion de l'eau[2]. Ces situations peuvent être réalisées soit en traitant le liquide lui-même (par exemple en recouvrant la goutte de spores de lycopodes [4]), soit en utilisant des surfaces microtexturées (par exemple les feuilles de certaines plantes telles que le ginkgo biloba) ou enfin en chauffant la surface au dessus d'une température critique, dite température de Leidenfrost [5]. L'existence de la superhydrophobie était connue depuis bien longtemps (les travaux de Leidenfrost dates du XVIII^e siècle), mais seul le développement des caméras ultra-rapides pouvant filmer à des vitesses de plusieurs milliers d'images par secondes a permis une étude de la dynamique du rebond, travail qui a fait notamment l'objet de la thèse de Denis Richard au Collège de France [6] et à laquelle les travaux présentés ci-dessous font suite. Lors de ces travaux, D. Richard avait en particulier montré le lien profond entre le rebond sur une surface superhydrophobe et le mode de vibration quadrupolaire de la goutte[3]. Nous avons approfondi ce lien en développant un modèle simple permettant d'expliquer les variations du temps de contact lors d'un impact, et en particulier de préciser le rôle de la gravité à basse vitesse (*Water spring : A model for bouncing drops*). Dans le cas de rebond sur des plaques chaudes, nous avons ensuite montré que pour des hauteurs de chute de faible amplitude, le rebond était parfaitement élastique ce qui permettait à la goutte de rebondir pratiquement indéfiniment (*On the elasticity of an inertial liquid shock*).

[1] Remarquons au passage que ce mécanisme de rebond est aussi présent lors des collisions entre gouttes de pluies dans les nuages et limite la croissance de la taille des gouttes en inhibant leur coalescence [2].

[2] On peut noter que d'autres applications demandent au contraire des conditions d'hydrophilie parfaite : Ainsi, si l'on cherche à développer des techniques d'épandage permettant d'empêcher les gouttelettes d'engrais de rebondir sur les feuilles des plantes à traiter, on cherchera à favoriser le mouillage des feuilles par l'eau, limitant ainsi le déversement d'engrais dans les sols et la pollution des nappes phréatiques [3].

[3] Le mode quadrupolaire correspond à l'oscillation libre de l'ellipticité.

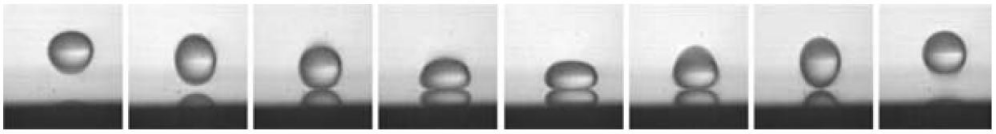

FIG. 2.1 – Rebond d'une goutte millimétrique en situation de mouillage nul (ici sur une plaque chauffée à 300 degrés Celsius). L'intervalle entre deux images vaut 2.5 ms.

2.2 Déformation et instabilité d'une goutte en chute libre

La connaissance de la forme précise des gouttes de pluie est d'une importance capitale pour l'évaluation des précipitations déduite des données radars en météorologie. Contrairement à l'opinion couramment répandue, une goutte de pluie n'a pas une forme de larme : lorsque la goutte est de petite taille et que la tension de surface domine tous les autres phénomènes, elle est sphérique [1] et s'aplatit en forme de crêpe lorsqu'elle est suffisamment grosse. Cette forme résulte de la compétition entre la friction de l'air tendant à écraser la goutte et la tension de surface cherchant plutôt à la garder sphérique. Lorsque la vitesse de la goutte reste faible, on peut montrer que l'équilibre des deux tendances aboutit à une simple déformation quadrupolaire du profil de la goutte, ainsi qu'on l'observe sur la figure 2.2. Lorsque la vitesse devient trop importante, les déformations induites par la friction conduisent à une déstabilisation de la goutte et à son éclatement. Pour évaluer le critère d'éclatement des grosses gouttes, on note pour commencer que dans les situations de grand nombre de Reynolds typiques des conditions expérimentales étudiées, la traînée turbulente subie par une goutte de rayon R se déplaçant à une vitesse V est de l'ordre de $F_t = \rho_a V^2 R^2$, où ρ_a désigne la masse volumique de l'air. La goutte éclate lorsque F_t domine la tension de surface, soit $F_t \gtrsim \gamma R$. Cependant, dans un mouvement de chute libre dans l'air, la vitesse d'une particule, et donc sa traînée, ne peut pas devenir arbitrairement grande et se trouve bornée par la vitesse limite résultant de l'équilibre entre poids et friction. Pour une goutte de masse m, on a donc l'inégalité $F_t < mg$, ce qui donne pour la condition d'éclatement $R^2 \gtrsim \gamma/\rho g$. La longueur caractéristique $\sqrt{\gamma/\rho g}$ (ou *longueur capillaire*) est conventionnellement notée κ^{-1} et vaut dans le cas de l'eau $\kappa^{-1} \sim 2.7$ mm. Ce simple argument d'ordre de grandeur explique pourquoi, contrairement

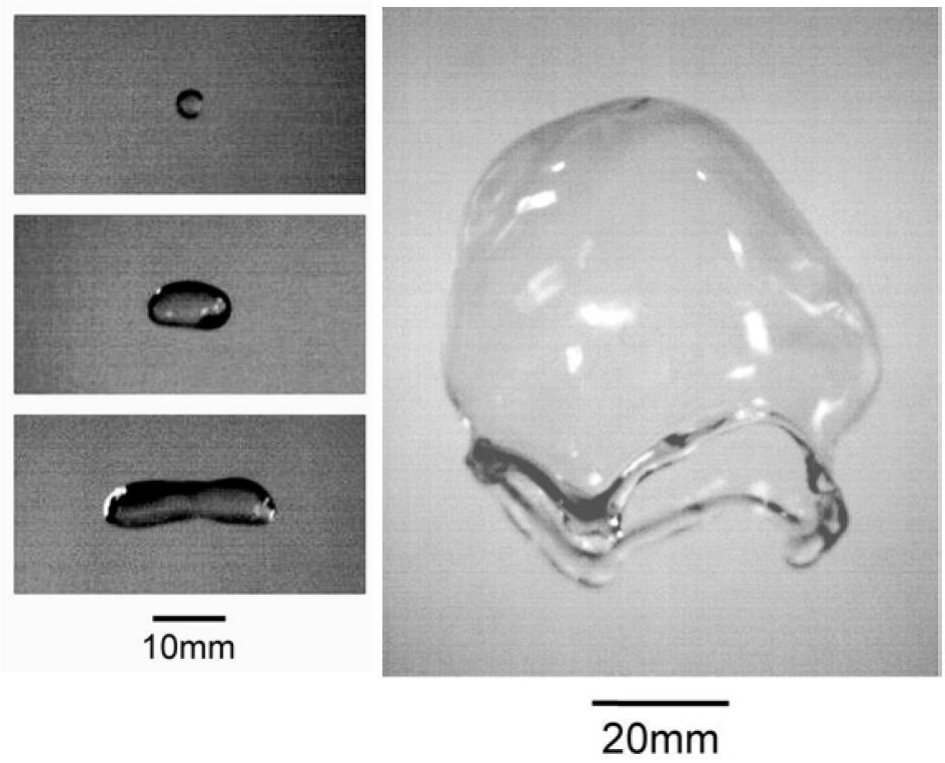

FIG. 2.2 – Allure de gouttes en chute libre. Gauche : gouttes en dessous du seuil d'instabilité. Droite : instabilité d'une grosse goutte résultant de la compétition entre traînée et capillarité.

aux grêlons, il n'existe pas de goutte de pluie centimétrique[4] et pour confirmer ce scénario et préciser le mécanisme d'instabilité, nous avons généré une "pluie" artificielle à l'aide d'un simple tuyau d'arrosage que nous avons laissé pendre d'une fenêtre du cinquième étage du Collège de France. Sous l'effet de l'instabilité de Rayleigh-Plateau, le cylindre liquide se déstabilise en gouttes de taille centimètrique et nous avons suivi leur évolution en plaçant une caméra rapide au quatrième puis au troisième étage du bâtiment[5].

Sur certaines images, il a été possible d'observer l'explosion des gouttes et

[4]Le grêlon le plus gros jamais observé faisait 15 cm de diamètre.

[5]Le choix des étages correspond à la première génération d'expériences et permettait de bénéficier de la lumière du soleil le matin. La deuxième génération, conçue par Étienne Reyssat, disposait d'une source d'éclairage autonome et a été réalisée à des étage moins élevés.

comme on le constate sur la figure 2.2, l'instabilité procède par le gonflement de la goutte, à la manière d'un parachute : son déclenchement peut être relié au mécanisme de Rayleigh-Taylor qui décrit l'instabilité d'une interface liquide lorsqu'un fluide dense (ici l'eau) est accéléré dans un liquide moins dense (l'air)[6] et au fur et à mesure de l'augmentation du volume de la protubérance, le film liquide s'amincit puis finit par se rompre lorsque son épaisseur atteint une dizaine de microns.

2.3 Super-hydrophobie et rebonds

L'impact d'une goutte de pluie sur le sol est essentiellement par la compétition entre capillarité (et plus généralement mouillage) et inertie. En effet, si l'on considère une goutte millimétrique tombant de sa propre hauteur, le nombre de Reynolds[7] associé est de l'ordre de 100. En particulier, lors d'un choc sur une surface, l'énergie cinétique initiale est temporairement stockée sous forme d'énergie de déformation de la goutte puis, si la ligne de contact ne s'ancre pas sur le substrat, peut être restituée pratiquement dans sa totalité[8] : c'est l'étude expérimentale ce type de situation où la goutte rebondit pratiquement élastiquement que nous allons aborder dans ce paragraphe.

Pour un impact à faible vitesse, la déformation de la goutte est de faible amplitude et peut donc être décrite par une théorie linéaire dominées par deux modes - le mode quadrupolaire associé à l'oscillation de l'ellipticité de la goutte et le mode dipôlaire de translation du centre de masse. Nous avons développé cette idée d'un couplage entre mouvement du centre de masse et un ressort fictif décrivant le mode quadrupolaire dans *Water spring : A model for bouncing drops* [9]. Cette approche simplifiée nous a permis de remplacer un problème complexe de mécanique des fluides en un simple exercice de mécanique du point grâce auquel nous pouvons calculer le temps de contact en fonction de la vitesse d'impact en prenant en compte les effets de la gravité (Fig. 2.3). On peut en effet montrer que l'écrasement de la

[6] Ce mécanisme d'instabilité explique ainsi pourquoi un récipient retourné se vide lorsque son diamètre est suffisamment grand, et permet aussi de comprendre la forme des nébuleuses stellaires.

[7] Le nombre de Reynolds Re compare les effets d'inertie et de viscosité, et pour une goutte de rayon R se déplaçant à une vitesse V, celui-ci vaut $\mathrm{Re} = VR\rho/\eta$, où ρ est la masse volumique de la goutte et η sa viscosité - $\eta \sim 10^{-3}$ Pa.s pour l'eau.

[8] Notons cependant que cette image simple n'est plus valable à haute vitesse, car une partie de l'énergie cinétique initiale est alors perdue dans les écoulements tourbillonaires internes à la goutte [7].

goutte durant l'impact suit les mêmes équations que celles d'un ressort de raideur $\sim \gamma$ et de longueur à vide $\sim R$. On prédit alors que le temps de contact à vitesse modérée (c'est-à-dire lorsque l'énergie cinétique l'emporte sur l'énergie potentielle de pesanteur de la goutte, mais reste dominée par les effets capillaire) est de l'ordre d'une demi-période d'oscillation du mode quadrupolaire $\pi\sqrt{\rho R^3/2\gamma}$ [8], ce qui est en bon accord avec les expériences (le désaccord entre le modèle du ressort et les données expérimentale est de seulement 15 %). En dessous d'une vitesse ~ 10 cm/s pour une goutte millimétrique, on observe une augmentation du temps de contact que l'on attribue à la gravité, ce que confirme le modèle ci-dessus (celui prédit que la gravité domine pour $V \lesssim V_c \sim (gR^3\kappa^2)^{1/2}$, qui donne le bon ordre de grandeur). Afin de confirmer expérimentalement cette interprétation, nous avons réalisé des impacts "inversés", dans lesquels la goutte est envoyée vers le haut sur une surface superhydrophobe renversée. Ainsi qu'on l'observe sur les données expérimentales et théoriques, on observe alors une inversion de la tendance et une diminution du temps de contact à basse vitesse (Fig. 2.3).

À très basse vitesse, les effets résiduels d'hystérésis de la ligne de contact[9] empêchent le redécollage de la goutte et limitent le coefficient de restitution sur une surface texturée à des valeurs typiques de l'ordre de 80%. Afin de contourner cet obstacle, nous avons mis à profit le phénomène de Leidenfrost, ou caléfaction, associé à l'apparition d'un mince film de vapeur sous une gouttelette déposée sur une plaque chaude. L'existence de ce film de vapeur, par définition sans défaut ni aspérité, permet de réaliser une situation de superhydrophobie quasi-parfaite dont l'étude à fait l'objet de la thèse d'Anne-Laure Biance. Nous avons pu constater qu'à très basse vitesse, le coefficient de restitution était pratiquement de 100% (Fig. 2.4) ce qui permettait d'observer de longues séquences de rebonds (jusqu'à un millier !) [10]. À plus haute vitesse, nous avons montré que le coefficient de restitution variait comme $1/V$, ce qui correspond à une vitesse de redécollage indépendante de la vitesse initiale. Cette propriété a pu être comprise en utilisant le modèle du ressort discuté précédemment. En effet, pour des grandes vitesses d'impact, la goutte prend une forme de crêpe d'épaisseur très faible devant le rayon initial. Si l'on identifie la longueur à vide du ressort avec le rayon de la goutte, la compression du ressort fictif sature donc à R et l'énergie cinétique restituée devient donc indépendante de la vitesse initiale. Pour les gouttes les plus grosses, le coefficient de restitution s'effondre brutalement,

[9] L'hystérésis de la ligne de contact correspond à des angles de raccordement θde la surface du liquide avec le substrat différents lors de l'étalement et la rétractation.

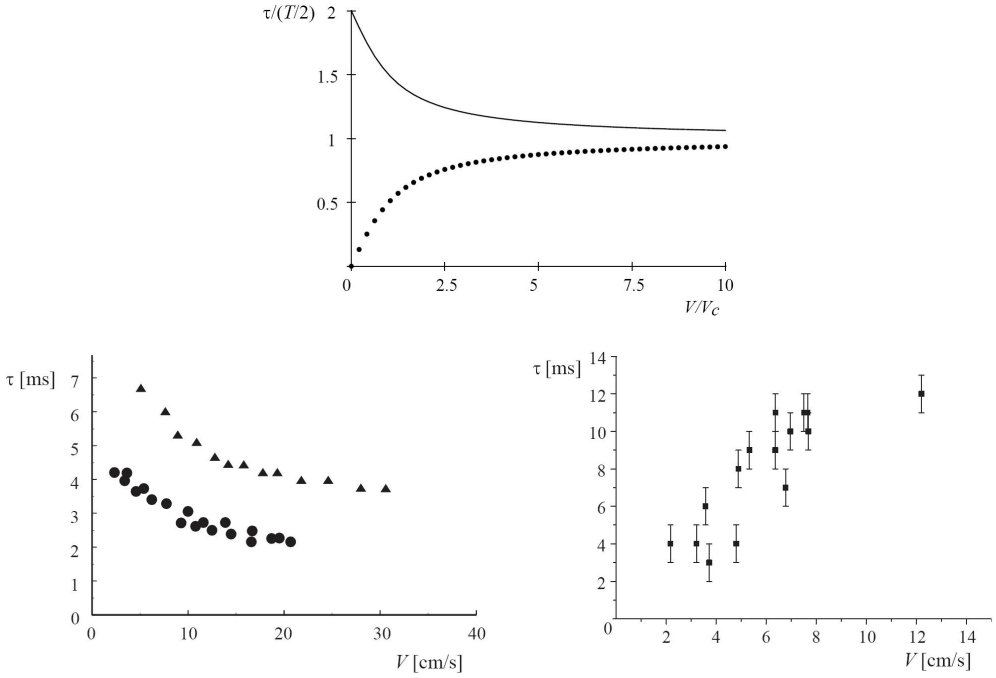

FIG. 2.3 – Evolution du temps de contact τ avec la vitesse V et influence de la gravité. Courbe du haut : prédiction du modèle du ressort pour un impact normal (trait plein) et en gravité inversée (pointillé). T désigne la période du mode quadrupolaire (que l'on identifie à la fréquence propre du ressort) et V_c désigne la vitesse au dessus de laquelle la gravité devient négligeable. Courbes du bas : à gauche, évolution du temps de contact pour des impacts normaux de gouttes de rayon $R = 0.4$ mm (cercles) et $R = 0.6$ mm (triangles). À droite : impact inversé pour une goutte millimétrique. On obtient dans les deux cas la même monotonie que celle prédite par le modèle du ressort.

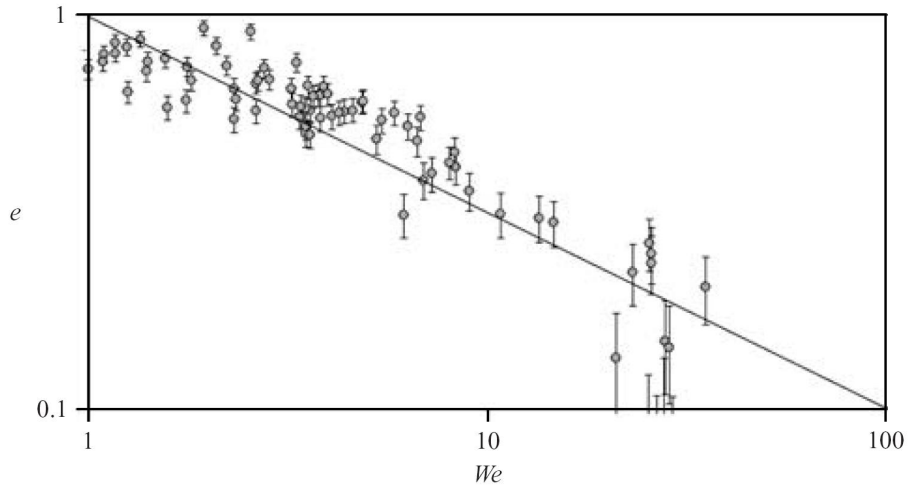

FIG. 2.4 – Évolution du coefficient de restitution e en fonction du nombre de Weber $We = \rho V^2 R/\gamma$ pour des gouttes d'eau, acétone, éthanol et azote liquide. La courbe en trait plein correspond à un comportement en $We^{-1/2}$.

un phénomène que nous avons attribué à l'effet de la gravité : l'énergie cinétique $\sim \gamma R^2$ après le choc n'est en effet plus suffisante pour vaincre la pesanteur et la goutte reste pas conséquent accrochée au substrat.

A très basse vitesse, lorsque le coefficient de restitution devient de l'ordre de 1, nous observons un intéressant verrouillage de phase entre les rebonds et le mode quadrupolaire excité à l'impact. On constate en effet que la durée du vol libre séparant deux impacts est strictement égale à la période du mode quadrupolaire. Nous avons pu montrer que cet accrochage résultait d'une dépendance du coefficient de restitution avec la phase du mode quadrupolaire au moment de l'impact. En effet, suivant celle-ci, la répartition entre mouvement du centre de masse et oscillation de l'ellipticité varie, et le comportement observé correspond à une conservation de l'énergie cinétique du centre de masse durant l'impact.

2.4 Conclusion

Les travaux précédents sur le rebond sur une surface non-mouillante ont montré que la dynamique du rebond pouvait, du moins qualitativement, être comprise dans un modèle de couplage du mode quadrupolaire et du mode dipolaire. L'accord quantitatif est cependant loin d'être encore atteint no-

tamment les mesures de l'évolution du temps de contact avec la vitesse dans le régime des petits nombre de Weber. Une cause possible serait l'existence d'une hystérésis de l'angle de contact qui, on le sait, limite le coefficient de restitution à 80% et pourrait par conséquent influer sur la durée de l'impact. Une autre possibilité, inspirée d'un travail récent de S. Courty *et al.* [12], et que nous développons avec E. Raphaël et A. Chepelianskii est l'existence de non-linéarités logarithmiques dans la fréquence de vibration qui pourraient expliquer une partie de la remontée du temps de contact à basse vitesse[10].

Du point de vue expérimental, les mesures de fréquence d'oscillation ou de temps de contact fournissent des sondes très précises des propriétés de la goutte, et peuvent ainsi être utilisées comme moyen de mesure de tension de surface dynamique. Ceci peut ainsi permettre d'étudier des phénomènes non-triviaux tels que la dynamiques des molécules tensio-actives dans les régime de forte excitation où les échange entre volumes et surface de la goutte sont importants. Enfin, comme nous l'avons mentionné au chapitre précédent, l'étude de goutte en caléfaction sur des surfaces liquides fournissent des systèmes expérimentaux prometteurs pour l'étude quantitative de la résistance de vague dans le régime de capillarité-gravité.

[10] Des corrections logarithmiques analogues ont déjà été observées et étudiées dans la dynamique de coalescence [13]

Bibliographie

[1] Hergé, *On a marché sur la Lune* (Casterman, 1954).

[2] G. Brant Foote, Journal of atmospheric sciences **32**, 390 (1975)

[3] V. Bergeron, D. Bonn, J.-Y. Martin et L. Vovelle, Nature **405**, 773 (2000)

[4] P. Aussillous, et D. Quéré, Nature **411**, 924 (2001).

[5] J. G. Leidenfrost, 1756 *De Aquae Communis Nonnullis Qualitatibus Tractatus*. Duisburg

[6] D. Richard, C. Clanet et D. Quéré, Nature **417**, 811 (2002)

[7] C. Clanet, C. Béguin , D. Richard, et D. Quéré *J. Fluid Mech.* **517**, 199 (2004).

[8] Lord Rayleigh, Proc. R. Soc. London **29**, 71 (1879).

[9] K. Okumura, F. Chevy, D. Richard, D. Quéré et C. Clanet, Europhys. Lett. **62**, 237 (2003).

[10] A.-L. Biance, F. Chevy, C. Clanet, G. Lagubeau et D. Quéré, J. Fluid Mech. **554**, 47 (2006).

[11] E. Reyssat, F. Chevy, A.-L. Biance, L. Petitjean et D. Quéré, Europhys. Lett., **80** 34005 (2007)

[12] S. Courty, G. Lagubeau et T. Tixier, PRE **73**, 045301 (2006)

[13] J. Eggers, J.R. Lister et H.A. Stone, J. Fluid Mech. **401**, 293 (1999).

Shape and instability of free-falling liquid globules

A Letters Journal Exploring the Frontiers of Physics

November 2007

EPL, **80** (2007) 34005
doi: 10.1209/0295-5075/80/34005

www.epljournal.org

Shape and instability of free-falling liquid globules

É. Reyssat[1], F. Chevy[1,2], A.-L. Biance[1], L. Petitjean[1] and D. Quéré[1]

[1] *Physique et Mécanique des Milieux Hétérogènes, UMR 7636 du CNRS, ESPCI - 75005 Paris, France*
[2] *LKB, ENS - 24 rue Lhomond, 75005 Paris, France*

received 7 September 2007; accepted 11 September 2007
published online 17 October 2007

PACS 47.20.Ma – Interfacial instabilities (*e.g.*, Rayleigh-Taylor)

Abstract – The velocity of a falling raindrop depends on its size, and thus so does its shape. Here we describe the different simple shapes which model drops falling in air. While millimetric drops remain spherical, owing to the action of surface tension, drops larger than the capillary length get flattened, as sessile drops on solids. Air penetrates still larger globules, which are observed to be unstable. They inflate till they burst, generating myriads of fragments.

We all know that drops or bubbles tend to be spherical, owing to surface tension: a sphere minimizes the surface area of a given volume. Here we discuss if this property still holds for drops falling in air, as a function of the drop size. In the limit of large velocities, inertial friction can exceed surface forces, which leads to spectacular deformations of the fluid globules [1], in both the drop and bubble cases [2]. If we restrict to raindrops, which mainly form from the coalescence of smaller globules, it must first be emphasized that they are polydisperse, with a typical size of a few millimeters [3,4]. Most studies on their shapes focused on sizes below 6 mm in diameter, which seems to be the largest drops hitting the ground [5,6]. The terminal velocity of raindrops was measured, and shown to result from a balance between weight and inertia [1,7]. These objects are nearly spherical, except the largest ones (about 4 mm in diameter), which are slightly flattened [1,8,9]. We first recall the well-known shapes and velocities in these regimes [1], using simple scaling laws. We then focus on centimeter-size drops, which can be flat objects if not too large, and instable globules if larger, which eventually break them in smaller fragments [1,10,11]. This, literally, is an avatar: this Sanskrit word originally meant "descent", before getting its modern meaning of "transformation". We describe and model the kinetics of these avatars, on which very few data are available.

The experiment is straightforward. A funnel filled with water is placed at the top of a building (height of 20 m). A jet of 10 mm in diameter comes out, and falls down, transforming in drops of different sizes (between a fraction of a millimeter and one centimeter), owing to the Plateau-Rayleigh instability and to air friction. Along the fall, high-speed cameras are placed to take images of the falling drops. The rate of imaging is 1000 frames per second. The drops fall at a velocity up to 10 m/s, requiring very short exposure times. The shutter time is typically set at 1/8000 s (*i.e.* less than 1 mm of fall), and the size of the image is about 30 cm allowing us to follow not only the shape, but also its evolution over about 30 ms.

The globule is characterized by its height h and equatorial diameter D, after 8 to 12 m of fall, allowing drops to reach their final velocity. The results are displayed in fig. 1a, where the full symbols correspond to stationary shapes. For small sizes ($D < 6$ mm), h and D are equal: droplets are spherical. For larger globules, h gets smaller than D, indicating a flattening of the profile; the average value of h saturates around 6 mm, whatever the drop size. These different shapes are displayed in fig. 1b. Figure 1a also shows the existence of a few "very" large objects (empty symbols), even bigger than the (at most) centimeter-size drops released from the funnel. These globules are unstable, and inflate during the experiment, which will be described hereafter.

If a drop has reached its terminal velocity V, air friction balances the weight. The fall takes place at a high Reynolds number (10^2 to 10^4), so that air viscosity can be ignored; the force balance can be dimensionally written $\rho_a V^2 R^2 \sim \rho g R^3$, for a spherical drop of radius R and density ρ, and denoting ρ_a as the air density [1]. Hence the terminal velocity can be classically written:

$$V \sim (\rho g R/\rho_a)^{1/2}, \tag{1}$$

V is found to be a few meters per second for millimeter-size drops. For a drop starting from the rest, V is reached after a distance $\rho R/\rho_a$ (about 1 m) much smaller than the observation distance (about 10 m). If falling drops are spherical, air friction must be weaker than surface forces, which tend to preserve the cohesion of liquid. This can be

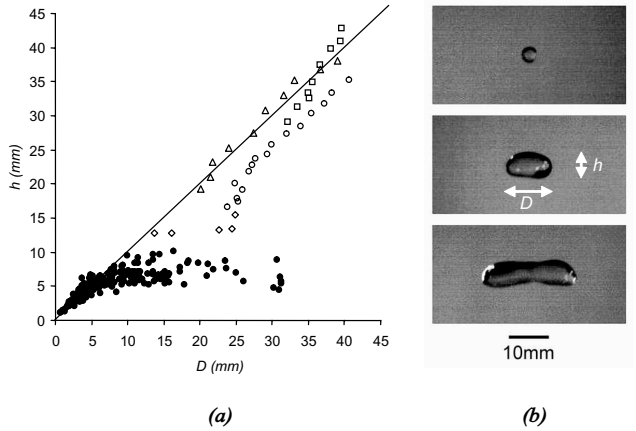

Fig. 1: Shape of a falling raindrop: the height h of the globule is plotted as a function of its equatorial diameter D, after 8 to 12 meters of free fall in air (a). Full symbols are for stationary states. Small drops are found to be spherical ($h = D$), while large ones tend to be flattened by the action of air (h becomes constant). The shapes are shown for three falling water drops of radius smaller, comparable, and larger than the capillary length (b). Empty symbols hold for larger globules; several data are displayed for each symbol, corresponding to different times. The data remain close to the line $h = D$, indicating an isotropic inflation of these very large objects (shown in fig. 4).

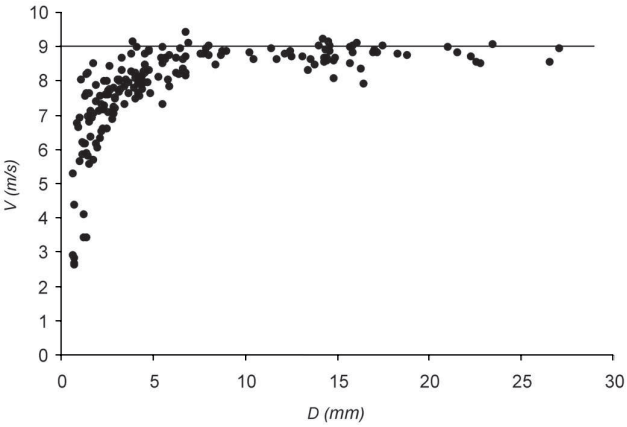

Fig. 2: Terminal velocity V of a water drop falling in air, as a function of its equatorial diameter D. For drops smaller than the capillary length, the velocity quickly increases with the size (eq. (1)). For larger drops, which are flattened (fig. 1a), the velocity saturates (eq. (4)).

written dimensionally: $\rho_a V^2 R^2 < \gamma R$, where γ is the liquid surface tension. Introducing the terminal velocity (eq. 1), the condition for sphericity simply reads [1]:

$$R < \kappa^{-1}, \tag{2}$$

where κ^{-1} the capillary length $= (\gamma/\rho g)^{1/2}$, that is, 2.7 mm for water at 20 °C. As observed in fig. 1a, a falling raindrop of characteristic size smaller than the capillary length (3 mm for water) indeed remains quasi-spherical.

What happens if inequality (2) is not satisfied? Figure 1 indicates that the drops are stretched along the horizontal plane, forming liquid "coins". The falling velocity of such an object is once again given by balancing the drag force with the weight. This writes $\rho_a V^2 R^2 \sim \rho g R^2 h$, but does not lead directly to the fall velocity, h and R being unknown (and related to each other by the volume conservation $\Omega \sim R^2 h$). A second equation expresses the equilibrium of the distorted shape. In the reference frame of the drop, air stream imposes a Bernoulli depression, which tends to stretch the globule in the horizontal plane. This pressure applies on a surface area which scales as Rh, so that the "stretching" force can be written $\rho_a V^2 Rh$. On the other hand, a force γR due to surface tension tends to restore a globular shape. Balancing these two forces ($\rho_a V^2 Rh \sim \gamma R$) provides (together with the fall equation) the drop height:

$$h \sim \kappa^{-1} \tag{3}$$

This thickness is independent of the drop size, as observed in fig. 1. The velocity of these stretched drops can be deduced from the same force balances. It reads

$$V \sim (\rho g \kappa^{-1}/\rho_a)^{1/2}, \tag{4}$$

V is the limit of eq. (1) as the drop reaches its maximum size ($R = \kappa^{-1}$) in the spheroidal state (eq. (2)). For larger objects ($R > \kappa^{-1}$), V becomes independent of the drop size. This final velocity is reached after a distance of about $\rho\kappa^{-1}/\rho_a$, *i.e.* a few meters (the drops are observed after 10 m of fall). Figure 2 shows the results for the terminal velocity as a function of the drop equatorial diameter. The velocity of a small drop (eq. (2)) is observed to strongly depend on its size (as expected from eq. (1)), while V indeed saturates for globules larger than the capillary length. The maximum velocity is around 9 m/s, of the order of the 5 m/s predicted by eq. (4) without any numerical coefficients.

We now wonder what happens for still larger globules. Such objects are not easy to generate: as they form, drops have a size often limited by the capillary length. However, owing to the centimetric aperture of our funnel, we could produce a few large drops of about 1 cm. These drops are unstable. In fig. 1a, we report the height h and diameter D of three of them (empty symbols); several data are displayed, corresponding to different times. All the data remain close to the line $h = D$, indicating an isotropic inflation. The largest observed diameter (not reported in fig. 1a) was 65 mm. The shape of such a globule is shown in fig. 3: the drop, initially full of water, becomes hollow, consisting of a thin aqueous shell surrounding air, and bounded at the bottom by a rim. These bag-shaped drops have been reported in wind tunnels [12] and in shock tubes [13,14]. They were also found to show up when accelerating a liquid drop either by a constant body force, or impulsively, and yielding backward-facing bags [15,16]. However, to the best of our knowledge, there

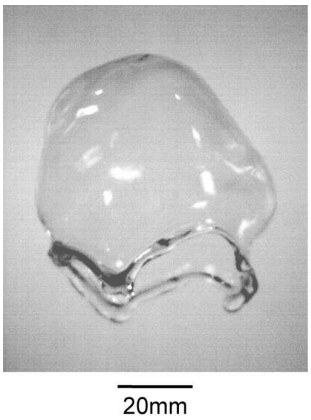

Fig. 3: Transient shape of a very large falling water drop (of initial diameter $D_o = 1.8 \pm 0.2$ cm, and falling velocity $V = 6.2 \pm 0.6$ m/s). The drop is a bag, consisting of a water shell surrounding air and bounded at the bottom by a rim. The bag quickly inflates as a function of time (fig. 4), allowing it to expand by a factor of order 3 (that is, 30 for the volume), before bursting.

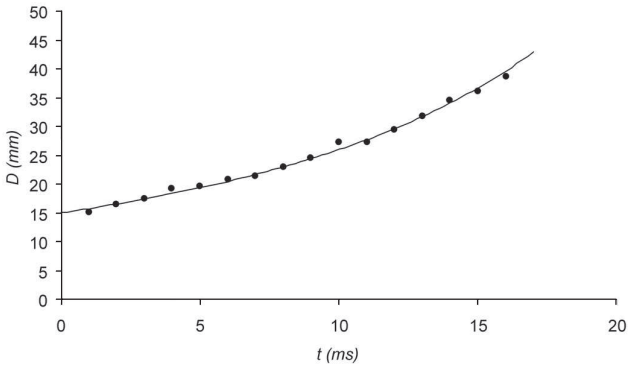

Fig. 4: Inflation of a bag-shaped drop: the bag diameter is plotted as a function of time. The non-linear growth is observed to be well fitted by eq. (5), drawn in full line with $\alpha = (6/\pi)^{1/2}$ (the value expected for a isotropic growth) and $m = 0.94$ g, in fair agreement with the mass unprecisely deduced from the bag-shaped drop ($m = 1.0 \pm 0.7$ g).

is no description of the kinetics of the instability for a drop moving at a constant velocity in air, and we intend here to describe the formation and death of these "bubbly" globules.

The formation of a bubbly state might be understood as follows: in the reference frame of the drop, air is coming at a velocity V, which tends to flatten the drop base with a force $\rho_a V^2 D^2$. For large drops, air should even induce a deformation of this bottom surface by a quantity δ (visible in the last photo in fig. 1). This implies a Laplace pressure of the order of $\gamma\delta/D^2$ (for $\delta \ll D$), and thus an elastic restoring force of the order of $\gamma\delta$. A balance between aerodynamic and surface forces yields: $\delta \sim \rho_a V^2 D^2/\gamma$. Our criterion for the invagination of the bottom surface, leading to the formation of a bubble, is $\delta > \kappa^{-1}$ (since we are in the regime where the thickness of the globule is κ^{-1}, as shown in eq. (3)). Introducing the law for the velocity of fall (eq. (4)), we immediately deduce that the bubbly state will form if $D > \kappa^{-1}$, where we expect a coefficient of the order of π, by analogy with the criterion of development of the Rayleigh-Taylor instability [1]: drops larger than 1 cm should transform in bags, as indeed observed experimentally.

At this large scale ($D \gg \kappa^{-1}$), surface tension cannot resist the deformation, and air penetrates. These "bags" should then inflate, as does the jacket of a biker on a highway. In the drop reference frame, the air inside the bag can be considered as still, at the atmospheric pressure. Outside the bag, air is moving at the falling velocity V, which yields a depression scaling as $\rho_a V^2$. The pressure difference between the outside and the inside of the bag makes it inflate like a balloon [17]. For a bag of diameter D and mass m, the balance between inertia and Bernoulli pressure can be written $m\partial^2 D/\partial t^2 \sim \rho_a V^2 D^2$. This equation is integrated, assuming a constant fall velocity (despite the change of size). Denoting D_o as the bag diameter at the origin of time, this provides an equation for the evolution of the bag diameter:

$$D \sim D_o/(1 - t/\tau^*)^2, \qquad (5)$$

where $\tau^* = \alpha(m/\rho_a V^2 D_o)^{1/2} \sim (\rho/\rho_a)^{1/2} D_o/V$, of the order of 30 ms for centimetric globules. Equation (5) implies that the bag explodes in a finite time τ^*, corresponding to the divergence of D. The numerical coefficient α in eq. (5) can be calculated, assuming that the bag remains close to spherical (as suggested by the isotropic inflation reported in fig. 1a): we find $\alpha = (6/\pi)^{1/2}$.

It is implicitly assumed for deriving eq. (5) that the velocity remains constant during the inflation. This might contradict the force balance during the fall ($\rho_a V^2 D^2 \sim \rho g D_o^3$), which suggests that the drop should slow down as inflating. However, the characteristic time τ associated with changes in the velocity scales as $\rho D_o^3/\rho_a V D^2$, so that τ is larger than τ^* if $(\rho/\rho_a)^{1/2} D_o^2/D^2$ is larger than unity. This should generally be the case: typical inflation factors D/D_o are of the order of 3, making τ^* at least three times smaller than τ. On the other hand, for $\tau < \tau^*$ (which might occur for small density contrast between the two fluids), the inflation equation together with the force balance can be easily integrated, yielding a remarkable result: $D \sim gt^2$! The globule also inflates, but its size does not diverge anymore in a finite time.

We checked experimentally that the fall velocity of an inflating globule remains nearly constant. If the force balance $\rho_a V^2 D^2 \sim \rho g D_o^3$ were satisfied, V should drop by a factor of about 3, while the velocity was observed to decrease by only 20%. Figure 4 shows the time evolution of the size of a bag-shaped globule. Equation (5) is

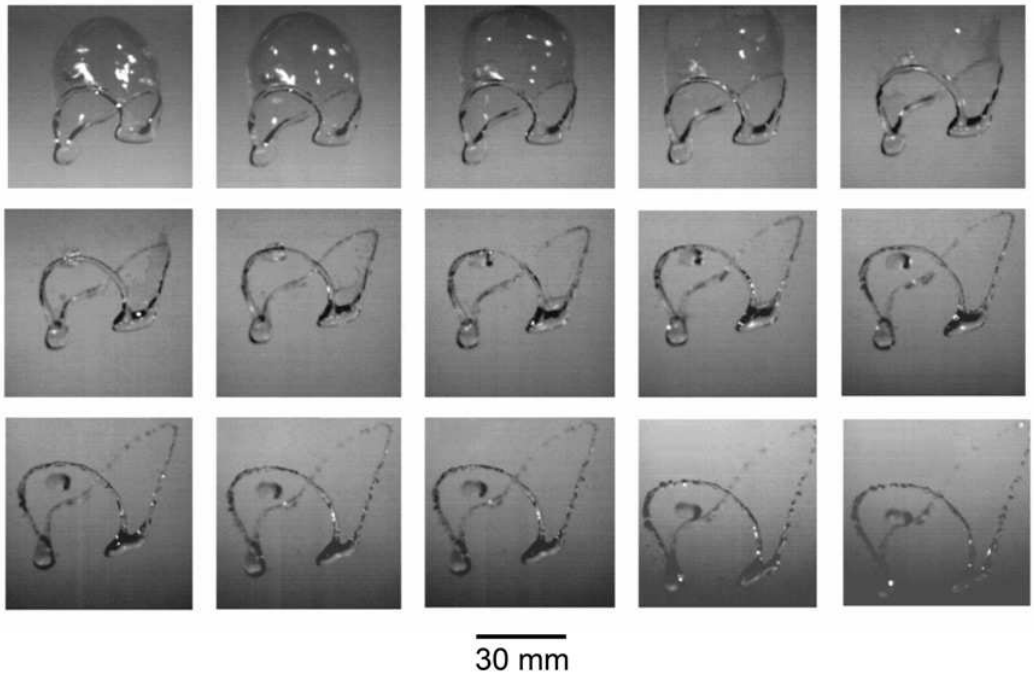

Fig. 5: Death of a bag-shaped drop. As the instability takes place, the shell becomes very thin so that, as a bubble, it bursts once a hole appears. The remaining liquid rim, at the bottom of the shape, later destabilizes because of Plateau-Rayleigh instability. This drop, of initial size 12 mm and falling velocity 7.5 m/s, eventually decays in multiple fragments of individual size smaller than the capillary length. The interval between two images is 1 ms.

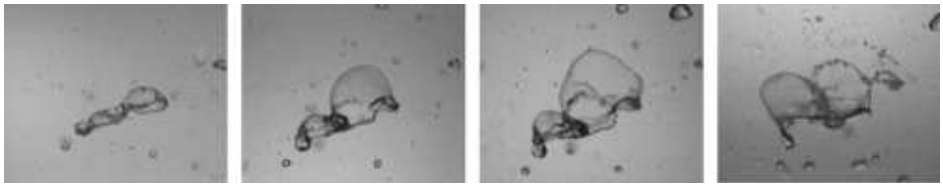

Fig. 6: Evolution of a very large globule of water (equatorial diameter larger than 3 cm). As expected from a Rayleigh-Taylor–like instability, several bags form. As single ones, they inflate and burst, leading to the destruction of the globule. Time is $t = 0$, 10, 13 and 20 ms.

superimposed to the data, and found to describe the non-linear growth of the globule, for $\alpha = (6/\pi)^{1/2}$ and $m = 0.9\,\mathrm{g}$ (in agreement with the mass deduced from the globule shape, and corresponding to an initial diameter $D_\mathrm{o} = 1.2 \pm 0.2\,\mathrm{cm}$). It is observed in particular that the speed of inflation ($\mathrm{d}D/\mathrm{d}t$) increases as a function of time, as predicted by eq. (5). This physically comes from the increase of surface area of the globule, which makes the action of the Bernoulli depression more and more efficient.

However, the globule diameter is not observed to diverge. As the bag grows, the shell gets thinner so that it eventually bursts: as shown in fig. 5, holes appear in the shell and expand. As proposed by Culick for the speed of retraction of a soap film, a balance between surface tension and inertia leads to a constant opening velocity $V = (2\gamma/\rho\varepsilon)^{1/2}$, denoting ε as the film thickness [18]. The holes are indeed observed to open at a constant velocity, of the order of 5 m/s, from which we deduce a shell thickness of about 10 μm. Later, the rim at the bottom also destabilizes, because of the Plateau-Rayleigh instability. Hence, if a large raindrop ever forms, it eventually decays in a spray of droplets, explaining why big liquid globules cannot reach the Earth, unlike hailstones.

Similar observations were made with liquid nitrogen. Because of a much smaller capillary length (about 1mm, instead of 3 mm for water), bag-shaped drops are much smaller than the aqueous ones. Starting from a drop of diameter around 5 mm, the diameter of the bag is about 14 mm before bursting. Multiplying these values by 3, one falls in the typical range of water bags. Our

scenario also suggests that if still larger, a globule might generate several bags (as a large suspended drop generates several drips). We succeeded in making a globule of a few centimeters in diameter. As seen in fig. 6, it is indeed observed to have two bags, which grow and explode nearly at the same time. It would be worth making even larger globules (of 10 cm in diameter) to see if many bubbles develop at the same time. As a natural complement, it would be useful to conduct simulations of these falling globules, in order to confirm the different scalings (some parameters are nearly impossible to vary in a large manner, while arbitrarily small surface tensions can be used in simulations); this would also allow to specify the numerical coefficients in the different laws. Questions remain about the stretched drops. We are not aware of the existence of such puddles in rain. These drops might be sensitive to turbulence and collisions, which both tend to break them [4,13], but the stability of these puddles remains to be discussed.

It is worth noticing that the succession of shapes reported here is very similar to what can be observed by depositing liquids on a very hot plate, so that they float on their own vapour. There again, drops smaller than the capillary length are quasi-spherical; if larger, they make puddles whose thickness scales as κ^{-1}, independently of their size. This similarity may be understood very simply: for a falling drop in the terminal velocity regime, air friction balances the weight, so that the shape results from a balance between surface tension and weight, as for a static non-wetting drop. Surprisingly, the analogy persists for very large puddles: on a hot plate, a centimetric puddle gets bubbly, because the underlying vapour can raise at this scale [19]; as for a falling globule, the number of bubbly chimneys is fixed by the size of the drop: in both cases, the instability can thus be seen as a variety of the Rayleigh-Taylor instability.

REFERENCES

[1] Clift R., Grace J. R. and Weber M. E., *Bubbles, Drops and Particles* (Dover) 1978.
[2] Moore D. W., *J. Fluid Mech.*, **23** (1965) 749.
[3] Mason B. J., *The Physics of Clouds* (Oxford University Press) 1971.
[4] List R. and McFarquhart G. M., *J. Atmos. Sci.*, **47** (1990) 2274.
[5] Bentley W. A., *Mon. Weather Rev.*, **32** (1904) 450.
[6] McDonald J. E., *Sci. Am.*, **190** (1954) 64.
[7] Gunn R. and Kinzer G. D., *J. Meteorol.*, **6** (1949) 243.
[8] Pruppacher H. R. and Pitter R. L., *J. Atmos. Sci.*, **28** (1971) 86.
[9] Andsager K., Beard K. V. and Laird N. F., *J. Atmos. Sci.*, **56** (1999) 2673.
[10] Pilch M. and Erdman C. A., *Int. J. Multiph. Flow*, **13** (1987) 741.
[11] Nomura K., Koshizuka S., Oka Y. and Obata H., *J. Nucl. Sci. Technol.*, **38** (2001) 1057.
[12] Cotton W. R. and Gokhale N. R., *J. Geophys. Res.*, **72** (1967) 4041.
[13] Simpkins P. G., *Nat. Phys. Sci.*, **233** (1971) 31.
[14] Hsiang L. P. and Faeth G. M., *Int. J. Multiph. Flow*, **18** (1992) 635.
[15] Han J. and Tryggvason G., *Phys. Fluids*, **11** (1999) 3650.
[16] Han J. and Tryggvason G., *Phys. Fluids*, **13** (2001) 1554.
[17] Gordon G. D., *J. Appl. Phys.*, **30** (1959) 1759.
[18] Culick F. E., *J. Appl. Phys.*, **31** (1960) 1128.
[19] Biance A. L., Clanet C. and Quéré D., *Phys. Fluids*, **15** (2003) 1632.

Water spring : A model for bouncing drops

EUROPHYSICS LETTERS 15 April 2003

Europhys. Lett., **62** (2), pp. 237–243 (2003)

Water spring: A model for bouncing drops

K. Okumura[1,2], F. Chevy[1], D. Richard[1], D. Quéré[1] and C. Clanet[3]

[1] *Laboratoire de Physique de la Matière Condensée, UMR 7125 du CNRS Collège de France - 75231 Paris Cedex 05, France*

[2] *Department of Physics, Graduate School of Humanities and Sciences Ochanomizu University - 2-1-1, Otsuka, Bunkyo-ku, Tokyo 112-8610, Japan*

[3] *Institut de Recherche sur les Phénomènes Hors Equilibre, UMR 6594 du CNRS BP 146, 13384 Marseille Cedex, France*

(received 19 November 2002; accepted in final form 19 February 2003)

PACS. 68.03.Cd – Surface tension and related phenomena.
PACS. 68.08.Bc – Wetting.
PACS. 47.85.Dh – Hydrodynamics, hydraulics, hydrostatics.

Abstract. – It has been shown that a water drop can bounce persistently, when thrown on a super-hydrophobic substrate. We present here scaling arguments which allow us to predict the maximal deformation and the contact time of the drop. This approach is completed by a model describing the flow inside the drop, and by original experimental data.

Introduction. – A *liquid ball* is a drop which remains quasi-spherical when brought into contact with a solid surface. Different examples of such objects have recently been described: let us quote *pearl drops*, which result from the extreme hydrophobicity of the solid [1–4], *liquid marbles*, achieved by texturing the surface of the liquid [5–7], and (more classically) *Leidenfrost drops*, obtained by putting a small amount of volatile liquid on a very hot plate [8]. In such cases, quick transportation of tiny amounts of liquid becomes possible without any leak, which can be of great interest in microfluidics applications. At the same time, these systems realize pure capillary "devices", and are worth being studied for their original properties.

For example, a liquid ball (with a typical diameter 1 mm) impinging onto a solid substrate bounces off, as if it were a tennis ball hitting the ground [9, 10]. The rebounds are persistent (the restitution coefficient can be very high, of the order of 0.9), and observed in a large window of impact velocity. If the velocity is too small (typically smaller than a few centimeters per second), the drop gets stuck on the substrate. If too large (above around 1 m/s), the drop endures extreme deformation during the shock, and finally breaks into several pieces. In between, a more detailed analysis of the shock itself shows that the contact time of the drop with the substrate does not depend on the impact velocity V over a large interval of velocity [11].

In this note, we discuss the maximal deformation of this sort of "water spring", and also the value of the contact time during the shock, in particular in the limit of elastic impact (small impact velocity). These predictions are compared with original experimental data.

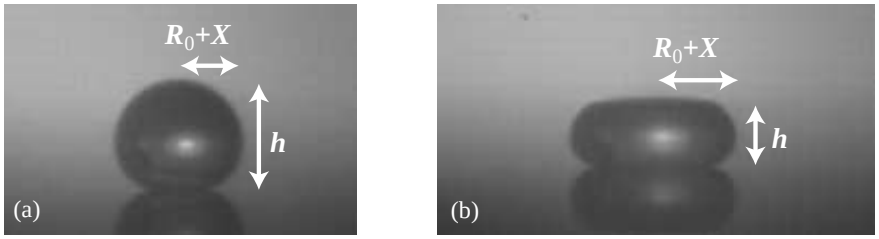

Fig. 1 – Maximal deformation of a liquid ball impinging a solid at a small velocity, (a) $R_0 \sim 0.4\,\mathrm{mm}$, $V = 0.094\,\mathrm{m/s}$, $W \sim 0.05$; or at a larger velocity, (b) $R_0 \sim 0.4\,\mathrm{mm}$, $V = 0.47\,\mathrm{m/s}$, $W \sim 1$.

We shall mainly focus on the limit of small deformations where a drop of initial radius R_0 bounces back with a high restitution coefficient of the order of 0.9. This corresponds to kinetic energies smaller than surface energies, *i.e.* to small Weber numbers, where the latter quantity is defined as

$$W = \rho R_0 V^2/\gamma. \tag{1}$$

This condition is achieved for small impact velocities, *i.e.* smaller than V_W:

$$V_W = \sqrt{\frac{\gamma}{\rho R_0}}\,. \tag{2}$$

For a millimetric water drop ($\gamma \sim 72\,\mathrm{mN/m}$, $\rho = 10^3\,\mathrm{kg/m^3}$), V_W is of the order of $1\,\mathrm{m/s}$. As seen in fig. 1, the drop at its maximal deformation looks like a flattened sphere for small impact velocities ($V < V_W$), or a pancake for larger velocities ($V \sim V_W$).

Scaling equations for a water spring ($V \ll V_W$). – We start from Euler's equation

$$\rho\frac{Dv}{Dt} = -\nabla p + \rho g, \tag{3}$$

neglecting the effect of viscosity thanks to the high restitution coefficient. We consider the limit $V \ll V_W$, in which the drop is deformed by a quantity X much smaller than the initial radius R_0 (see fig. 1a); the characteristic time of deformation scales as X/V. On the other hand, the Laplace pressure gradient scales as $\gamma X/R_0^3$ (for example, assuming an ellipsoidal form for the drop, the pressure jump at the equator or the apex scales as $\Delta p \sim \gamma/R_0(1 \pm X/R_0)$ and changes over the length R_0). Thus, eq. (3) can be dimensionally written as

$$\rho V^2 R_0^3 \sim \gamma X^2 - \rho g R_0^3 X. \tag{4}$$

This equation also expresses the transfer of kinetic energy into the surface and gravitational terms associated with the drop deformation. If the velocity is zero, the drop is deformed by gravity by a quantity δ, as first discussed by Mahadevan and Pomeau [12], which reads

$$\delta \sim R_0^3/\kappa^{-2}, \tag{5}$$

by use of the capillary length $\kappa^{-1} = \sqrt{\gamma/(\rho g)}$, which is about $3\,\mathrm{mm}$ for water.

We first consider the case where capillarity dominates gravity ($X \gg \delta$). Then, we find from eq. (4) that the maximal deformation scales as the velocity:

$$X \sim \left(\rho R_0^3/\gamma\right)^{1/2} V. \tag{6}$$

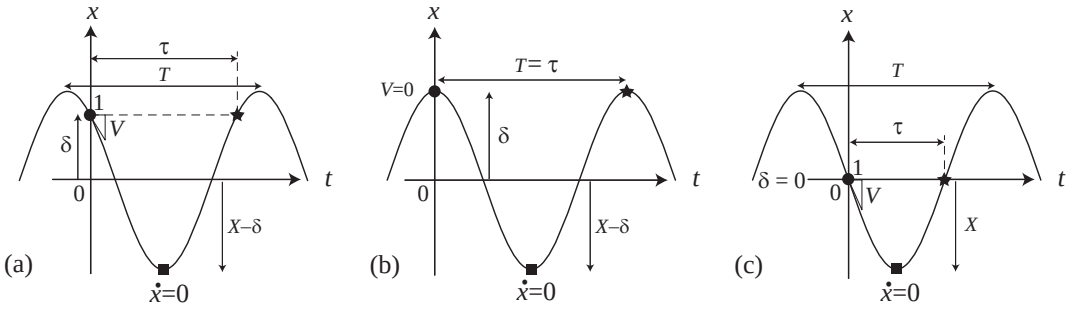

Fig. 2 – Analogy with a spring system: elongation x is plotted as a function of time t. The circle ($t = 0$) corresponds to the moment of impact and the square to the maximal deformation. The star thus indicates the moment of rebound. (a) General case. (b) Small velocity limit. (c) Large velocity limit.

The contact time should be of the order of X/V, and thus can be written as

$$\tau \sim \left(\rho R_0^3/\gamma\right)^{1/2}. \tag{7}$$

Equation (7), which yields a V-independent contact time of about one millisecond, indeed corresponds to the plateau observed experimentally [11].

Equation (6) allows us to make clear the limit of this regime. Since X must be larger than δ, we find that the velocity must be larger than a characteristic velocity,

$$V_c \sim \left(gR_0^3\kappa^2\right)^{1/2}, \tag{8}$$

which is about a few cm/s. If V approaches V_c, gravity cannot be neglected any more; we recast eq. (4) as

$$\rho V^2 R_0^3 + \gamma\delta^2 \sim \gamma(X-\delta)^2, \tag{9}$$

which expresses the energy conservation of an *imaginary* spring-mass system of initial velocity V and initial elongation δ.

Figure 2 may help to have an intuitive picture for eq. (9). The elongation x of the imaginary spring is plotted as a function of time t, setting $t = 0$ at the moment of impact. The left-hand side of eq. (9) is represented by a circle ($x = \delta$, $\dot{x} = V$ at $t = 0$), while the right-hand side by a square ($\dot{x} = 0$ at $t = \tau/2$). The moment of taking-off is marked by a star, and τ is compared in the plot with the period of the oscillator $T \sim (\rho R_0^3/\gamma)^{1/2}$.

Thus, we can graphically deduce the contact time τ. In the small velocity limit $V \ll V_c$ ($\rho V^2 R_0^3 \ll \gamma\delta^2$), we see in fig. 2b that the contact time τ is equal to the vibration period T. In contrast, in the interval commented above ($V_c \ll V \ll V_W$) and with increase in V, τ decreases from T and approaches the plateau value $T/2$. The complete variation of the contact time τ as a function of the impact velocity V will be calculated more precisely in the next section. Note finally that, as stated above, the maximal deformation, in the limit of extremely small impact velocities, tends towards the constant δ, as seen from eq. (9): we logically recover the static deformation.

Local model. – The previous scaling arguments can be completed by considering local flows during the impact. We start from the incompressibility condition ($\nabla \cdot \boldsymbol{v} = 0$), which reduces to

$$\frac{1}{r}\frac{\partial r v_r}{\partial r} + \frac{\partial v_z}{\partial z} = 0, \tag{10}$$

in the cylindrical coordinate system (r, θ, z) with $v_\theta = 0$. Looking for a solution of the type $v_r = v_r(r)$ and $v_z = v_z(z)$ satisfying appropriate boundary conditions, and introducing the equatorial radius R (see fig. 1b), we find

$$v_r = \frac{\dot{R}}{R} r, \qquad v_z = -2\frac{\dot{R}}{R} z, \tag{11}$$

setting $z = 0$ at the substrate surface. The velocity potential ϕ defined by $\boldsymbol{v} = \nabla\phi$ can thus be written as

$$\phi = \frac{\dot{R}}{R}\left(\frac{r^2}{2} - z^2\right). \tag{12}$$

If the viscosity is neglected, the dynamics of ϕ is governed by Bernoulli's equation

$$\rho\frac{\partial\phi}{\partial t} + \frac{1}{2}\rho v^2 + p + \rho g z = \text{constant}. \tag{13}$$

Here, the pressure p at the surface of the drop is given by the Laplace pressure, *i.e.* $p = \gamma C(r, z)$, where the local curvature is denoted C.

We evaluate eq. (13) at the apex ($r = 0$, $z = h$) and at the equator ($r = R$, $z \simeq h/2$), in the limit of small deformation ($\ddot{x} \gg \dot{x}^2/R_0$) for which $h \simeq 2R_0$. (Here, x is defined as in fig. 1 but not necessarily at its maximal deformation; the maximum magnitude of x is X.) To estimate the curvature difference $\Delta C = C(0, h) - C(R, h/2)$, we take the value in the static limit since we are in the regime of small velocities; the condition of constant pressure inside the drop can be integrated numerically, which gives $\Delta C = 6.8x/R_0^2$. In this way, we obtain

$$-7\rho R_0^3\ddot{x}/2 + 6.8\gamma x - \rho g R_0^3 = 0. \tag{14}$$

Writing $\delta = \kappa^2 R_0^3/6.8$ and $\omega^2 = 12.8\gamma/(7\rho R_0^3)$ (which gives as a plateau value for the contact time $T/2 = 2.3\sqrt{\rho R_0^3/\gamma}$), we find a general solution:

$$x - \delta = x_0 \cos(\omega t + \varphi). \tag{15}$$

The initial conditions lead to the relations $\cos\varphi = \delta/x_0$ and $\sin\varphi = V/(\omega x_0)$, from which we get $x_0 = \sqrt{\delta^2 + V^2/\omega^2}$ and $X = \delta + x_0$. The time of rebound τ should be given by the equation $\delta = x_0\cos(\omega\tau + \varphi)$, with $\pi \leq \omega\tau + \varphi \leq 2\pi$. Hence, we find $\omega\tau + \varphi = 2\pi - \arccos(\delta/x_0)$ with $\varphi = \arccos(\delta/x_0)$ $(0 \leq \varphi \leq \pi)$ or

$$\tau = 2\tau_c\left(1 - \frac{1}{\pi}\arccos\left(\frac{\delta}{x_0}\right)\right), \tag{16}$$

where

$$\delta/x_0 = \left(1 + (V/V_c)^2\right)^{-1/2}.$$

The analytical result, eq. (16), is plotted in fig. 3, and allows us to recover the predictions made via fig. 2: the contact time decreases by a factor 2 when the impact velocity is increased from about V_c to V_W.

Experiments. – We measured the contact time of bouncing drops at small impact velocities for millimetric water droplets hitting a super-hydrophobic substrate. Rebounds were sequentially recorded with a high-speed camera with a typical sampling time of 10^{-4} s for a contact time around 10^{-3} s, which gives a precision higher than 10%. The results are plotted in fig. 4 for two drop sizes. We indeed observed that the contact time significantly increases at

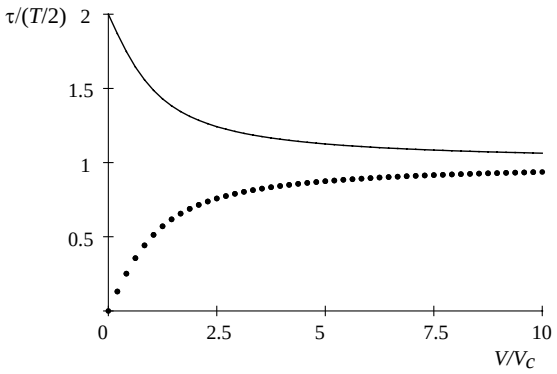

Fig. 3

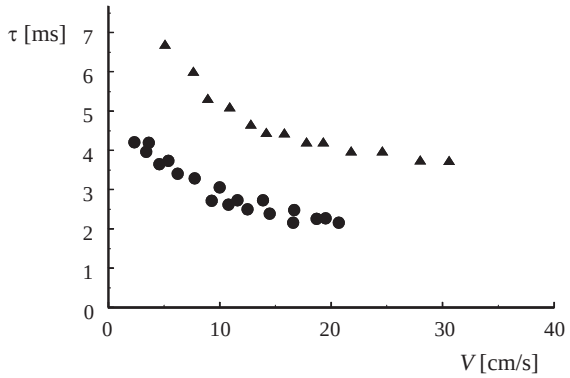

Fig. 4

Fig. 3 – Contact time τ *vs.* the impact velocity V in the elastic collision limit. The line is calculated from eq. (16). The dotted line corresponds to the case of inverted gravity (see the text).

Fig. 4 – Contact time of a water drop bouncing on a super-hydrophobic substrate as a function of impact velocity. Triangles correspond to $R_0 = 0.6 \pm 0.06\,\text{mm}$, and circles to $R_0 = 0.4 \pm 0.04\,\text{mm}$.

low impact velocity (in the range below 10 cm/s). In addition, the ratio between the largest and the shortest times is found to be very close to 2, for both sizes. Finally, the velocity above which a plateau is observed increases with the drop size.

All these observations are qualitatively in agreement with our predictions. A fully quantitative comparison would require a very accurate measurement of the drop radii (which determine the value of V_c), and also taking into account the possibility for the drop to stick at very small velocity: for $V \sim V_c$, it is observed that the drop does not bounce off but remains stuck to the solid. In contrast, the comparison between the model and the data becomes quite precise at higher speeds: the plateau value is well described by eq. (7) with a numerical coefficient of 2.6 ± 0.1 [11], in good agreement with 2.3, the value obtained above.

We also measured the maximal deformation X of the drop during the impact as a function of the impact velocity V (fig. 5). We found a linear behavior, in agreement with eq. (6).

This first series of experiments confirms that the contact time of the bouncing drop deviates from its asymptotic value when we are in the regime of low impact velocity, *i.e.* in the linear regime of deformation. We interpreted this effect as due to gravity, and tried to confirm this interpretation thanks to a second series of experiments. There, we studied the bouncing with gravity working in the opposite direction (*inverted gravity*). Drops were dropped from centimetric heights onto a super-hydrophobic substrate slightly tilted. After bouncing off, they hit at a height close to their maximum rebound height on a second plate of the same nature and inclined by the same angle. We recorded the contact time for rebounds on this second plate. The data are plotted in fig. 6, as a function of the impact velocity. The error bars are there larger (because of the experimental resolution and the effects due to the vibrations induced by the first impact), but the data clearly indicate that the contact time *increases* with the impact velocity. This is in agreement with our theory: transforming g into $-g$ (equivalently, δ into $-\delta$) in eq. (16) makes τ increase with V as plotted in the dotted line in fig. 3. Interestingly, here, the contact time can vary between 0 and τ (between τ and 2τ in the previous experiments) which can be understood qualitatively using the construction suggested in fig. 2. In the inverted gravity case, the whole sequence takes place below the line $x = 0$, so that we recover that the contact time should vary between 0 and τ.

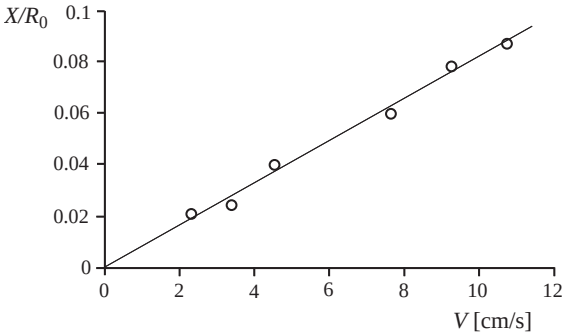

Fig. 5

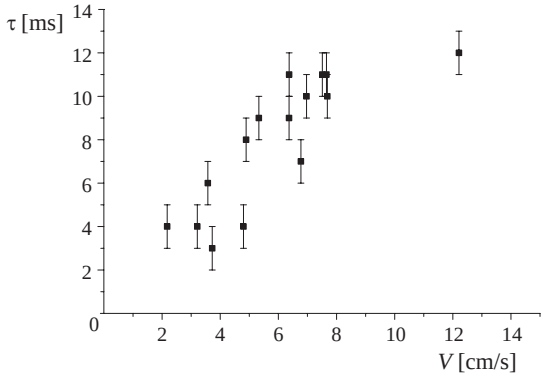

Fig. 6

Fig. 5 – Maximal deformation X of a water drop ($R_0 \sim 0.4\,\mathrm{mm}$) as a function of its impact velocity. Experimental data (circles) are compared with the scaling prediction (line) of eq. (6).

Fig. 6 – Contact time of a water drop ($R_0 \sim 1\,\mathrm{mm}$) in the field of an inverted gravity.

Perspectives. – Interesting perspectives can be given in the regime of higher impact velocities ($V > V_W$), where the drop is highly deformed and makes some kind of (transient) pancake of radius $R_0 + X \sim X$ and thickness h (fig. 1b). Since the drop crashes on the solid during a *crashing time* R_0/V, we expect the inertial term in Euler's equation to be of the order of $\rho V^2/R_0$. The Laplace pressure scales as γ/h at the equator and it changes over the length h. The pressure gradient thus scales as γ/h^2. The gravity term can be neglected in this regime of large deformation, so that Euler's equation can be cast dimensionally into

$$\rho R_0^3 V^2 \sim \gamma X^4/R_0^2 \tag{17}$$

via the conservation of the volume ($R_0^3 \sim hR^2$). Thus, the maximal size of the pancake is deduced as

$$X \sim R_0 W^{1/4}, \tag{18}$$

where W is defined in eq. (1). X is indeed found to be larger than R_0 for $W > 1$. We note that if the initial kinetic energy were transformed mainly into a surface term, namely,

$$\rho R_0^3 V^2 \sim \gamma X^2, \tag{19}$$

we would find $X \sim R_0 W^{1/2}$ instead of eq. (18).

Equation (17) is in striking contrast with the case of a small deformation where the kinetic energy was found to be stored in surface (and gravitational) energy during the shock as in eq. (4). Namely, eq. (17) tells us that the initial energy is transferred primarily into other forms, identities of which (internal flow in the pancake, and possibly, the phonon energy of the substrate, etc.) remain to be clarified.

In this regime, the contact time can be regarded as the dewetting time of the pancake. In this inertial case, the dewetting velocity V_d scales as $\sqrt{\gamma/(\rho h)}$ [4], which corresponds to the retraction speed of a liquid sheet [13]. Thus, the contact time is given by $\tau \sim X/V_\mathrm{d}$, which happens to result in eq. (7). Indeed, the contact time was observed to be independent of V and to increase as $R_0^{3/2}$ even for such high velocities [11]. This fact emphasizes that the drop is no longer in a linear-spring regime, for which eq. (19) would hold, and the contact time would be given by $\tau \sim X/V$. Note also that both X/V_d and X/V are certainly much longer than

the crashing time R_0/V in the present case ($W \gg 1$), which justifies our previous estimation of the inertial term in eq. (17).

Conclusion. – In the limit of small deformations (*i.e.* for small impact velocities), a liquid ball thrown on a solid behaves as a quasi-ideal spring. This can be understood as a conventional spring-mass system with a stiffness given by surface tension and a mass given by that of the ball; the deformation of the small ball during the impact linearly depends on the impact velocity and the contact time scales as the period of this spring-mass system, as observed with high speed photographs. The contact time was found to *increase* (typically by a factor of 2) at small impact velocity, which can be interpreted as the result of the weight of the ball. This was confirmed by achieving a similar experiment in an inverted field of gravity, which indeed leads to a *decrease* of the contact time at small velocities.

In this system, the effect of viscosity could be ignored. This might be physically due to the absence of a contact line in a situation of non-wetting; most of viscous dissipation usually takes place near the contact. It would be interesting to see how our views would be modified when the viscosity of the liquid forming the ball is increased. Extensions to similar (but different) systems such as gel balls [14] or drops of surfactant solution would also be worth studying.

* * *

We thank Y. Tanaka for useful discussions. KO is grateful to P.-G. de Gennes and to the members of his group for their warm hospitality during his second and third stays in Paris. The second stay was financially supported by Joint Research Project between JSPS and CNRS while the third by Collège de France. This work is also supported by an internal grant of Ochanomizu University.

REFERENCES

[1] Onda T., Shibuichi S., Satoh N. and Tsujii K., *Langmuir*, **12** (1996) 2125.
[2] Tadanaga K., Katata N. and Minami T., *J. Am. Ceram. Soc.*, **80** (1997) 1040.
[3] Bico J., Marzolin C. and Quéré D., *Europhys. Lett.*, **47** (1999) 220.
[4] de Gennes P.-G., Brochard-Wyart F. and Quéré D., *Gouttes, Bulles, Perles et Ondes* (Belin, Paris) 2002.
[5] Aussillous P. and Quéré D., *Nature (London)*, **411** (2001) 924.
[6] Mahadevan L., *Nature (London)*, **411** (2001) 895.
[7] Nathan P., Richard D., Foster W. and Mahadevan L., *Proc. R. Soc. London, Ser. B*, 02PB0036.1 (2002).
[8] Frohn A. and Roth R., *Dynamics of Droplets* (Springer Verlag) 2000, and references therein.
[9] Hartley G. S. and Brunskill R. T., in *Surface Phenomena in Chemistry and Biology*, edited by Danielli J. F. (Pergamon Press, London) 1958, pp. 214-223.
[10] Richard D. and Quéré D., *Europhys. Lett.*, **50** (2000) 769.
[11] Richard D., Clanet C. and Quéré D., *Nature (London)*, **417** (2002) 811.
[12] Mahadevan L. and Pomeau Y., *Phys. Fluids*, **11** (1999) 2449.
[13] Taylor G. I., *Proc. R. Soc. London, Ser. A*, **259** (1960) 1.
[14] Tanaka Y., Yamazaki Y. and Okumura K., *Bouncing gel balls* (2003), cond-mat/0302167.

On the elasticity of an inertial liquid shock

J. Fluid Mech. (2006), *vol.* 554, *pp.* 47–66.
doi:10.1017/S0022112006009189 Printed in the United Kingdom

On the elasticity of an inertial liquid shock

By ANNE-LAURE BIANCE[1], FRÉDÉRIC CHEVY[1], CHRISTOPHE CLANET[2], GUILLAUME LAGUBEAU[2] AND DAVID QUÉRÉ[1]

[1]Laboratoire de Physique de la Matière Condensée, FRE 2844 du CNRS, Collège de France 75231 Paris Cedex 05, France

[2]Institut de Recherche sur les Phénomènes Hors Équilibre, UMR 6594 du CNRS BP 146, 13384 Marseille Cedex, France

(Received 26 September 2005 and in revised form 10 January 2006)

A drop of low viscosity hitting a solid may bounce, provided that the material is highly hydrophobic. As a model of such a situation, we consider here the case of a very hot solid. Then, as discovered by Leidenfrost, a thin layer of vapour sustains the drop, preventing any contact with the substrate. On hitting such a solid, a drop rebounds, and we discuss here the elasticity of the shock. Two very different cases are described: at a large velocity, the weaker the impact velocity, the weaker the elasticity; at a small velocity, a quasi-elastic regime is found. The boundary between the two domains is set by a Weber number, which compares the kinetic and surface energies of the drop, of order unity.

1. Introduction

In 1756, two hundred years before the foundation of the *Journal of Fluid Mechanics*, Johan Leidenfrost, a German physician from Duisburg, published a summary of his discoveries on the physics of drops (Leidenfrost 1756). He described in particular the remarkable behaviour of volatile liquids when deposited on substrates whose temperature is significantly higher than the liquid's boiling point (Gottfried, Lee & Bell 1966; Baumeister & Simon 1973). For water on copper or iron at a temperature of about 200 °C (or more), it is observed that drops are extremely mobile and quickly roll off the substrate if any slope is present. On a curved surface (such as the inside of a spoon, in order to keep the drop trapped), the liquid does not boil and remains for a very long time (typically a few minutes for millimetric drops), despite the high temperature of the substrate (Bell 1967).

Leidenfrost correctly interpreted these experiments. He understood that a vapour film forms between the drop and the substrate, allowing the liquid to levitate (Goldshtik, Khanin & Ligai 1985). Because of the absence of contact, bubble nucleation is inhibited (no boiling), and the existence of a cushion of air dramatically reduces the friction with the substrate. Since a gas is a good insulator, the heat transfer is not efficient in the film, so that there is a relatively slow evaporation for the liquid (Berenson 1961; Watchers, Bonn & Van Nouhuis 1966; Michiyoshi & Makino 1978; Zhang & Gogos 1991; Chandra & Avedisian 1994). By placing a candle behind the drop and looking through the base, Leidenfrost saw a sheet of light of thickness of about 100 μm (a hair's diameter), allowing him not only to prove the existence of the vapour film, but also to measure its (correct) typical thickness (Biance, Clanet & Quere, 2003).

The shape of the drops is also of interest. While large centimetric drops are flattened by gravity, small millimetric droplets are quasi-spherical, which was understood (by Young and Laplace) 50 years after Leidenfrost's observations to be a consequence of the cohesion of liquids: a drop has a surface energy proportional to its area, whose minimum corresponds to a spherical shape. The surface energy per unit area is called the surface tension and denoted as γ. For a Leidenfrost water drop, evaporation maintains the drop temperature at 100 °C, so that the surface tension is fixed at $58\,\mathrm{mN\,m^{-1}}$ (this condition of constant temperature should limit Marangoni effects in the drop). This allows us to specify when gravity can be neglected: while the surface energy of a drop of size R scales as γR^2, its gravitational energy is proportional to $\rho g R^4$, where ρ denotes the liquid density and g denotes the acceleration due to gravity. Hence, gravity is negligible provided that the drop is smaller than the so-called capillary length, $\kappa^{-1} = (\gamma/\rho g)^{1/2}$. For water at 100 °C, $\kappa^{-1} = 2.5\,\mathrm{mm}$; for less cohesive liquids (such as light oils or liquid nitrogen), it can be as low as 1 mm.

Apart from these classical static properties, such non-adhesive Leidenfrost drops have a remarkable dynamic characteristics: if they impact a surface, they bounce, as solid spheres do (Richard & Quéré 2000; Karl & Frohn 2000). This does not happen for common liquid impacts; then, the kinetic energy is dissipated by viscosity as the drop spreads on its substrate (Rein 1993), in particular owing to the moving contact lines close to which viscous losses are enhanced. For Leidenfrost drops, there is no contact line, and the kinetic energy efficiently converts to surface energy (the drop deforms as it hits the solid) and then to kinetic energy again, allowing the system to behave as an elastic spring. This directly shows how the contact time of a bouncing drop scales with the different parameters (Richard, Clanet & Quéré 2002): the liquid surface tension γ is the stiffness of this spring and ρR^3 is its mass, so that the natural response time scales as $(\rho R^3/\gamma)^{1/2}$, of the order of a few milliseconds for a millimetric drop – a time negligible compared to the lifetime of the globule.

Here we discuss the elasticity of this kind of liquid shock. We shall see that unlike what happens for solid shocks, the elasticity is very sensitive to the impact velocity. It is found in particular that the shock is more elastic when the impact speed is small. In the limit of very small velocities, the use of Leidenfrost drops leads to a regime of quasi-elastic rebounds. For larger velocities, the shock can be much less elastic; in addition, elasticity is lost above a critical radius (whatever the impact velocity), for which the weight dominates the surface effects. These series of experiments are interpreted using a minimal model.

2. Characteristics of a liquid impact

Figure 1 shows a typical sequence of events, observed as a water drop hits a silicon plate whose temperature (300 °C) is much larger than the boiling point of water. Here, the drop has a radius $R = 1\,\mathrm{mm}$, and it is released from a height $H = 3.2\,\mathrm{cm}$, so that the impact speed $V = \sqrt{2gH}$ is about $0.8\,\mathrm{m\,s^{-1}}$. The pictures are taken with a high-speed camera (1000 frames per second), using back-lighting to improve the contrast.

As it impacts the solid, the drop deforms: it first spreads until it transiently forms a kind of non-wetting puddle, as it reaches its maximum extension. Then, it retracts and elongates in the vertical direction: the globule is highly deformed at take off (after a 'contact' time of 11 ms, in figure 1). As a consequence, it strongly vibrates as it rises; then, it reaches its maximum height, whose position can be measured. We deduce from such sequences the restitution coefficient $e = V'/V$ of the shock, defined

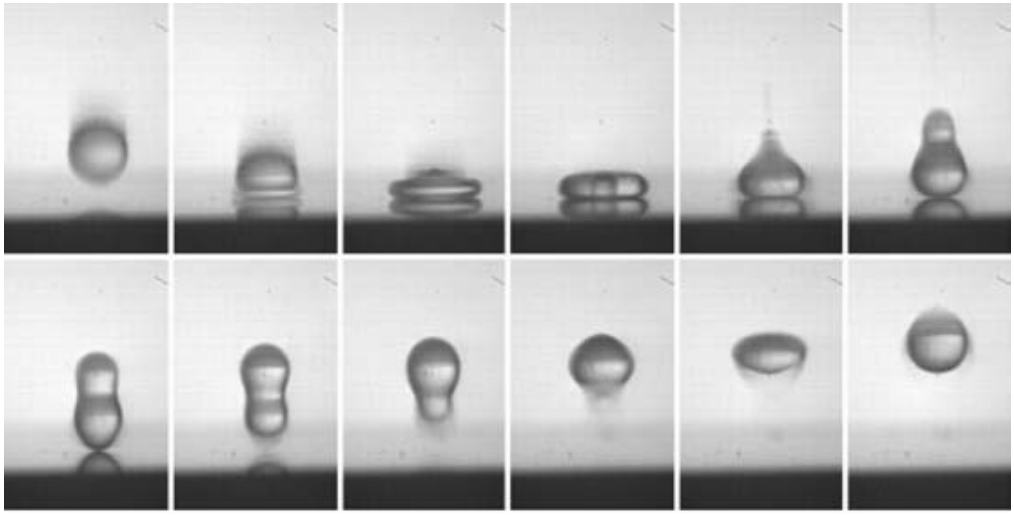

FIGURE 1. Rebound of a millimetric water drop hitting a steel plate heated at 300 °C. The time interval between two pictures is 1.8 ms. The drop radius is 1 mm, and the impact velocity is 80 cm s^{-1}. The corresponding Weber number (equation (1)) is about 10, meaning that large deformations are observed during the impact, leading to strong oscillations.

as the ratio between the velocities of the centre of mass after and before impact. In the example in figure 1, e is 0.6, showing a modest elasticity (the final height of the drop is only 36 % of that from which it was released).

The contact time τ is defined as the interval between the moment when the drop reaches the plate and that when it leaves it. Measurements of τ are shown in figure 2 as a function of the impact velocity (for a fixed drop radius $R = 1.06$ mm), and as a function of drop radius (for a fixed impact velocity of 0.7 m s^{-1}). The results are very close to those observed for drops bouncing off super-hydrophobic substrates (Richard *et al.* 2002). On the one hand, the contact time is almost independent of the impact speed; it decreases very slightly as the speed increases, which might be related to the nonlinear regime of oscillation for strong deformations. On the other hand, the contact time rapidly increases with the drop size, as $R^{3/2}$ (shown with line). As the solid noted in the introduction, the contact time should be of the order of the oscillation time. This quantity was calculated by Rayleigh, for a drop freely oscillating in air (Rayleigh 1879). For the simplest (quadrupolar) mode of oscillation, this time is $\pi(\rho R^3/2\gamma)^{1/2}$, which exhibits the different scalings observed in figure 2. However, the numerical coefficient is slightly different: the Rayleigh coefficient $\pi/\sqrt{2}$ is about 2.2, while we deduce from the experiments a coefficient of 2.65 ± 0.10. Courty, Lagubeau & Tixier (2006) recently showed that the period of oscillation of a non-wetting drop is increased by the presence of a plate below, compared to a free drop. This might explain the slight disagreement found in the coefficient.

We also noted the existence of a well-defined state of maximal extension. We denote the radius of this transient puddle as R_M, and its thickness as δ. We shall first consider the strong-deformation regime ($R_M \gg \delta$), which will occur if the kinetic energy of the impacting drop is much larger than its surface energy. The Weber number We compares these two energies:

$$We = \frac{\rho V^2 R}{\gamma}. \tag{1}$$

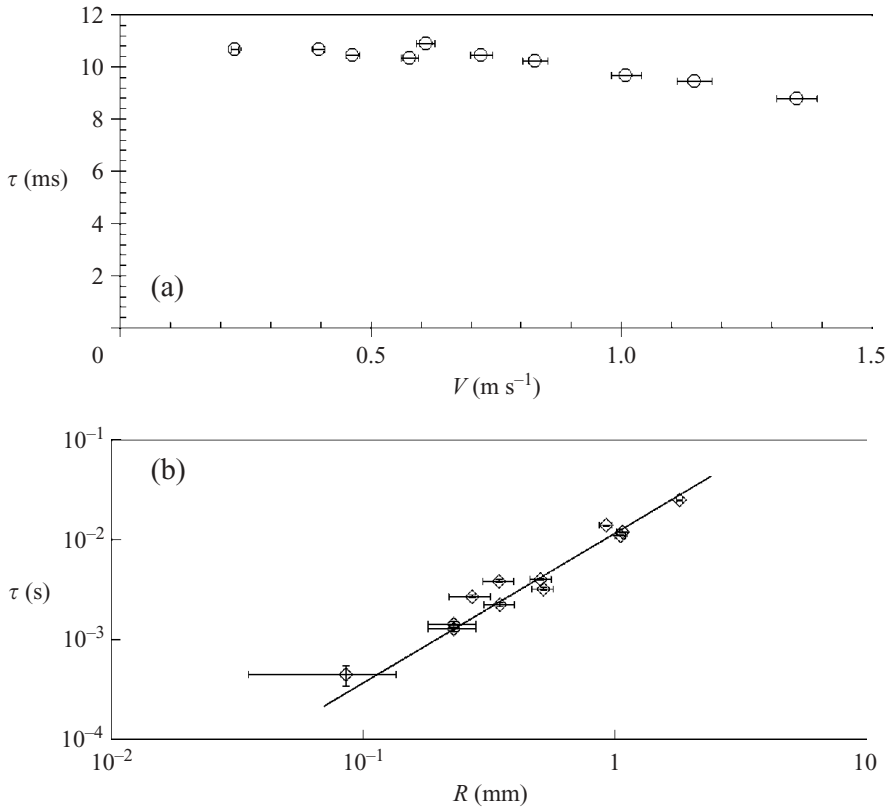

FIGURE 2. Contact time τ of a drop bouncing on plate heated at 280 °C. (*a*) τ is plotted as a function of the impact velocity V (for a fixed drop radius $R = 1.06$ mm), and found to be quite insensitive to V (multiplying V by a factor of about 7 makes τ decrease by only 15 %). (*b*) τ is observed (in a log-log plot) to increase rapidly with the drop radius R, as $R^{3/2}$ (solid line). Writing $\tau = \alpha\ (\rho R^3/\gamma)^{1/2}$, we deduce from the fit a numerical coefficient $\alpha = 2.65 \pm 0.20$.

A strong deformation at impact corresponds to *We* larger than unity. The maximum radius should generally be a function of the Weber number. We could assume that the shock simply converts the kinetic energy (of the order of $\rho R^3 V^2$) to surface energy (of the order of γR_M^2 in the limit considered here), which would yield (Chandra & Avedisian 1991):

$$R_M \sim R We^{1/2}. \tag{2}$$

But energy conservation is never straightforward in this kind of system, in particular because of the existence of internal flows during the contact time. We instead propose that the drop, as it hits the solid, is subjected to an acceleration which scales as V^2/R, since the velocity decreases from V to 0 over a distance of about R (Clanet *et al.* 2004). This acceleration is typically $100\,g$, in impact experiments, so that the drop will be (transiently) flattened, in this reinforced gravity field. The thickness δ of a non-wetting gravity puddle is proportional to a rescaled capillary length $\kappa^{-1} = (\gamma/\rho g)^{1/2}$, where g must be replaced by V^2/R. Together with the volume conservation ($R^3 \sim \delta R_M^2$), this yields an extension:

$$R_M \sim R We^{1/4}. \tag{3}$$

This scaling appears to be different from the one arising from energy conservation: in the limit of large *We*, the drop is expected to be more contracted than predicted by (2), by a factor of $We^{1/4}$ (1.8 to 3.2, for *We* between 10 and 100). Of course, this

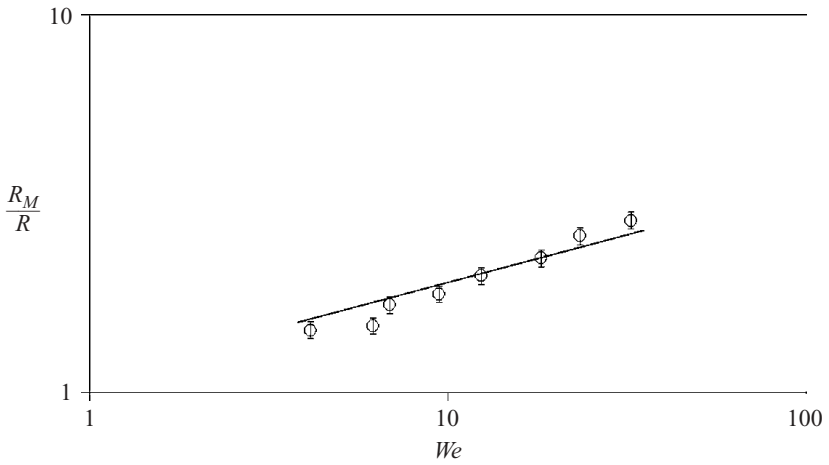

FIGURE 3. Maximum radius R_M of a water drop impacting a plate heated at $T = 280\,^{\circ}\mathrm{C}$, as a function of the Weber number We characterizing the shock and defined by equation (1). Drops radius is $R = 1.02\,\mathrm{mm}$, and the Weber number is varied by changing the impact velocity. The diagram has logarithmic scales, and the line shows the slope 0.25 – suggested by equation (3). Writing $R_M = \alpha We^{1/4}$, we deduce from the fit a numerical coefficient $\alpha = 1.1 \pm 0.1$.

description can only hold provided that the drop size R is larger than the 'dynamic' capillary length $(\gamma R/\rho V^2)^{1/2}$ (only these drops will be flattened), so that again $We \gg 1$.

Figure 3 shows that the extension observed for the drop (and obtained owing to the variation of the impact velocity) follows a behaviour compatible with the scaling proposed in equation (3) (the exponent deduced from figure 3 is 0.30 ± 0.05). It is useful to define the maximum extension of the drop, because it defines the state from which the drop will retract and take off.

3. Elasticity of the shock: observations

We focus here on the elasticity of the shock. Our experiments consisted of filming rebounds for various liquids (water, ethanol, acetone, and liquid nitrogen), different drop radii R (between 0.8 mm and 2 mm) and impact velocities V (between $0.02\,\mathrm{m\,s^{-1}}$ and $1\,\mathrm{m\,s^{-1}}$). The case of larger drops (of size approaching the capillary length κ^{-1}) will be discussed separately (see § 4.2, and in particular figure 8). The plates were systematically at a 'high' temperature, that is, more than 100 °C above the boiling point of the liquid. Before impact, the drop is spherical and we extracted from the movies the position of the bottom of the drop. The impact velocities were varied by using different release heights, and the drop radii were changed using various hypodermic needles. The take-off speed V' was deduced from the time t at which the drop touched the solid again – during the flight, the drop is subject only to gravity, so that we simply have $V' = gt/2$.

We display in figure 4(*a*) the variation of the restitution coefficient $e = V'/V$, as a function of the Weber number We (defined in (1)). It is first observed that all the data collapse onto the same curve, showing that the Weber number is indeed the parameter which governs the shock elasticity. At low Weber number, e is close to unity: the shock is quasi-elastic. At large We, the elasticity abruptly drops, to reach values as low as 0.2 for We of about 30 (meaning that the drop rises after the shock to a height which is only 4 % of the initial height). This is our main finding: unlike solid shocks, the elasticity of liquid shocks (which imply strong deformations of the whole globule of matter) is extremely sensitive to the impact speed. Displaying the

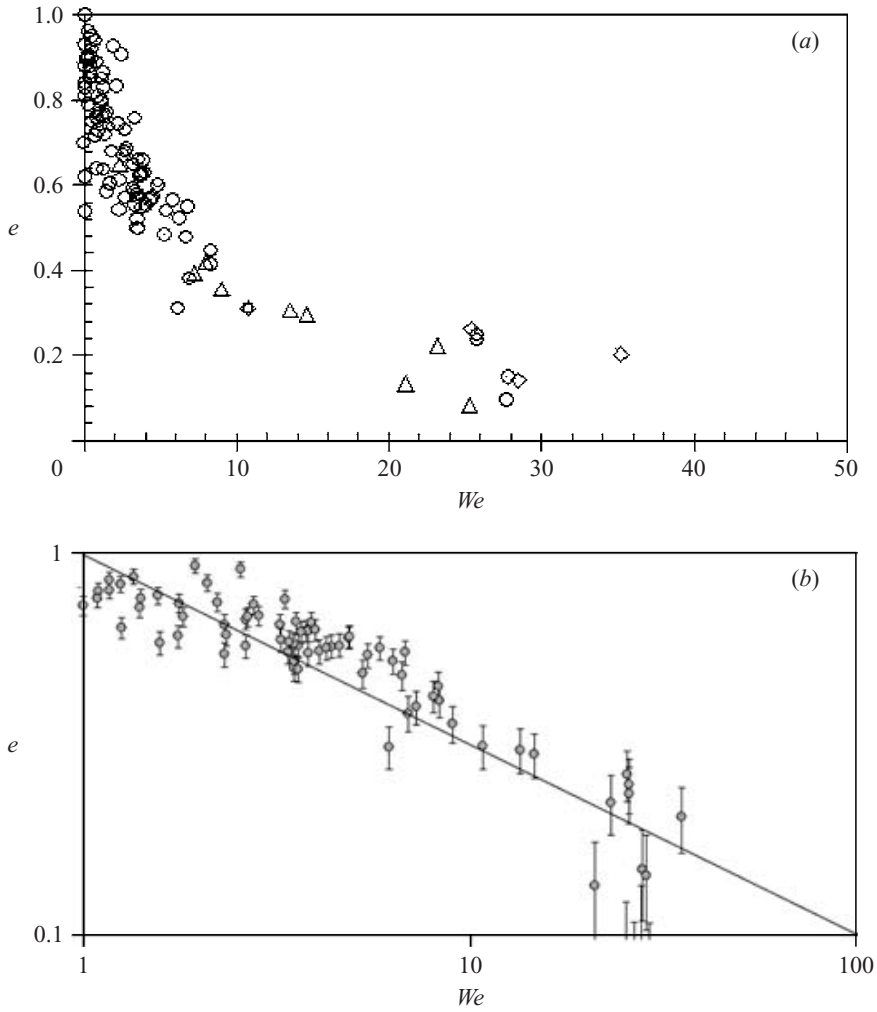

FIGURE 4. Restitution coefficient e for Leidenfrost drops (○, water; △, acetone; ◇, ethanol; -, nitrogen) bouncing on plates at temperature much larger than the boiling point of the liquid. The drop radii vary between 0.8 and 2 mm, and the impact velocities between 0.02 and 1 m s^{-1}. (*a*) It is found that the data collapse on a single curve, if they are plotted as a function of the Weber number We defined in (1). The elasticity strongly decreases with We. (*b*) If the same data are displayed in a log-log plot, e is observed to decrease as $We^{-1/2}$ drawn with a line. Writing $e = \alpha We^{-1/2}$, we find from the fit a numerical coefficient $\alpha = 1.0 \pm 0.1$.

function $e(We)$ in a log-log plot (figure 4*b*) shows that the data for $We > 1$ can be described by the scaling $e \sim We^{-1/2}$.

These behaviours differ from what can be observed for drops impacting a super-hydrophobic surface (that is, a micro-textured hydrophobic surface on which contact angles are typically of the order of 160°). Then, as seen in figure 5, a strong decrease of the elasticity (compatible with a variation of e as $1/V$) is also observed for 'large' impact velocities (corresponding, again, to large We). However, drops are found to stick to the substrate ($e = 0$) for moderate impact velocities ($V < 10\,\mathrm{cm\,s^{-1}}$). This can be interpreted as the result of the existence of a small adhesion force in this case: the kinetic energy of the drop becomes too low, so that pinning of the line on the surface textures allows the drop to remain stuck. This implies that smaller drops (of larger ratio surface/volume) will stick more easily than large ones, which was indeed observed (Richard 2000). As a consequence, the elasticity is maximum for some intermediate velocity, for which the restitution coefficient can (in this case) be

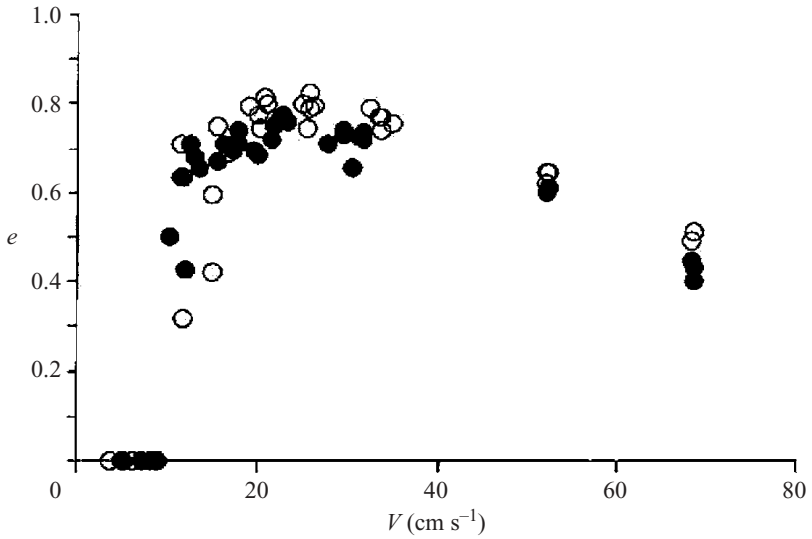

FIGURE 5. Restitution coefficient for millimetric water drops hitting a super-hydrophobic surface. As in figure 4, a loss of elasticity is observed with increasing the impact speed. Contrasting with Leidenfrost drops, the elasticity sharply decreases at small impact velocity, for which a sticking transition is observed. These data also emphasize that the drop behaviour is quite similar for water (open symbols) and a mixture of water and glycerol twice as viscous (solid symbols).

as large as 0.85 – a value significantly lower than reported for Leidenfrost drops in figure 4. This also suggests that the minimum velocity above which a rebound can be seen could be taken as a criterion of super-hydrophicity: the smaller this velocity, the better the surface – the limit being a hot plate for which this velocity appears to be zero.

4. Poorly elastic shocks

4.1. *Liquid springs*

As sketched in figure 6, we propose to model a bouncing drop as a spring. The simplest object which can be imagined for this purpose is a spring of initial length l_0 and stiffness k with two masses $m/2$ attached at each end. The rebound can be divided in two phases: first, the drop spreads owing to its kinetic energy, so that it (partially) stores it as surface energy (as a compressed spring does as elastic energy); then, the drop transfers its surface energy to translational kinetic energy (allowing it to take off) and to oscillatory kinetic energy. Similarly, a compressed spring will oscillate as it takes off. We shall justify in the final discussion (§ 5.3) why usual sources of dissipation can be neglected in our model.

We now describe the spring case in more detail. Newton's equation of motion can be written for the two masses, whose positions are denoted x_1 (at the top of the drop) and x_2 (at the bottom):

$$\tfrac{1}{2}m\frac{\mathrm{d}^2x_1}{\mathrm{d}t^2} = -\tfrac{1}{2}mg - k(x_1 - x_2 - l_0) \tag{4}$$

for the first mass and:

$$\tfrac{1}{2}m\frac{\mathrm{d}^2x_2}{\mathrm{d}t^2} = -\tfrac{1}{2}mg - k(x_2 - x_1 + l_0) + F \tag{5}$$

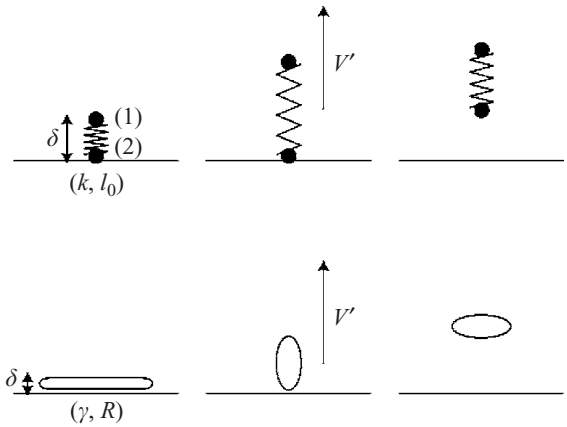

FIGURE 6. Comparison between a spring consisting of two attached masses, with an initial length l_0, a stiffness k and compressed to a height δ and a bouncing drop of initial radius R, stiffness γ and compressed to a height δ.

for the second one, denoting the reaction of the solid F (without adhesion, F is positive). Initially, and as long as the force acting on mass 2 is negative (and balanced by F), we have $x_2 = 0$. Equation (4) can be integrated, taking as initial conditions an imposed compression δ, and a zero velocity. Thus we find:

$$x_1(t) = l_0 - \frac{mg}{2k} + \left(\delta - l_0 + \frac{mg}{2k}\right)\cos\omega t \tag{6}$$

where ω is the natural pulsation of the mass:

$$\omega = \sqrt{\frac{2k}{m}}. \tag{7}$$

The bottom mass 2 leaves the substrate if the force which acts on it is positive ($k(x_1 - l_0) - mg/2 > 0$). Replacing x_1 by the quantity calculated above in (6), we find the time t_o after which the mass takes off:

$$-mg + k\left(\delta - l_0 + \frac{mg}{2k}\right)\cos\omega t_o = 0. \tag{8}$$

This equation only admits a solution if the absolute value of $\cos\omega t_o$ is smaller than unity. Since also $\delta < l_0$, we finally find:

$$\delta < l_0 - \frac{mg}{k}. \tag{9}$$

The spring must be compressed enough to overcome its weight. If this criterion is fulfilled, we can calculate the speed at take off. Then $x_2(t_o) = 0$ and (from (6))

$$\frac{\mathrm{d}x_1}{\mathrm{d}t}(t_o) = -\omega\left(\delta - l_0 + \frac{mg}{2k}\right)\sin\omega t_o.$$

In the limit of a compressed spring ($\delta \ll l_0$), and denoting $x(t)$ as the position of the centre of mass of the spring, we find for the speed of take off:

$$V' = \frac{\mathrm{d}x}{\mathrm{d}t}(t_o) = \frac{\omega l_0}{2}\sqrt{\left(1 - \frac{g}{\omega^2 l_0}\right)\left(1 + \frac{3g}{\omega^2 l_0}\right)}. \tag{10}$$

If, in addition, the weight is negligible compared to the elastic energy typically stored in the spring ($mg \ll kl_0$), we simply find

$$V' = \frac{\omega l_0}{2} \tag{11}$$

These two limits ($\delta \ll l_0$ and $mg \ll kl_0$) are satisfied in our experiments: the size of the spring is the drop radius (or diameter); the compression due to impact is the drop thickness δ as it reaches its maximum extension (given by (3), which together with volume conservation yields $\delta \sim R\,We^{-1/2}$); and the stiffness of the spring is the surface tension γ. Thus these two conditions can be written for a bouncing drop as $We > 1$ and $R < \kappa^{-1}$, respectively, which are both fulfilled in this section. More generally, the results found for a spring should hold for a drop: the main difference between the two systems is the way the mass is distributed in space, which should affect the numerical coefficients but not the scaling laws. Equation (11) can be used for evaluating the speed after take off:

$$V' \sim V_o = \sqrt{\frac{\gamma}{\rho R}}. \tag{12}$$

This is quite a surprising result: the speed of take off V' is independent of the impact speed V (for $We > 1$, i.e. in the regime of large deformation), so that the restitution coefficient $e = V'/V$ should decrease with V, as

$$e \sim We^{-1/2}. \tag{13}$$

This result is in good agreement with the results displayed in figures 4 and 5. This shows *a contrario* that the speed after take off is the same whatever the impact speed. For a millimetric drop, this speed is about $25\,\mathrm{cm\,s^{-1}}$, in agreement with the value deduced from (12). With such a speed, the drop rises to a height of about 3.5 mm (as can be observed in figure 1). Since V' does not depend on the compression of the drop, the details of the model providing the rate of compression ((2) or (3), for example) do not have an impact on the result. This also helps in understanding the difference between these kinds of shock and shocks of solid marbles. In the latter case, the impact object mainly deforms close to its contact with the solid on which it bounces, and it stores its kinetic energy as (volumetric) elastic energy. Then, the restitution coefficient increases with the speed V at impact, before saturating (and very slightly decreasing) at very large V (Falcon *et al.* 1998). It seems that the energy transferred (and later lost) to vibrational modes is negligible, compared to the energy dissipated in elastic waves at the substrate surface and in plastic deformation in the impacting body.

4.2. *Conditions for a rebound*

The mass–spring analogy also helps in understanding the criterion for observing a rebound. We stressed earlier that the elastic force must overcome the weight to allow take off, (9). In our case, the compression is the height of the drop after it has been squeezed by the impact: the drop is more compressed when the impact is violent (figure 3). Thus, we expect from (9) that a rebound can only occur provided that the speed is large enough. For $We > 1$, (3) can be considered as a law for the compression; using volume conservation, it yields $\delta \sim R\ We^{-1/2}$. Then, replacing the different terms in (9) (i.e. taking $l_0 \sim R, k \sim \gamma$ and $m \sim \rho R^3$) yields as a criterion of bouncing:

$$V > V_c = \frac{V_o}{(1 - R^2\kappa^2)} \tag{14}$$

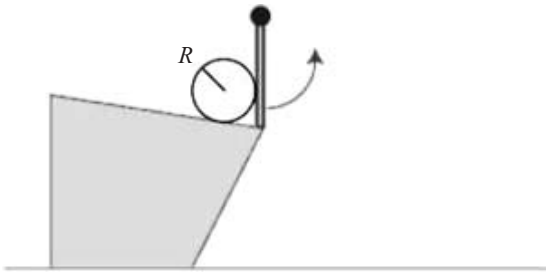

FIGURE 7. Our device for varying the size of the bouncing drop: a volume of water (radius R) is deposited on a slightly inclined plate. When the gate is opened, the drop falls and bounces on the plate below. All the elements are made of steel and heated, so that the drop is everywhere in a Leidenfrost situation.

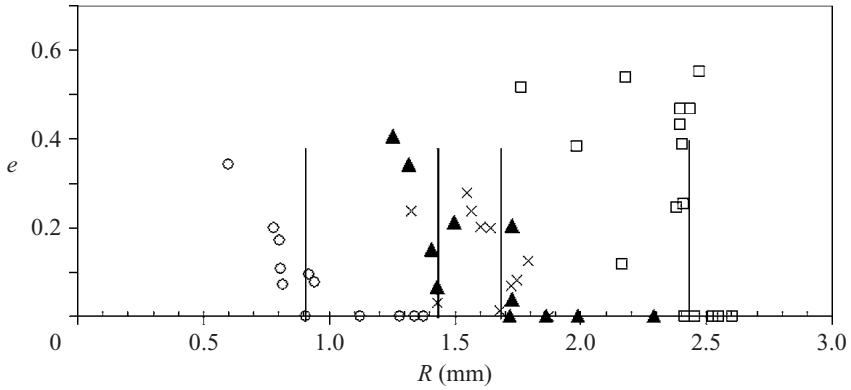

FIGURE 8. Restitution coefficient of the shock for a drop of varying radius R falling from a given height $H = 1\,\mathrm{cm}$, as a function of R for different liquids (○, liquid nitrogen; ▲, ethanol; ×, acetone; □, water). In each case, an abrupt decrease is observed around a critical radius R_c marked with a vertical line.

where V_o is defined by (12), and is about $25\,\mathrm{cm\,s^{-1}}$ for a millimetric water drop. For small droplets ($R \ll \kappa^{-1}$), (14) indicates that drops will only bounce if $V > V_o$, that is, $We > 1$, which is the limit considered in this section. But it can be different if drops are larger: as R approaches the capillary length κ^{-1}, the velocity V_c diverges, meaning that drops which satisfy the condition $We > 1$ will not necessarily bounce. Note that this result does not depend on the choice of the model for spreading: using (2) for evaluating the compression of the drop leads to a relation similar to (14), but with a different diverging behavior as R approaches κ^{-1} (then, we find $V > V_c = V_o/(1 - R^2\kappa^2)^2$).

To test these ideas, we performed the experiment sketched in figure 7. A steel block with a slightly inclined (by 1° or 2°) top plate is heated above the Leidenfrost temperature T_L. Liquids are kept trapped on the top plate by a steel gate, which is similarly brought above T_L. When the gate is opened, the drop falls down till it reaches another flat plate also above T_L. Movies of the fall and the (possible) rebound were made for different liquids (water, ethanol, acetone and liquid nitrogen). In each case, the size of the initial drop was varied, and the velocity of impact kept as constant as possible, between 42 and $51\,\mathrm{cm\,s^{-1}}$. This variation together with the uncertainty in the measurement of V' generate some scatter in the results displayed in figure 8, where the restitution coefficient e is plotted as a function of the drop radius.

For each liquid, it is observed that e dramatically decreases when approaching some critical size R_c of the drop. This size is quite comparable for ethanol and acetone, but

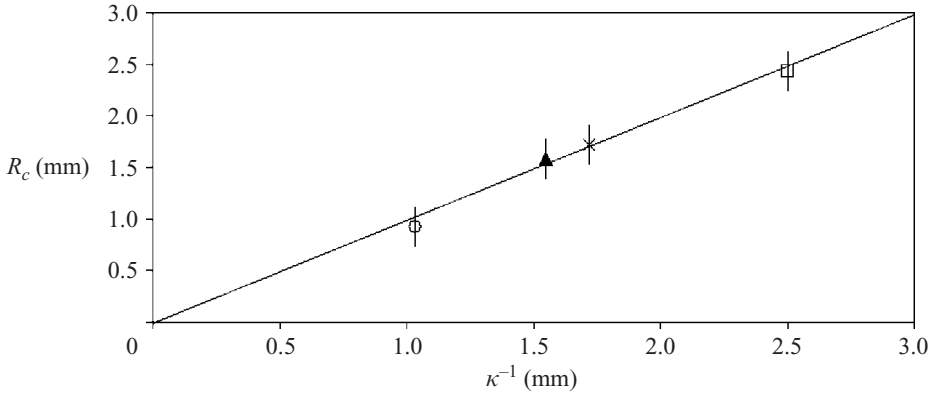

FIGURE 9. Critical radius R_c above which a Leidenfrost drop does not bounce, as a function of the capillary length associated with the liquid (○, liquid nitrogen; ▲, ethanol; ×, acetone; □, water), as deduced from figure 8.

significantly smaller for liquid nitrogen, and larger for water. For drops larger than R_c, the shock is inelastic ($e = 0$): a 'large' drop cannot bounce, despite the (quasi-) absence of friction for these non-wetting systems.

We plot in figure 9 the critical radius R_c as a function of the capillary length. It is observed that the two quantities are proportional to each other, with a constant of proportionality close to unity ($R_c\kappa = 1.0 \pm 0.1$). This result agrees with (14), which predicts that bouncing should not occur (whatever the impact velocity) for drops of the order of (or larger than) κ^{-1}. This result can be summarized in a very simple way: a drop larger than the capillary length is subject to gravity, which makes it flatten. Thus, such a drop loses its elasticity, which makes it unable to bounce. Such large drops were observed to just oscillate on the plate, after hitting it; these oscillations were damped by viscosity, yet sometimes reappeared spontaneously, as reported by Yoshiyasu, Matsuda & Takaki (1996) or by Strier *et al.* (2000). More generally, the loss of elasticity could arise from other factors, such as viscosity or adhesion. However, transitions to sticking in these cases remain to be described.

5. Quasi-elastic shocks

5.1. *Phenomenology*

It was observed in figure 4 that a rebound at a small Weber number is characterized by a very high restitution coefficient. Let us first stress that such impacts are difficult to achieve: $We \ll 1$ implies for a millimetric drop an impact velocity smaller than $25\,\mathrm{cm\,s^{-1}}$, corresponding to a drop released from a height smaller than 3 mm. Thus we chose to study series of rebounds: a given drop is released from a centimetric height, and its successive rebounds are monitored as a function of time. This allows us to reach (after a few rebounds, and provided that the substrate is exactly horizontal) impact velocities of the order of $0.1\,\mathrm{m\,s^{-1}}$, or even smaller. However, this does not avoid the vibrations of the drop (which oscillates after each rebound, as described in § 2), which will be found to affect the rebound.

Figure 10 shows the restitution coefficient of a water drop bouncing off hot plates, as a function of the number of rebounds. Very numerous rebounds are observed: for similar experiments, we monitored up to 1000 successive rebounds, which emphasizes the quasi-elasticity of the shocks. In figure 10, the restitution coefficient is indeed observed to tend after about 10 shocks towards a value which is very close to

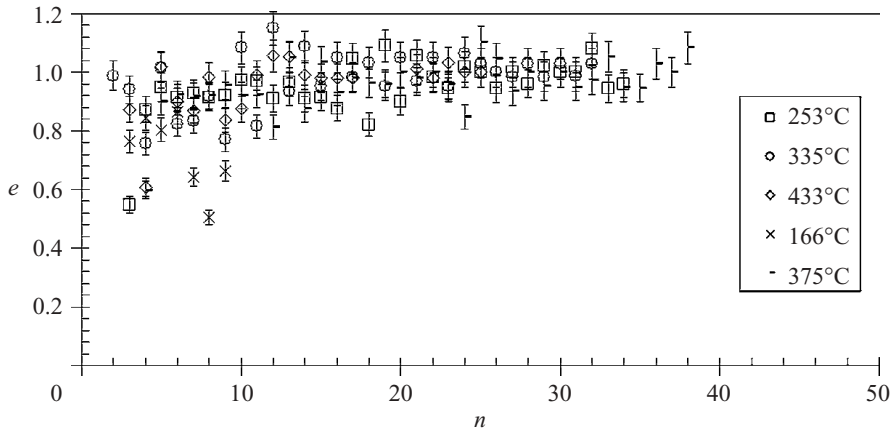

FIGURE 10. Restitution coefficients observed for series of successive rebounds experienced by water drops falling from an initial height of 16 mm; n designates the number of rebounds. Whatever the plate temperature, the restitution coefficient tends towards a value very close to unity (quasi-elastic regime), allowing a very large number of successive rebounds (here tens, but we often observed hundreds).

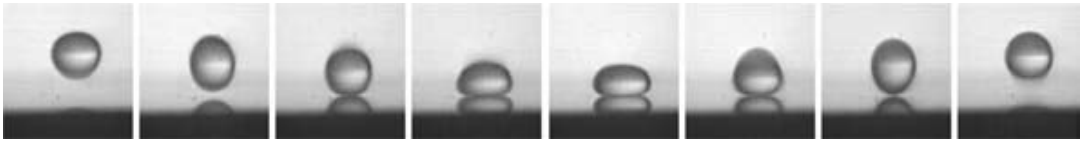

FIGURE 11. Sequence of pictures showing the rebound of a water Leidenfrost drop in the quasi-elastic regime. The drop radius is $R = 1$ mm, the impact velocity is $V = 7\,\mathrm{cm\,s^{-1}}$, which yields a Weber number $We = 0.1$. The interval between two pictures is 2.5 ms.

unity, whatever the plate temperature (provided it is larger than the Leidenfrost temperature). Hence the drop always rises to the same height (independent of the position from which it is released), which is of the order of 2 mm for a drop of radius $R = 1$ mm. Note also in figure 10 that the restitution coefficient can be larger than unity; this is partially related to the uncertainty in the measurement, but values larger than 1 might indeed exist, because of the oscillations of the drop (which store some energy), and possibly because of the energy gained on the hot plate (close to which the drop slightly evaporates).

Figure 11 shows the successive positions of a drop in one period of this stationary elastic regime. The drop deforms modestly during the contact ($We \ll 1$). Its size remains constant during the period, showing that evaporation can be neglected at this time scale (this allows the drop to bounce several hundreds times). The period in figure 11 is 17.5 ± 1.0 ms, a time negligible compared to the lifetime of this Leidenfrost drop, if deposited (and trapped) on the hot plate, namely 40 s (at 250 °C). (This lifetime is observed to remain of the same order for a bouncing drop.) But most importantly, it can be seen in figure 11 that the vibrations of the drop coincide with its rebound: the drop is spherical at impact and take off; it flattens twice, namely during the contact and when it reaches its maximum height. It thus seems that the oscillations are synchronized with the motion of the centre of mass.

We recorded the mean height of the drop h (that is, the position of its centre of mass) together with its equatorial diameter d, as a function of time, for several successive oscillations (and rebounds). Figure 12(a) shows that both curves are periodic, without significant damping, and that the period is indeed the same. For a better visualization,

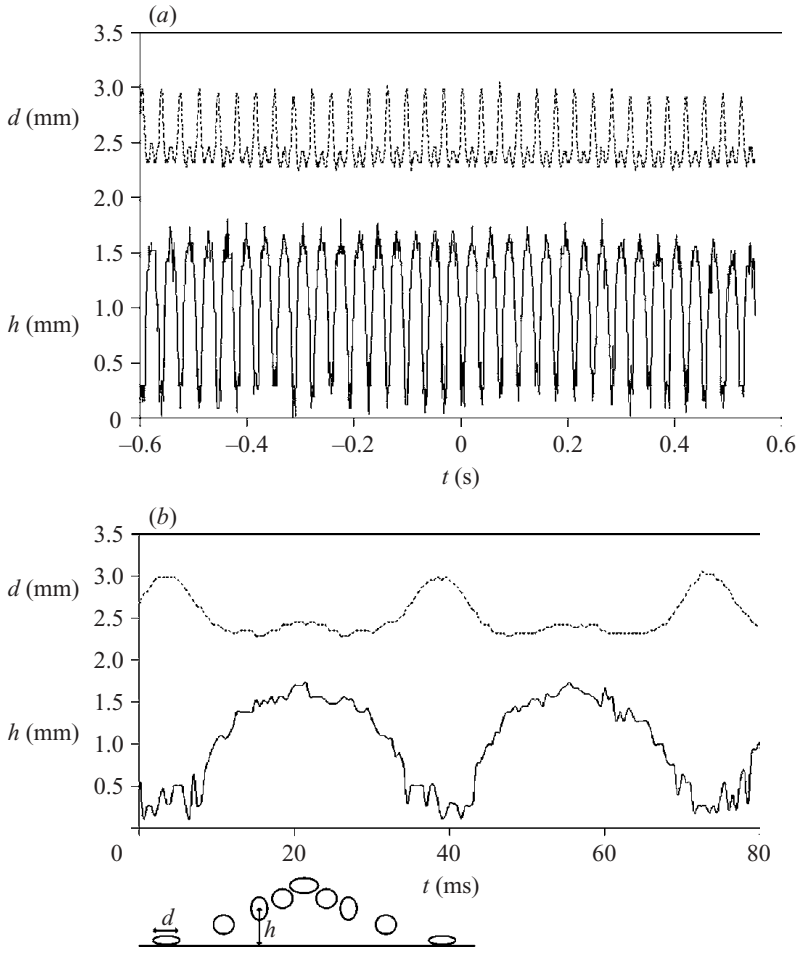

FIGURE 12. (*a*) Height h of the centre of mass of a water drop ($R = 1.25$ mm) in the quasi-elastic regime: no appreciable decrease of the height is observed over more than 30 successive rebounds. We show in the same plot the equatorial diameter d of the drop: the vibrations generated by the impact (and seen in figure 11) are observed to be in phase with the flight. (*b*) Zoom of two periods of (*a*). We sketch below the shape at the drop for different moments of its flight.

figure 12(*b*) is a zoom of two periods, together with a sketch of the successive shapes of the drop within a period. The drop undergoes half an oscillation on the plate, and one and a half in air. The respective durations of these two regimes are 10 ms and 25 ms, from which we deduce that the period of oscillation is different when the drop is contacting the solid (then, the period is 20 ms) and when it is free (then, the period is 16.7 ms), as mentioned in Courty *et al.* (2006).

Taking the flight time to be of the order of the oscillation time, we can deduce a simple formula for the height of the drop h_c in the regime of multiple rebounds. Taking the Rayleigh time $\pi(\rho R^3/2\gamma)^{1/2}$ of oscillation of a free drop (Rayleigh 1879), and that the time of the flight t (related to the height by $h = gt^2/8$) is 1.5 the oscillation time of a drop, we find a relation between h_c and the drop radius:

$$h_c = \frac{9\pi^2}{64}\frac{R^3}{\kappa^{-2}}. \tag{15}$$

We tested this relation, and plot our results in figure 13. The domain of variation is quite limited for the drop radius. On the one hand, we are limited by the capillary

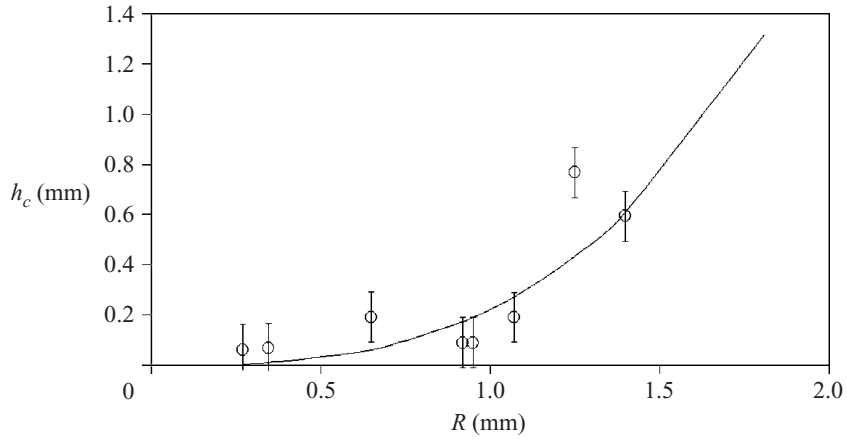

FIGURE 13. Height for which multiple rebounds are observed as a function of the drop radius. The data are compared with (15), drawn as a line.

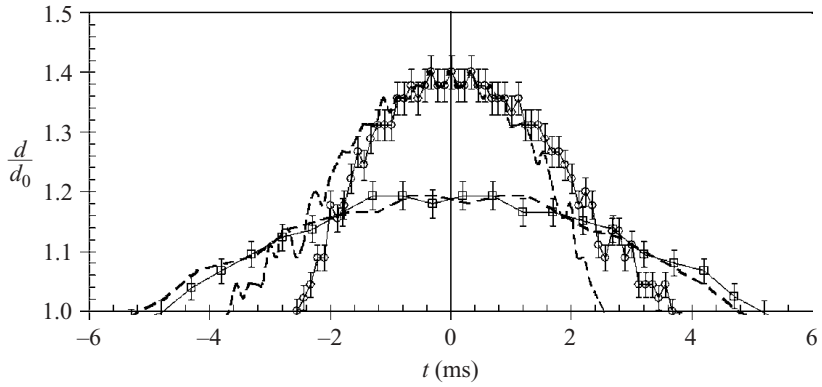

FIGURE 14. Equatorial diameter of an impacting drop (normalized by its diameter before impact) as a function of time, for a drop in the quasi-elastic regime (squares) and for a drop for which the oscillation and flight periods differ (circles). The origin of time is chosen at the maximal extension. It is observed that only the drop deformation is time-reversible, in the quasi-elastic regime only.

length κ^{-1}, as shown in § 4.2. On the other hand, the drop cannot be smaller than a fraction of a millimetre for the observation to be feasible. On the whole, a fair agreement is found, without any adjustable parameter.

5.2. *Conditions for observing a quasi-elastic rebound*

We tried to characterize the conditions which favour a quasi-elastic rebound. We first compared shocks for which the restitution coefficient e could not be distinguished from unity with shocks for which it was found to be significantly smaller. We display in figure 14 an interesting difference between the two cases: the drop diameter (normalized by its value without oscillation) is plotted as a function of time during the shock: it thus in both cases increases from unity to a value slightly larger (1.2 and 1.4), before decreasing back to unity (when the drop takes off). The origin of time is chosen as the maximum extension. For each series of data (symbols), we superimposed (thin lines) curves and they are time-symmetric. It is found that only the quasi-elastic rebound (squares) is time-reversible, which stresses the phase locking between the two sources of oscillation (drop vibration, parabolic flight).

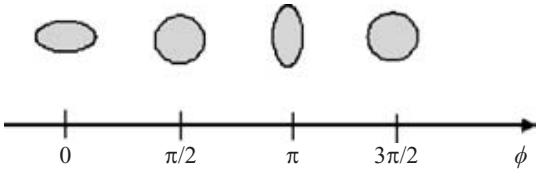

FIGURE 15. Our phase convention for a drop subjected to a quadrupolar oscillation.

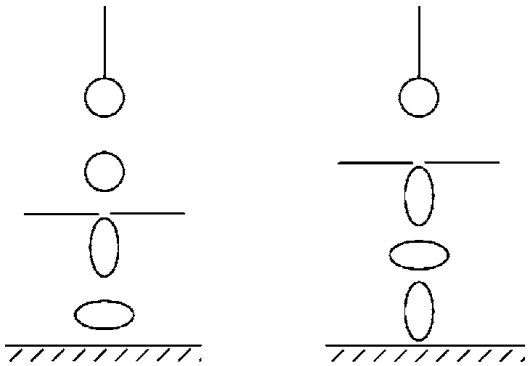

FIGURE 16. Experimental set-up for tuning the phase of a drop at impact. A plate pierced with a hole of millimetric diameter (and heated to be non-wettable) is placed between the height from which the liquid is released and the bottom plate on which the rebound is observed. Passing through the hole elongates the drop, which later oscillates. Varying the position of the pierced plate thus allows us to vary the phase at impact.

A natural question, at this point, is how elastic (or less elastic, as shown in figure 4) regimes may be generated. We noted above (figure 10) that the elastic regime spontaneously sets in after a short transient. It happens in about 70 % of the experiments where we followed successive rebounds, and always exhibits the characteristics reported above (synchronization of the oscillation with the flight, time-reversibility). This suggests that the phase of the drop influences the rebound, and we thus tried to demonstrate the role of this phase.

We chose for the phase of the drop oscillation the convention sketched in figure 15. Note that the two spherical states ($\phi = \pi/2$ and $\phi = 3\pi/2$) differ by the internal motion of the liquid: the equatorial diameter tends to contract in the phase $\phi = \pi/2$, while it tends to expand in the phase $\phi = 3\pi/2$. Our experiment consisted of monitoring impacts for similar drops having a similar velocity, yet a different phase at impact. The phase was varied using the device drawn in figure 16: a plate pierced with a thin hole (diameter comparable with that of the drop) is placed between the point from which the drop is released and the plate. Because of the presence of this hole, the drop is forced to elongate (and then vibrates), so that changing the height of the pierced plate allowed us to vary the phase at impact. The impact was recorded and the restitution coefficient of the shock deduced from the record.

Despite its apparent simplicity, this experiment is extremely delicate to perform at very small impact velocities (where the elastic regime is observed), because this corresponds to small heights, which makes it impossible to place the pierced plate. We thus were forced to do this experiment with various heights (of the order of one centimetre), corresponding to impact velocities between 20 and 80 $\mathrm{cm\,s^{-1}}$. We carefully measured the restitution coefficients for about 100 shocks in this interval of impact velocities, allowing us to determine a mean value $\bar{e}$ of e for each velocity. The results are displayed in figure 17, where for each shock we normalized the measured

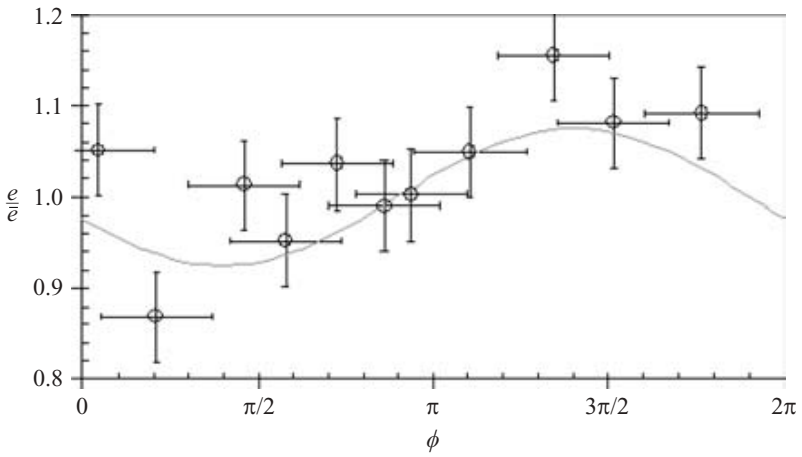

FIGURE 17. Restitution coefficient of a drop bouncing off a hot plate as a function of its phase at impact (defined in figure 15). The restitution coefficient is normalized by its mean value at a given impact velocity. Each datum corresponds to at least five experiments, and the corresponding error bars are indicated.

restitution coefficient by its mean value at this velocity. This explains why in our results the quantity $e/\bar{e}$ can be larger than unity. The uncertainty in the determination of the phase at impact is 0.3 rad. We performed (on average) 5 measurements per interval of 0.3 rad, which provides the uncertainty in the coefficient of restitution.

It appears that the phase does affect the elasticity of the shock: the data can be fitted by a sinusoidal function, whose maximum is observed for $\phi = 1.4\pi$, close to $3\pi/2$. The effect is small, yet significant: the relative increase in measured restitution coefficient between $\phi = \pi/2$ and $3\pi/2$ is about 40 %, larger than the uncertainty on the measurement (± 10 %). The maximum elasticity is found to be reached for the phase ($\phi = 3\pi/2$) observed for impacting drops in the quasi-elastic regime. The system thus locks onto the state of minimum dissipation. By definition, the phase $\phi = 3\pi/2$ is the one for which the drop is spherical, coming back from an oblate configuration. In the reference frame of the drop, the velocity of the bottom of the drop is directed towards the top, and it is maximum in this phase. Since the drop is moving at a velocity V, this phase thus corresponds to the minimum velocity of the bottom of the drop. On the other hand, the phase $\phi = \pi/2$ has a maximal velocity, and was observed to be the less elastic. It seems that the local velocity at impact might influence the elasticity, which is advantageous since this velocity is small.

We can evaluate this minimal velocity. In the regime of small deformation, we assume that there is energy conservation (Okumura *et al.* 2003): at impact, the drop stores its kinetic energy as surface energy. Denoting as ε_o the increase of radius in the oblate state ($\phi = \pi$, see figure 15), the conservation of energy is written dimensionally as $\rho R^3 V^2 \sim \gamma \varepsilon_o^2$, which gives ε_o ($\varepsilon_o \sim RWe^{1/2}$). The elongation of the drop radius can be written $\varepsilon = \varepsilon_o \sin(\omega t - 3\pi/2)$, where ω is the Rayleigh pulsation of a free drop ($\omega \sim (\gamma/\rho R^3)^{1/2}$). As the drop impacts, the bottom moves up at a velocity $\varepsilon_o \omega$, that is, of the order of V, the impact velocity of the centre of mass. Hence, the drop touches the solid with a minimized velocity, which accounts for a minimized energy loss during the shock.

5.3. *Discussion*

Periodic rebounds are also observed for solid marbles bouncing off vibrated plates. Depending on the pulsation ω and amplitude A of the vibrations, the marble may

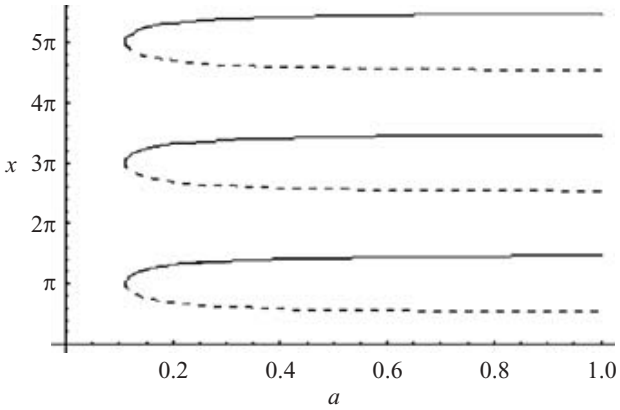

FIGURE 18. Numerical solution of (20), as a function of the amplitude of the oscillation. For the resolution, we have chosen $R = 1.1$ mm and $e_o = 0.9$. For each family of solution, there is one stable branch (solid line), and one unstable branch (dashed line).

bounce, or not. Also, there is a correlation between the time of flight and the period of vibration. In our case, we must first write an equation for the shock – as discussed above, the restitution coefficient varies with the phase, and with the impact velocity: $e = e_o\ (1 - kA/R\ \sin\phi)\ (b + cV)$, where A is the amplitude of the oscillation and b, c and β are coefficients. Neglecting the variation of the restitution coefficient with the velocity (which yields a second-order correction), we obtain a relationship between the take-off and impact velocities:

$$V' = Ve_o(1 - \beta A/R \sin\phi). \tag{16}$$

The phase at take-off is $\pi/2$. Denoting the time of flight (between two impacts) as τ, we thus find for the phase at impact:

$$\phi = \omega\tau + \frac{\pi}{2}. \tag{17}$$

When in the air, the drop is subject only to gravity; in the quasi-elastic regime, it falls towards the plate at the same velocity V as for the previous shock, which is written

$$V = V' - g\tau. \tag{18}$$

Since the trajectory of the bottom of the drop z_b is $z_b = -gt^2/2 + V't + A\cos(\omega t + \pi/2)$, we obtain a third equation at contact:

$$-\tfrac{1}{2}g\tau^2 + V'\tau - A\sin\omega\tau = 0. \tag{19}$$

Denoting $x = \omega\tau$ and $a = A/R$, the solution of these equations satisfies

$$(1 - e_o)\frac{x^3R^2\kappa^2}{16} + \frac{e_o}{2}a\sin 2x + e_o\frac{R^2\kappa^2}{16}\beta x^2\cos x + (1 - e_o)\sin x = 0 \tag{20}$$

where κ is the inverse of the capillary length. Equation (20) can be solved numerically (x being the unknown), which was done for $\beta = 1$ (the solutions depend little on the value of this parameter). The solutions are displayed in figure 18, as a function of a, the reduced amplitude of the oscillation, for a water drop at 100 °C of radius $R = 1.1$ mm and for $e_o = 0.9$.

It is observed that periodic solutions exist provided that the amplitude of the oscillation is larger than a threshold $a_c = (1 - e_o)/e_o$, i.e. about 0.1 in the example of figure 18. These solutions tend towards π, 3π, 5π at small amplitude, which seems in

good agreement with our experimental results: the periodic regime described above corresponds to $x = 3\pi$, and we observed drops oscillating twice during the flight, corresponding to $x = 5\pi$. A different choice for β would slightly shift the threshold amplitude a_c. Note also that only half of the branches are stable in figure 18, as indicated (the stability is deduced from the evolution of the trajectory after perturbing the time of flight). It is thus possible to observe periodic regimes – and, as found experimentally, this might be not the case, which is found to be due to an too small amplitude. For most observations, the amplitude was found to be about $0.15R$, in qualitative agreement with the results in figure 18. Because of the modest value of this amplitude, x should be close to its minimal value of 3π, as indeed found in the experiments.

We assumed in this description that the amplitude of the oscillation remains constant throughout the sequence, which was observed experimentally. This raises the question of dissipation and energy input in these processes, which we discuss finally.

The oscillations might be damped principally by viscosity. The typical time associated with this damping scales as $\rho R^2/\eta$, and is found to be about 3 s for a millimetric drop of water (whose viscosity falls to about 0.3 mPa s at 100 °C). It is much longer than a typical time of flight (i.e. a few milliseconds), allowing us to understand the negligible role of the liquid viscosity in these experiments.

Conversely, the drop can gain momentum during the impact because of its evaporation (by a quantity δm), which might sustain the rebounds. The corresponding gain of energy scales as $\delta m V^2$. Denoting as τ the contact time of the drop (see figure 2), and τ_L as its lifetime, we expect δm to be of the order of $m\tau/\tau_L$; for $\tau = 10$ ms, $\tau_L = 40$ s and $R = 1$ mm, we find δm of about 10^{-9} kg. On the other hand, the loss of translational kinetic energy due to impact can be written $mV^2(1 - e^2)$. Taking e of about 0.9, that is, a typical value observed on a cold super-hydrophobic surface in the regime of high elasticity, the ratio between these two energies scales as $\delta m/m(1 - e^2)$. This is typically 10^{-3}, suggesting that the main cause of elasticity, in this system, is the absence of pinning on the hot solid, rather than drop evaporation. The elasticity could also be reduced by the presence of the vapour film, which was treated in the paper as a passive medium allowing a non-wetting situation. The viscous force associated with the spreading of the drop (roughly) scales as $\eta_a V/h_f R_M^2$ (with η_a and h_f the vapour film viscosity and thickness), and thus the energy dissipated by viscosity as $\eta_a V/h_f R_M^3$. For large Weber numbers, equation (3) gives R_M ($R_M \sim R\,We^{1/4}$). We can thus compare the energy lost by viscosity to the kinetic energy of the impinging drop, which is written $\eta_a/\rho V h_f\ We^{3/4}$. For standard values of the different parameters (in particular taking h_f of the order of 100 μm), we find a value of about 10^{-4} for the first dimensionless group $\eta_a/\rho V h_f$, which implies a negligible viscous loss (in the vapour film) during the spreading stage. This partially justifies why we could ignore dissipation in our spring model.

6. Conclusion

We report in this paper a series of experiments showing the rebounds of liquid droplets of low viscosity hitting very hot plates, in the so-called Leidenfrost situation – a question of practical importance in cooling and deposition processes. We focused on the elasticity of the shock, and found that two regimes of bouncing can be distinguished, depending on the Weber number.

When the inertia of the falling droplet is large compared to its surface tension (high Weber number), the rebound is less elastic since the impact speed is large.

This considerably differs from solid elastic shocks at similar velocities, for which the elasticity only weakly depends on the impact velocity. This difference is related to the loss of energy associated with the shock in a liquid, which has two main causes: dissipation during the spreading at the impact, and partition of the energy between drop oscillations and translation at take-off. The higher the velocity, the larger the part of energy which is transferred to oscillations, and thus the less elastic the shock. In a similar vein, it is found that elasticity will be lost for large drops: then, the impact is found to be inelastic; owing to gravity, drops larger than the capillary length cannot restore enough translational energy to take off, and thus remain stuck on the hot plate where they oscillate without bouncing.

For shocks at a small Weber number, we report the existence of a quasi-elastic regime of rebounds: a drop may bounce hundreds of times, always coming back to the same (millimetric) height. Then, it is observed that there is a strong correlation between the oscillations of the drop and the rebound: the sequence of oscillations exactly fits with the drop trajectory, so that time reversibility is obeyed. The effect of the drop oscillations at the first impact is experimentally addressed, and results suggest that a bouncing drop maximizes its elasticity by adjusting its flying time to its oscillations. A successively bouncing drop reaches a resonant state where the energy loss is minimized.

As has been mentioned in the past, the bouncing of a drop is very similar to its oscillation. In this respect, one can not the strong similarity between the behaviour of a drop on an oscillating plate and a Leidenfrost drop (Yoshiyasu *et al.* 1996). If the frequency and the amplitude are in the correct range, a small drop on a non-wetting oscillating plate bounces periodically. If the size of the drop is increased (puddles), the drop remains stuck to the plate because of gravity (as for large Leidenfrost drop impact) and oscillates, displaying star shapes (spontaneously oscillating Leidenfrost stars may also be observed (Strani & Sabetta 1983; Strier *et al.* 2000)). We proposed in some (favourable) cases qualitative explanations for the observed phenomena, but many questions remain, often related to energy conservation (or loss) in these systems: it might be worth describing how viscosity modifies our picture. It would also be useful to understand if the quasi-elastic regime is specific to the Leidenfrost situation: would a drop in zero-wetting bounce similarly on a cold solid (i.e. without any evaporation)? Owing to residual adhesion, it would be very difficult to answer this question experimentally. Numerical simulations, well-adapted to these slippery states of water where the absence of any contact lines simplifies the approach (Renardy *et al.* 2003) might be very useful. They would also contribute to showing how the frequency locking is found by the system. The same kind of approach would be very useful to confirm and make more quantitative our observation on the dependence of the restitution coefficient on the oscillation phase of the impacting drop.

REFERENCES

Baumeister, K. J. & Simon, F. F. 1973 Leidenfrost temperature – its correlation for liquid metals, cryogens, hydrocarbons, and water. *Trans. ASME: J. Heat Transfer* **95**, 166–173.

Bell, K. J. 1967 The Leidenfrost phenomenon: a survey. *Chem. Engng Prog. Symp. Series AIChE* **63**, 351–358.

Berenson, P. J. 1961 Film-boiling heat transfer from a horizontal surface. *Trans. ASME: J. Heat Transfer* **83**, 351–358.

Biance, A. L., Clanet C. & Quere, D. 2003 Leidenfrost drops. *Phys. Fluids* **15**, 1632–1637.

Chandra, S. & Avedisian, C. T. 1991 On the collision of a droplet with a solid surface. *Proc. R. Soc. Lond.* A **432**, 13–41.

Chandra, S. & Aziz, S. D. 1994 Leidenfrost evaporation of liquid nitrogen droplets. *Trans. ASME: J. Heat Transfer* **116**, 999–1006.

Clanet, C., Béguin, C., Richard, D. & Quéré, D. 2004 Maximal deformation of an impacting drop. *J. Fluid Mech.* **517**, 199–208.

Courty, S., Lagubeau, G. & Tixier, T. 2006 Oscillating droplets by decomposition on the spherical harmonic basis. *Phys. Rev.* E (in press).

Eggers, J., Lister, J. & Stone, H. A. 1999 Coalescence of liquid drops. *J. Fluid Mech.* **401**, 293–310.

Falcon, E., Laroche, C., Fauve, S. & Coste, C. 1998 Behaviour of one inelastic ball bouncing repeatedly off the ground. *Eur. Phys. J.* B **3**, 45–57.

Goldshtik, M., Khanin, V. & Ligai, V. 1985 A liquid drop on an air cushion as an analogue of Leidenfrost boiling. *J. Fluid Mech.* **166**, 1–20.

Gottfried, B. S., Lee, C. J. & Bell, K. J. 1966 The Leidenfrost phenomenon: film boiling of liquid droplets on a flat plate. *Intl J. Heat Mass Transfer* **9**, 1167–1187.

Karl, A. & Frohn, A. 2000 Experimental investigation of interaction processes between droplets and hot walls. *Phys. Fluids* **12**, 785–796.

Leidenfrost, J. G. 1756 *De Aquae Communis Nonnullis Qualitatibus Tractatus.* Duisburg.

Michiyoshi, I. & Makino, K. 1978 Heat transfer characteristics of evaporation of a liquid droplet on heated surface. *Intl J. Heat Mass Transfer* **21**, 605–613.

Okumura, K., Chevy, F., Richard, D., Quéré, D. & Clanet, C. 2003 Water spring: a model for bouncing drops. *Europhys. Lett.* **62**, 237–243.

Rayleigh, Lord 1879 On the capillary phenomena of jets. *Proc. R. Soc. Lond.* **29**, 71–97.

Rein, M. 1993 Phenomena of liquid drop impact on solid and liquid surfaces. *Fluid Dyn. Res.* **12**, 61–93.

Renardy, Y., Popinet, S., Duchemin, L. *et al.* 2003 Pyramidal and toroidal water drops after impact. *J. Fluid Mech.* **484**, 69–83.

Richard, D. 2000 Situations de mouillage nul. PhD Thesis, University of Paris VI.

Richard, D., Clanet, C. & Quéré, D. 2002 Contact time of a bouncing drop. *Nature* **417**, 811.

Richard, D. & Quéré, D. 2000 Bouncing water drops. *Europhys. Lett.* **50**, 769.

Strani, M. & Sabetta, F. 1983 Free vibrations of a drop in partial contact with a solid support. *J. Fluid Mech.* **141**, 233–247.

Strier, D. E., Duarte, A. A., Ferrari, H. & Mindlin, G. B. 2000 Nitrogen stars: morphogenesis of a liquid drop. *Physica* A **283**, 261–266.

Wachters, L. H. J., Bonne, H. & van Nouhuis, H. J. 1966 The heat transfer from a hot horizontal plate to sessile water drops in the spheroidal state. *Chem. Engng Sci.* **21**, 923–936.

Yoshiyasu, N., Matsuda, K. & Takaki, R. 1996 Self-induced vibration of a water drop placed on an oscillating plate. *J. Phys. Soc. Japan* **65**, 2068–2071.

Zhang, S. & Gogos, G. 1991 Film evaporation of a spherical droplet over a hot surface: fluid mechanics and heat/mass transfer. *J. Fluid Mech.* **222**, 543–563.

Deuxième partie

Fluides quantiques

Chapitre 1

Modes de vibration d'un condensat de Bose-Einstein en rotation

Ses tourbillons, ses friselis
Font tomber les rayons du soleil dans son lit
Anne Sylvestre : La petite rivière

1.1 Introduction

On montre en mécanique quantique que l'équation de Schrödinger pour une particule de masse M peut se récrire comme une équation d'Euler pour un fluide de densité $\rho = |\psi|^2$ et un champ de vitesse

$$\boldsymbol{v} = \hbar \boldsymbol{\nabla} \chi / M, \tag{1.1}$$

où $\psi = \sqrt{\rho} e^{i\chi}$ désigne la fonction d'onde : la nature intrinsèquement potentielle de cette forme de champ de vitesse a ainsi longtemps fait penser que les écoulement dans un condensat de Bose-Einstein, dont la dynamique est décrite par une fonction d'onde macroscopique, était nécessairement irrotationnel. Feynman et Onsager ont cependant montré que les singularités de phase associés aux points de densité nulle pouvaient être interprétées comme des tourbillons de circulation quantifiée en unité de h/M [1, 2]. La première vérification de cette intuition fut apportée par Vinen qui, en étudiant la fréquence de vibration d'un fil tendu dans un récipient d'hélium

superfluide en rotation, démontra expérimentalement la quantification de la circulation [5]. Dans ce système, les vortex ont un diamètre caractéristique très faible, de l'ordre de la distance interatomique, et il fallut par conséquent attendre encore une dizaine d'années avant de développer des expériences suffisamment précises pour les observer directement. Packard réussit en effet à piéger des électrons au cœur des vortex puis à les accélérer vers une plaque fluorescente grâce à un champ électrique parallèle à l'axe de rotation du superfluide, aboutissant au résultat de la figure 1.1. Ces tourbillons quantifiés ont par la suite été observées dans tous les superfluides : dans les condensats de Bose-Einstein gazeux [4, 6], les supraconducteurs, l'hélium 3 [3] ou encore les superfluides fermioniques gazeux récemment observés dans les systèmes de fermions ultra-froids [7]. Dans les circonstances habituelles, un vortex portant plus d'un quantum de circulation est instable[1]. Lorsque l'on tourne plus vite que le seuil de nucléation du premier vortex, on constate de façon assez générale qu'un nombre de plus en plus grands de vortex portant un seul quantum de circulation pénètrent dans le système. Ces vortex s'agencent alors selon un réseau régulier, dit *réseau d'Abrikosov*[2] dont une manifestation spectaculaire est fournie par l'expérience de MIT (Fig. 1.1).

L'existence du réseau d'Abrikosov confère des propriétés originales à la dynamique d'un condensat en rotation. En effet, alors que dans un superfluide immobile les excitations de basse énergie sont associées à des modes hydrodynamiques de compression (phonons), la rigidité du réseau de vortex ajoute des degrés de libertés "élastiques" au système et enrichit par conséquent le spectre du système. C'est Lord Kelvin qui le premier a étudié dans le cadre de la mécanique classique les modes de vibration d'une ligne tourbillonaire isolée [8]. À cette occasion il montra que, comme pour une corde vibrante, des ondes transverses pouvaient se propager le long du vortex, avec une relation de dispersion

$$\omega(k) = \Gamma k^2 \ln(1/kb), \tag{1.2}$$

[1]Cette instabilité est due à la force de Magnus qui décrit la force exercée sur un objet tournant sur lui même et se déplaçant dans un fluide. Cette force est en particulier responsable des multiples effets utilisés en football ou au tennis pour dévier la balle de sa trajectoire rectiligne. Dans le cas de deux tourbillons tournant dans le même sens, l'interaction du premier vortex avec le champ de vitesse du second *via* la force de Magnus induit une répulsion mutuelle. Si l'on considère un vortex portant deux quanta comme deux vortex unités, la force de Magnus tend à séparé ceux-ci.

[2]Comme on le verra plus bas, la densité de vortex est fixée par la vitesse de rotation du superfluide *via* le Principe de correspondance. L'organisation en réseau triangulaire résulte alors de la force de Magnus qui cherche à éloigner le plus possible les vortex les uns des autres.

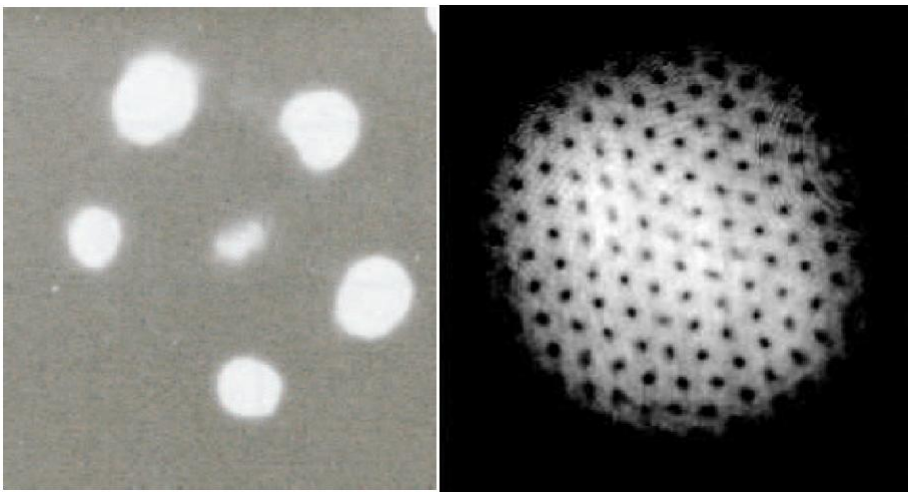

FIG. 1.1 – Visualisation de réseaux de réseaux de vortex dans l'hélium superfluide (gauche) et dans un condensat de Bose-Einstein gazeux de sodium (droite). Les deux images sont prises dans le plan orthogonal à l'axe de rotation.

où Γ est la circulation du champ de vitesse autour du tourbillon et b la taille de son cœur. Une particularité de ces modes de Kelvin est leur hélicité : du fait de la force de Magnus, les modes de Kelvin ont toujours une polarisation circulaire tournant en sens opposée à la rotation du fluide. Le travail de Kelvin fut plus tard généralisé au cadre quantique par Pitaevskii [9, 10]. Il démontra que les vortex quantiques possédaient essentiellement les mêmes propriétés dynamiques que leurs équivalents classiques et que la relation de dispersion (1.2) restait applicable à condition de prendre pour b la longueur de cicatrisation ξ du condensat[3].

Dans le cas d'un fluide incompressible comme l'hélium superfluide, l'étude des modes élastiques du réseau de vortex peut se réaliser en négligeant l'effet de déplétion de densité au cœur des tourbillons. Dans ce cas particulier Tkatchenko [11] montra que les vibrations transverses d'un réseau infini tournant à une vitesse angulaire Ω possédaient une relation de dispersion linéaire de la forme

[3]La longueur de cicatrisation, ou *healing length* en anglais désigne la distance sur laquelle l'effet d'une impureté ponctuelle plongée dans le condensat influera sur le profil de densité de celui-ci. ξ est relié au potentiel chimique par $\hbar^2/m\xi^2 \sim \mu$.

$$\omega = \sqrt{\frac{\hbar\Omega}{4M}}k$$

Dans ce chapitre, nous aborderons trois problèmes liés aux modes d'excitation d'un condensat en rotation. Dans la première section, nous présenterons une extension de l'hydrodynamique superfluide au cas d'un condensat en rotation rapide. Nous montrerons comment ces équations permettent de décrire les décalage de fréquences des modes du condensat, mais aussi qu'elles prédisent l'existence de nouveaux modes purement liés à la rotation du système (les modes dits *inertiels*). Nous montrerons ensuite que pour les modes de basse énergie se propageant le long de l'axe d'un condensat allongé, l'élasticité ne peut plus être négligée. Afin d'étudier ce problème, nous présenterons un formalisme permettant de décrire le couplage entre les phonons et les ondes de torsion du nuage (les *twistons*). Pour finir, nous nous concentrerons sur les modes de vibration d'une ligne de vortex unique et nous montrerons comment des effets de couplage non linéaires permettent d'observer expérimentalement les modes de Kelvin à partir de l'excitation du mode quadrupolaire de vibration de l'ellipticité transverse du nuage.

1.2 Hydrodynamique rotationnelle

Lorsque le condensat est en rotation rapide, on observe la nucléation d'un grand nombre de vortex selon un réseau triangulaire. Lorsque le pas du réseau devient petit devant la taille du nuage et que l'on s'intéresse uniquement à des excitation de grande longueur d'onde, on peut adopter une description "à gros grain" du réseau en moyennant son comportement sur une échelle de longueur ℓ grande devant la distance inter-vortex, mais petite devant le rayon du condensat. Cette approche est formellement proche de celle utilisée pour décrire la matière ordinaire dans les situations macroscopiques en passant des échelles atomiques à macroscopique où la matière est continue. Dans cette image, la vorticité $\boldsymbol{\Omega} = \boldsymbol{\nabla} \times \boldsymbol{v}/2$ n'est plus localisée sur les singularités que constituent les cœurs des vortex, mais est répartie selon une distribution continue $\Omega = n_v h/m$, où n_v la densité surfacique de tourbillons. La condition d'irrotationalité du champ de vitesse est alors levée pour le champ de vitesse moyen et on peut décrire le comportement dynamique du condensat par une équation d'Euler incluant un terme rotationnel. En régime permanent, cette description permet de calculer la densité de vortex dans un condensat maintenu dans un piège tournant à la vitesse angulaire Ω_0. En effet, l'énergie du système est minimale lorsque la vorticité

du champ de vitesse est égale à Ω_0, ce qui donne donc $n_v = m\Omega_0/h$, une prédiction qui a pu être vérifiée à plusieurs occasions [12].

En régime dynamique, il faudrait en toute rigueur ajouter à cette équation les termes décrivant l'élasticité du réseau de vortex. Cependant, sauf pour les modes de très basses énergies, tels que les phonons ou les modes de Tkatchenko, la force de rappel dominante est due à la compressibilité du nuage. En effet, la densité d'énergie élastique d'un réseau de vortex subissant un champ de déformation $\boldsymbol{\epsilon}$ peut s'écrire [13]

$$E_{\text{él}} \sim \rho\hbar\Omega_0(\boldsymbol{\nabla}\boldsymbol{\epsilon})^2,$$

où ρ désigne la densité de particules. Dans le cas d'ondes acoustiques, l'énergie associée à la compression du fluide est de l'ordre

$$E_{\text{comp}} \sim \rho M v^2,$$

où $\boldsymbol{v}$ est le champ de vitesse. Pour un piège allongé dont on note $\omega_\perp$ et $\omega_\parallel$ les fréquences transverses et longitudinales ($\omega_\perp \gg \omega_\parallel$), la condition de rotation rapide s'exprime par[4] $\Omega_0 \sim \omega_\perp$. Pour des fréquences de modes transverses, on a $\omega \sim \omega_\perp$, et l'on obtient après un bref calcul d'ordre de grandeur[5]

$$\frac{E_{\text{comp}}}{E_{\text{él}}} \sim \frac{R_\perp^2}{a_\perp^2},$$

où $R_\perp$ désigne la taille transverse du nuage et $a_\perp^2 = \hbar/m\omega_\perp$ désigne la taille de l'état fondamental transverse en l'absence d'interaction. Dans les situations expérimentales typiques où les interactions sont répulsives et dominent les effets de pression quantique[6], $R_\perp \gg a_\perp$, ce qui permet de négliger l'élasticité du réseau de vortex dans l'étude des modes transverses d'un condensat en rotation. Le calcul des modes de basse énergie en utilisant l'approximation de l'hydrodynamique rotationnelle à gros grain est présentée dans *Kelvin modes of a fast rotating Bose-Einstein condensate*. Dans un piège à symétrie cylindrique, ces modes peuvent être classés selon leur moment cinétique $\hbar m_z$, $m_z \in \mathbb{Z}$, selon l'axe z de symétrie. Dans le cas d'un condensat au repos, chaque mode de nombre quantique m_z est dégénéré

[4] En effet, la fréquence de rotation du nuage ne peut pas dépasser la fréquence de piégeage transverse puisqu'au delà de ce seuil, la force centrifuge l'emporte sur la force de piégeage et aboutit à une déstabilisation du condensat.

[5] On fait ici l'hypothèse que le théorème de Kelvin-Helmholtz reste valable et que les vortex se déplace avec le reste du fluide, ce qui permet d'écrire $\boldsymbol{v} \sim -i\omega\boldsymbol{\epsilon}$.

[6] C'est-à-dire la pression cinétique induite par les fluctuations quantiques de l'impulsion d'un atome.

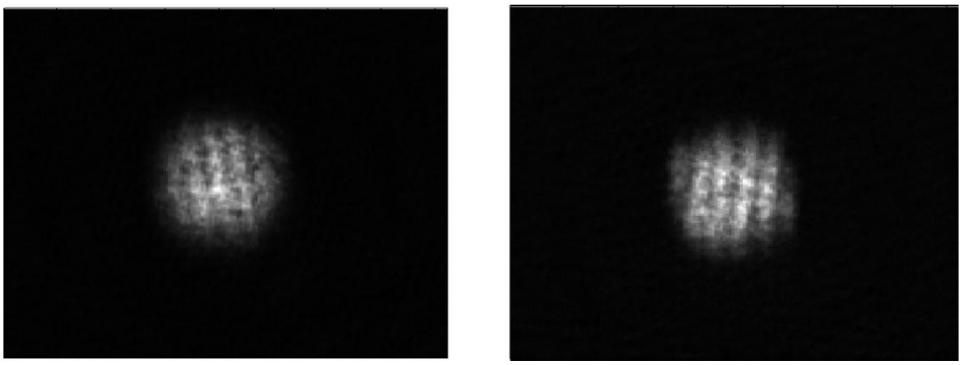

FIG. 1.2 – Observation du mode de précession du réseau de vortex par le groupe de C. Foot à Oxford [16]. Ce mode prédit par la théorie de l'hydrodynamique rotationnelle précesse toujours dans la même direction.

avec un mode de moment cinétique opposé et nous avons montré que cette dégénéréscence était levée lorsque le nuage est mis en rotation, un effet qui avait déjà été montré théoriquement en utilisant la technique des règles de sommes [14] et utilisé notamment dans la mesure du moment cinétique d'un condensat en rotation [15]. Un second résultat, inattendu celui-ci, a été de prouver l'existence d'une nouvelle famille de modes n'existant qu'en présence de vortex. Ces nouveaux modes sont associés à la précession du réseau de vortex et sont les analogues des modes inertiels rencontrés en géophysique ou dans certaines applications industrielles [17, 18]. Ils constituent la généralisation des modes de Kelvin au cas d'un réseau de vortex et par conséquent, ils ne possèdent qu'une seule hélicité (le nombre quantique m_z est toujours de signe opposé au moment cinétique du condensat).

Cette description hydrodynamique des modes de vibration d'un condensat en rotation a pu être testée expérimentalement en deux occasions. Le mode inertiel de précession du réseau a été observé expérimentalement par le groupe de C. Foot à Oxford (Fig. 1.2 extraite de [16]). Nous avons aussi calculé le décalage des fréquences de respiration induites par les non-linéarités du potentiel optique utilisé durant les thèses de V. Bretin et S. Stock pour étudier les condensats en rotation rapide (*Shape oscillation of a rotating Bose-Einstein condensate*). Dans les deux cas, les expériences confirment qualitativement les prédictions du modèle hydrodynamiques, la densité de vortex n'étant cependant expérimentalement pas suffisante pour atteindre un accord quantitatif précis.

1.3 Elastodynamique d'un réseau de vortex

Les travaux précédents négligent l'élasticité du réseau de vortex pour se concentrer sur les effets acoustiques induits par les variations de densités du nuage, une approche justifiée, comme nous l'avons vu, dans le cas de modes de vibrations transverses. Si à présent on considère des modes de plus basse fréquence, tels qu'une perturbation de grande longueur d'onde se propageant le long de l'axe d'un condensat allongé, cette approximation n'est plus valable et il est nécessaire de considérer l'énergie élastique associée aux déformations du réseau de vortex.

Une étude des couplages élasto-hydrodynamique dans un condensat de Bose-Einstein en rotation est présentée dans *Low lying twisting and acoustic modes of a rotating Bose-Einstein condensate*. Ce travail se fonde sur le théorème de Goldstone qui indique que toute symétrie brisée d'un système quantique doit donner lieu à une branche d'excitation de fréquence nulle à grande longueur d'onde. Dans un condensat en rotation piégé dans un potentiel cylindrique, deux symétries sont brisées : d'une part la symétrie U(1) associé au choix de la phase de la fonction macroscopique décrivant le condensat[7] et d'autre part la symétrie SO(2) associée à l'orientation du réseau de vortex dans le plan orthogonal à l'axe de rotation. La brisure de la symétrie U(1) donne lieu à une branche de phonons lorsque l'on modifie la phase de la fonction d'onde le long de l'axe du condensat. En effet, la modulation de la phase est équivalente à l'apparition d'un courant (Eq. 1.1) et donc une modification de la densité du système. La symétrie SO(2) est quant à elle responsable d'un mode de torsion du réseau de vortex (le mode "twiston"). Partant des équations de Bogoliubov - de Gennes, nous avons commencé par généraliser une approche présentée dans [19] pour isoler les modes de fréquence nulle associés à une modification globale de la phase de la fonction d'onde et de la direction du réseau. Nous avons ensuite étendu ces modes au cas de fluctuations de phase et d'angle dépendant de la position. En procédant à un développement à grande longueur d'onde, nous avons pu mettre en évidence un couplage entre modes élastiques et acoustiques. En particulier, nous avons pu énoncer un théorème de réponse linéaire reliant l'élasticité de torsion du réseau de vortex aux fluctuations de moment cinétique du nuage. La résolution des équations élastodynamiques dans le cas d'un gaz piégé nous permet alors de trouver la relation de dispersion des branches de twiston et de phonons, qui restera à tester dans des expériences

[7] Notons que cette brisure de symétrie U(1) caractérise la condensation de Bose-Einstein : cette symétrie est donc aussi brisée dans un condensat au repos.

à venir.

1.4 Observation expérimentale des modes de Kelvin d'une ligne de vorticité

Dans l'hélium superfluide, les modes de Kelvin ont pour la première fois été observés par Packard en les excitant indirectement à l'aide d'un champ radio-fréquence *via* les électrons piégés au cœur des tourbillons. Dans le cas de condensats de Bose-Einstein gazeux, l'excitation est toute aussi délicate car elle nécessite de perturber le nuage sur des petites échelles de distance, typiquement de l'ordre de la taille du cœur du vortex. Or, la méthode la plus directe d'excitation d'un condensat est la modification des fréquences de piégeage qui se couple préférentiellement aux modes de grande longueur d'onde, de l'ordre de la taille du nuage. Afin de contourner cette difficulté, nous avons décidé de procéder comme dans l'expérience de Packard à une excitation indirecte des modes de Kelvin, non plus à l'aide d'électrons, mais en utilisant un couplage non-linéaire entre le mode quadrupolaire d'oscillation de l'ellipticité - que nous avions déjà utilisé dans la mesure du moment cinétique du condensat [15] - et le mode de vibration de la ligne tourbillonaire. En effet, Beliaev a montré l'existence de processus non-linéaires que l'on peut représenter schématiquement par une équation bilan

$$\gamma \rightarrow \gamma' + \gamma'',$$

où γ, γ' et γ'' sont trois quanta d'excitation du nuage satisfaisant les relation de conservation de l'énergie, de l'impulsion (dans l'espace libre) ou du moment cinétique (dans un piège invariant par rotation). Si l'on fait le parallèle avec l'optique non linéaire, ce mécanisme est l'équivalent acoustique du mélange non-linéaire induit par l'effet Pockels. Le mécanisme de Beliaev étant responsable de l'amortissement du mode γ à basse température, on remarque que plus le nombre de modes γ' et γ'' accessibles est important plus le taux d'amortissement augmente : un mode couplé aux kelvons verra donc sa durée de vie réduite par rapport à un autre pour lequel d'éventuels règles de sélection interdisent un tel couplage lorsque le nuage est mis en rotation. Du fait de la chiralité $m_z = -1$ des modes de vibration d'une ligne de vortex, une telle asymétrie existe justement entre les deux modes quadrupolaires $m_z = \pm 2$. En effet la conservation du moment cinétique indique que la formations de deux kelvons ne peut procéder que du couplage avec un mode de moment cinétique $m_z = -2$. Le mode quadrupolaire $m_z = +2$ ne peut donc se désexciter dans ce canal et on s'attend par conséquent à ce

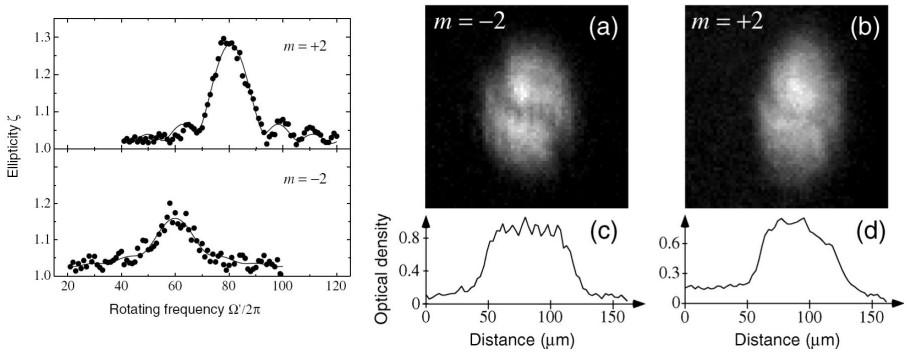

FIG. 1.3 – Mise en évidence expérimentale des excitations de Kelvin d'un vortex quantique. À gauche, réponse de l'éllipticité du nuage à une anisotropie tournant dans le même sens ou en sens opposé à celui de rotation. La présence du réseau de vortex induit une levée de dégénérescence des deux modes et le couplage aux modes de Kelvin introduit un élargissement du mode $m_z = -2$. À droite : imagerie d'absorption de la ligne de vorticité. Les modulations dans le profil de densité après excitation résonnante du mode $m_z = -2$ traduit la présence d'un mode de Kelvin.

que sa durée de vie soit supérieure à celle du $m_z = -2$, ce que l'on observe expérimentalement sur la Fig .1.3. Nous avons pu aussi observer directement l'excitation de la ligne de vorticité par imagerie d'absorption dans la direction orthogonale à l'axe de rotation puisque les oscillations spatiales du champ de vitesse se traduisent après temps de vol en modulations de densité

1.5 Conclusion

Dans ce chapitre, nous avons abordé certaines propriétés dynamiques des condensats en rotation et nous avons montré que l'étude du spectre d'énergie du nuage permettait d'acquérir de précieuses informations sur les propriétés du réseau de vortex. Une première extension de ce travail consiste à généraliser cette étude aux modes de haute énergie de la ligne de vorticité, associés à une dynamique du cœur du vortex qui n'ont pas encore été étudiés expérimentalement. Un autre prolongement intéressant de ces travaux concerne le régime de rotation rapide. Dans ce cas, on peut montrer que le condensat passe dans un régime de fortes corrélations analogue aux états de Laughlin utilisés pour décrire l'effet Hall Quantique Fractionnaire, dont l'observation reste un défi posé à la communauté des atomes froids.

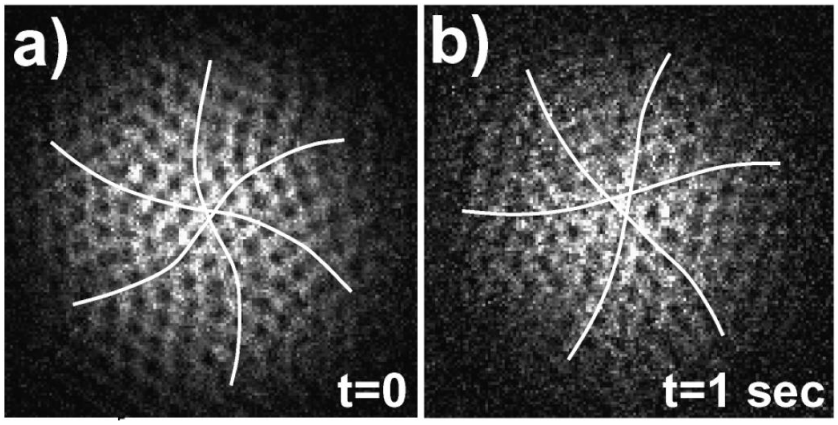

FIG. 1.4 – Observation des modes de Tkatchenko par le groupe d'E. Cornell au JILA. Les lignes blanches indiquent la déformation du réseau associée au mode de Tkatchenko.

Entre ces deux régimes existe une situation intermédiaire, dite LLL-champ moyen (pour *Lowest Landau Level*) dans laquelle l'énergie cinétique de rotation l'emporte sur l'énergie d'interaction sans que les corrélations quantiques soient suffisantes pour détruire la condensation de Bose-Einstein. Ce régime a été observé par le groupe d'Eric Cornell au JILA, qui l'a caractérisé par spectroscopie des modes de Tkatchenko du réseau de vortex (Fig. 1.4 extraite de [20]).

Bibliographie

[1] R. P. Feynman, in Progress in Low Temperature Physics, edited by C. J. Gorter (North-Holland, Amsterdam, 1955), Vol. 1, Chap. 2.

[2] L. Onsager, Nuovo Cimento 6, Suppl. **2**, 249 (1949).

[3] R. Blaauwgeers *et al.*, Nature **404**, 471 (2000).

[4] M. R. Matthews et al., Phys. Rev. Lett. **83**, 2498 (1999).

[5] W.F. Vinen, Nature **181**, 1524 (1958).

[6] K. W. Madison, F. Chevy, W. Wohlleben, and J. Dalibard, Phys. Rev. Lett. **84**, 806 (2000).

[7] M. W. Zwierlein, J. R. Abo-Shaeer, A. Schirotzek, C. H. Schunck et W. Ketterle, Nature (London) **435**, 1047 (2005).

[8] W. Thomson (Lord Kelvin), Philos. Mag. **10**, 155 (1880).

[9] L.P. Pitaevskii, Zh. Eksp. Teor. Fiz. **40**, 646 (1961) ; Sov. Phys. JETP **13**, 451 (1961).

[10] R.I. Epstein and G. Baym, Astrophys. Jour. **387**, 276 (1992).

[11] V.K. Tkachenko, Zh. Eksp. Teor. Fiz. **56**, 1973 (1969) ; Sov. Phys. JETP **29**, 945 (1969).

[12] V. Bretin, S. Stock, Y. Seurin, et J. Dalibard, Phys. Rev. Lett. **92**, 050403 (2004).

[13] G. Baym et E. Chandler, J. Low Temp. Phys. **50**, 57 (1983)

[14] F. Zambelli et S. Stringari, Phys. Rev. Lett. **81**, 1754 (1998)

[15] F. Chevy, K.W. Madison et J. Dalibard, Phys. Rev. Lett. **85**, 2223 (2000) ;

[16] N. L. Smith, W. H. Heathcote, J. M. Krueger et C. J. Foot Phys. Rev. Lett. **93**, 080406 (2004).

[17] Landau, L. D. et E. M. Lifschitz (1987). Fluid Mechanics, Second Edition. New York : Elsevier

[18] K. E. Heikes et T. Maxworthy, J. Fluid Mech. **125** 319 (1982).

[19] M. Lewenstein et L. You, Phys. Rev. Lett. **77**, 3489 (1996) ; Y. Castin and R. Dum, Phys. Rev. A **57**, 3008 (1998).

[20] V. Schweikhard, I. Coddington, P. Engels, V. P. Mogendorff et E. A. Cornell, Phys. Rev. Lett. **92**, 040404 (2004)

Kelvin modes of a fast rotating Bose-Einstein condensate

Kelvin modes of a fast rotating Bose-Einstein condensate

F. Chevy*
Laboratoire Kastler Brossel,† 24 rue Lhomond, 75005 Paris, France

S. Stringari
Dipartimento di Fisica, Università di Trento and BEC-INFM, I-38050 Povo, Italy
(Received 23 May 2003; published 3 November 2003)

Using the concept of diffused vorticity and the formalism of rotational hydrodynamics we calculate the eigenmodes of a harmonically trapped Bose-Einstein condensate containing an array of quantized vortices. We predict the occurrence of a new branch of anomalous excitations, analogous to the Kelvin modes of the single vortex dynamics. Special attention is devoted to the excitation of the anomalous scissors mode.

DOI: 10.1103/PhysRevA.68.053601 PACS number(s): 03.75.Kk

I. INTRODUCTION

The existence of the macroscopic wave function describing a quantum fluid imposes a velocity flow curl free everywhere except on singularity lines known as vortices. Around these lines, the circulation of the velocity is nonzero and is quantized in unit of h/m where m is the mass of the particles of the fluid. Recent experiments have demonstrated the nucleation of such quantized vortices in stirred gaseous Bose-Einstein condensates [1–4].

Multiple quantized vortices are energetically unstable in harmonic traps so that for large rotation frequencies, Bose-Einstein condensates nucleate several singly quantized vortices that were observed to form regular triangular lattices known as Abrikosov lattices [4–6]. In this configuration, the circulation of the velocity field over a circle orthogonal to the rotation axis and of radius R much larger than the vortex interspacing is simply $\pi R^2 n_v h/m$, where n_v is the density of the vortex lines. This is the same formula as that of the velocity field of a rigid body rotating at the angular velocity

$$\Omega_0 = n_v \frac{h}{2m}. \tag{1}$$

The dynamical properties of a single vortex line were first studied by Lord Kelvin [7] and his results were transposed to quantum fluids [8–10]. For an excitation of wave vector k propagating along the rotation axis, the dispersion relation ω_K of these modes (Kelvin modes or kelvons) is

$$\omega_K \sim \frac{\hbar k^2}{2m} \ln(1/k\xi), \tag{2}$$

where $\xi = (8\pi\rho a)^{-1/2}$ is the healing length giving the vortex core diameter, a is the scattering length characterizing atom binary interactions, and ρ is the density of the gas. These modes present the very peculiar feature that they only exist with a single helicity as recently proved in the experiments of Ref. [11]. Indeed, the Kelvin-Helmholtz theorem that constrains the vorticity to move along with the fluid imposes an angular momentum equal to $-\hbar$ to the Kelvin modes.

Although the problem of studying the dynamics of a vortex array seems more involved at first sight, it is considerably simplified for long wavelength perturbations. Indeed, in this case a coarse grain averaging method permits to smooth the discrete nature of vortices. In the case of a homogeneous condensate, it was shown that excitations of wave vector k propagating transversally to the rotation axis satisfy the Tkatchenko dispersion relation [12,13]

$$\omega_T^2 = \frac{\hbar\Omega_0}{4m} k^2,$$

where Ω_0 is the effective angular frequency of the condensate defined by Eq. (1). The Tkatchenko modes are elastic excitations of the lattice and have been recently investigated theoretically also in the presence of harmonic traps [14]. First experimental evidence for such modes has been reported in Ref. [15].

In this paper we use the coarse grain method to study the eigenmodes of a rotating Bose-Einstein condensate confined by a harmonic trap using a fully hydrodynamic approach including vorticity [16]. In addition to the usual collective modes exhibited by the condensate in the absence of rotation, we identify an additional branch, analogous to the Kelvin modes exhibited by a single vortex line. With respect to the Tkatchenko modes, whose frequencies vanish in the Thomas-Fermi limit [14], the Kelvin excitations emerging from our hydrodynamic picture approach a finite value in the Thomas-Fermi limit. In the case of elongated traps their frequencies actually scale like $\omega_z^2/\omega_\perp$ for a fixed value of $\Omega_0/\omega_\perp$.

The paper is organized as follows. In Sec. II we develop the formalism of rotational hydrodynamics in the presence of harmonic trapping and derive the general equations (10) for the dispersion law of the linearized excitations. In Sec. III we briefly summarize the results for the surface excitations which represent a natural generalization of the modes exhibited by nonrotating Bose-Einstein condensates. Section IV is devoted to the scissors mode where an anomalous mode of

*Also at Laboratoire de la Matière Condensée, Collège de France, Paris, France.

†Unité de Recherche de l'Ecole normale supérieure et de l'Université Pierre et Marie Curie, associée au CNRS.

Kelvin nature is predicted. The properties of the scissors oscillations for a rotating condensate are discussed in detail using the formalism of linear-response theory. Finally, in Sec. V we obtain a general dispersion relation for the Kelvin modes in elongated traps.

II. ROTATIONAL HYDRODYNAMICS AND ELEMENTARY EXCITATIONS

It is well known that in the so-called Thomas-Fermi regime, where the mean-field interaction dominates over the quantum pressure, the dynamics of a nonrotating condensate can be described by the classical equations of hydrodynamics:

$$\partial_t \rho = -\nabla \cdot (\rho \mathbf{v}), \tag{3}$$

$$m \partial_t \mathbf{v} = -\nabla (U_t + g\rho + m v^2/2), \tag{4}$$

where ρ is the local particle density, $g = 4\pi\hbar^2 a/m$ is the coupling constant characterizing the interatomic force, and $\mathbf{v}$ is the velocity field satisfying the irrotational condition $\nabla \times \mathbf{v} = 0$. In the case of cylindrical harmonic trapping,

$$U_t = \frac{m}{2}[\omega_\perp^2 (x^2+y^2) + \omega_z^2 z^2],$$

the hydrodynamic equations (3) and (4) admit a class of analytic solutions [17] whose frequencies have been confirmed experimentally with high accuracy.

In the presence of vortex lines the hydrodynamical formalism must be modified. Here we will employ a simplified procedure by assuming that the characteristic wavelength of excitations is large enough so that we can average all the physical quantities over domains containing several vortices. In this case the average lab frame velocity field $\overline{\mathbf{v}}$ is no longer curl free. Since each vortex carries a flux h/m, the average vorticity of the flow is

$$\overline{\mathbf{\Omega}} = \frac{\nabla \times \overline{\mathbf{v}}}{2} = n_v \frac{h}{2m} \mathbf{u}, \tag{5}$$

where n_v is the vortex surface density and the unit vector $\mathbf{u}$ is the local direction of the vortex lines. According to Eq. (5), the average vorticity $\overline{\mathbf{\Omega}}$ characterizes the local vortex distribution: its direction indicates the orientation of the vortex lines while its modulus is proportional to the vortex density.

As in Refs. [16,18], we shall simply assume that the average velocity field and density satisfy classical hydrodynamical equations, including rotational terms, namely:

$$\partial_t \overline{\rho} = -\nabla \cdot (\overline{\rho \mathbf{v}}),$$

$$m \partial_t \overline{\mathbf{v}} = -\nabla \left(U_t + g\overline{\rho} + m \frac{\overline{v^2}}{2} \right) - m(\nabla \times \overline{\mathbf{v}}) \times \overline{\mathbf{v}}. \tag{6}$$

This set of equations omits terms arising from the shearing of the vortex lattice and leading to the Tkatchenko modes. Nevertheless, it can be shown that these are vanishingly small in the Thomas-Fermi approximation [13]. Thus, as long as we restrict ourselves to modes whose frequencies do not vanish in this regime, the effects of the lattice deformation can be neglected.

A stationary solutions of Eqs. (6) is given by

$$\overline{\mathbf{v}}_0 = \mathbf{\Omega}_0 \times \mathbf{r},$$

$$g\overline{\rho}_0/m = \mu - (\omega_\perp^2 - \Omega_0^2)(x^2+y^2)/2 - \omega_z^2 z^2/2, \tag{7}$$

where μ is the chemical potential and $\mathbf{\Omega}_0 = \Omega_0 \mathbf{u}_z$ characterizes the vortex density and direction according to Eq. (5). As expected, the stationary velocity field is equivalent to that of a rigid body rotating at angular velocity $\mathbf{\Omega}_0$, while the density is described by the usual Thomas-Fermi profile with the trapping potential U_t corrected by the centrifugal potential $U_c = -m\Omega_0^2(x^2+y^2)/2$. The static behavior described above has been verified experimentally. In particular, the modification of the transverse trapping is used to measure experimentally the effective angular velocity $\mathbf{\Omega}_0$ [4,6]. More interesting effects concern the study of the dynamics of the condensate. In Ref. [18] the hydrodynamic equations have been used to study the time evolution of a condensate containing a vortex array, following the sudden switch on of a static deformation in the plane of rotation. This produces peculiar nonlinear effects that have been experimentally observed in Ref. [6]. In the following we will focus on the behavior of the linearized solutions which can be derived by looking for small perturbations of the density and velocity field:

$$\overline{\rho} = \overline{\rho}_0 + \delta\rho,$$

$$\overline{\mathbf{v}} = \mathbf{\Omega}_0 \times \mathbf{r} + \delta\mathbf{v},$$

with respect to the equilibrium values (in this case, $\delta\mathbf{v}$ can be interpreted as the velocity in the rotating frame). If the characteristic wavelength of the perturbation is much larger than the vortex spacing, the ''averaged'' hydrodynamical equations (6) can still be applied and, in the *frame rotating at the angular velocity* $\mathbf{\Omega}_0$, they read, in linear approximation,

$$\partial_t \delta\rho = -\nabla' \cdot (\overline{\rho}_0 \delta\mathbf{v}), \tag{8}$$

$$\partial_t \delta\mathbf{v} = -\nabla' \left(\frac{g\,\delta\rho}{m} \right) - 2\mathbf{\Omega}_0 \times \delta\mathbf{v}, \tag{9}$$

where ∇' denotes the derivation with respect to the coordinates in the rotating frame. These equations are strictly identical to the usual hydrodynamical linearized equations leading to the phonon spectrum, except for the $2\mathbf{\Omega}_0 \times \delta\mathbf{v}$ term which arises from the Coriolis force. The system of equations (8) and (9) constitutes the starting point of our analysis. We will study its eigenmodes and show that the spectrum in addition to the usual ''phonon'' modes displays a new class of solutions carrying negative angular momentum and that can be physically regarded as Kelvin excitations.

Let us set $\partial_t = -i\omega'$ in Eqs. (8) and (9). Using Eq. (9), we can then express $\delta\overline{\mathbf{v}}$ as a function of $\delta\rho$ as

$$\delta\mathbf{v}=\frac{1}{\omega'^2-4\Omega_0^2}[i\omega'(\mathbf{f})_\perp+2\boldsymbol{\Omega}_0\times\mathbf{f}]-\frac{1}{i\omega'}(\mathbf{f})_\parallel,$$

where $\mathbf{f}=-\boldsymbol{\nabla}'(g\delta\rho)/m$ and $(\mathbf{f})_\parallel$ and $(\mathbf{f})_\perp$ are, respectively, the projections of $\mathbf{f}$ on the directions parallel and orthogonal to z.

Inserting this expression for the velocity field in the linearized mass conservation equation (8), we get a closed equation for the density fluctuations that can be written as

$$i\omega'(\omega'^2-4\Omega_0^2)\delta\rho=\mathcal{A}\cdot\delta\rho, \tag{10}$$

where $\mathcal{A}$ denotes the linear operator

$$\mathcal{A}\cdot\delta\rho=-\nabla'_\perp\cdot\left[\frac{g\rho_0}{m}(i\omega'\nabla'_\perp\delta\rho+2\boldsymbol{\Omega}_0\times\nabla'_\perp\delta\rho)\right]+\nabla'_\parallel\left[\frac{g\rho_0}{m}\left(\frac{\omega'^2-4\Omega_0^2}{i\omega'}\nabla'_\parallel\delta\rho\right)\right], \tag{11}$$

and ρ_0 is the equilibrium density profile (7). Equations (10) and (11) are the main result of this paper. Simple solutions can be found in the form of polynomials.

Let us stress again that the calculation of ω' is performed in the *rotating frame*. The corresponding frequency ω in the lab frame is obtained through the simple relation $\omega'=\omega-m_z\Omega_0$, where $\hbar m_z$ is the angular momentum of the excitation along the rotation axis. Since both $\delta\rho$ and its complex conjugate are solutions of Eq. (11) we find that for any solution with angular momentum m_z and eigenfrequency ω', there should be another solution with angular momentum $-m_z$ and frequency $-\omega'$. Since the unperturbed state (condensate rotating at angular velocity $\boldsymbol{\Omega}_0$) is the ground state of the system in the rotating frame, the physical solutions carrying energy $\hbar\omega'$ should correspond to positive frequencies ω'.

Note also that Eq. (10) is valid for $\omega'\neq 0$ and $\omega'^2\neq 4\Omega_0^2$ and that these two special cases must be treated separately. The case $\omega'^2-4\Omega_0^2=0$ does not lead to any new mode. The case $\omega'=0$ is instead more interesting since it is related to the Tkatchenko's modes, as stressed in the Introduction. Starting the analysis back from Eqs. (8) and (9), we can show that the density perturbation $\delta\rho$ of a zero energy modes depends only on the radial coordinate $r_\perp=\sqrt{x^2+y^2}$ and that the velocity field is given by

$$v_z=0,$$

$$\mathbf{v}_\perp=\frac{g}{2m\Omega_0^2}\boldsymbol{\Omega}_0\times\boldsymbol{\nabla}\delta\rho.$$

In the case where $\delta\rho$ is parabolic, this zero energy mode can be simply interpreted as a modification of Ω_0, i.e., a change of the vortex density.

The rest of the paper is devoted to the solution of Eq. (11) for special cases of physical interest. We will first discuss the surface oscillations and then the scissors modes, which will be shown to exhibit a kelvonlike branch. Finally, we will derive the general dispersion law for the Kelvin modes working in the geometry of elongated traps.

III. SURFACE MODES

Surface modes are characterized by the form $\delta\rho=(x\pm iy)^l$ and carry angular momentum $m_z=\pm l$. Inserting this ansatz into the differential equation (10) yields the following equation for the eigenfrequencies $\omega'_{\pm l}$ in the rotating frame:

$$\omega'^2_{\pm l}\pm 2\Omega_0\omega'_{\pm l}-l(\omega_\perp^2-\Omega_0^2)=0.$$

The positive solution of this equation reads

$$\omega'_{\pm l}=\sqrt{l\omega_\perp^2-(l-1)\Omega_0^2}\mp\Omega_0$$

or, in the laboratory frame,

$$\omega_{\pm l}=\sqrt{l\omega_\perp^2-(l-1)\Omega_0^2}\pm(l-1)\Omega_0.$$

Contrary to what happens in the case of a nonrotating condensate, the two modes are no longer degenerate, and the degeneracy lift amounts to

$$\Delta\omega_l=\omega_{+l}-\omega_{-l}=2(l-1)\Omega_0. \tag{12}$$

This result is valid for any l [20] but can be checked for some special cases previously reported in the literature.

In the $l=1$ case (dipole motion) one finds $\Delta\omega=0$. In this case the eigenfrequencies are actually unaffected by the rotation since $\omega_{\pm l}=\omega_\perp$ irrespective of the value of Ω_0. This is not surprising since we know that the generalized Kohn theorem [19] implies that the center of mass motion is determined only by the frequency of the harmonic trap.

The case $l=2$ is also well documented, both theoretically and experimentally [21,22]. Using sum-rule approach, it can be shown in particular that the degeneracy lift amounts to

$$\Delta\omega=2\frac{\langle\ell_z\rangle}{m\langle r_\perp^2\rangle}, \tag{13}$$

ℓ_z is the angular momentum per particle along z of the unperturbed condensate. Since the unperturbed velocity field is rigidlike, the angular momentum is given by the classical formula $\langle\ell_z\rangle=m\langle r_\perp^2\rangle\Omega_0$. Inserting this relation into Eq. (13) yields result (12) for $l=2$.

IV. SCISSORS MODES

The scissors modes are associated with a density fluctuation $\delta\rho=(x\pm iy)z$ carrying angular momentum $m_z=\pm 1$ along the z axis. Using Eq. (11), one finds that the eigenfrequencies ω' must satisfy the nontrivial cubic equation:

$$\omega'^3\pm 2\Omega_0\omega'^2-\omega'(\omega_z^2+\omega_\perp^2-\Omega_0^2)\mp 2\Omega_0\omega_z^2=0. \tag{14}$$

This equation is analogous to that found by the authors of Ref. [16] using the tensor virial method. Two of the resulting modes can be identified with the usual $m_z=\pm 1$ scissors previously studied in the case of nonrotating Bose-Einstein condensates [23]. The splitting between these two modes is eas-

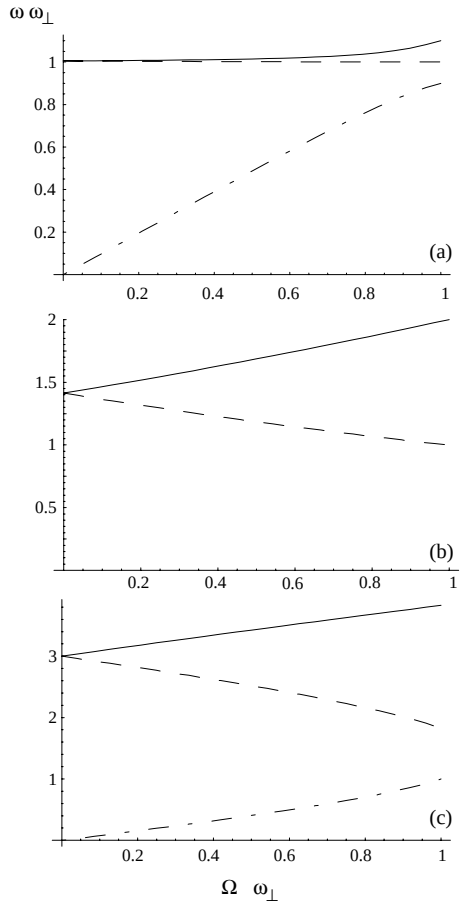

FIG. 1. Absolute values of the lab frame frequencies of the $m_z=+1$ (full line), $m_z=-1$ (dashed line), and anomalous (dash-dotted line) scissors modes for three trap geometries. (a) Cigar shaped, with $\omega_\perp=10\omega_z$. (b) Isotropic trap with $\omega_z=\omega_\perp$. In this case the frequency of the anomalous mode is zero. (c) Pancake trap with $\omega_z=\sqrt{8}\omega_\perp$.

ily calculated when $\Omega_0\to 0$. In the laboratory frame one finds $\Delta\omega=2\Omega_0\omega_z^2/(\omega_z^2+\omega_\perp^2)$ in agreement with the sum-rule result of Ref. [21] that was confirmed experimentally in Ref. [25]. This splitting is at the origin of the gyroscopic effect investigated in Ref. [24] in the presence of a single vortex line. The third mode predicted by Eq. (14) has instead no analog for $\Omega_0=0$. A sign analysis shows that the frequency ω_a' of this *anomalous* mode is positive for $m_z=-1$. Just like the kelvons, this new scissor mode can only exist with negative helicity. The analog of this mode in the case of a single vortex line was investigated by Ref. [10]. The solutions of Eq. (14) as a function of Ω_0 are shown in Fig. 1 for different trapping geometries. The interpretation of this mode is straightforward for an isotropic trap: in this case, the anomalous mode is associated with an overall rotation of the condensate and of its lattice. In an isotropic trap this rotation indeed costs no energy and the frequency in the lab frame is exactly zero.

For very deformed traps, i.e., for $|\omega_\perp^2-\omega_z^2|\gg\Omega_0^2$, the anomalous mode is associated with a scissors mode of the vortex lattice while the density profile remains almost at rest.

In the second part of this section we discuss how the scissors modes, and in particular the anomalous mode, can be excited and observed by suddenly tilting the trapping potential in the (x,z) plane. To this purpose we make use of the formalism of linear-response theory. Let us apply a perturbing potential of the form

$$\delta U=\epsilon z'(x'+iy')e^{-i\omega' t}+\epsilon^* z'(x'-iy')e^{i\omega' t}$$

in the rotating frame. Using the hydrodynamical equations, we find that the density and the vorticity will be perturbed as

$$\delta\rho=\epsilon\lambda_{\omega'}z'(x'+iy')e^{-i\omega' t}+\epsilon^*\lambda_{\omega'}^* z'(x'-iy')e^{i\omega' t},$$

$$\delta\mathbf{\Omega}=\epsilon\mu_{\omega'}e^{-i\omega' t}\mathbf{u}_+ +\epsilon^*\mu_{\omega'}^* e^{i\omega' t}\mathbf{u}_-,$$

where $\mathbf{u}_\pm=\mathbf{u}_x\pm i\mathbf{u}_y$. The quantities λ and μ can be calculated using the hydrodynamical equations and one finds the result

$$\lambda_{\omega'}=\frac{2\Omega_0\omega_z^2+\omega'(\omega_\perp^2+\omega_z^2-\Omega_0^2)}{gP(\omega')} \tag{15}$$

$$\mu_{\omega'}=-\frac{\omega'\Omega_0}{mP(\omega')}, \tag{16}$$

where $P(\omega')=\omega'^3+2\Omega_0\omega'^2-\omega'(\omega_z^2+\omega_\perp^2-\Omega_0^2)-2\Omega_0\omega_z^2$ is a polynomial whose roots fix the eigenfrequencies of the system [see Eq. (14)]. Notice that the change $\delta\mathbf{\Omega}_0$ in the vorticity, lying in the (x,y) plane, actually corresponds to a rotation of the vector lattice. This rotation could be imaged experimentally, allowing, together with the changes in the shape of the atomic cloud, for a direct identification of the various scissors modes.

On the one hand, the expectation value $\langle z'(x'-iy')\rangle\equiv\int d^3r\,\delta\rho z'(x'-iy')$ can be written as

$$\langle z'(x'-iy')\rangle=\epsilon\chi_\omega^{\mathrm{HD}}e^{-i\omega' t}+\epsilon^*(\chi_\omega^{\mathrm{HD}})^* e^{-i\omega' t},$$

and one obtains the result

$$\chi_{\omega'}^{\mathrm{HD}}=\lambda_{\omega'}\frac{\pi R_z^3 R_\perp^4}{6} \tag{17}$$

for the hydrodynamic response function $\chi_\omega^{\mathrm{HD}}$.

On the other hand, this expectation value can be calculated using the formalism of quantum mechanics. Using first-order perturbation theory the linear-response function relative to the operator $F=\Sigma_{k=1}^N z_k'(x_k'-iy_k')$ can be in fact written as

$$\chi_{\omega'}^{\mathrm{QM}}=\sum_n\frac{|\langle n|F^\dagger|0\rangle|^2}{\hbar\omega'-E_n'}-\frac{|\langle n|F|0\rangle|^2}{\hbar\omega'+E_n'}, \tag{18}$$

where $|0\rangle$ and $|n\rangle$ are, respectively, the ground state and the excited states of the many-body system and E_n' are the associated eigenenergies in the rotating frame. From Eq. (18), we see that the poles of χ_ω are the eigenfrequencies of the sys-

tem. Moreover, the sign of the residue at the pole gives its helicity: positive residues are associated with positive helicity [i.e., with modes excited by $z(x+iy)$] and negative residues are instead associated with negative helicity.

By identifying χ^{QM} and χ^{HD} and by close examination of Eqs. (15), we can conclude the following.

(1) The anomalous mode has positive energy in the rotating frame and its angular momentum is $m=-1$.

(2) For $\omega_z<\omega_\perp$, we have $\omega_{\mathrm{a}}<0$. For cigar geometries the anomalous mode is then associated with a thermodynamical instability of the vortex lattice in the laboratory frame [26].

(3) On the contrary, for $\omega_z>\omega_\perp$, we have $\omega_{\mathrm{a}}>0$. For pancake geometries, the vortex lattice is stable versus scissor perturbations.

Let us now consider the special case of the sudden tilting at $t=0$ of the longitudinal axis of the trap in the lab frame. This excitation leads to the following perturbing potential:

$$\delta U=\alpha xzY(t)=\alpha z(x+iy)+\alpha z(x-iy)Y(t),$$

where Y is the Heaviside step function equal to 0 for $t<0$ and 1 otherwise. Expressed in the rotating frame, δU reads

$$\delta U=[\alpha z(x+iy)e^{i\Omega_0 t}+\alpha z(x-iy)e^{-i\Omega_0 t}]Y(t).$$

The Fourier transform of this perturbation then yields:

$$\epsilon_{\omega'}=\alpha[\pi\delta(\omega'+\Omega_0)+i/(\omega'+\Omega_0)].$$

According to Eqs. (15) and (16), the induced density and vorticity changes are given by

$$\delta\rho=\left(\int d\omega'\,\epsilon_{\omega'}\lambda_{\omega'}e^{-i\omega' t}\right)z(x+iy)+\text{c.c.}, \tag{19}$$

$$\delta\mathbf{\Omega}=\left(\int d\omega'\,\epsilon_{\omega'}\mu_{\omega'}e^{-i\omega' t}\right)\mathbf{u}_+ +\text{c.c.} \tag{20}$$

These integrals can be calculated using standard integration techniques in the complex plane. In particular, $\delta\rho$ and $\delta\mathbf{\Omega}$ present terms oscillating at the driving frequency Ω_0, as well as at the scissor frequencies $\omega_{\pm 1}$ and ω_{a}. Let us introduce the Fourier components of these modes:

$$\delta\rho=\left(\delta\hat{\rho}_0 e^{i\Omega_0 t}+\sum_{k=\pm 1,a}\delta\hat{\rho}_k e^{-i\omega_k' t}\right)z(x+iy)+\text{c.c.},$$

$$\delta\mathbf{\Omega}=\left(\delta\hat{\Omega}_0 e^{i\Omega_0 t}+\sum_{k=\pm 1,a}\delta\hat{\Omega}_k e^{-i\omega_k' t}\right)\mathbf{u}_+ +\text{c.c.}$$

According to Eqs. (19) and (20), $\delta\hat{\rho}_k$ and $\delta\hat{\Omega}_k$ are given, respectively, by the residues of $\lambda_{\omega'}/(\omega'+\Omega_0)$ and $\mu_{\omega'}/(\omega'+\Omega_0)$. We have plotted the density response $\delta\hat{\rho}_k$ in Fig. 2. We see that the anomalous mode weight is very weak, both in the pancake and cigar traps (except for $\Omega_0\sim\omega_\perp$). The behavior of the vorticity is dramatically different, as observed in Fig. 3. Indeed, while the anomalous mode remains weak in the case of an elongated trap [Fig. 3(a)], we see that it dominates the dynamics in the pancake geometry.

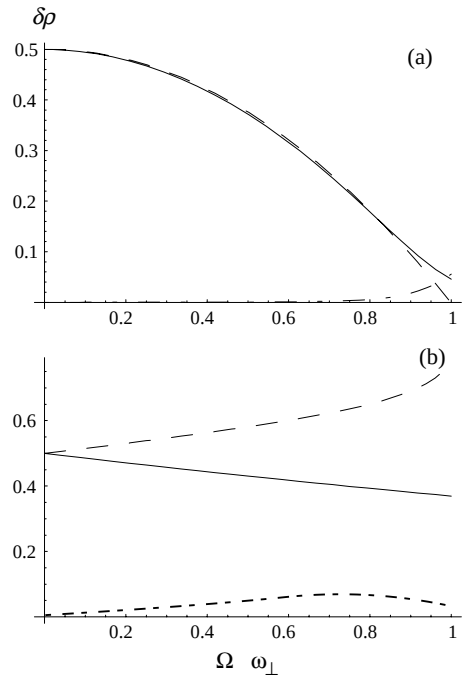

FIG. 2. Density coupling of the scissor $m_z=+1$ (full line), $m_z=-1$ (dashed line), and anomalous (dash dotted line) transitions for different trapping geometries. (a) Elongated trap ($\omega_\perp=10\omega_z$) and (b) pancake trap ($\omega_z=\sqrt{8}\omega_\perp$).

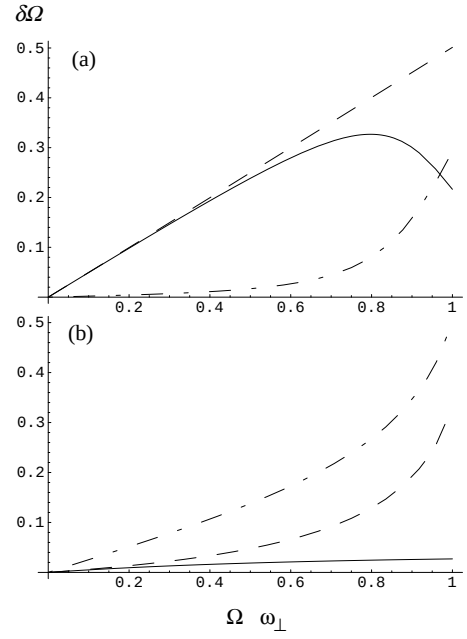

FIG. 3. Change of vorticity of the scissor $m_z=+1$ (full line), $m_z=-1$ (dashed line), and anomalous (dash-dotted line) transitions for different trapping geometries. (a) Elongated trap ($\omega_\perp=10\omega_z$) and (b) pancake trap ($\omega_z=\sqrt{8}\omega_\perp$). For these modes the change of vorticity is associated with a change of direction of the vortical lattice.

This effect should be detectable experimentally by imaging the orientation of the vortex lattice.

V. KELVIN SPECTRUM

The study of the scissor modes has revealed the existence of an anomalous kelvonlike mode with angular momentum $m_z=-1$. For very elongated traps ($\omega_\perp \gg \omega_z$), the corresponding solution is given by

$$\omega' \sim 2\Omega_0 \frac{\omega_z^2}{\omega_\perp^2-\Omega_0^2}$$

showing that the frequency of the anomalous mode goes to zero in the limit of small ω_z. In what follows, we shall generalize this result by looking for more general solutions of Eq. (12) associated with pure lattice vibrations and satisfying $\omega' \sim \omega_z^2$ when $\omega_z \to 0$. In this approximation, we can restrict Eq. (11) to nonvanishing terms in ω and ω_z, which yields the simplified equation

$$\boldsymbol{\nabla}'_\perp [2\rho_0 \boldsymbol{\Omega}_0 \times \boldsymbol{\nabla}'_\perp \delta\rho] + \boldsymbol{\nabla}'_\parallel \left[\rho_0 \left(\frac{4\Omega_0^2}{i\omega'} \boldsymbol{\nabla}'_\parallel \delta\rho \right) \right] = 0. \quad (21)$$

Let us now write the density perturbation as the most general polynomial of order $p+l$ associated with angular momentum $m_z=-l$:

$$\delta\rho = r_\perp^l e^{-il\theta} \sum_{q=0}^{q_m} b_q z^{p-2q} r_\perp^{2q} + \cdots,$$

where the expression is restricted to terms of leading order in the $(r_\perp, \theta, z)$ cylindrical coordinates and q_m is the highest q such that $p-2q \geqslant 0$. According to Eq. (21), the coefficients $b_{q>0}$ must satisfy the following recursive relation:

$$b_q = -\frac{(p-2q+2)(p+1-2q)\Omega_0^2}{[-l\Omega_0\omega_\perp^2\omega' + (p-2q)(p-2q+1)\Omega_0^2\omega_z^2]} b_{q-1},$$

while, for $q=0$

$$\left(-l\Omega_0\omega_\perp^2 + p(p+1)\frac{\Omega_0^2}{\omega'}\omega_z^2 \right) b_0 = 0. \quad (22)$$

In order to get nonvanishing b_q, the coefficient of b_0 in Eq. (22) must cancel out. This ensures the quantization of the eigenfrequencies, since we must have

$$\omega' = p(p+1)\frac{\Omega_0\omega_z^2}{l(\omega_\perp^2-\Omega_0^2)}. \quad (23)$$

This dispersion relation represents the generalization of the classical Kelvin law to the case of a rotating gas confined in a harmonic trap. Similar to kelvons, these new modes have always a negative angular momentum and possess a quadratic behavior for large p. If R_z and $R_\perp$ denote the condensate radii in the longitudinal and transverse directions, respectively, these two quantities are related by [see Eq. (7)]

$$\omega_z^2 R_z^2 = (\omega_\perp^2 - \Omega^2) R_\perp^2 .$$

Moreover, $\delta\rho$ is a polynomial of order p in z. The quantity $k=p/R_z$ can then be interpreted as the longitudinal wave vector of the excitation. Using the relation $\Omega_0 = n_v h/2m$, Eq. (23) yields, for large quantum numbers p,

$$\omega' = N_v \frac{\hbar}{lm} k^2,$$

where $N_v = n_v \pi R_\perp^2$ is the number of vortices present in the condensate. This dispersion law is very similar to Eq. (2), except for the logarithmic factor that vanished through the averaging procedure.

Note also that Eq. (23) is singular for $l=0$. This is due to the fact that in this case $\omega' \sim \omega_z$ so terms neglected in Eq. (21) must be taken into account. In this case, there is no decoupling between the phonon and kelvon branches, and no simple analytical expression can be extracted.

ACKNOWLEDGMENTS

We wish to thank M. Cozzini, L. Pitaevskii, and G. Baym for very helpful discussions.

[1] M.R. Matthews, B.P. Anderson, P.C. Haljan, D.S. Hall, C.E. Wieman, and E.A. Cornell, Phys. Rev. Lett. **83**, 2498 (2000).
[2] K.W. Madison, F. Chevy, W. Wohlleben, and J. Dalibard, Phys. Rev. Lett. **84**, 806 (2000).
[3] E. Hodby, G. Hechenblaikner, S.A. Hopkins, O.M. Maragò, and C.J. Foot, Phys. Rev. Lett. **88**, 010405 (2001).
[4] J.R. Abo-Shaer, C. Raman, J.M. Vogels, and W. Ketterle, Science **292**, 476 (2001).
[5] K.W. Madison, F. Chevy, W. Wohlleben, and J. Dalibard, J. Mod. Opt. **47**, 2715 (2000).
[6] P.C. Haljan, I. Coddington, P. Engels, and E.A. Cornell, Phys. Rev. Lett. **87**, 210403 (2001).
[7] W. Thomson (Lord Kelvin), Philos. Mag. **10**, 155 (1880).
[8] L.P. Pitaevskii, Zh. Eksp. Teor. Fiz. **40**, 646 (1961) [Sov. Phys. JETP **13**, 451 (1961)].
[9] T. Isoshima and K. Machida, Phys. Rev. A **59**, 2203 (1999).
[10] A.A. Svidzinsky and A.L. Fetter, Phys. Rev. A **62**, 063617 (2000).
[11] V. Bretin, P. Rosenbusch, F. Chevy, G.V. Shlyapnikov, and J. Dalibard, Phys. Rev. Lett. **90**, 100403 (2003).
[12] V.K. Tkachenko, Zh. Eksp. Teor. Fiz. **56**, 1973 (1969) [Sov. Phys. JETP **29**, 945 (1969)].
[13] G. Baym and E. Chandler, J. Low Temp. Phys. **50**, 57 (1983); **62**, 119 (1986); G. Baym, Phys. Rev. Lett. **91**, 110402 (2003).
[14] J.R. Anglin and M. Crescimanno, e-print cond-mat/0210063.
[15] I. Coddington, P. Engels, V. Schweikhard, and E.A. Cornell, Phys. Rev. Lett. **91**, 100402 (2003).
[16] A. Sedrakian and I. Wasserman, Phys. Rev. A **63**, 063605 (2001).
[17] S. Stringari, Phys. Rev. Lett. **77**, 2360 (1996).

[18] M. Cozzini and S. Stringari, Phys. Rev. A **67**, 041602 (2003).
[19] J.F. Dobson, Phys. Rev. Lett. **73**, 2244 (1994).
[20] l must be compatible with the large wavelentgh hypothesis, that is, $2\pi R_{\perp}/l$ should be much larger than the vortex interspacing.
[21] F. Zambelli and S. Stringari, Phys. Rev. Lett. **81**, 1754 (1998).
[22] F. Chevy, K.W. Madison, and J. Dalibard, Phys. Rev. Lett. **85**, 2223 (2000).
[23] D. Guery-Odelin and S. Stringari, Phys. Rev. Lett. **83**, 4452 (1999).
[24] S. Stringari, Phys. Rev. Lett. **86**, 4725 (2001).
[25] E. Hodby, S.A. Hopkins, G. Hechenblaikner, N.L. Smith, and C.J. Foot, Phys. Rev. Lett. **91**, 090403 (2003).
[26] It also means that, from an experimental point of view, the anomalous mode will correspond to a scissor excitation rotating in the *positive* direction.

Shape oscillation of a rotating Bose-Einstein condensate

EUROPHYSICS LETTERS 1 March 2004

Europhys. Lett., **65** (5), pp. 594–600 (2004)
DOI: 10.1209/epl/i2003-10179-x

Shape oscillation of a rotating Bose-Einstein condensate

S. Stock, V. Bretin, F. Chevy and J. Dalibard

Laboratoire Kastler Brossel(*) - 24 rue Lhomond, F-75231 Paris Cedex 05, France

(received 5 November 2003; accepted 5 January 2004)

PACS. 03.75.Kk – Dynamic properties of condensates; collective and hydrodynamic excitations, superfluid flow.
PACS. 32.80.Pj – Optical cooling of atoms; trapping.

Abstract. – We present a theoretical and experimental analysis of the transverse monopole mode of a fast rotating Bose-Einstein condensate. The condensate's rotation frequency is similar to the trapping frequency and the effective confinement is only ensured by a weak quartic potential. We show that the non-harmonic character of the potential has a clear influence on the mode frequency, thus making the monopole mode a precise tool for the investigation of the fast-rotation regime.

The investigation of rotating gases or liquids is a central issue in the study of superfluids [1, 2]. During the recent years, several experiments using rotating atomic Bose-Einstein condensates have provided a spectacular illustration of the notion of quantized vortices [3–6]. Depending on the rotation frequency of the gas, a single vortex or a regular array of vortices can be observed experimentally. When the rotation frequency is increased to a very large value, a new class of phenomena is predicted, in connection with quantum Hall physics [7–15]. For a gas confined in a harmonic potential, the fast-rotation domain corresponds to stirring frequencies Ω of the order of the trapping frequency $\omega_\perp$ in the plane perpendicular to the rotation axis (hereafter denoted z). From a classical point of view, the transverse trapping and centrifugal forces compensate each other for this stirring frequency, and the motion of the particles in the xy plane is only driven by Coriolis and interatomic forces. This situation is similar to that of an electron gas in a magnetic field, since Lorentz and Coriolis forces have the same mathematical structure.

In order to approach the regime of fast rotation, two paths are currently being explored. The first approach is implemented in a pure harmonic potential and is based on evaporative spin-up, *i.e.* the selective removal of particles with low angular momentum [16]. The stirring frequency Ω can then be raised close to $\omega_\perp$ ($\Omega = 0.993\,\omega_\perp$ was reached in [17]). The second approach, which is followed here, consists in adding to the quadratic confinement a small positive quartic potential, which ensures that the particles will remain confined even when Ω exceeds $\omega_\perp$ [18–23]. We have recently proven that this method can be successfully implemented and we have mechanically stirred a rubidium Bose-Einstein condensate up to $\Omega \simeq 1.05\,\omega_\perp$ [24].

(*) LKB is a unité de recherche of Ecole Normale Supérieure and Université Paris 6, associated to CNRS.

All experiments performed so far (including the present one) are still deeply within the mean-field regime, characterized by a number of vortices N_v well below the number of particles N. Nevertheless, in order to prepare for future investigations of possible quantum-Hall–like states, one must design proper tools of investigation, such as the study of the eigenmodes of the rotating gas. Possible examples are the transverse quadrupole modes, which allow for a measurement of the z component of the angular momentum [24], and the Tkachenko oscillations of the vortex lattice, recently observed in [16]. Here we report on the experimental and theoretical study of the lowest transverse monopole mode of an ultra-cold gas of rubidium atoms in the fast rotation regime.

In a trap with axial symmetry along the z-axis, excitations can be characterized by their angular momentum along z (quantum number m_z) [25]. Here we are interested in excitations carrying no angular momentum ($m_z = 0$). In the limit $\omega_z \ll \omega_\perp$ which is of interest here, it is possible to identify $m_z = 0$ "transverse monopole" modes, which mostly affect the atom distribution in the xy plane. For a non-rotating condensate the lowest frequency for these $m = 0$ transverse modes is $\omega_\mathrm{mp} \simeq 2\,\omega_\perp$ (transverse breathing mode) [26, 27]. In the present work we show experimentally that the relation $\omega_\mathrm{mp} \simeq 2\,\omega_\perp$ remains valid for large rotation frequencies (as predicted by [28]), as long as the quartic term in the confinement is not significant. We also explore the region $\Omega \sim \omega_\perp$, where the quartic term plays an essential role. We compare the measured monopole frequency with that derived from a simple hydrodynamic model of an infinite, cylindrical condensate. Finally, we discuss the structure of the mode, which exhibits a very particular behavior in the range $\Omega \gtrsim \omega_\perp$.

Our ^{87}Rb Bose-Einstein condensate contains 3×10^5 atoms. It is produced by radio-frequency evaporation in a Ioffe-Pritchard magnetic trap, to which we superimpose a far-blue detuned laser beam. The magnetic trap provides a harmonic confinement with cylindrical symmetry along the z-axis, with $\omega_z/2\pi = 11.0\,\mathrm{Hz}$ and $\omega_\perp^{(0)}/2\pi = 75.5\,\mathrm{Hz}$. The laser beam adds a negative quadratic and a positive quartic potential in the xy plane. The quadratic term decreases the trap frequency $\omega_\perp$ by $\sim 15\%$. The quartic term allows to explore rotation frequencies around and slightly above the trapping frequency $\omega_\perp$. It reads $kr^4/4$, with $r^2 = x^2 + y^2$ and $k = 2.6(3) \times 10^{-11}\,\mathrm{J/m^4}$. The oscillation frequency of the condensate center-of-mass (dipole motion) in the xy plane is $\omega_\mathrm{dp}/2\pi = 65.6\ (\pm 0.3)\,\mathrm{Hz}$. Because of the quartic component of the trapping potential, ω_dp is slightly larger than $\omega_\perp$, even for an arbitrarily small amplitude of the dipole motion. The condensate has indeed a finite radius $R_\mathrm{c} \simeq 6.5\,\mu\mathrm{m}$ and therefore explores regions of space where the contribution of the quartic term is significant. Using a perturbative treatment of the quartic term we infer that $\omega_\mathrm{dp} - \omega_\perp \simeq 2kR^2/(7\,m\omega_\perp^2)$, so that $\omega_\perp/(2\pi) = 64.8\ (\pm 0.3)\,\mathrm{Hz}$.

The procedure for setting the gas in rotation at a frequency $\Omega \sim \omega_\perp$ has been described in detail in [24]. We apply an additional laser beam creating a rotating anisotropy in the xy plane for two successive phases, with respective durations of 300 ms and 600 ms. During the first phase the rotation at frequency $\Omega \sim \omega_\perp/\sqrt{2}$ resonantly excites the transverse quadrupole mode, and vortices subsequently penetrate the condensate. After a 400 ms relaxation period we apply the second stirring phase at the final desired frequency. This phase is followed by a 500 ms relaxation period. By measuring the transverse size of the condensate, we have checked that it is then rotating at a frequency close to the stirrer frequency Ω (within 2%) for the regime of interest $\Omega \leq 1.05\,\omega_\perp$. In particular, for $\Omega \lesssim \omega_\perp$ we observe large vortex arrays involving up to ~ 50 vortices. During the stirring and relaxation periods, we apply radio frequency (r.f.) evaporative cooling. The r.f. is set 24 kHz above the value which removes all particles from the trap. Assuming $\Omega = \omega_\perp$, so that the transverse confinement is purely quartic, this gives a trap depth $U_0 \sim 40\,\mathrm{nK}$. From the estimated collision rate ($\sim 10\,\mathrm{s^{-1}}$), we

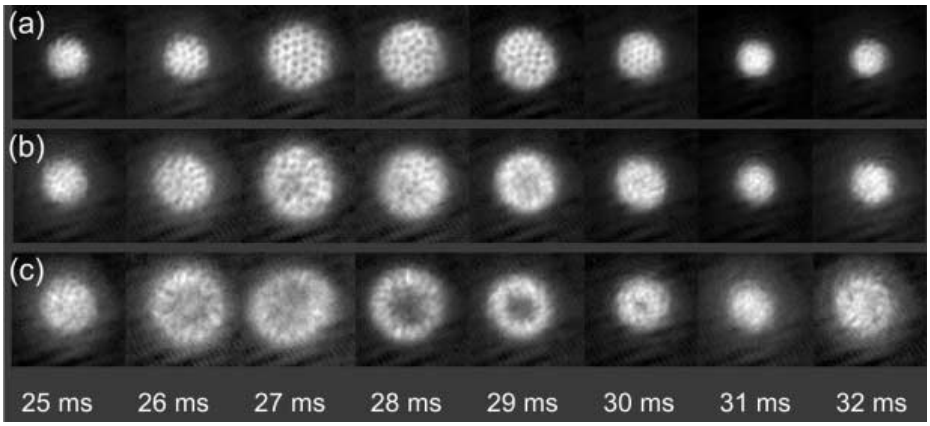

Fig. 1 – Series of images of the condensate for various waiting times τ after excitation. Row a) corresponds to a rotation frequency $\Omega/(2\pi) = 62\,\mathrm{Hz}$, row b) to $\Omega/(2\pi) = 64\,\mathrm{Hz}$ and row c) to $\Omega/(2\pi) = 66\,\mathrm{Hz}$.

infer a temperature $T \lesssim 10\,\mathrm{nK}$ after the relaxation period.

We then excite the transverse monopole mode(s) of the gas by changing for a period τ_0 the intensity of the laser creating the quartic potential from I to I'. We choose $\tau_0 = 2\,\mathrm{ms}$, which is short compared to the oscillation period of the monopole oscillation $2\pi/\omega_{\mathrm{mp}} = 7.5\,\mathrm{ms}$. We then wait for an adjustable duration τ before performing a time-of-flight expansion and absorption imaging. The images are taken along the rotation axis z so that we have access to the column density in the xy plane.

Typical results are shown in fig. 1 for $\Omega/2\pi = 62$, 64, 66 Hz. Each image corresponds to a destructive measurement of the atom density after a duration $\tau = 25, \ldots, 32\,\mathrm{ms}$ and a 18 ms time of flight. In order to check that the oscillation is in the linear regime, we explored values between 0 and 4 for the ratio I'/I: we found that the frequency ω_0 is (within experimental uncertainties) independent of the excitation strength $|I - I'|/I$, and that the amplitude of the oscillation varies linearly with this strength. We have also varied the duration of the time of flight between 6 and 18 ms. We thus verify that all features reported here are independent of this duration, which corresponds to a mere scaling of the initial spatial density distribution.

We have taken similar sequences of images for various stirring frequencies Ω, with τ varying from 0 to 40 ms by steps of 1 ms. We extract from these images the transverse size $R(\tau)$ of the gas. The variations of $R(\tau)$ are well fitted by a single sinusoidal function, with frequency ω_{mp}. The characteristic lifetime of the excitation is larger than 100 ms, so that its decay is negligible during the 40 ms period. The variations of ω_{mp} as a function of Ω are plotted in fig. 2. An obvious feature of this plot is that ω_{mp} varies very weakly for Ω except in the vicinity of $\omega_\perp$. We now discuss in more details three relevant domains of this graph.

1) For a non-rotating gas ($\Omega = 0$) we find $\omega_{\mathrm{mp}}/(2\pi) = 130.6\ (\pm 1.5)\,\mathrm{Hz}$, which is close to the well-known result $\omega_{\mathrm{mp}} \simeq 2\omega_\perp = 2\pi \times 129.6\,(\pm 0.6)\,\mathrm{Hz}$ [29].

2) When the gas rotates at a frequency Ω not too close to $\omega_\perp$, the effect of the quartic potential remains small. In these conditions we find that the monopole frequency ω_0 stays approximately constant. At first sight this may seem a surprising result. For a rotating gas in a pure harmonic potential, the transverse confinement is reduced due to the centrifugal force. In the calculation of the equilibrium shape of the gas, the trapping frequency $\omega_\perp$ is

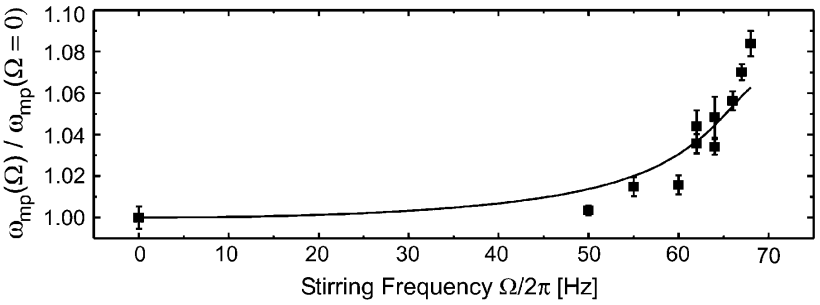

Fig. 2 – Transverse monopole frequency $\omega_{\rm mp}(\Omega)$ normalized by $\omega_{\rm mp}(\Omega = 0)$ as a function of the stirring frequency Ω. For a non-rotating condensate ($\Omega = 0$) we measure $\omega_{\rm mp}(0)/(2\pi) = 130.6\,$Hz. The vertical bars indicate the error given by the fitting routine. Full line: result of the 2D hydrodynamic analysis.

thus replaced by the weaker value $(\omega_\perp^2 - \Omega^2)^{1/2}$. One might have expected that a similar replacement should be done also for the monopole frequency; this is clearly not the case. For a cigar-shaped condensate in the hydrodynamic regime, it was proven in [28] that ω_0 stays equal to $2\omega_\perp$ when Ω varies. In the case of an ideal gas described by classical mechanics, the equality $\omega_{\rm mp} = 2\,\omega_\perp$ also holds for any Ω as a consequence of the combined action of centrifugal and Coriolis forces.

3) When the rotation frequency Ω approaches $\omega_\perp$, the contribution of the quartic term becomes more important and the monopole frequency $\omega_{\rm mp}$ deviates significantly from $2\omega_\perp$. As shown in fig. 2, this deviation reaches $\sim 8\%$ for $\Omega/(2\pi) = 68\,$Hz, *i.e.* $\Omega/\omega_\perp \simeq 1.05$. We have also plotted in fig. 2 the prediction of a theoretical treatment of the monopole mode in the quartic + quadratic trap, neglecting the harmonic confinement along the z-direction. The agreement between these predictions and the experimental data is satisfactory, given the difference in geometry between the experiment and the model.

The starting point of our theoretical treatment is the set of equations for rotational hydrodynamics [28], which we write in the laboratory frame:

$$\partial_t \rho \;=\; -\boldsymbol{\nabla}\cdot(\rho \boldsymbol{v}), \tag{1}$$

$$\partial_t \boldsymbol{v} \;=\; -\boldsymbol{\nabla}\big((U + g\rho)/m + v^2/2\big) + \boldsymbol{v}\times(\boldsymbol{\nabla}\times\boldsymbol{v}), \tag{2}$$

where ρ and $\boldsymbol{v}$ are the density and velocity field of the atom distribution. $U = m\omega_\perp^2 r^2/2 + kr^4/4$ stands for the trapping potential and $g = 4\pi\hbar^2 a/m$ characterizes the strength of the atomic interactions (a is the scattering length). As explained in [28,30,31], these equations are valid when one is interested in a phenomenon whose characteristic length scale is larger than the distance between vortices.

The eigenmodes are obtained by linearizing (1)-(2) around the rotating equilibrium solution

$$\boldsymbol{v}_{\rm eq} = \boldsymbol{\Omega}\times\boldsymbol{r}\,, \qquad g\rho_{\rm eq} = \mu - U - U_{\rm cen}\,, \tag{3}$$

where μ is the chemical potential and $U_{\rm cen} = -m\Omega^2 r^2/2$ the centrifugal potential. We eliminate the velocity field to get a closed equation for the density variation $\delta\rho$, assuming an oscillation at frequency ω:

$$-\boldsymbol{\nabla}\cdot\big(\rho_{\rm eq}\,\boldsymbol{\nabla}[\delta\rho]\big) = \frac{m}{g}\,\big(\omega^2 - 4\Omega^2\big)\,[\delta\rho]. \tag{4}$$

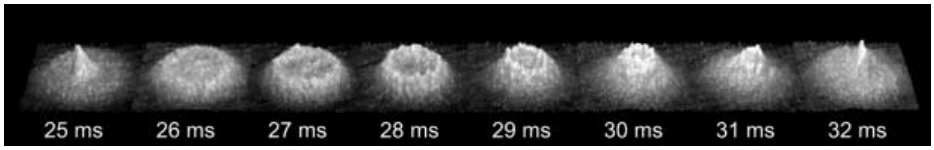

Fig. 3 – Time evolution of the density profile of the oscillating cloud, for $\Omega/2\pi = 68\,\mathrm{Hz}$.

In the absence of a quartic term the eigenfrequencies for the $m = 0$ modes are

$$\omega_n^2 = 4\Omega^2 + 2n(n+1)\big(\omega_\perp^2 - \Omega^2\big), \quad n \text{ positive integer}, \tag{5}$$

and the corresponding eigenmodes are polynomials of degree n with respect to r^2. For $n = 1$, we recover in particular $\omega_1 \equiv \omega_{\mathrm{mp}} = 2\,\omega_\perp$.

When Ω approaches $\omega_\perp$, all transverse modes $m = 0$ become degenerate. Such a macroscopic degeneracy is reminiscent of the degeneracy of the energy levels of a single particle in a uniform magnetic field, leading to the well-known Landau level structure [32]. An equivalent degeneracy occurs, still at the single particle level, for an isotropic 2D harmonic oscillator of frequency $\omega_\perp$, considered in a frame rotating at frequency $\Omega = \omega_\perp$ [33]. However, we emphasize that our result here holds not for a single-particle spectrum, but for the eigenmodes of an N-body system treated in the mean-field approximation. The occurrence of such a macroscopic degeneracy raises interesting questions concerning the linear response of the rotating system to an arbitrary excitation.

When the quartic potential is present, the above degeneracy is lifted. We set $x = r/R$ in (4) with $R = (4\mu/k)^{1/4}$, to get the dimensionless eigenvalue equation for the $m = 0$ modes:

$$-\frac{1}{x}\frac{\mathrm{d}}{\mathrm{d}x}\left(x\big(1 - \epsilon x^2 - x^4\big)\,\frac{\mathrm{d}[\delta\rho]}{\mathrm{d}x}\right) = \Lambda(\epsilon)\,[\delta\rho], \quad \text{where } \epsilon = \frac{mR^2}{2\mu}\big(\omega_\perp^2 - \Omega^2\big). \tag{6}$$

For each Ω, *i.e.* for each ϵ, we are interested in the lowest eigenvalue $\Lambda_0(\epsilon)$ of the Hermitian operator in the left-hand side of (6). We can then deduce the frequency of the lowest transverse monopole mode which is plotted as a continuous line in fig. 2:

$$\omega_{\mathrm{mp}}^2 = 4\Omega^2 + \frac{\mu\Lambda_0(\epsilon)}{mR^2}\,. \tag{7}$$

The quantity $\Lambda_0(\epsilon)$ is an increasing function of ϵ which we calculate numerically using a variational method with polynomial trial functions. Just at the critical rotation $\Omega = \omega_\perp$, $\epsilon = 0$ and we get $\Lambda(0) \simeq 11.5$. The slow-rotation limit corresponds to $\epsilon \gg 1$, in which case $\Lambda(\epsilon) \simeq 8\epsilon$; we then recover the result $\omega_{\mathrm{mp}} = 2\omega_\perp$.

This analysis also explains the periodic apparition of a hole at the center of the density profile for $\Omega \sim \omega_\perp$, as observed in fig. 1. The stationary density profile (3) varies as r^4 around the origin, whereas the mode $\delta\rho$ varies as r^2 in this region. The curvature of the density profile is therefore dominated by the phase of the perturbation.

For $\Omega \geq \omega_\perp$ and a relatively strong excitation ($I'/I = 4$), we observe that the time evolution of the mode structure becomes asymmetric (see fig. 3; this asymmetry is also slightly visible in the last row of fig. 1). It consists of a periodic entering positive-density wave, which starts on the edge of the condensate and gradually moves to the center in a time period $\sim \pi/\omega_\perp$. A possible interpretation of this unusual structure is that two (or more) transverse modes $m = 0$ are simultaneously excited with a non-zero relative phase. Since these modes

have similar frequencies (cf. eq. (5)) the initial phase difference between them stays nearly constant, and this can give rise to the observed phenomenon.

To summarize, we have presented in this paper a detailed study of the transverse monopole mode of a fast rotating degenerate Bose gas. We have shown that the non-harmonic character of the potential (which is essential for the confinement of the gas) has a clear influence on the mode frequency. We have also given a simple analysis of this mode for an infinitely long condensate which is in good agreement with the experimental data.

Theoretical studies have shown that the addition of a quartic term in the harmonic potential may lead to the formation of a "giant vortex", *i.e.* a vortex with a circulation larger than the single quantum h/m [19–23,34]. The large hole appearing at the center of the condensate during the monopole oscillation when $\Omega \gtrsim \omega_\perp$ should not be confused with such a giant vortex. We are dealing here with a transient state of the condensate, while the predicted giant vortex state is a stationary state of the system, for an appropriate angular momentum. Another example for a transient large core in a condensate is provided by an experiment recently performed in Boulder, in which a hole pierced in a rotating condensate confined in a purely quadratic trap was shown to persist for a long time [35].

A natural extension of the present work is to switch to a two-dimension geometry, using a strong confining potential along the rotation axis. Vortices then become point objects and the predicted properties of the system depend on the ratio between the atom number N and the number of vortices N_v. When N is large, the Bose-Einstein condensate presents a regular vortex array, as already observed in [17]. The array is expected to melt when N decreases to a value of the order of N_v [36] (see also [11]). For $N < N_\mathrm{v}$, the quantum Hall regime for particles should emerge. It is an interesting problem to determine the signature of these various regimes on the eigenmodes of the system. For the monopole mode considered here and for a pure harmonic confinement, it has been predicted in [37,38] that the frequency ω_mp of the breathing motion of a 2D gas remains strictly equal to $2\,\omega_\perp$ for any equilibrium state. This does not hold anymore in the presence of the quartic term, and thus the deviation of ω_mp from $2\,\omega_\perp$ can in principle be used to monitor the emergence of new quantum phases in the rotating gas.

* * *

We thank S. Stringari and the ENS group for useful discussions. SS acknowledges support from the European Union (CQG network HPRN-CT-2000-00125), the Studientstiftung des deutschen Volkes and the DAAD. This work is partially supported by CNRS, Collège de France, Région Ile de France, and DRED.

REFERENCES

[1] Donnelly R. J., *Quantized Vortices in Helium II* (Cambridge University Press) 1991, Chapts. 4 and 5.
[2] Tinkham M., *Introduction to Superconductivity* (McGraw-Hill) 1996.
[3] Matthews M. R., Anderson B. P., Haljan P. C., Hall D. S., Wieman C. E. and Cornell E. A., *Phys. Rev. Lett.*, **83** (1999) 2498.
[4] Madison K. W., Chevy F., Wohlleben W. and Dalibard J., *Phys. Rev. Lett.*, **84** (2000) 806.
[5] Abo-Shaeer J. R., Raman C., Vogels J. M. and Ketterle W., *Science*, **292** (2001) 476.
[6] Hodby E., Hechenblaikner G., Hopkins S. A., Maragò O. M. and Foot C. J., *Phys. Rev. Lett.*, **88** (2002) 010405.
[7] Cooper N. R., Wilkin N. K. and Gunn J. M. F., *Phys. Rev. Lett.*, **87** (2001) 120405.

[8] Paredes B., Fedichev P., Cirac J. I. and Zoller P., *Phys. Rev. Lett.*, **87** (2001) 010402.
[9] Ho T.-L., *Phys. Rev. Lett.*, **87** (2001) 060403.
[10] Regnault N. and Jolicœur Th., *Phys. Rev. Lett.*, **91** (2003) 030402.
[11] Fischer U. R., Fedichev P. O. and Recatti A., cond-mat/0212419 Preprint (2002).
[12] Read N. and Cooper N. R., cond-mat/0306378 Preprint (2003).
[13] Baym G. and Pethick C. J., cond-mat/0308325 Preprint (2003).
[14] Baksmaty L. O., Woo S. J., Choi S. and Bigelow N., cond-mat/0310567 Preprint (2003).
[15] Akkermans E. and Ghosh S., cond-mat/0307418 Preprint (2003).
[16] Coddington I., Engels P., Schweikhard V. and Cornell E. A., *Phys. Rev. Lett.*, **91** (2003) 100402.
[17] Schweikhard V., Coddington I., Engels P., Mogendorff V. P. and Cornell E. A., cond-mat/0308582 Preprint (2003).
[18] Fetter A. L., *Phys. Rev. A*, **64** (2001) 063608.
[19] Lundh E., *Phys. Rev. A*, **65** (2002) 043604.
[20] Kasamatsu K., Tsubota M. and Ueda M., *Phys. Rev. A*, **66** (2002) 053606.
[21] Kavoulakis G. M. and Baym G., *New J. Phys.*, **5** (2003) 51.1.
[22] Tsubota M., Kasamatsu K. and Araki T., cond-mat/0309364 Preprint (2003).
[23] Aftalion A. and Danaila I., cond-mat/0309668 Preprint (2003).
[24] Bretin V., Stock S., Seurin Y. and Dalibard J., cond-mat/0307464 Preprint (2003).
[25] For a review, see, *e.g.*, Dalfovo F., Giorgini S., Pitaevskii L. P. and Stringari S., *Rev. Mod. Phys.*, **71** (1999) 463.
[26] Fort C., Prevedelli M., Minard F., Cataliotti F. S., Ricci L., Tino G. M. and Inguscio M., *Europhys. Lett.*, **49** (2000) 8.
[27] Chevy F., Bretin V., Rosenbusch P., Madison K. W. and Dalibard J., *Phys. Rev. Lett.*, **88** (2002) 250402.
[28] Cozzini M. and Stringari S., *Phys. Rev. A*, **67** (2003) 041602.
[29] As for the dipole mode there is actually a small correction ($\sim 1\%$) to this relation due to the presence of the quartic potential $kr^4/4$.
[30] Sedrakian A. and Wasserman I., *Phys. Rev. A*, **63** (2001) 063605.
[31] Chevy F. and Stringari S., cond-mat/0305559 Preprint (2003).
[32] Landau L. D. and Lifchitz E. M., *Quantum Mechanics, Course of Theoretical Physics*, Vol. **3** (Butterworth-Heinemann, Stoneham, Mass.) 1981, Chapt. 15.
[33] In a frame rotating at angular velocity Ω, the single-particle Hamiltonian becomes $H' = H - L_z$. Therefore, all the levels of the 2D harmonic oscillator with an angular momentum m equal to the excitation number n have an energy $n\hbar(\omega_\perp - \Omega)$ that goes to zero when $\Omega = \omega_\perp$.
[34] Fischer U. R. and Baym G., *Phys. Rev. Lett.*, **90** (2003) 140402.
[35] Engels P., Coddington I., Haljan P. C., Schweikhard V. and Cornell E. A., *Phys. Rev. Lett.*, **90** (2003) 170405.
[36] Sinova J., Hanna C. B. and MacDonald A. H., *Phys. Rev. Lett.*, **89** (2002) 030403.
[37] Pitaevskii L. P. and Rosch A., *Phys. Rev. A*, **55** (1997) R853.
[38] Kagan Yu., Surkov E. L. and Shlyapnikov G. V., *Phys. Rev. A*, **54** (1996) R1753.

Low lying twisting and acoustic modes of a rotating Bose-Einstein condensate

PHYSICAL REVIEW A **73**, 041604(R) (2006)

Low-lying twisting and acoustic modes of a rotating Bose-Einstein condensate

F. Chevy
Laboratoire Kastler-Brossel (Unité de Recherche de l'Ecole normale supérieure et de l'Université Pierre et Marie Curie, associée au CNRS), ENS, 24 rue Lhomond, 75005 Paris, France
(Received 22 November 2005; published 13 April 2006)

We present a calculation of the low lying spectrum of a rotating Bose-Einstein condensate. We show that in a cylindrical geometry, there exist two linear branches, one associated with usual acoustic excitations, the other corresponding to a twisting mode of the vortex lattice. Using a hydrodynamical approach, we derive the elasticity coefficient of the vortex lattice and calculate the spectrum of condensate in a three-dimensional harmonic trap with cylindrical symmetry.

DOI: 10.1103/PhysRevA.73.041604 PACS number(s): 03.75.Kk, 03.75.Lm, 67.90.+z, 05.30.Fk

By contrast with classical hydrodynamics, a quantum fluid cannot rotate like a solid body. Instead, it carries quantized vortices self-organizing along a triangular Abrikosov lattice when the rotation is fast enough. Vortices constitute a universal characteristic of quantum fluids and were directly observed in systems as different as liquid helium [1], superconductors [2], gaseous Bose-Einstein condensates (BEC) [3–6], and very recently fermionic superfluids [7]. The study of the excitations of a vortex lattice was initiated by the work of Tkachenko [8] that was restricted to the study of the propagation of waves transversely to the rotation axis in an incompressible superfluid. The full understanding of these excitations in the case of dilute gases remains a challenge, due to the nontrivial interplay between the elasticity of the vortex lattice and the phonon modes associated with the compressibility of these systems. Partial results were obtained in the case of a single vortex line [9,10], two-dimensional systems [11–13], fast rotating systems [14–16] or using the rotational hydrodynamics formalism [17,18,20], but a complete theory remains to be found.

In this paper, we present a study of the low lying modes propagating along the axis of an elongated vortex lattice. Up until now, these modes have only been considered for homogeneous and unbounded fluids [16]. In the more realistic case of a trapped gaseous BEC, we show that these modes can be understood as Goldstone modes arising from U(1) and O(2) broken symmetries, associated respectively with the choice of the phase of the macroscopic wave function of the condensate and of the direction of the vortex lattice. These two broken symmetries thus give rise to two low-energy excitation branches associated, respectively, to a modulation of the phase of the wave function and of the direction of the vortex lattice in the z direction. Since the gradient of the phase is proportional to the velocity of the BEC, the first branch is associated with an acoustic wave propagating along the cloud ("phonon" branch). The second mode corresponds to the twisting of the vortices and is related to the elasticity of the lattice ("twiston" branch, Fig. 1). This scheme will be worked out first using a perturbative resolution of the Bogoliubov–de Gennes equations in a cylindrical trap, a method already used in the stability analysis of solitons [19]. We will show that this solution can be interpreted in a macroscopic framework, leading to elastohydrodynamical equations for the motion of the BEC in the presence of the vortex lattice. In particular, we propose the first derivation of the elastic response coefficient of the vortex lattice, starting from first principles. Finally, local density approximation will allow for the calculation of the lowest-energy modes in the presence of an axial trapping.

We consider a dilute Bose-Einstein condensate rotating at an angular velocity Ω_0 along the z axis. At rest, the system is described in the mean-field approximation by a macroscopic wave-function ψ_0 solution of the Gross–Pitaevskii equation

$$(\hat{h}_0 + g|\psi_0|^2)\psi_0 = 0, \tag{1}$$

where the single particle Hamiltonian $\hat{h}_0$ is given by $\hat{h}_0 = -\frac{\hbar^2}{2m}\nabla^2 + V(x,y) - \Omega_0 \hat{L}_z - \mu_0$. V is the transverse trapping potential, $\hat{L}_z$ is the angular momentum in the z direction, μ_0 is the chemical potential, and g is the coupling constant characterizing the two-body interactions. We assume for the moment there is no confining potential in the z direction. Nevertheless, we impose periodic boundary conditions in this

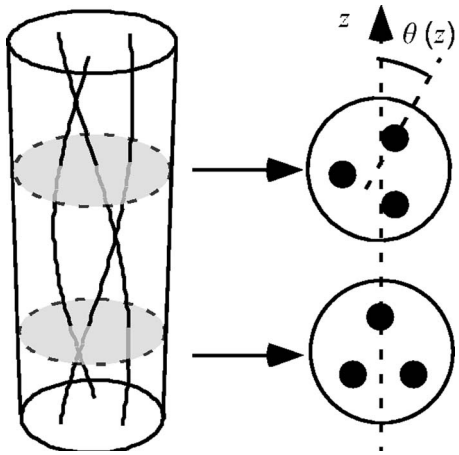

FIG. 1. Left: Structure of the twiston mode for a cylindrical BEC carrying three vortex lines. Right: Arrangement of the vortex lattice in the planes defined by the shaded areas. The vortex lattice is rotated by an angle $\theta(z)$ depending on the axial position along the trap. This twisting induces the propagation of an elastic wave along the condensate axis.

direction, with period L, to allow for the normalization of the wave function.

In the linear regime, we write function ψ of the condensate is given by $\psi=\psi_0+\delta\psi$. $\delta\psi$ is then solution of the Bogoliubov–de Gennes equations $i\hbar\partial_t\mathbf{\Phi}=\hat{\mathcal{L}}\mathbf{\Phi}$, with $\mathbf{\Phi}=(\delta\psi,\delta\psi^*)$ and

$$\hat{\mathcal{L}}=\begin{pmatrix}\hat{h}_0+2g|\psi_0|^2 & g\psi_0^2\\ -g\psi_0^{*2} & -\hat{h}_0-2g|\psi_0|^2\end{pmatrix}. \tag{2}$$

We recall a few properties of $\hat{\mathcal{L}}$ relevant for the discussion [21,22]. First, although $\hat{\mathcal{L}}$ is not Hermitian, it is orthogonal for the quadratic form with signature $(1,-1)$ defined by $(\mathbf{\Phi}_1|\mathbf{\Phi}_2)=\int d^3\boldsymbol{r}\mathbf{\Phi}_1^\dagger\hat{\sigma}_3\mathbf{\Phi}_2$, where $\hat{\sigma}_3$ is the diagonal Pauli matrix. Second, the eigenvectors $\mathbf{\Phi}_\alpha$ of $\hat{\mathcal{L}}$ do not constitute a complete basis. Indeed, one can show that each zero energy mode is associated with an anomalous Jordan mode $\mathbf{\Phi}'_\alpha$ such that $\hat{\mathcal{L}}\mathbf{\Phi}'_\alpha=\mathbf{\Phi}_\alpha$. In the case under study here, we assume there are only two-zero energy modes associated, respectively, with the U(1) and O(2) freedom of choice of the phase of the wave function and the orientation of the vortex lattice. The associated eigenvectors are, respectively, denoted by $\mathbf{\Phi}_p$ (phase symmetry) and $\mathbf{\Phi}_r$ (rotational symmetry) and are given by [21,22]

$$\mathbf{\Phi}_p=\begin{pmatrix}\psi_0\\ -\psi_0^*\end{pmatrix}\quad\mathbf{\Phi}'_p=\begin{pmatrix}\partial_\mu\psi_0\\ \partial_\mu\psi_0^*\end{pmatrix}$$

$$\mathbf{\Phi}_r=\begin{pmatrix}\hat{L}_z\psi_0\\ -(\hat{L}_z\psi_0)^*\end{pmatrix}\quad\mathbf{\Phi}'_r=\begin{pmatrix}\partial_\Omega\psi_0\\ \partial_\Omega\psi_0^*\end{pmatrix}, \tag{3}$$

Let us now proceed with the calculation of the long wavelength modes of $\hat{\mathcal{L}}$. Using the translational invariance of the system, we can write $\mathbf{\Phi}_\alpha(x,y,z)=\bar{\mathbf{\Phi}}_\alpha(x,y)e^{ik_\alpha z}$. We therefore see that $\hat{\mathcal{L}}=\hat{\mathcal{L}}_0+\delta\hat{\mathcal{L}}$, where $\hat{\mathcal{L}}_0$ acts on the transverse degrees of freedom only, $\delta\hat{\mathcal{L}}=\epsilon_{k_\alpha}\hat{\sigma}_3$, with $\epsilon_{k_\alpha}=\hbar^2k_\alpha^2/2m$.

Since we only care for long wavelength eigenmodes, we have ϵ_{k_α} vanishingly small and we can treat $\delta\hat{\mathcal{L}}$ as a perturbation of $\hat{\mathcal{L}}_0$. However, starting the perturbation expansion from the zero energy modes $\mathbf{\Phi}_r$ and $\mathbf{\Phi}_p$ of $\mathcal{L}_0$ associated with the rotational and phase symmetries gives rise to *linear* excited branches. Indeed, due to the nondiagonalizability of $\hat{\mathcal{L}}_0$ the first-order term of the low momentum expansion scales like $\epsilon_{k_\alpha}^{1/2}$ rather than ϵ_{k_α} [23]. This singularity can be proven rigorously by diagonalizing the projection of $\delta\hat{\mathcal{L}}$ on the vector space spanned by the zero energy and anomalous modes. Physically, this result corresponds to the fact that one should recover a linear phonon dispersion law $E_\alpha\propto k_\alpha\propto\epsilon_{k_\alpha}^{1/2}$ associated with usual acoustic waves.

Working out the perturbative expansion in power of $\sqrt{\epsilon_{k_\alpha}}$ yields

$$\bar{\mathbf{\Phi}}_\alpha=(a_r\mathbf{\Phi}_r+a_p\mathbf{\Phi}_p)+E_\alpha(a_r\mathbf{\Phi}'_r+a_p\mathbf{\Phi}'_p)+\cdots, \tag{4}$$

where E_α is solution of the eigenequation

$$\sum_{\gamma=r,p}(\epsilon_{k_\alpha}A_{\beta\gamma}-E_\alpha^2B_{\beta\gamma})a_\gamma=0, \tag{5}$$

with $\beta\in\{r,p\}$, $A_{\beta\gamma}=(\mathbf{\Phi}_\beta|\hat{\sigma}_z\mathbf{\Phi}_\gamma)/L$, and $B_{\beta\gamma}=(\mathbf{\Phi}_\beta|\mathbf{\Phi}'_\gamma)/L$. L is introduced here so that A and B are defined as one-dimensional (1D) linear quantities that we can use in a local density approach as demonstrated later in this paper. Using Eq. (3) yields the simple expressions

$$(\mathbf{\Phi}_p|\hat{\sigma}_z\mathbf{\Phi}_p)=2N\quad(\mathbf{\Phi}_p|\mathbf{\Phi}'_p)=\partial_{\mu_0}N$$

$$(\mathbf{\Phi}_r|\hat{\sigma}_z\mathbf{\Phi}_r)=2\langle\hat{L}_z^2\rangle\quad(\mathbf{\Phi}_r|\mathbf{\Phi}'_r)=\partial_{\Omega_0}\langle\hat{L}_z\rangle$$

$$(\mathbf{\Phi}_p|\hat{\sigma}_z\mathbf{\Phi}_r)=2\langle\hat{L}_z\rangle\quad(\mathbf{\Phi}_p|\mathbf{\Phi}'_r)=\partial_{\Omega_0}N$$

$$(\mathbf{\Phi}_r|\hat{\sigma}_z\mathbf{\Phi}_p)=2\langle\hat{L}_z\rangle\quad(\mathbf{\Phi}_r|\mathbf{\Phi}'_p)=\partial_{\mu_0}\langle\hat{L}_z\rangle, \tag{6}$$

where N is the total atom number [24]. The set of two equations (5) yields two different linear excitation branches. The highest branch has a nonzero velocity for vanishing Ω_0 and can therefore be identified with a phonon mode. The other branch has a vanishing velocity at small Ω and is therefore the twiston mode.

It is striking that the coefficients of Eq. (5) can be expressed as simple combinations of macroscopic quantities, such as the atom number or the angular momentum. Similarly to superfluid hydrodynamics, this suggests that the formalism developed here can be expressed in terms of an elastohydrodynamical theory. In order to clarify this link, we first note that the frequency of the long-wavelength modes, we are interested in is much smaller than the frequencies characterizing the evolution of the transverse degrees of freedom. This means in particular that the dynamics in the (x,y) plane is frozen and that we can therefore define local chemical potential $\mu(z,t)$, angular velocity $\Omega(z,t)$, phase of the wave function $\chi(z,t)$ and angle of the vortex lattice $\theta(z,t)$. In other words, the wave function can be written as

$$\psi(x,y,z,t)=\psi_0(\mu(z,t),\Omega(z,t),\chi(z,t),\theta(z,t),x,y), \tag{7}$$

where ψ_0 is the solution of the Gross–Pitaevskii equation (1). Expanding the macroscopic quantities around their equilibrium values yields

$$\delta\psi=\delta\mu\partial_{\mu_0}\psi_0+\delta\Omega\partial_{\Omega_0}\psi_0+\delta\chi\partial_{\chi_0}\psi_0+\delta\theta\partial_{\theta_0}\psi_0, \tag{8}$$

where $\mu=\mu_0+\delta\mu$, $\Omega=\Omega_0+\delta\mu$, etc. Noting further that $\delta\psi$ is the first component of $\mathbf{\Phi}_\alpha$ and that $\partial_\chi\psi_0=i\psi_0$ and $\partial_\theta\psi_0=-i\hat{L}_z\psi_0/\hbar$, we see that Eq. (8) is equivalent to

$$\mathbf{\Phi}=i\delta\chi\mathbf{\Phi}_p-i\frac{\delta\theta}{\hbar}\mathbf{\Phi}_r+\delta\mu\mathbf{\Phi}'_p+\delta\Omega\mathbf{\Phi}'_r. \tag{9}$$

Comparing to Eq. (4), this leads to the identification

$$a_r=-i\delta\theta/\hbar=\delta\Omega/E_\alpha \tag{10}$$

$$a_p=i\delta\chi=\delta\mu/E_\alpha, \tag{11}$$

which gives, using the identity $\partial_t=-iE_\alpha/\hbar$,

$$\partial_t\delta\theta=\delta\Omega \tag{12}$$

$$\hbar\partial_t\delta\chi = -\delta\mu. \tag{13}$$

The interpretation of these two relations is straightforward. Indeed, Eq. (12) is the analog of the Kelvin-Helmholtz theorem [25] and implies that the vortex lattice rotates at the same speed as the local velocity flow. As for Eq. (13), it is a version of the Bernoulli theorem, with $\hbar\delta\chi/m$ playing the role of the velocity potential.

Starting from the identification of the $a_{r,p}$ coefficient, we now show that the eigensystem (5) can be interpreted as conservation laws for the system. Indeed, the conservation of particle number, momentum and angular momentum in the z direction yield at first order in perturbation the very general set of equations

$$\partial_t\delta n + \partial_z(n_0 v) = 0, \tag{14}$$

$$mn_0\partial_t v + \partial_z f = 0, \tag{15}$$

$$\partial_t\delta\ell_z + \partial_z\Gamma = 0, \tag{16}$$

where n_0 is the linear particle density, v is the local velocity in the z direction, ℓ_z is the angular momentum per unit length. f and Γ are, respectively, the 1D momentum and angular momentum currents, which can be identified with a force and a torque and will be calculated from the microscopic formalism presented above.

Combining Eqs. (14) and (15) and using a generalized Gibbs-Duhem relation [26] for a rotating system, $df = n_0 d\mu + \ell_z^0 d\Omega$ yields

$$\partial_t^2[\delta\mu\partial_{\mu_0}n_0 + \delta\Omega\partial_{\Omega_0}n_0] = \frac{1}{m}\partial_z[n_0\partial_z\delta\mu + \ell_z^0\partial_z\delta\Omega], \tag{17}$$

where we have used the adiabatic following of the transverse degrees of freedom to set $\delta n = \delta\mu\partial_{\mu_0}n_0 + \delta\Omega\partial_{\Omega_0}n_0$.

After making the replacement $\hbar\partial_t = -iE_\alpha$ and $\partial_z = ik_\alpha$, we see that Eq. (17) is strictly equivalent to the $\alpha = p$ component of Eq. (5).

A similar analysis shows that the $\alpha = r$ component of Eq. (5) is equivalent to the angular momentum conservation if the current Γ is taken to be

$$\Gamma = \ell_z^0 v - \kappa\partial_z\delta\theta, \tag{18}$$

where $\kappa = \Delta L_z^2/Lm$, and $\Delta L_z^2 = \langle\hat{L}_z^2\rangle - \langle\hat{L}_z\rangle^2/N$ is the fluctuation of the angular momentum. The term of Γ proportional to the local velocity v corresponds to the convective part of the angular momentum current. The second term is associated with the elastic response of the vortex lattice to a torsion and κ is therefore the elastic modulus of the lattice.

The hydrodynamical formalism developed above can be used to extend our calculation to the case of a weak trapping in the z direction. In this case, local density approximation can be applied. At equilibrium, the angular velocity is still uniform along the cloud. By contrast, the local chemical potential is now given by $\mu_0(z) = \mu_c - m\omega_z^2 z^2/2$, where μ_c is the chemical potential at the center of the trap. This permits us to define local matrices $A(z)$ and $B(z)$ and yields the equation for the vector $\mathbf{X}(z,t) = (\delta\mu(z,t), \delta\Omega(z,t))$

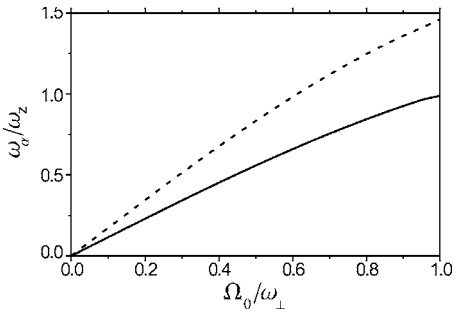

FIG. 2. Low lying twiston spectrum of a trapped rotating Bose-Einstein condensate. The two branches correspond to the frequency of the lowest odd (full line) and even (dashed line) twiston modes and were calculated using polynomials trial wave functions.

$$2m\partial_t^2[B(z)\cdot\mathbf{X}(z,t)] = \partial_z[A(z)\cdot\partial_z\mathbf{X}(z,t)]. \tag{19}$$

In general, A and B must be calculated using a numerical resolution of the Gross–Pitaevskii equation. However, in the regime of fast rotation, quantities appearing in Eq. (19) can be evaluated assuming a classical rotational flow $\mathbf{v} = \mathbf{\Omega}_0 \times \mathbf{r}$. We have first checked that at zero-angular velocity we could recover the spectrum of an elongated condensate studied in [27]. We have also verified that the center of mass was indeed evolving at a frequency ω_z, in accordance with Kohn's theorem. The other eigenfrequencies ω_α are evaluated using a variational method. We indeed note that the ω_α^2 are the eigenvalues of the operator $\hat{T} = B^{-1}\cdot\partial_z(A\cdot\partial_z\cdot)/2m$ which is hermitian for the scalar product defined by $\langle\mathbf{Y}|\mathbf{X}\rangle = \int\mathbf{Y}^\dagger(z)\cdot B(z)\cdot\mathbf{X}(z)dz$. We have calculated the ω_α using polynomial trial wave functions of order 5. The variation of ω_α for the two lowest twiston modes—corresponding respectively to odd and evensymmetries [28]—is displayed in Fig. 2.

In conclusion, we have demonstrated the existence of two low-energy excitation branches of a rotating elongated Bose-Einstein condensate. The validity of our calculation is limited by two conditions. First the applicability of the hydrodynamical formalism to evaluate the matrix elements of A and B requires a dense vortex lattice, hence a large rotation frequency. Using an imaginary time evolution of two-dimensional (2D) Gross–Pitaevskii equation [29], we have checked it was true for $\Omega_0 \gtrsim 0.8\omega_\perp$. Second, the breakdown of the perturbation expansion will happen when the ω_α become comparable with the frequency ω_T of the first transverse excited mode, i.e., the lowest Tkachenko mode. Using the expression of ω_T found in [15], we find that for typical values $\mu/\hbar\omega_\perp = 20$ and $\omega_\perp/\omega_z = 20$, the perturbation expansion fails for $\Omega_0/\omega_\perp \lesssim 0.96$. Although the width of validity of our approximation might seem narrow at first sight, it must be noted that experimentally regular vortex lattices are only observed on a relatively narrow range of rotation frequencies, comparable to our validity domain ($\Omega_0/\omega_\perp \in [0.7, 0.96]$ for [30]). A last issue concerns the experimental observation of twistons. It must be noted that, in practice, it is difficult to excite directly the vortex degrees of freedom of a gaseous BEC and it is therefore more convenient to excite an acoustic mode by perturbing the trapping potential and to use the linear [31,32] or nonlinear [33] coupling to vortical

modes. In principle, the coupling existing between acoustic and torsional degrees of freedom should permit an excitation of the twiston mode using an external potential. However, one can show using perturbation theory that a simple modulation of the trap center or frequency is only weakly coupled to the twiston mode. To obtain a significant coupling to torsional modes, one therefore needs to impart cubic or quartic perturbation to the gas.

The author especially thanks S. Stringari for initiating this work and acknowledges fruitful discussion with G. Baym, Y. Castin, and H.T.C. Stoof, as well as the Cold atom group of the ENS. He is also very grateful to J. Dalibard, D. Guéry-Odelin, and C. Salomon for careful reading and suggestions. This work is partially supported by CNRS, Collège de France, ACI Nanosciences and Région Ile de France (IFRAF).

[1] R. J. Donnelly, *Quantized Vortices in Helium II* (Cambridge University Press, UK, 1991).
[2] D. Cribier, B. Jacrot, L. M. Rao, and B. Farnoux, Phys. Lett. **9**, 106 (1964).
[3] K. W. Madison, F. Chevy, W. Wohlleben, and J. Dalibard, Phys. Rev. Lett. **84**, 806 (2000).
[4] M. R. Matthews *et al.*, Phys. Rev. Lett. **83**, 2498 (1999).
[5] J. R. Abo-Shaeer, C. Raman, J. M. Vogels, and W. Ketterle, Science **292**, 476 (2001).
[6] E. Hodby, G. Hechenblaikner, S. A. Hopkins, O. M. Marago, and C. J. Foot, Phys. Rev. Lett. **88**, 010405 (2001).
[7] M. W. Zwierlein, J. R. Abo-Shaeer, A. Schirotzek, C. H. Schunck, and W. Ketterle, Nature (London) **435**, 1047 (2005).
[8] V. K. Tkachenko, Zh. Eksp. Teor. Fiz. **50**, 1573 (1966) [Sov. Phys. JETP **23**, 1049 (1966)].
[9] L. Pitaevskii, Sov. Phys. JETP **13**, 451 (1961).
[10] J.-P. Martikainen and H. T. C. Stoof, Phys. Rev. Lett. **91**, 240403 (2003).
[11] J. R. Anglin and M. Crescimanno, e-print cond-mat/0210063.
[12] T. Mizushima *et al.*, Phys. Rev. Lett. **92**, 060407 (2004).
[13] L. O. Baksmaty, S. J. Woo, S. Choi, and N. P. Bigelow, Phys. Rev. Lett. **92**, 160405 (2004); L. O. Baksmaty, S. J. Woo, S. Choi, and N. P. Bigelow, *ibid.* **92**, 170402 (2004).
[14] G. Baym, Phys. Rev. Lett. **91**, 110402 (2003).
[15] M. Cozzini, L. P. Pitaevskii, and S. Stringari, Phys. Rev. Lett. **92**, 220401 (2004).
[16] S. A. Gifford and G. Baym, Phys. Rev. A **70**, 033602 (2004).
[17] A. Sedrakian and I. Wasserman, Phys. Rev. A **63**, 063605 (2001).
[18] F. Chevy and S. Stringari, Phys. Rev. A **68**, 053601 (2003).
[19] E. A. Kuznetsov and J. J. Rasmussen, Phys. Rev. E **51**, 4479 (1995).
[20] S. Choi, L. O. Baksmaty, S. J. Woo, and N. P. Bigelow, Phys. Rev. A **68**, 031605(R) (2003).
[21] M. Lewenstein and L. You, Phys. Rev. Lett. **77**, 3489 (1996).
[22] Y. Castin and R. Dum, Phys. Rev. A **57**, 3008 (1998).
[23] C. Lobo and Y. Castin, Phys. Rev. A **72**, 043606 (2005).
[24] Note that $B_{\alpha\beta}$ is symmetric since Hellman–Feynman theorem yields $\partial_{\Omega_0} N = \partial_{\mu_0} \langle \hat{L}_z \rangle = -\partial^2_{\Omega_0 \mu_0} \langle \hat{H} \rangle$.
[25] Note that by contrast with a classical fluid, Kelvin–Helmholtz theorem is not valid in general in the presence of quantized vortices, see e.g., B. Damski and K. Sacha, J. Phys. A **36**, 2339 (2003) or H. M. Nilsen, G. Baym, and C. J. Pethick, e-print cond-mat/0508195.
[26] C. Kittel, *Thermal Physics* (Wiley, New York, 1969), p. 347.
[27] S. Stringari, Phys. Rev. A **58**, 2385 (1998).
[28] Note that the real lowest even mode has zero frequency and corresponds to $\delta\mu$ and $\delta\Omega$ constant. To get rid of it, we have carried out the variationnal method in the vector space orthogonal to constant polynomials.
[29] Y. Castin and R. Dum, Eur. Phys. J. D **7**, 399 (1999).
[30] V. Bretin, S. Stock, Y. Seurin, and J. Dalibard, Phys. Rev. Lett. **92**, 050403 (2004).
[31] I. Coddington, P. Engels, V. Schweikhard, and E. A. Cornell, Phys. Rev. Lett. **91**, 100402 (2003).
[32] N. L. Smith, W. H. Heathcote, J. M. Krueger, and C. J. Foot, Phys. Rev. Lett. **93**, 080406 (2004).
[33] V. Bretin, P. Rosenbusch, F. Chevy, G. V. Shlyapnikov, and J. Dalibard, Phys. Rev. Lett. **90**, 100403 (2003).

Quadrupole Oscillation of a Single-Vortex Condensate : Evidence for Kelvin Modes

Quadrupole Oscillation of a Single-Vortex Bose-Einstein Condensate: Evidence for Kelvin Modes

V. Bretin, P. Rosenbusch, F. Chevy, G.V. Shlyapnikov,* and J. Dalibard

Laboratoire Kastler Brossel,† 24 rue Lhomond, 75005 Paris, France

(Received 5 November 2002; published 12 March 2003)

We study the two transverse quadrupole modes of a cigar-shaped Bose-Einstein condensate with a single centered vortex. We show that the counterrotating mode is more strongly damped than in the absence of a vortex, whereas the corotating mode is not affected appreciably by the vortex. We interpret this result as a decay of the counterrotating quadrupole mode into two excitations of the vortex line, the so-called Kelvin modes. This is supported by direct observation of the vortex line.

DOI: 10.1103/PhysRevLett.90.100403 PACS numbers: 03.75.Lm, 32.80.Pj, 67.40.Vs

When a superfluid described by a macroscopic wave function $\psi(\mathbf{r})$ is set into rotation, quantized vortex lines appear, along which the density $|\psi|^2$ is zero [1–3]. Since ψ is single valued, its phase variation on a closed contour around a vortex line is $2n\pi$ (n is an integer). Such vortices have been observed in many systems, e.g., superconductors [4], superfluid liquid helium [5], and gaseous Bose-Einstein condensates [6–9].

A vortex line is a dynamic object. As for a classical string, transverse vibration modes of the line can be excited. For a classical vortex, the modes were calculated by Kelvin in 1880 [10]. His result can be transposed to a single quasilinear quantum vortex with unit charge ($n = 1$) in a homogeneous superfluid. This gives the relation between the energy $\hbar\omega_{\mathrm{K}}$ of a quantum of the Kelvin modes (kelvon) and its wave vector k [3,11,12]:

$$\hbar\omega_{\mathrm{K}} \simeq \frac{\hbar^2 k^2}{2m}\ln(1/k\xi) \qquad (k\xi \ll 1). \tag{1}$$

Here m is the mass of a particle of the fluid and $\xi = (8\pi\rho a)^{-1/2}$ is the healing length (a is the scattering length characterizing the binary interactions in the fluid and ρ is the fluid density). Because of the Kelvin-Helmoltz theorem [13], the Kelvin modes rotate always in the sense opposite to the vortex velocity field [3,10]. Consequently, the angular momentum of a kelvon associated with a $n = 1$ vortex is $-\hbar$ [14].

The Kelvin modes play an important role in the dynamics of superfluids [5,15] or neutron stars [14]. In superfluid liquid helium ^{4}He, they have been observed by trapping ions in the vortex core and exciting them by a circularly polarized electromagnetic field [16].

In this Letter, we present experimental evidence for Kelvin modes excited through nonlinear (Beliaev) decay of the quadrupole mode $m = -2$. An elementary excitation of the quadrupole mode $m = -2$ decays into a pair of kelvons with wave vectors k and $-k$. We measure the corresponding increase of the decay rate with respect to the decay of the $m = +2$ mode, for which angular momentum conservation forbids such a mechanism. We also present pictures of the rotating condensate obtained after the excitation of the $m = -2$ mode. They show a density modulation close to the vortex line. The spatial period of the modulation is in good agreement with the one deduced from the generalization of Eq. (1) to a trapped condensate [17,18] and the energy conservation $\omega_{-2} = 2\omega_K$ (ω_{-2} is the frequency of the $m = -2$ quadrupole mode).

We use a cigar-shaped ^{87}Rb condensate held in an axisymmetric Ioffe-Pritchard magnetic trap. The atoms are spin-polarized in the $F = m_F = 2$ state. The trapping frequencies are $\omega_z/2\pi = 11.8$ Hz (longitudinal axis) and $\omega_\perp/2\pi = 98.5$ Hz (transverse plane). The temperature is $\sim$70 nK, corresponding to a 70% condensed fraction. The number of atoms in the condensate is 1.3×10^5 and the chemical potential is 40 nK.

In order to produce in a reliable way a single vortex centered on the z axis [19], we follow the procedure outlined in Ref. [20]. We use an off-resonant laser beam, whose motion is controlled by acousto-optic modulators, to superimpose a rotating dipole potential onto the magnetic potential. This dipole potential is asymmetric in the x-y plane and reads $m\omega_\perp^2\,\epsilon(X^2 - Y^2)/2$ with $\epsilon = 0.07$. The axes X, Y are deduced from the fixed axes x, y by a rotation of an angle Ωt. The dipole potential is switched on after the condensate formation for a period of 0.3 s. We choose Ω close to the rotating quadrupole resonance $\omega_\perp/\sqrt{2}$, thus creating a lattice with five to seven vortices. During the next 2 sec, the laser stirrer is blocked and the vortex lattice decays due to a slight ($\sim 1\%$) static anisotropy of the magnetic potential in the x-y plane. The condensate is then left with a single centered vortex. The lifetime of this last vortex is $\sim$7 sec, which is much longer than the rest of the experimental sequence. Experiments without vortices performed for comparison follow the same procedure, except that rotation is kept at a lower frequency to prevent any nucleation of vortices.

The dipole potential is then used again on the single vortex condensate to selectively excite the modes $m = +2$, $m = -2$ or their superposition. During this excitation, the angular frequency and deformation parameter of the dipole potential are set to Ω' and ϵ'. The duration of the excitation is denoted by τ. The state of the condensate

is finally probed after a 25 ms time of flight by simultaneous absorption imaging along the two directions y and z. Transverse images (imaging beam along y) give indications on the behavior of the vortex line. Quantitative information is obtained from the longitudinal images (imaging beam along z). These are fitted assuming an elliptic Thomas-Fermi profile for the spatial density of the condensate in the x-y plane. We measure the size R_l and the polar angle θ of the long axis, and the size R_s of the short axis. $\zeta = R_l/R_s$ denotes the ellipticity in the x-y plane.

The first series of experiments aims at observing the free evolution of the two quadrupole surface modes $m = \pm 2$, in the presence and absence of a vortex. A percussional excitation is performed using the laser stirrer with fixed axes ($\Omega' = 0$) for a short duration $\tau = 0.5$ ms $\ll \omega_\perp^{-1}$ ($\epsilon' \sim 1$). This excites a superposition of $m = +2$ and $m = -2$ modes with equal amplitudes. We then let the cloud evolve freely in the magnetic trap for a variable time t and we perform the time of flight analysis. The quantities θ and ζ are plotted as a function of t in Fig. 1.

In the case where the condensate is vortex-free [Fig. 1(a)], the angle θ jumps periodically between 0 and $\pi/2$, indicating that the amplitudes of the two quadrupole modes $m = +2$ and $m = -2$ stay equal. The situation is dramatically different in the presence of a vortex [Fig. 1(b)]. In this case two successive regimes occur: for short times, one still observes the quadrupole oscillation, now with precessing axes. The precession is due to the lift of degeneracy between the frequencies $\omega_{\pm 2}$ of the two modes $m = \pm 2$ with $\omega_{+2} > \omega_{-2}$ [21–24]. This well known effect is often used to measure the angular momentum of the condensate [25–27]. For $t > 5$ ms, the precession rate increases and the jumps of $\pi/2$ in θ become more and more rounded. This behavior indicates that the mode $m = -2$ decays faster than $m = +2$, which will eventually lead to an atom cloud with nonoscillating ellipticity and constant rotation at ω_{+2}.

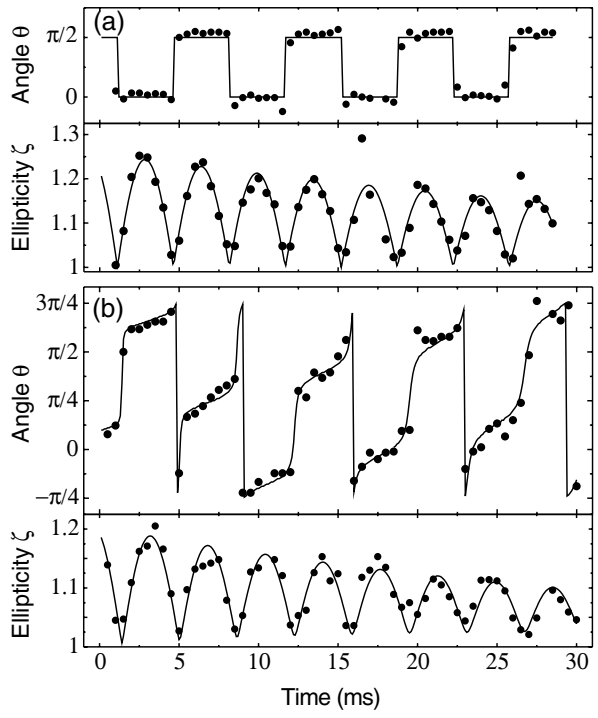

FIG. 1. Angle θ and ellipticity ζ as a function of t in the absence (a) and in the presence of a single centered vortex (b). In (b) the precession of the main axes observed for small t increases at longer times, and the jumps in θ become rounded indicating that the mode $m = -2$ decays faster than the mode $m = +2$. The solid lines are fits using the solutions of Eq. (2).

For a quantitative analysis, we have fitted $\theta(t)$ and $\zeta(t)$ assuming that the amplitudes α_m of the modes $m = \pm 2$ vary as

$$\dot{\alpha}_m + (i\omega_m + \Gamma_m)\,\alpha_m = 0 \qquad (2)$$

with $\alpha_{+2}(0) = \alpha_{-2}(0)$. The decay of the quadrupole modes is modeled using phenomenological linear damping rates Γ_m. A more refined treatment should take into account the nonlinear character of the Beliaev-type process under investigation.

In the case of no vortex [Fig. 1(a)], where the symmetry between the modes $m = \pm 2$ is preserved, we deduce from the fit $\omega_{\pm 2}^{(0)}/2\pi = 142.0 \pm 0.5$ Hz, which is close to the prediction in the Thomas-Fermi regime $\sqrt{2}\omega_\perp/2\pi = 139.3$ Hz [28]. For the decay rate we find $\Gamma_{\pm 2}^{(0)} = 21.3 \pm 1.3\ \mathrm{s}^{-1}$. In the presence of a vortex [Fig. 1(b)], the fit gives $\omega_{+2}/2\pi = 159.5 \pm 1.0$ Hz, $\omega_{-2}/2\pi = 116.8 \pm 1.0$ Hz, $\Gamma_{+2} = 19.1 \pm 2.0\ \mathrm{s}^{-1}$, and $\Gamma_{-2} = 35.7 \pm 4.0\ \mathrm{s}^{-1}$. We note that the two measured frequencies satisfy the sum rule $\omega_{+2}^2 + \omega_{-2}^2 = 4\omega_\perp^2$ [24] with a good accuracy. The fit confirms the difference in the two decay rates with the addition that the mode $m = -2$ decays faster in the presence of a vortex ($\Gamma_{-2} > \Gamma_{\pm 2}^{(0)}$), whereas $\Gamma_{+2} \simeq \Gamma_{\pm 2}^{(0)}$ [29].

In a second series of experiments, we excite the two modes $m = +2$ and $m = -2$ separately by a near resonant drive. For the excitation, we set $\epsilon' = 0.025$ and apply the laser stirrer for $\tau = 40$ ms. It is rotating with Ω' either with the same (excitation of $m = +2$) or the opposite sense ($m = -2$) with respect to the vortex. We perform the usual time of flight and imaging and measure the ellipticity ζ as a function of Ω'. We observe a clear resonance for each mode (Fig. 2). The two resonances occur at different central frequencies according to the already mentioned lift of degeneracy. The key feature of the present study is that the width of the $m = -2$ resonance is significantly larger than that of $m = +2$. Hence, as seen before, the vortex causes larger damping for the counterrotating surface wave than for the corotating.

To analyze our data, we assume that the amplitude of the relevant mode varies according to Eq. (2) with a driving term $Ae^{-2i\Omega' t}$ on the right-hand side. This assumption leads to a good fit to the data (Fig. 2) and yields $\omega_{+2}/2\pi = 161.0 \pm 1.0$ Hz, $\omega_{-2}/2\pi = 119.8 \pm 1.0$ Hz.

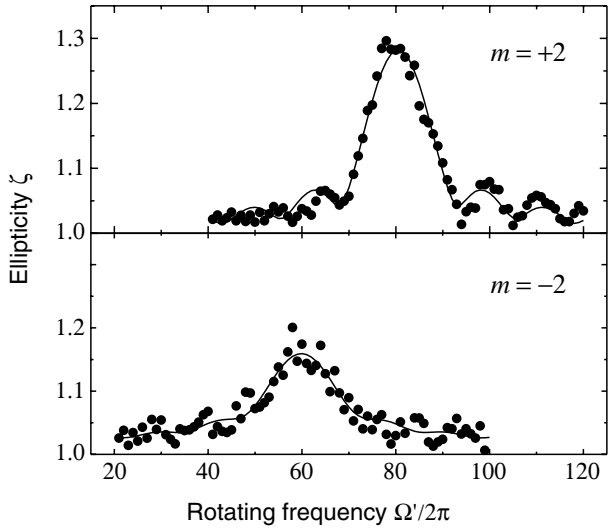

FIG. 2. Resonance of the ellipticity ζ for the $m = +2$ and $m = -2$ modes. The lines are fits deduced from the solution of Eq. (2) with a sinusoidal drive. The resonance of the mode $m = -2$ is broader than that of the $m = +2$, as a consequence of a larger damping rate.

These frequencies are in excellent agreement with those obtained by the percussional excitation. The ~ 2 Hz shift is due to the increase of the trapping frequency by the laser stirrer. The fitted damping rates are $\Gamma_{+2} = 24 \pm 5\ \mathrm{s}^{-1}$ and $\Gamma_{-2} = 57 \pm 10\ \mathrm{s}^{-1}$. These are slightly larger than those obtained from the percussional experiment, possibly due to an additional heating caused by the stirrer. However, the main feature $\Gamma_{-2} \sim 2\Gamma_{+2}$ remains valid.

We now discuss the possible physical origin of this increased damping of the $m = -2$ mode. The starting point of our analysis is the behavior of the uncondensed part of the gas. Is it still rotating when we perform the percussional or near resonant excitation? If it rotates, the symmetry between the two senses of rotation is broken and the corotating mode experiences less friction than the counterrotating mode. In [30], it has been shown that in this case $\Gamma_{-2} > \Gamma^{(0)}_{\pm 2}$ and $\Gamma_{+2} < \Gamma^{(0)}_{\pm 2}$. Moreover, one gets $\Gamma_{-2} + \Gamma_{+2} \simeq 2\Gamma^{(0)}_{\pm 2}$. This latter relation does not correspond to our observations. Although we do observe an increase of Γ_{-2} when a vortex has been nucleated, we do not observe a corresponding reduction of Γ_{+2}. From this we infer that the uncondensed fraction does not rotate significantly in our experiment. Furthermore, no such rotation is expected for our experimental conditions. The $\sim 1\%$ static trap anisotropy, which barely affects the behavior of the condensate, rapidly damps the rotation of a noncondensed gas [31,32]. The thermal cloud thus experiences two competitive forces in the bare magnetic trap: a rotational drive from the velocity flow of the condensate and a friction from the static trap anisotropy. Unlike in the case of a complete vortex array [33], the rotational drive due to a condensate with a single vortex is small compared to the friction term. Therefore the rotation of the thermal cloud is expected to be negligible.

Assuming now that the uncondensed gas is at rest, the other possible reason for a faster damping of the $m = -2$ mode is the existence of a decay channel open for $m = -2$ and closed for $m = +2$. The natural candidate for this mechanism is the Beliaev conversion of the $m = -2$ mode into two Kelvin modes k and $-k$ [34]. Since the Kelvin excitations have negative angular momentum with respect to the vortex charge, this mechanism is specific to the $m = -2$ mode. A recent theoretical analysis of this decay process, taking into account both Beliaev and Landau damping, has led to damping rates in good agreement with those that we measure experimentally [35].

To support this interpretation, we present time-of-flight images of the vortex line. The images are taken immediately after the excitation of the $m = -2$ or $m = +2$ mode. For each mode we choose Ω' at the center of the resonance and apply the probe for $\tau = 33$ ms. Figure 3 shows two condensates in the transverse view. The left picture [Fig. 3(a)] was taken counterrotating ($m = -2$), the right picture [Fig. 3(b)] corotating ($m = +2$). Below these are shown the horizontal density profiles taken at the center of the vortex line [Figs. 3(c) and 3(d)].

The vortex line is visible in both images with good contrast. As already observed in [20], the line at equilibrium is curved at both ends. It takes in the present case the form of an unfolded "N" (similar results have been obtained with "U shaped" lines). After excitation of the $m = -2$ mode, the atom density presents a periodic structure apparent as vertical stripes in the vicinity of the vortex line [Figs. 3(a) and 3(c)]. A Fourier analysis of the density profile reveals a peak centered at $k_0 = 0.70\ \mu\mathrm{m}^{-1}$ with a full width at half maximum $\Delta k_0 \simeq 0.15\ \mu\mathrm{m}^{-1}$. The area of the peak, which can be observed reproducibly

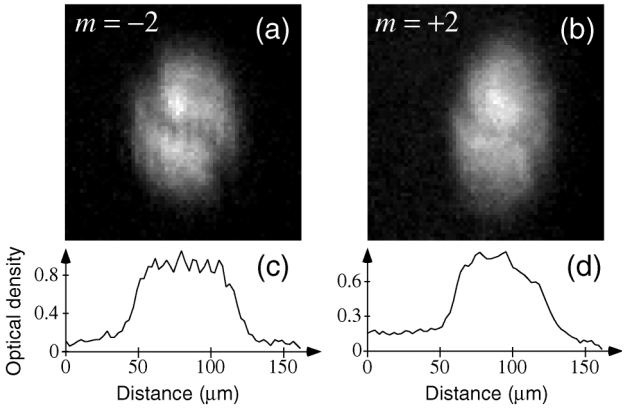

FIG. 3. Transverse images of the condensate after a 33 ms resonant excitation of the $m = -2$ mode (a) and the $m = +2$ mode (b). The picture on the left shows a periodic structure superimposed on the vortex line. The horizontal density profiles (c),(d) have been obtained by averaging over three vertical pixels around the center of the vortex line.

for similar experimental conditions, is 6 standard deviations above noise. On the contrary, such a periodic structure never appears in the images corresponding to $m = +2$ [see, e.g., Figs. 3(b) and 3(d)].

This observation supports the proposed decay mechanism of the $m = -2$ mode into a pair of Kelvin modes. At any given time, the excited vortex line is expected to have an almost sinusoidal shape with a spatial period of $2\pi/k$ along the z axis. It is located in a plane containing the z axis and rotating around this axis in the sense opposite to the vortex. At the center of the condensate, the healing length is $\xi \sim 0.3$ μm. Using Eq. (1) and energy conservation, we find $k = 0.8$ μm^{-1}. Assuming that during the time of flight, the expansion factor Λ_z along the z axis is the same for the shape of the vortex line as it is for the longitudinal size of the condensate ($\Lambda_z \sim 1.3$ [36]), we recover the measured wave vector k_0 within Δk_0. This gives approximately nine oscillation periods over the $L \sim 70$ μm length of the condensate, which is consistent with the observation in Fig. 3(a). With the quantization condition $k = \mathcal{N}\pi/L$ for the vortex line, we get $\mathcal{N} \sim 18$. The splitting between the adjacent Kelvin modes is then $\sim 20\ \text{s}^{-1}$, so that we have one or two Kelvin modes within the width $\Gamma^{(0)}_{+2}$ of the quadrupole resonance. We note that a detailed treatment of the relation between the observed density modulation and the oscillations of the vortex line remains to be done. The principle of such a treatment may follow that of Ref. [37], where phase fluctuations due to a short coherence length in a quasicondensate appear as density fluctuations after a time of flight.

In conclusion, we have observed a strong difference between the damping rates of the corotating ($m = +2$) and counterrotating ($m = -2$) quadrupole modes of a single vortex condensate. We explain this difference as due to the decay of the $m = -2$ mode into Kelvin excitations of the vortex line. This is confirmed by images of the condensate, which show a spatial density modulation around the vortex line only for counterrotating excitation.

We thank K. Madison for participation in earlier stages of this experiment, and L. Carr, Y. Castin, and K. Machida for useful discussions. P. R. acknowledges support by the Alexander-von-Humboldt Stiftung and the EU (Contract No. HPMF CT 2000 00830). This work is partially supported by CNRS, Collège de France, Région Ile de France, DGA, DRED, and EU (Contract No. HPRN-CT-2000-00125).

*Also at *FOM Institute for Atomic and Molecular Physics,* Amsterdam, The Netherlands, and *Russian Research Center Kurchatov Institute,* Moscow, Russia.

†Unité de Recherche de l'Ecole normale supérieure et de l'Université Pierre et Marie Curie, associée au CNRS.

[1] L. Onsager, Nuovo Cimento **6**, Suppl. 2, 249 (1949).
[2] R. P. Feynman, in *Progress in Low Temperature Physics*, edited by C. J. Gorter (North-Holland, Amsterdam, 1955), Vol. 1, Chap. 2.
[3] E. M. Lifshitz and L. P. Pitaevskii, *Statistical Physics, Pt. 2* (Butterworth-Heinemann, Oxford, 1980), Chap. III.
[4] M. Tinkham, *Introduction to Superconductivity* (McGraw-Hill, New York, 1996).
[5] R. J. Donnelly, *Quantized Vortices in Helium II* (Cambridge University Press, Cambridge, 1991).
[6] M. R. Matthews *et al.*, Phys. Rev. Lett. **83**, 2498 (1999).
[7] K. W. Madison *et al.*, Phys. Rev. Lett. **84**, 806 (2000).
[8] J. R. Abo-Shaeer *et al.*, Science **292**, 476 (2001); C. Raman *et al.*, Phys. Rev. Lett. **87**, 210402 (2001).
[9] E. Hodby *et al.*, Phys. Rev. Lett. **86**, 2196 (2001).
[10] W. Thomson (Lord Kelvin), Philos. Mag. **10**, 155 (1880).
[11] L. P. Pitaevskii, Sov. Phys. JETP **13**, 451 (1961).
[12] A. L. Fetter, Phys. Rev. **162**, 143 (1967).
[13] L. D. Landau and E. M. Lifshitz, *Fluid Mechanics* (Pergamon Press, London, 1987), Sec. 8.
[14] R. I. Epstein and G. Baym, Astrophys. J. **387**, 276 (1992).
[15] E. B. Sonin, Rev. Mod. Phys. **59**, 87 (1987).
[16] R. A. Ashton and W. I. Glaberson, Phys. Rev. Lett. **42**, 1062 (1979).
[17] T. Isoshima and K. Machida, Phys. Rev. A **59**, 2203 (1999).
[18] A. A. Svidzinsky and A. L. Fetter, Phys. Rev. A **62**, 063617 (2000).
[19] When several vortices are present and interact together, the nature of the excitations changes and Tkachenko modes appear (see, e.g., [15]). The quadrupole modes under study can then couple to these collective lattice modes as observed in P. Engels *et al.*, Phys. Rev. Lett. **89**, 100403 (2002).
[20] P. Rosenbusch, V. Bretin, and J. Dalibard, Phys. Rev. Lett. **89**, 200403 (2002).
[21] R. Dodd *et al.*, Phys. Rev. A **56**, 587 (1997).
[22] S. Sinha, Phys. Rev. A **55**, 4325 (1997).
[23] A. A. Svidzinsky and A. L. Fetter, Phys. Rev. A **58**, 3168 (1998).
[24] F. Zambelli and S. Stringari, Phys. Rev. Lett. **81**, 1754 (1998).
[25] F. Chevy, K. W. Madison, and J. Dalibard, Phys. Rev. Lett. **85**, 2223 (2000).
[26] P. C. Haljan *et al.*, Phys. Rev. Lett. **86**, 2922 (2001).
[27] A. E. Leanhardt *et al.*, cond-mat/0206303.
[28] S. Stringari, Phys. Rev. Lett. **77**, 2360 (1996).
[29] Without the constraint of symmetry between the modes $m = \pm 2$, the zero-vortex data lead to $\omega^{(0)}_{+2}/2\pi = 142.4$ Hz, $\omega^{(0)}_{-2}/2\pi = 141.2$ Hz, $\Gamma^{(0)}_{+2} = 22.6\ \text{s}^{-1}$, $\Gamma^{(0)}_{-2} = 20.0\ \text{s}^{-1}$.
[30] J. E. Williams *et al.*, Phys. Rev. Lett. **88**, 070401 (2002).
[31] D. Guéry-Odelin, Phys. Rev. A **62**, 033607 (2000).
[32] P. C. Haljan *et al.*, Phys. Rev. Lett. **87**, 210403 (2001).
[33] O. N. Zhuravlev, A. E. Muryshev, and P. O. Fedichev, Phys. Rev. A **64**, 053601 (2001).
[34] Each kelvon can subsequently decay into another kelvon with a slightly smaller momentum and a phonon.
[35] T. Mizushima *et al.*, cond-mat/0211396.
[36] Y. Castin and R. Dum, Phys. Rev. Lett. **77**, 5315 (1996).
[37] S. Dettmer *et al.*, Phys. Rev. Lett. **87**, 160406 (2001).

Chapitre 2

Superfluidité des gaz de fermions ultra-froids

Comme le loup le canard et vous
J'ai trouvé le froid partout
Comme le loup le canard et vous
J'ai trouvé le froid partout
Le charbonnier le voit tout en noir
Mais il est blanc pour le montagnard
Anne Sylvestre : Un froid de canard

2.1 Introduction

En 2007, la communauté physicienne a célébré les cinquante ans de la résolution d'une des énigmes les plus ardues de la physique du vingtième siècle. C'est en effet en 1957 que Bardeen-Cooper et Schrieffer publièrent le célèbre article levant le voile sur les mécanismes microscopiques de la supraconductivité, un phénomène qui était resté quarante six ans sans explication après son observation en 1911 par Kammerling-Onnes. Ce tour de force ne marqua cependant pas la fin des études sur la supraconductivité, et fut au contraire à l'origine d'une longue suite de travaux aussi bien théoriques qu'expérimentaux culminant avec la découverte des supraconducteurs à haute température critique dans les années 80. Bien que la physique des cuprates et des autres composés supraconducteurs au dessus de la température de l'azote ait été abondamment étudiée dans les vingt dernières années, les mécanismes microscopiques d'appariement dans ces systèmes restent encore mal compris en raison des corrélations fortes entre électrons dans

ces composés qui empêchent la résolution des modèles théoriques dans les régimes de paramètres pertinents pour les expériences. Cette question de la nature de l'ordre quantique dans les systèmes fermioniques en fortes interactions s'était d'ailleurs déjà posée dans le cadre conceptuel du rapport liant supraconductivité et condensation de Bose-Einstein : dans une expérience de pensée où l'on imagine pouvoir modifier l'intensité des interactions attractives entre fermions, le régime de forte interaction correspond à un condensat de Bose-Einstein de dimères fortement liés[1]. En effet, si le potentiel est suffisamment profond, il existe un état lié à deux corps. Les fermions s'apparient alors entre eux pour former des dimères qui sont des bosons puisque composés de deux particules de spin demi-entier. À basse température, ces dimères forment alors une phase superfluide sous forme d'un condensat de Bose-Einstein (CBE). Lorsque l'on diminue la profondeur du potentiel attractif, il arrive un moment où les fluctuations quantiques détruisent l'état lié dont l'absence suggère alors naïvement l'impossibilité d'obtenir une phase superfluide. Bardeen, Cooper et Schrieffer (BCS) ont cependant montré que lorsque l'on ne se restreignait plus au problème à deux corps, mais que l'on incluait tous les électrons du métal, la présence de la Mer de Fermi bloquant l'accès aux états de plus basse énergie stabilise des paires de fermions sous forme de paires de Cooper.

L'étude de ce passage entre le régime de condensation de Bose-Einstein de molécules et le régime BCS (transition CBE-BCS, ou *crossover BEC-BCS* en anglais) a fait l'objet d'une importante littérature théorique depuis les années 60 [2, 3, 4] et les diverses manifestations (supraconductivité à haute et basse température, hélium 3, hélium 4 etc, cf. fig. 2.1) connues de la superfluidité semblaient valider cette image d'un passage continu du régime d'interaction faible au régime d'interaction forte. Cependant, faute de disposer d'un système expérimental dans lequel il soit possible de contrôler à volonté les interactions, les différents modèles développés n'avaient jusqu'à récemment pu être réellement testés expérimentalement sur un système unique. Deux découvertes ont cependant permis de quitter cette impasse : d'une part, faisant suite à l'observation des condensats de Bose-Einstein gazeux en 1995, les premiers gaz de Fermi ultra froids dans le régime de dégénérescence quantique ont été obtenus en 2001 [5, 6]. D'autre part, la découverte des résonances de Fano-Feshbach dans les atomes froids permet à présent de contrôler la longueur de diffusion atomique[2] à l'aide d'un

[1] On trouvera une introduction – je l'espère – pédagogique dans l'article *les gaz de Fermi ultra-froids* paru dans Images de la physique 2005 et fourni en annexe de ce chapitre.

[2] Dans les systèmes dilués et froids que sont les gaz d'atomes froids, la distance interatomique et la longueur d'onde de de Broglie des atomes sont très grandes devant la portée

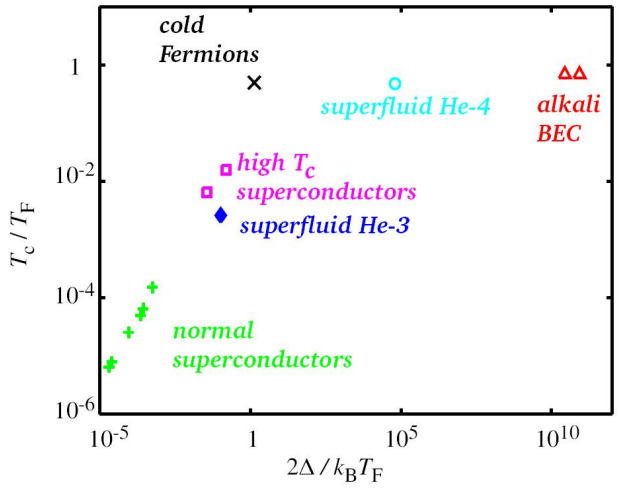

FIG. 2.1 – Transition CBE-BCS sur divers systèmes expérimentaux. En abscisse, Δ désigne l'énergie de liaison des paires responsables de la superfluidité et mesurent donc la force des interactions. T_c désigne la température critique d'apparition de la superfluidité, T_F est la température de Fermi en dessous de laquelle le Principe de Pauli l'emporte sur l'agitation thermique.

simple champ magnétique. Ce chapitre est consacré à l'étude expérimentale des systèmes de fermions ultra froids et débute avec les résultats obtenus au LKB sur l'exploration de la transition CBE-BCS. Dans le premier paragraphe dont les résultats sont présentés dans *Experimental Study of the BEC-BCS Crossover Region in Lithium 6*, les collisions entre atomes sont essentiellement isotropes (on parle d'interaction en *onde s*, par analogie avec les orbitales isotropes s de l'atome d'hydrogène) mais nous verrons dans une deuxième partie qu'il existe des résonances de Feshbach permettant d'amplifier les processus anisotropes (*P-wave Feshbach resonances of ultracold* ^6Li). En principe, ces résonances permettent d'aboutir à des superfluides fermioniques exotiques dans lesquels les paires de Cooper possèdent un spin. Ce couplage entre spin et moment cinétique orbital des paires de Cooper donne lieu à un diagramme de phase plus riche encore que celui du *crossover BEC-BCS* en onde s, faisant en particulier apparaître des *phases texturées* ana-

caractéristique du potentiel d'interaction entre particules que l'on décrit donc par un potentiel de contact $V(\boldsymbol{r}) = g\delta(\boldsymbol{r})$, où δ est la distribution de Dirac et g est une constante de couplage que l'on met sous la forme $g = 4\pi\hbar^2 a/m$. a est alors une longueur baptisée longueur de diffusion. Le régime *BCS* correspond à $a < 0$, le régime BEC à $a > 0$ et le crossover se situe lorsque $|a| \to \infty$.

logues à celles rencontrées dans l'hélium 3. Au contraire de résonances d'onde s, nous verrons cependant que les résonances d'onde p (car associées à des dimères caractérisés par une orbitale à deux lobes analogue aux états p de l'atome d'hydrogène) sont associées à d'importantes pertes inélastiques à 2 ou 3 corps réduisant considérablement la durée de vie du système.

2.2 La transition CBE-BCS dans les gaz d'atomes ultra-froids

Au LKB, l'expérience de refroidissement et de manipulation de l'isotope ^{6}Li du lithium a eu un rôle moteur dans l'observation expérimentale de la transition CBE-BCS. Le lithium 6 possède dans son état fondamental un spin $F = 1/2$ et les collisions entre atomes dans les états $m_F = 1/2$ et $m_F = -1/2$ présente une résonance de Feshbach pour une champ magnétique de $B = 834$ G qui la rend particulièrement adaptée à cette étude (Fig. 2.2). Après l'observation au JILA et au LKB des premiers gaz de fermions quantiquement dégénérés dans lesquelles les premiers effets du Principe de Pauli étaient observables [5, 6], l'exploration du régime de superfluidité fermionique a démarré dans le régime moléculaire. en commençant par la formation de ces dimères, puis la démonstration de leur longue durée de vie [7] et enfin en 2003 leur condensation à Innsbruck, au JILA, au MIT et à l'ENS [8].

En utilisant la précision inhérente aux techniques de mesures propres à la physique atomique, ces expériences nous donnent accès au comportement physique de systèmes à N corps en interactions fortes. Ainsi, dans le régime de condensation de molécules, la mesure du rayon du condensat permet de mesurer la longueur de diffusion entre deux dimères[3]. Ce problème est complexe à résoudre théoriquement puisqu'il implique la résolution d'un problème à quatre corps, mais a récemment été résolu par D. Petrov *et al.* par une résolution directe de l'équation de Schrödinger [9] puis par des méthodes diagrammatiques par Brodsky *et al.* [10]. Ces calculs montrent que les interactions à basse énergie peuvent être décrites par une longueur de diffusion entre dimères valant $a_m \sim 0.6a$, où a est la longueur de diffusion entre atomes. Cette valeur est compatible avec celle déduite de nos expériences, puisque la mesure du rayon du condensat, déterminée dans les conditions expérimentales par la répulsion entre dimères, vaut à 770 G

[3]En effet, dans le régime BEC $a > 0$, les interactions effectives entre dimères sont répulsives. Par conséquent, plus la longueur de diffusion est grande, plus le rayon du nuage est grand lui aussi.

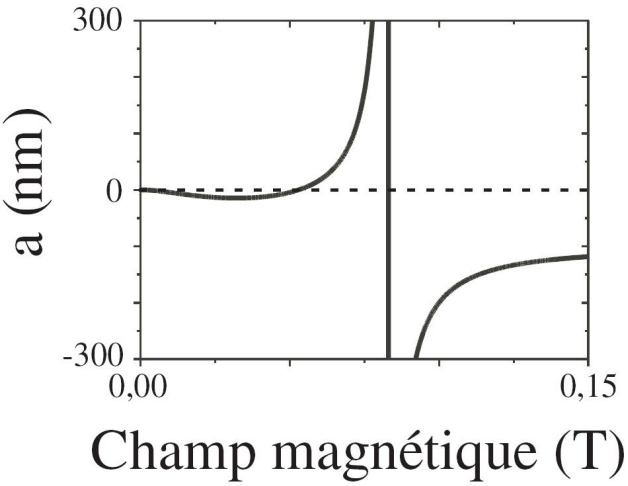

FIG. 2.2 – Évolution de la longueur de diffusion a du Lithium 6 dans l'état fondamental $F = 1/2$. La divergence de la longueur de la longueur de diffusion au voisinage de $B = 834$ G marque la résonance de Feshbach qui est utilisée dans l'expérience. Les côtés $a > 0$ et $a < 0$ correspondent respectivement au régime de condensation de Bose-Einstein de dimères et BCS.

$a_m = 170^{+100}_{-60}$ nm, à comparer avec la prédiction $a_m = 184$ nm pour cette valeur de champ magnétique, et qui exclut en particulier la prédiciton BCS $a_m = 2a = 613$ nm. Nous avons ensuite étendu cette étude des propriétés collisionnelles des dimères de fermions au cas des collisions inélastiques, dont l'étonnante faiblesse a permis le succès des expérience de transition BEC-BCS sur des atomes froids. En effet, dans les deux états de spin de plus basse énergies, la durée de vie du condensat de molécules est limitée par la désexcitation des dimères faiblement liés vers les états plus profonds. D. Petrov *et al.* ont montré que ces processus de recombinaison, qui nécessitent d'avoir trois atomes à des distances de l'ordre de la taille de l'état fondamental vibrationnel, étaient fortemement inhibés par la combinaison du principe de Pauli, qui interdit d'avoir deux atomes de même spin proche l'un de l'autre, et la grande taille des dimères au voisinage de la résonance[4] [9]. Leur calcul prédit que, contrairement aux collisions élastiques dont le taux croît comme a^2, le taux de pertes dues à ces processus de désexcitation vers les états profonds varie comme $a^{-2.55}$, en accord de nouveau avec nos résultats expérimentaux fournissant une décroissance en $a^{-1.9\pm0.8}$.

La seconde série de mesures concerne l'équation d'état du gaz à la résonance de Feshbach[5] où la longueur de diffusion diverge et où les fortes corrélations empêchent en principe toute détermination analytique des propriétés du gaz. Cependant, un simple argument dimensionnel montre qu'à basse température et dans la limite des grandes longueurs de diffusion, la relation liant le potentiel chimique μ à la densité n se met sous la forme[6]

$$\mu = \xi E_F(n), \tag{2.1}$$

où E_F désigne l'énergie de Fermi d'un gaz parfait de densité n et ξ est un simple facteur numérique. En d'autres termes, l'équation d'états du gaz dans le régime de fortes corrélations est, au facteur ξ près, identique à celle d'un gaz parfait, et pour ce qui est des propriétés macroscopiques du gaz, seule est nécessaire la connaissance de la valeur de ce paramètre ξ. Comme nous l'avons souligné plus haut, la détermination de ξ à partir de modèles microscopiques est un défi qui est, pour le moment du moins, hors de portée des techniques analytiques et se fonde donc sur des méthodes numériques (en

[4] On peut en effet montrer que la taille d'un dimère est de l'ordre de la longueur de diffusion a, et diverge donc à la résonance.

[5] Ce régime est aussi baptisé "unitaire", en lien avec certaines propriétés collisionnelles imposées par la conservation de la probabilité lors de la diffusion d'une particule quantique, l'*unitarité de la matrice S* en jargon de la théorie quantique des collisions.

[6] C'est effectivement cette équation d'état qui permet de retrouver le profil de densité du nuage dans un piège puisque le potentiel chimique doit être uniforme.

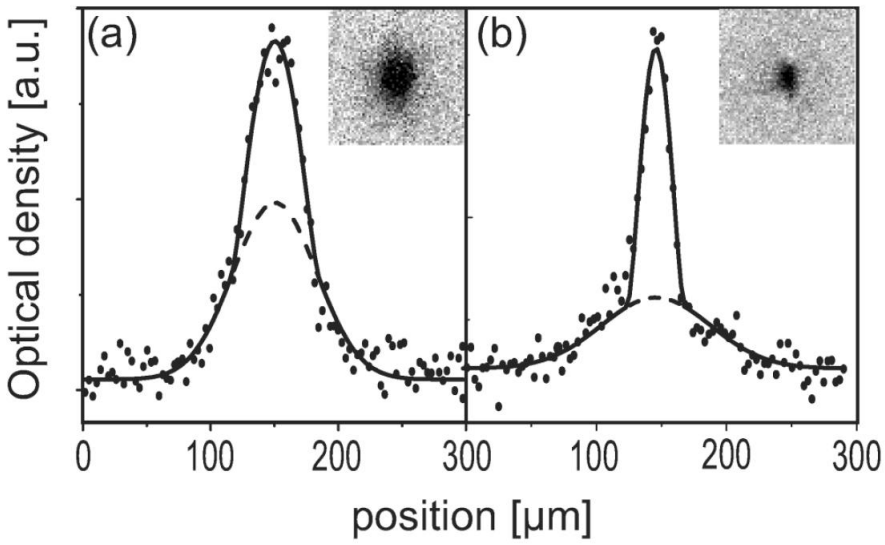

FIG. 2.3 – a) Condensat de molécules du côté BEC de la résonance de Feshbach du litium 6. b) En guise de comparaison : condensat de lithium 7 pour un nombre d'atomes équivalent. Dans les deux cas, l'apparition du condensat de molécules se manifeste par l'existence d'une double structure correspondant au condensat de Bose-Einstein au centre et aux atomes non condensés dans les ailes. L'écart de taille est essentiellement dû à la grande différence des longueurs de diffusion.

particulier *Fixed-Node Monte-Carlo* [11] ou *Monte Carlo diagrammatique* [12]). Les plus récents de ces calculs convergent vers $\xi \sim 0.42$. Nous avons cherché à déterminer la valeur de ce paramètre en mesurant de nouveau le rayon du nuage après expansion. Nous obtenons alors $\xi = 0.41(15)$ en accord avec ces prédictions théoriques, ainsi que les autres valeurs obtenues depuis expérimentalement [13].

Par les expériences brièvement présentées ci-dessus et celles d'autres groupes, un vaste ensemble de données nous fournit à présent une image claire du comportement des superfluides fermioniques en interactions fortes. Parmi les résultats les plus marquants, citons par exemple une série de mesures des modes de basse énergie d'un nuage piégé qui a permis de déterminer précisément l'équation d'état du gaz généralisant la relation (2.1) à toute la transition CBE-BCS [14] ; la mise en évidence directe de la superfluidité par l'observation de vortex au MIT [15] ou enfin l'étude de l'appariement par

des mesures de spectroscopie radio-fréquence[7] [16].

2.3 Résonance de Feshbach en onde p

La théorie classique de la supraconductivité se fonde sur la création de paires isotropes donnant lieu à un diagramme de phase de structure relativement simple, puisque pour toute valeur de la longueur de diffusion, il existe une transition de phase du second ordre entre une phase normale et une phase superfluide[8]. Lorsque l'on considère des symétries d'ordre plus élevé pour les paires de Cooper (par exemple en onde p dans l'hélium 3 superfluide), on s'attend à une structure du diagramme de phase plus complexe du fait du couplage entre le spin et le moment cinétique orbital des atomes de la paire [17]. Si l'on désire étudier expérimentalement ces effets de superfluidité fermionique induite par un appariement anisotrope, il est nécessaire de disposer de résonances de Feshbach couplant les états de diffusion d'une paire d'atomes à des états moléculaires possédant la bonne symétrie : dans le cas du lithium, on peut ainsi montrer qu'en plus des résonances de Feshbach dans l'onde s discutées dans les paragraphes précédents, il existait des résonances d'onde p dans un mélange d'atomes situés dans les deux états de spin de plus basse énergie[9] $|F = 1/2, m_F = \pm 1/2\rangle$. Nous avons localisé expérimentalement leur position en étudiant les pertes induites au voisinage de la résonance que nous avons comparées à des calculs *ab initio* de Servaas Kokkelmans utilisant les potentiels d'interactions exacts entre atomes de lithium 6. Ces résultats sont présentés dans le tableau (2.1) et montre le bon accord entre théorie et expérience.

Comme nous l'avons vu au paragraphe précédent, une des raisons du succès des expérience sur la transition BEC-BCS dans les atomes froids est l'absence de pertes inélastiques au voisinage de la résonance de Feshbach. Les règles de sélection garantissant la stabilité des gaz d'atomes ultrafroids au voisinages de résonances en onde s n'ayant *a priori* plus cours dans le cas d'interaction en onde p, nous avons caractérisé précisément ces

[7] Ce dernier point est cependant toujours sujet à d'intenses discussions car certains artefacts expérimentaux liés à la force des interactions dans le régime étudié empêchent la comparaison quantitative entre théorie et expérience.

[8] Notons que ceci n'est vrai que pour des populations de spins égales. Pour des populations de spin déséquilibrés, on attend aussi une transition normal/superfluide du premier ordre que nous aborderons au prochain chapitre.

[9] Notons que le lithium n'est pas l'atome le plus riche en résonance de Feschbach d'ordre élevé. Le record est pour le moment détenu par le césium pour lequel des résonances dans l'onde f ont été observées.

Mélange (m_F, m'_F)	Théorie (G)	Expérience (G)
(1/2,1/2)	159	160.2(6)
(1/2,-1/2)	185	186.2(6)
(-1/2,-1/2)	215	215.2(6)

TAB. 2.1 – Position des résonances de Feshbach d'onde p pour les collisions de deux atomes dans les états spin m_F et m'_F.

pertes dans le cas des résonances d'onde p et observé des comportements différents suivant les spins m_F des particules mises en jeux[10]. Nous avons tout d'abord constaté que pour les mélanges $(m_F = 1/2, m'_F = -1/2)$ et $(m_F = -1/2, m'_F = -1/2)$, la durée de vie était limitée par des collisions inélastiques à deux corps où les interactions dipôlaires provoquent le retournement d'un atome de spin $-1/2$ et libère l'énergie Zeeman correspondante. À haut champ, l'écart entre les deux niveaux vaut à peu près 80 MHz, ce qui correspond à un gain d'énergie de l'ordre du milliKelvin, bien plus grand que la température du système, ou même la profondeur du piège optique. En revanche, lorsque tous les atomes sont polarisés dans l'état fondamental (1/2,1/2), les processus de retournement du spin sont interdits par conservations de l'énergie : conformément aux observations expérimentales, les pertes à trois corps vers des états moléculaires profonds constituent le seul canal de pertes autorisé. Contrairement à ces processus de recombinaison qui nécessitent de résoudre le problème à trois corps en onde p et n'ont trouvé que très récemment une solution [19], l'étude théorique de la relaxation dipôlaire s'est avérée bien plus simple. Nous avons en particulier montré que, contrairement au cas de l'onde s où la physique collisionnelle était essentiellement dominé par le comportement à basse énergie, les pertes dans les canaux en onde p sont dominées par des processus de Wigner[11] couplant le canal entrant et le canal sortant, *via* l'état moléculaire responsable de la résonance de Feshbach (Fig. 2.4.a). Ceci signifie que les pertes sont dominées par les atomes du canal entrant d'énergie $E \sim E_m$, où E_m est l'énergie de l'état moléculaire. Comme, dans le cas d'un gaz non dégénéré, la distribution d'énergie des atomes est piquée autour de $E \sim k_B T$, on en déduit que l'évolution du taux de perte inélastique avec la température doit présenter un maximum pour $k_B T \sim E_m$, en accord avec les observations

[10] On rappelle que les atomes de lithium dans leur état fondamental possèdent un spin 1/2. Par convention, on prend l'état $m_F = 1/2$ comme état de plus basse énergie en présence d'un champ magnétique.

[11] Les processus de Wigner sont une généralisation de la Rèle d'or de Fermi et correspondent au couplage d'un état initial à un continuum *via* un état relais.

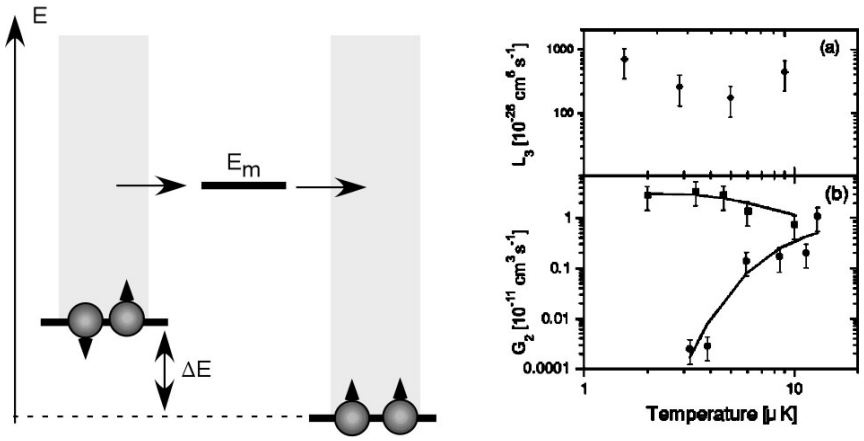

FIG. 2.4 – Gauche : Processus de Wigner résonnants. Les paires excitées (ici dans (1/2,-1/2)), se désexcitent par retournement de spin dans l'état fondamental (1/2,1/2), en dégageant l'éenrgie Zeeman ΔE. Ce processus est résonnant Ce mécanisme prédit un maximum du taux de perte pour $k_B T \sim E_b$. Droite : mesure expérimental des taux de pertes à trois corps (a) et à deux corps (b). Dans ce dernier cas, les deux séries de données correspondent respectivement aux canaux (-1/2,-1/2) et (1/2,-1/2). Les courbes en trait plein correspondent à un fit des données expérimentales à l'aide d'un seul paramètre correspondant au désaccord à résonnance.

expérimentales (Fig. 2.4).

Afin de détecter d'éventuelles molécules en onde p, nous avons ensuite réalisé une expérience de nucléation adiabatique de paires par rampe du champ magnétique dans un mélange d'atomes polarisés dans les états $m_F = 1/2$ et $m'_F = -1/2$ où les pertes dipolaires sont les plus faibles[12]. Nous mesurons alors un taux de formation de dimères de l'ordre de 20(10)% et confirme donc l'observation des premières molécules dans l'onde p. Par la suite, l'existence de ces molécules anisotropes a pu être confirmée par de groupe de D. Jin au JILA en utilisant une technique de "photoassociation" par radiofréquence [18].

[12]Pour une raison non élucidée, nous n'avons détecté aucun signal de formation de dimères dans le cas d'un nuage polarisé dans $m_F = 1/2$ où les pertes dipolaires sont pourtant complètement absentes.

2.4 Conclusion : Construction d'expériences de deuxième génération

Après l'observation de la transition BEC-BCS, la direction vers laquelle se dirigent à présent les expériences de fermions ultra-froids a trait à la simulation analogique quantique de systèmes de matière condensée. Dans cette optique, le but des expériences de prochaine génération sera de reproduire avec des atomes froids les hamiltoniens modèles utilisés pour décrire le comportement des électrons en physique du solide, de façon à confirmer ou infirmer les différentes approches mises en œuvre pour résoudre de façon approchée ces modèles. Le problème le plus direct à simuler est le modèle de Hubbard, dans lequel les particules sont libres de se déplacer sur les nœuds d'un réseau périodique et dont on pense qu'il peut receler les mécanismes microscopiques de la supraconductivité à haute température critique. L'implémentation pratique de ce modèle consiste à placer des atomes ultra-froids dans un réseau optique, un potentiel périodique obtenu par interférence de plusieurs faisceaux lasers et, afin d'explorer ces nouvelles perspectives ouvertes par les expériences de fermions ultra-froids, nous développons deux expériences de nouvelle génération.

Tout d'abord, une phase de mise à niveau de l'expérience sur le lithium est en voie d'achèvement. Ainsi, nous savions que le diamètre de la cellule avait été sous-dimensionné en comparaison de la taille du nuage après la phase de piégeage magnéto-optique et aboutissait à une perte de 90% des atomes durant le transfert dans le piège d'évaporation. La cellule a par conséquent été élargie, ce qui a nécessité l'élaboration de nouvelles bobines de champ magnétiques pouvant l'accommoder. Un effort considérable a aussi été fourni en vue de l'amélioration du système laser qui est un des points critiques de l'expérience puisque la nécessité de travailler avec les deux isotopes du lithium double le nombre de longueurs d'ondes nécessaires et oblige à garder pas moins de onze lasers verrouillés en permanence sur les transitions atomiques. Ces modifications, ainsi que de multiples autres d'importance moindre, ont porté leurs fruits et aboutissent à une nette amélioration du taux de chargement (qui passe d'une minute à quinze secondes) et nombre d'atomes (d'un facteur 5). Ces chiffres encourageants nous permettrons d'aborder dans les meilleurs conditions les expériences à venir sur les gaz de lithium 6 ultra-froids : tout d'abord sur l'effet d'un déséquilibre des populations de spin sur la superfluidité et sur les propriétés dynamiques du nuage (cf. chapitre suivant) et ensuite l'étude des systèmes fermioniques dans des réseaux optiques en nous penchant en particulier sur

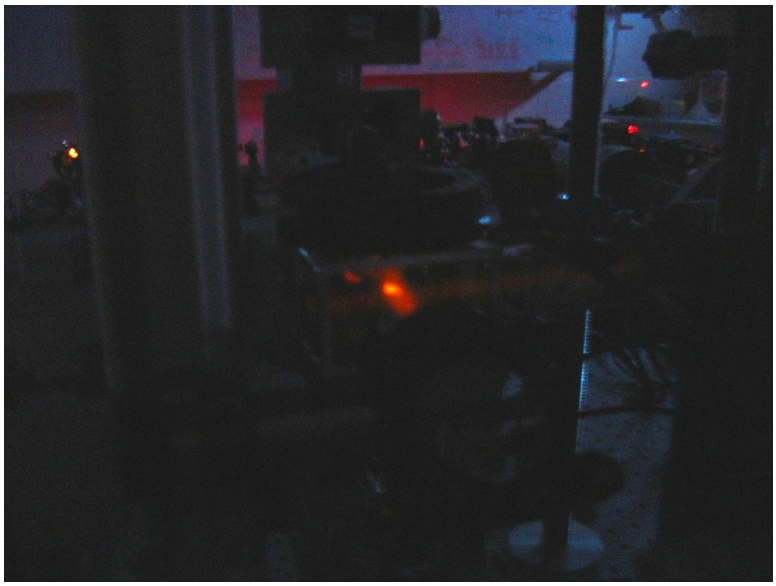

FIG. 2.5 – Le piège magnéto-optique de potassium de l'expérience Li-K.

les aspects de magnétisme itinérant, tel que l'antiferromagnétisme.

En parallèle de cette rénovation de l'expérience lithium, nous avons démarré une nouvelle activité sur les mélanges de fermions. Cette expérience, dont la construction a démarré en septembre 2007 porte sur le mélange potassium-lithium, dont le choix a été guidé par l'existence d'isotopes fermioniques et bosoniques stables pour ces deux atomes, et qui permettra ainsi l'étude de mélanges de gaz quantiques variés. Cette expérience, qui en est encore aux premiers stades de construction (sur la fig. 2.5, une photo du piège magnéto-optique de potassium prise au printemps 2008) permettra d'étudier des situations physiques telle que la superfluidité fermionique en présence de masses différentes, la cristallisation de Wigner de dimères LiK [20] ou encore la localisation d'Anderson d'atomes de lithium évoluant dans un ensemble de diffuseurs aléatoires [21].

Bibliographie

[1] J. Bardeen, L. N. Cooper, and J. R. Schrieffer, Phys. Rev. **108**,1175 (1957).

[2] D. M. Eagles, Phys. Rev. **178**, 668 (1969).

[3] P. Nozières and S. Schmitt-Rink, J. Low Temp. Phys. **59**, 195 (1985).

[4] A. J. Legget, J. Phys. C **41**, 7 (1980).

[5] B. DeMarco, S.B. Papp et D.S. Jin, Phys. Rev. Lett. **86**, 5409 (2001).

[6] F. Schreck, L. Khaykovich, K. L. Corwin, G. Ferrari, T. Bourdel, J. Cubizolles et C. Salomon, Phys. Rev. Lett. **87**, 080403 (2001).

[7] J. Cubizolles, T. Bourdel, S. Kokkelmans, G. Shlyapnikov et C. Salomon, Phys. Rev. Lett. **91**, 240401 (2003).

[8] M. Greiner, C. A. Regal et D. S Jin, Nature (London) **426**, 537 (2003) ; S. Jochim *et al.*, Science **302**, 2101 (2003) ; M.W. Zwierlein *et al.*, Phys. Rev. Lett. **91**, 250401 (2003).

[9] D.S Petrov, C. Salomon, G.V Shlyapnikov, Phys. Rev. Lett. **93**, 090404 (2004).

[10] I. V. Brodsky, M. Yu. Kagan, A. V. Klaptsov, R. Combescot et X. Leyronas, Phys. Rev. A **73**, 032724 (2006).

[11] G. E. Astrakharchik, J. Boronat, J. Casulleras, et S. Giorgini, Phys. Rev. Lett. **93**, 200404 (2004).

[12] N. V. Prokof'ev et B. V. Svistunov, Phys. Rev. B **77**, 125101 (2008).

[13] M. Bartenstein, A. Altmeyer, S. Riedl, S. Jochim, C. Chin, J. H. Denschlag, et R. Grimm, Phys. Rev. Lett., **92** 120401 (2004) ; J. Kinast, A. Turlapov, J. Thomas, Q. Chen, J. Stajic et K. Levin, Science, **307** 1296 (2005) ; G. B. Partridge, W. Li, R. I. Kamar, Y. Liao et R. G. Hulet, Science **311**, 503 (2005) ; J. T. Stewart, J. T. Gaebler, C. A. Regal et D. S. Jin, Phys. Rev. Lett. **97**, 20406 (2006).

[14] A. Altmeyer, S. Riedl, C. Kohstall, M. J. Wright, J. H. Denschlag et R. Grimm, Phys. Rev. Lett. **92**, 203201 (2006).

[15] M.W. Zwierlein, J.R. Abo-Shaeer, A. Schirotzek, C.H. Schunck et W. Ketterle, Nature **435**, 1047 (2005).

[16] C. Chin, M. Bartenstein, A. Altmeyer, S. Riedl, S. Jochim, J. Hecker Denschlag et R. Grimm, Science **305**, 1128 (2004).

[17] Chi-Ho Cheng et S.-K. Yip, Phys. Rev. Lett. **95**, 070404 (2005).

[18] J. P. Gaebler, J. T. Stewart, J. L. Bohn, et D. S. Jin, Phys. Rev. Lett. **98**, 200403 (2007).

[19] M. Jona-Lasinio, L. Pricoupenko et Y. Castin, Phys. Rev. A 77, 043611 (2008).

[20] D. S. Petrov, G. E. Astrakharchik, D. J. Papoular, C. Salomon et G. V. Shlyapnikov Phys. Rev. Lett. **99**, 130407 (2007).

[21] U. Gavish et Y. Castin, Phys. Rev. Lett. **95**, 020401 (2005).

Les gaz de fermions ultra-froids

Les gaz de fermions ultra-froids

Après l'observation en 1995 des premiers condensats de Bose-Einstein gazeux, la physique des atomes ultrafroids s'est tout récemment ouverte à l'étude de gaz de fermions dans le régime quantique. En présence d'interactions attractives, les fermions acquièrent un comportement bosonique qui conduit à l'observation du phénomène de condensation de Bose-Einstein à basse température. La possibilité d'ajuster la force des interactions dans les systèmes d'atomes froids permet d'établir un lien profond entrecondensation de Bose-Einstein et supraconductivité.

Introduction

La mécanique quantique influence les propriétés macroscopiques d'un système à N-corps lorsque les fonctions d'ondes des particules commencent à se recouvrir, c'est-à-dire lorsque la longueur d'onde de de Broglie $\Lambda_{\rm th} = h/\sqrt{2\pi m k_{\rm B} T}$ associée à l'agitation thermique devient de l'ordre de la distance interparticule. Ce régime, dit aussi de dégénérescence quantique, se manifeste pour une densité n du système satisfaisant la condition $n\Lambda_{\rm th}^3 \lesssim 1$. On distingue alors deux cas très différents, suivant que le moment cinétique intrinsèque (ou spin) des particules du gaz est, en unité de $\hbar = h/2\pi$, entier ou demi-entier. Dans le cas des particules de spin entier (les bosons), le passage dans le régime quantique s'accompagne d'une transition de phase vers un état superfluide où toutes les particules s'accumulent dans l'état fondamental (figure 1.a). C'est la *condensation de Bose-Einstein*, conséquence de l'effet d'*amplification bosonique* qui pousse les bosons à tous occuper un même état. Pour les gaz piégés, la Condensation de Bose-Einstein a été observée pour la première fois en 1995 par les équipes de E. Cornell et C. Wieman au JILA et de W. Ketterle au MIT et a constitué un thème d'étude important depuis (voir *Images de la Physique 2000*). Pour des particules de spin demi-entier (des fermions) sans interactions, l'état fondamental du système est déterminé par le principe de Pauli qui interdit à deux particules fermioniques d'occuper le même état quantique (figure 1.b). Il suffit donc de remplir un à un les états d'énergie du piège avec exactement un atome par niveau et par état de spin, et ceci jusqu'à épuisement du nombre d'atomes disponibles. L'on parle alors de mer de Fermi et l'énergie correspondant au dernier état peuplé est baptisée énergie de Fermi, notée $E_{\rm F} = \hbar^2 k_{\rm F}^2/2m$. Dans le cas d'un système homogène, le vecteur d'onde de Fermi $k_{\rm F}$ est inversement proportionnel à la distance moyenne d entre particules, c'est-à-dire $k_{\rm F} \propto n^{1/3}$. Cette dépendance explicite de l'énergie avec la densité traduit simplement le fait que plus le nombre d'atomes piégés est grand, plus l'énergie de Fermi est élevée. Les phénomènes quantiques se manifesteront naturellement si la température de l'échantillon est plus basse que $T_{\rm F} = E_{\rm F}/k_{\rm B}$ mais, à la différence des bosons, le passage du comportement classique au comportement quantique ne s'accompagne d'aucune transition de phase. La manifestation la plus spectaculaire de l'entrée dans le régime quantique est l'existence d'une pression résiduelle à température nulle, dite pression de Fermi : au contraire d'un gaz parfait « classique » pour lequel l'équation des gaz parfaits $p = nk_{\rm B}T$ donne une pression p nulle à température nulle, la pression d'un gaz de fermions est non nulle même à $T = 0$. La pression de Fermi est une simple conséquence du principe d'exclusion qui empêche deux fermions de même spin de se trouver au même endroit et s'oppose donc à toute tentative de compression du gaz.

L'ajout des interactions enrichit le panorama des effets physiques observables dans les fluides quantiques. Ainsi, dans le cas des électrons dans les solides, la présence d'interactions attractives propagée par les phonons provoque à basse température l'apparition d'une phase supraconductrice également présente dans les noyaux atomiques ou les étoiles à neutrons. Bien que les superfluides fermioniques soient au cœur d'une immense variété de systèmes physiques, la compréhension de leur propriété n'est encore que très partielle et constitue l'un des enjeux majeurs de la physique contemporaine.

Article proposé par :

Frédéric Chévy, chevy@lkb.ens.fr
Christophe Salomon, Christophe.Salomon@lkb.ens.fr
Laboratoire Kastler-Brossel, CNRS/ENS
Ont également participé à ce travail T. Bourdel, J. Cubizolles, L. Khaykovich, S. Kokkelmans, F. Schreck et J. Zhang.

Encadré 1

Piégeage d'atomes neutres

Le piège magnéto-optique

L'exploration de la physique des atomes ultra-froids a été rendue possible le développement dans les années 80 des techniques de piégeages et de refroidissement d'atomes par laser, travaux couronnés par le prix Nobel 1997 attribué à S. Chu, C. Cohen-Tannoudji et W. Phillips. Le piège magnéto-optique, qui utilise une combinaison de champs magnétiques et de lasers accordés proche d'une résonance atomique, permet de refroidir des vapeurs d'atomes depuis la température ambiante jusqu'à des températures de l'ordre de la dizaine de microkelvin.

Le principe de ce dispositif a été décrit dans Images de la physique 1990 *et repose sur la pression de radiation exercée par un faisceau lumineux sur un atome. Cette force qui résulte simplement de l'effet de recul subi par un atome lorsqu'il absorbe un photon (figure a) est d'autant plus efficace que la fréquence du faisceau laser est proche de celle d'une transition atomique. Si l'on envoie sur un atome deux faisceaux contre-propageants avec des fréquences légèrement inférieures à la fréquence de résonance atomique (en pratique quelques MHz) la combinaison de la pression de radiation et de l'effet Doppler, qui rapproche de résonance le faisceau se propageant en sens opposé à l'atome, provoque une force totale opposée à la vitesse de l'atome (figure b). Cette force de friction induite par la lumière est équivalente à un refroidissement qui peut être complété par un effet de piégeage en ajoutant un gradient de champ magnétique.*

Ce type de piège ne permet cependant pas d'atteindre des températures arbitrairement basses. En effet, les fluctuations de la force de pression de radiation induite par l'émission spontanée aléatoire de photons provoque un chauffage qui s'oppose au refroidissement Doppler. La température la plus basse accessible par ce procédé est la température de recul, correspondant à l'énergie $\hbar^2k^2/2m$ acquise par un atome de masse m émettant un photon de vecteur d'onde k.

Piégeage magnétique

De manière générale, on montre en mécanique quantique que toute particule possède un moment magnétique $\vec{\mu}$ proportionnel à son spin. De l'existence de ce moment magnétique, il résulte une énergie potentielle d'interaction dipolaire magnétique $E_p = -\vec{\mu} \cdot \vec{B}$ entre un atome et un champ magnétique $\vec{B}$. Si le moment magnétique est de sens opposé au champ magnétique, l'énergie potentielle μB permet de piéger les atomes au voisinage d'un minimum de B[a]*. Une évaporation est possible dans un piège magnétique si l'on ajoute une onde radio-fréquence de fréquence ν_{rf}. Lorsque $h\nu_{rf} = 2\mu B$, le champ radio-fréquence peut basculer le moment magnétique atomique de l'état anti-parallèle jusqu'à l'état parallèle ce qui provoque l'expulsion de l'atome sous l'effet de la force magnétique qui a changé de sens.*

Piégeage dipolaire

Le piège dipolaire consiste à utiliser un faisceau laser très désaccordé afin de limiter au maximum les transitions atomiques vers un état excité et donc l'émission spontanée qui était la principale source de chauffage dans le piège magnéto-optique. Lorsque l'on s'éloigne de résonance, la force de pression de radiation devient de plus en plus faible et laisse place à une force de type dipolaire électrique. On sait en effet qu'un atome possède une polarisabilité électrique α et son énergie d'interaction E_p avec un champ électrique $\vec{E}$ se met sous la forme $E_p = -\alpha E^2/2$. On montre que le signe de α est uniquement déterminé par le désaccord de l'onde lumineuse avec la transition atomique : lorsque la fréquence optique est inférieure à la fréquence de transition atomique, α est positif et négatif sinon. Un faisceau laser focalisé et accordé en dessous de résonance réalise donc un piège pour atomes, puisque dans une telle configuration l'énergie potentielle est minimale au point d'intensité lumineuse maximale, c'est-à-dire au foyer du laser.

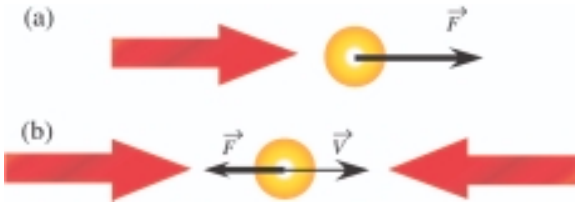

Figure - *Principe du refroidissement Doppler et du piège magnéto-optique. (a) Un faisceau lumineux provoque sur un atome une force de pression de radiation dans la direction de propagation du faisceau et maximale à résonance. (b) Lorsqu'un atome se déplace à une vitesse $\vec{V}$ au sein de deux faisceaux contre-propageants, l'effet Doppler décale la fréquence lumineuse vue par l'atome : le faisceau se propageant dans le même sens que l'atome voit sa fréquence apparente diminuer alors que celui se propageant en sens opposé voit sa fréquence augmenter. Si la fréquence des deux lasers était choisie légèrement inférieure à la fréquence de résonance atomique, on constate que le faisceau contre propageant sera rapproché de résonance, ce qui lui permet d'exercer une force de pression de radiation plus importante et donc un effet de freinage.*

a. On pourrait imaginer un piégeage au voisinage d'un maximum de B en prenant μ et B parallèles. Cependant, les lois de l'électromagnétisme interdisent l'existence d'un tel maximum dans le vide.

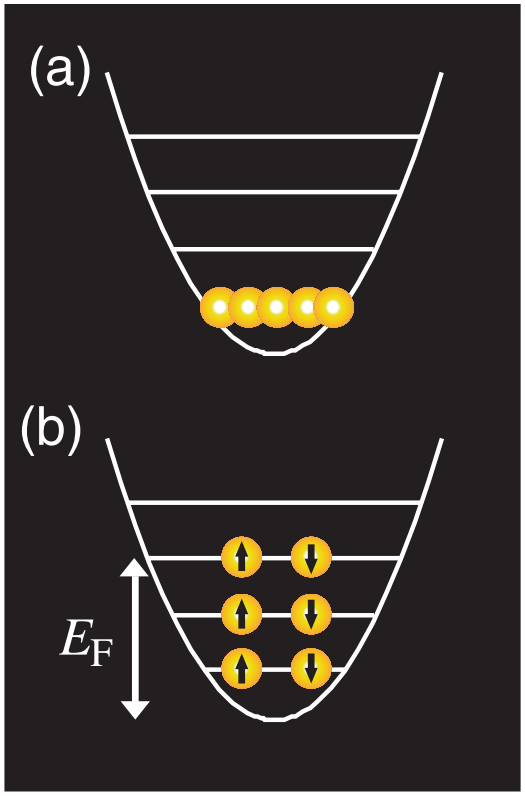

Figure 1 - *Etat fondamental d'un gaz de bosons et de fermions piégés. (a) Condensat de Bose-Einstein où tous les atomes occupent l'état fondamental du piège. (b) Mer de Fermi : pour un gaz de fermions sans interaction, l'état fondamental est obtenu en remplissant un à un les niveaux d'énergies les plus bas jusqu'à une énergie maximum, dite énergie de Fermi. Dans le cas de particules de spin 1/2, chaque état peut contenir deux particules correspondant aux états « spin en haut » et « spin en bas ».*

Refroidissement par évaporation et refroidissement sympathique

A température ambiante, le paramètre de dégénérescence $n\Lambda_{th}^3$ d'une vapeur est de l'ordre de quelques 10^{-18}. Les techniques de refroidissement par laser (encadré 1) développées au cours des années 80 permettent de parcourir la plus grande partie du chemin séparant du régime de dégénérescence quantique, jusqu'à des densités dans l'espace des phases typiques de l'ordre de 10^{-6}. Pour parcourir les six ordres de grandeurs nous séparant de la dégénérescence quantique, la seule méthode connue à ce jour est le refroidissement par évaporation forcée dont le principe a été décrit dans *Image de la physique 2000*. Pour résumer, il s'agit de confiner les atomes dans un piège tronqué à une énergie de coupure E_c, ce qui permet d'éliminer les atomes les plus énergétiques du gaz. Si après une collision entre deux atomes l'un des partenaires acquiert une énergie supérieure E_c, celui-ci est évacué hors du piège. Ceci diminue l'énergie moyenne des atomes restant piégés et provoque le refroidissement du gaz. Cependant, plus la température du gaz est basse, plus la probabilité d'obtenir un atome d'énergie E_c après un choc diminue, ce qui provoque un ralentissement notable du refroidissement dès que la température devient égale à une fraction de l'énergie de coupure. Afin de maintenir le rythme de l'évaporation, on force l'évaporation en abaissant progressivement E_c de façon à garder le rapport E_c/k_BT constant (typiquement entre 5 et 10).

Historiquement, le refroidissement par évaporation a été développé pour des bosons piégés magnétiquement en les polarisant de façon à garder leur moment magnétique de sens opposé à la direction du champ magnétique (encadré 1). Cette particularité, additionnée au rôle central joué par les collisions dans le processus d'évaporation, empêche d'utiliser cette technique pour le refroidissement d'atomes fermioniques de spin 1/2. En effet, d'après la proportionnalité existant entre spin et moment magnétique, des atomes de même moment magnétique sont aussi dans un même état de spin. Le principe de Pauli, qui interdit à deux fermions de se trouver dans le même état quantique, empêche deux atomes de cette famille de se trouver proche l'un de l'autre, ce qui provoque une forte diminution du taux de collisions par rapport à ce que l'on obtiendrait avec un gaz de bosons. Afin de pouvoir obtenir un gaz de fermions dégénérés, nous avons adapté la technique de refroidissement par évaporation en développant une méthode de refroidissement appelée *refroidissement sympathique*, qui consiste à piéger magnétiquement un mélange de bosons et de fermions polarisés. On évapore comme précédemment les bosons qui servent alors de réfrigérant aux fermions.

Gaz de Fermi dégénéré

Les expériences réalisées à l'ENS utilisent des atomes de lithium pour lequel il existe à la fois un isotope fermionique (^{6}Li) et bosonique (^{7}Li) stables. La première partie de notre séquence expérimentale consiste à utiliser un piège magnéto-optique afin de refroidir jusqu'à 1 mK une vapeur de lithium issue d'un four à 550 °C et contenant les deux isotopes. Le mélange de quelques 10^6 atomes de ^{6}Li et 10^9 atomes de ^{7}Li est ensuite transféré dans un piège magnétique où nous débutons le refroidissement en évaporant le ^{7}Li. Le bon déroulement de la séquence est surveillé en mesurant le nombre d'atomes et la température par *temps de vol*. Cette technique consiste à éteindre brusquement le potentiel de piégeage pour ensuite laisser le nuage s'étendre balistiquement pendant environ 1 ms. A l'issue de cette phase d'expansion, nous mesurons l'absorption d'un faisceau résonnant avec une transition atomique, ce qui nous permet d'obtenir simplement le profil de densité atomique. Dans le cas d'atomes en interactions faibles, la densité atomique mesurée après temps de vol est une image de la distribution de vitesse dans le piège. En effet, un atome détecté à une distance d du centre du piège après un temps de vol τ devait posséder une vitesse $v = d/\tau$ au moment de l'extinction du potentiel de confinement. Cette propriété nous permet d'utiliser le temps de vol comme thermomètre, puisque

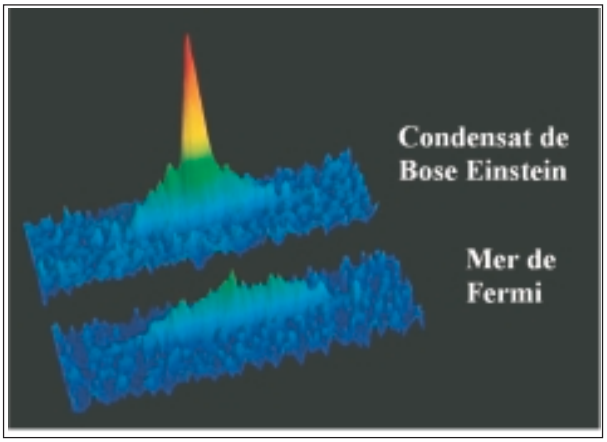

Figure 2 - *Images d'un condensat de Bose-Einstein d'atomes de ^{7}Li, immergé dans une mer de Fermi d'atomes de ^{6}Li confinés dans un piège magnétique. Le condensat (pic central étroit) comporte 1×10^4 atomes et le piédestal large correspond aux atomes non condensés. L'extension axiale plus importante du nuage de fermions (2.5×10^4 atomes) reflète la pression de Fermi s'opposant au potentiel de confinement.*

la largeur du nuage est directement reliée à la température (on sait par exemple que pour un gaz parfait classique, $\langle v^2 \rangle = 3k_B T/m$)[1].

Après quelques dizaines de secondes d'évaporation, nous atteignons le régime de dégénérescence quantique pour les deux isotopes. Les profils de densité des gaz de ^{6}Li et de ^{7}Li obtenus par absorption dans le piège sont représentés sur la figure 2. La flagrante différence de taille entre les deux nuages est une conséquence directe de la différence de statistiques quantiques des deux isotopes. Dans le cas du condensat de Bose-Einstein de ^{7}Li les atomes se trouvent condensés au centre du piège et forment un pic de densité très étroit superposé à une distribution plus large correspondant aux atomes non condensés. Dans le cas des fermions, l'élargissement de la distribution de position des atomes est une simple conséquence de la pression de Fermi qui s'oppose à la compression imposée par le potentiel de confinement. Pour ces conditions expérimentales, la température $T = 1,6\,\mu$K correspond à $T = 0,87 T_C = 0,57 T_F$ (T_C désigne ici la température de condensation de Bose-Einstein), ce qui nous place près du seuil d'apparition des effets quantiques. Lorsque l'évaporation est poursuivie plus avant, les meilleurs degrés de dégénérescence obtenus correspondent à $T \lesssim 0,2\,T_F$.

L'état fondamental d'un gaz de Fermi en interaction

Si l'on considère le cas de fermions en interactions attractives (ce qui est toujours le cas pour des atomes dont les interactions à longue distance sont de type Van der Waals), on sait que pour un potentiel suffisamment profond, il existe un état lié correspondant à un dimère de deux atomes. Lorsque la température est plus basse qu'un certaine valeur T_c^* de l'ordre de l'énergie de liaison de ces molécules, on s'attend donc à observer un appariement des atomes. Or, dans le cas d'une expérience sur des fermions de spin demi-entier, leur association fournit un composé de spin entier, donc un boson. A suffisamment basse température, on atteint la température de T_c de condensation de Bose-Einstein et il apparaît une phase superfluide.

Si l'on diminue suffisamment la force des interactions attractives, le potentiel d'interaction devient si peu profond qu'il ne contient plus aucun état lié (dans le cas d'un potentiel de profondeur V_0 et de rayon R, ceci se produit lorsque $V_0 \lesssim \hbar^2/mR^2$) : puisque les molécules n'existent plus au delà de ce ce seuil, la condensation de Bose-Einstein n'est bien entendue plus possible et on s'attend donc naïvement à la disparition de la superfluidité. Cette affirmation est cependant fausse, comme le prouve la supraconductivité des métaux à basse température. La théorie BCS (pour Bardeen-Cooper et Schrieffer) montre que l'état supraconducteur d'un système de fermions en interactions faiblement attractives résulte lui aussi d'un appariement de particules. Ces « paires de Cooper » sont cependant radicalement différentes des molécules discutées précédemment puisque l'appariement ne résulte pas simplement de l'interaction des deux particules constitutives de la paire, mais implique la mer de Fermi dans son ensemble. Ce caractère collectif se manifeste de deux façons : tout d'abord, contrairement aux dimères « classiques » qui correspondent à deux particules physiquement proches l'une de l'autre, les paires de Cooper sont associées à un appariement dans l'espace des impulsions et si l'une des particules de la paire possède une quantité de mouvement $\overrightarrow{p}$, l'autre partenaire possède automatiquement une quantité de mouvement $-\overrightarrow{p}$. Ensuite, l'énergie de liaison de la paire, Δ dépend explicitement de la densité de particules. En effet, si l'on introduit la longueur de diffusion a caractérisant les interactions interparticules à basse énergie (encadré 2), on montre que la limite de faible interaction correspond à $a \to 0^-$ et que l'on a $\Delta \propto E_F \exp(-1/k_F|a|)$, qui dépend de la densité *via* E_F et k_F. Une des conséquence fondamentale de cette origine collective est que, contrairement aux molécules discutées plus haut qui préexistaient à l'apparition de la superfluidité, l'ordre quantique naît à la même température $T_c = T_c^* \sim \Delta/k_B$ que les paires de Cooper.

L'état fondamental d'un gaz de fermions en interaction attractive étant qualitativement très différent dans les régimes de fortes et faibles attractions, on est naturellement amené à s'interroger sur la nature de la transition entre ces deux régimes et sur la transformation des paires de Cooper en molécules. C'est le problème dit de la transition CBE-BCS dont les premières études théoriques, ont été réalisées par T. Leggett, P. Nozières et S. Schmitt-Rink. Dans leurs

1. Notons que cette technique est destructive puisque l'absorption d'un faisceau résonnant crée un chauffage tel que le gaz ne survit pas à la prise d'image. Elle oblige donc à recréer un gaz d'atomes froids à la prise de chaque point expérimental.

Encadré 2

Notion de longueur de diffusion

Tout comme en physique classique, l'étude d'une collision entre deux particules quantiques de masse m peut être remplacée par celle de la diffusion d'une particule fictive de masse réduite $\mu = m/2$ évoluant dans un potentiel statique. De manière analogue à la diffusion de la lumière par un atome, la fonction d'onde ψ décrivant la diffusion de la particule fictive est la somme d'une onde plane incidente et d'une onde diffusée. A longue distance du point de collision, l'onde diffusée est une onde sphérique, de sorte que l'on peut écrire pour une particule fictive de quantité de mouvement $\overrightarrow{p} = \hbar\overrightarrow{k}$ avant le choc

$$\psi(\overrightarrow{r}) = e^{i\overrightarrow{k}\cdot\overrightarrow{r}} + \frac{f(\overrightarrow{k})}{r}e^{ikr},$$

où r et $\overrightarrow{k} = k\overrightarrow{r}/r$ désignent respectivement la distance au point d'impact et la direction dans laquelle la particule est diffusée. Dans le cas d'une collision élastique où l'énergie cinétique totale des deux particules est conservée les modules des vecteurs d'ondes sont identiques pour l'onde incidente et l'onde diffusée.

L'amplitude de diffusion f est homogène à une longueur et caractérise complètement les propriétés de diffusion. D'après l'interprétation probabiliste de la fonction d'onde, $|f(\overrightarrow{k})|^2$ est proportionnel à la probabilité d'être diffusé dans la direction $\overrightarrow{k'}$. Bien souvent dans les expériences d'atomes froids, la température des atomes, et donc leur énergie cinétique $\hbar^2k^2/2m$ est tellement basse que l'on peut remplacer $f(\overrightarrow{k'})$ par sa valeur en $k = 0$. On pose alors conventionnellement $f(0) = -a$, où a est appelé longueur de diffusion. *a peut être aussi bien positif que négatif et physiquement sa valeur absolue représente la « taille » effective de l'atome puisqu'en intégrant $|f|^2$ sur toutes les directions de l'espace, on trouve que la section efficace de diffusion élastique à basse énergie vaut simplement $4\pi a^2$.*

Il est notable que, dans la limite de basse énergie, l'amplitude de diffusion ne soit caractérisée que par cette seule longueur de diffusion. En particulier, si l'on considère deux systèmes de particules interagissant par des potentiels différents mais possédant la même longueur de diffusion, on s'attend à ce que la physique à basse température soit la même pour les deux systèmes. Dans la description des nuages d'atomes ultra froids, ceci permet de remplacer le potentiel d'interaction interatomique réel (de type Lennard Jones comprenant une partie attractive à longue portée et une partie répulsive à courte portée) par un potentiel plus simple et de même longueur de diffusion sans que les prédictions théoriques ne soient modifiées.

travaux, ceux-ci ont montré que cette transition se faisait probablement sans accident ni transition de phase, mais jusqu'à l'observation des premières résonances de Feshbach dans les atomes ultra-froids, aucun système physique ne permettait d'explorer expérimentalement l'intégralité du diagramme de phase décrivant un gaz de fermions en interactions.

La résonance de Feshbach décrite dans l'encart 3 correspond à un déplacement d'un état lié diatomique d'énergie ΔE à l'aide d'un champ magnétique (figure 3). Dans la région $\Delta E < 0$, a est positif et la résonance de Feshbach est associée à un état moléculaire stable. Ce régime correspond au gaz de fermions en interaction forte dans lequel l'état fondamental est décrit par un condensat de Bose-Einstein de molécules. La région $\Delta E > 0$ correspond quant à elle à une longueur de diffusion négative et l'état fondamental dans ce domaine de paramètre est bien décrit par un état de type BCS. Pour finir, la transition CBE-BCS se situe autour de la résonance de Feshbach $\Delta E = 0$ pour laquelle a diverge. La largeur de cette région de transition peut être obtenue par un argument simple. En effet, on sait que, près de la résonance à $\Delta E < 0$, la taille des molécules est de l'ordre de la longueur de diffusion a. Le gaz de particule ne peut être décrit par un gaz de molécules ponctuelles uniquement si la taille des molécules reste très petite devant la distance interparticules d. Puisque la densité n de particules est de l'ordre de $1/d^3$, cette condition est vérifiée si le produit na^3 reste petit devant 1. Au contraire, lorsque na^3 devient grand, les molécules sont si étendues qu'elles se recouvrent les unes les autres et leurs constituants internes fermioniques commencent à se manifester. On parle dans ce cas d'un régime de *fermions fortement corrélés*, ou régime *unitaire*, dans lequel il n'est plus possible d'isoler un constituant élémentaire du gaz (molécule ou atome) réellement pertinent.

Bien que le régime unitaire soit théoriquement très difficile d'accès du fait des fortes corrélations entre particules, on montre que dans le régime où $n|a|^3 \gg 1$ l'énergie de Fermi est la seule énergie pertinente du problème. Dans ces conditions, le potentiel chimique du gaz peut s'écrire

$$\mu = (1+\beta)E_F,$$

où le nombre β est universel et ne dépend pas de la nature exacte du système fermionique étudié (quarks, neutrons, atomes froids…). Son évaluation par des moyens théoriques ou expérimentaux est donc d'une importance capitale pour la compréhension des systèmes de fermions en interactions fortes. De récents calculs Monte Carlo réalisés dans le groupe de V. R. Pandharipande ont montré que $\beta \sim -0.56$, résultat qui restait à être confirmé expérimentalement.

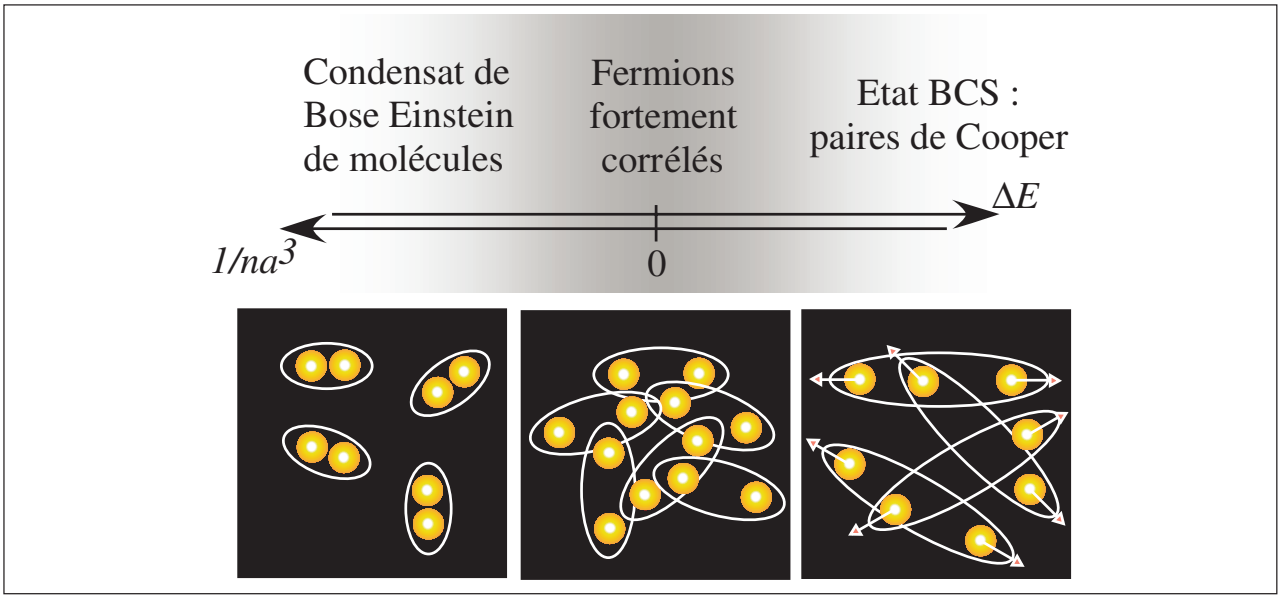

Figure 3 - *Diagramme de phase de l'état fondamental d'un gaz de fermions au voisinage d'une résonance de Feshbach en fonction de l'écart ΔE entre l'énergie de l'état entrant de collision et l'état moléculaire. De gauche à droite : pour $\Delta E < 0$, il existe un état moléculaire stable dans lequel les atomes s'apparient dès que $k_B T \lesssim |\Delta E|$. Composés de deux fermions, les dimères ainsi formés sont des bosons. Lorsqu'on poursuit le refroidissement, les molécules subissent une condensation de Bose-Einstein amenant le gaz dans un état superfluide. Pour $\Delta E > 0$, l'état lié à deux corps disparaît. Un appariement est néanmoins possible à très basse température sous la forme de paires dans l'espace des impulsions mettant en jeu la mer de Fermi dans son ensemble. Entre ces deux régimes, la région $\Delta E \sim 0$ et $n|a|^3 \gtrsim 1$ correspond à une situation de fermions fortement corrélés dans laquelle les paires se chevauchent et la notion de molécule ou d'atomes individuels perd sa pertinence.*

Etude expérimentale de la transition CBE-BCS

Les atomes de ^{6}Li piégés magnétiquement sont polarisés et ne peuvent donc interagir entre eux. Pour pouvoir espérer sonder la transition CBE-BCS, il est donc nécessaire de travailler avec un mélange de plusieurs états de spin. Après la phase de refroidissement sympathique décrite dans la première partie, et nous permettant d'atteindre le régime de dégénérescence quantique, nous transférons les atomes dans un piège dipolaire réalisé par l'intersection de deux faisceaux lasers. A l'aide d'une impulsion radio-fréquence, nous plaçons ensuite les atomes dans une superposition des états de spin haut et de spin bas de façon à permettre l'apparition d'interactions entre fermions de spins opposés. En diminuant la puissance du laser de piégeage, on évapore les atomes les plus chauds et la température du nuage s'abaisse.

La résonance de Feshbach que nous utilisons est située à un champ $B_F = 834$ G (encadré 3) et la région de stabilité des molécules est caractérisée par les champs magnétiques inférieurs à B_F. Si l'on se place dans cette région, on commence à former des molécules lorsque la température devient de l'ordre de T_c^*.

Si l'on forme un nuage quasi-pur de dimères et que l'on diminue encore la température, on atteint le régime de condensation de Bose-Einstein de molécules. Le condensat est détecté par temps de vol : on coupe brusquement le piège et on laisse le nuage de molécules s'étendre. A la fin de l'expansion, nous augmentons le champ magnétique de façon à franchir la résonance de Feshbach et à rompre les liaisons entre atomes, ainsi qu'on l'a vu précédemment. Ce procédé nous permet d'observer directement le profil densité de molécules représenté sur la figure 4.a et de le comparer à un condensat de ^{7}Li obtenu dans le même piège 4.b.

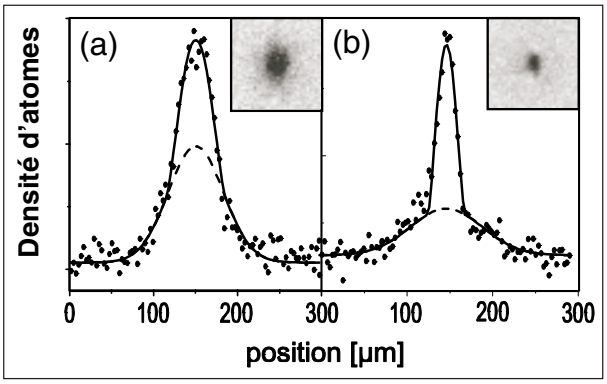

Figure 4 - *(a) Condensat de Bose-Einstein de molécules $^6Li_2$. (b) Condensat de Bose-Einstein de ^{7}Li. Les deux profils présentent une double structure somme d'une fraction condensée et non condensée (ligne tiretée). En insert les profils bidimensionnels elliptiques sont caractéristiques d'une expansion superfluide. La différence de largeur est essentiellement due à l'écart de longueur de diffusion dans les deux systèmes.*

Encadré 3

Résonance de Feshbach et états moléculaires

Un atout majeur des atomes ultra-froids provient de la possibilité de manipuler les interactions interatomiques (et donc la longueur de diffusion) à l'aide d'un simple champ magnétique, en mettant à profit le phénomène dit de résonance de Feshbach. *Pour comprendre cette résonance, il est nécessaire de prendre en compte la structure interne des atomes, c'est-à-dire la possibilité qu'un des atomes passe dans un état excité durant la collision. Considérons la diffusion de deux atomes initialement dans leur état fondamental $|f\rangle$. Cette diffusion est décrite par un potentiel d'interaction V_f du type de celui représenté sur la figure. Si lors de la collision un des atomes peut passer dans un état excité $|e\rangle$, les deux atomes n'interagissent plus par le potentiel V_f défini ci-dessus, mais par un potentiel V_e décalé en énergie. Lors des collisions à faible énergie que l'on rencontre en physique des atomes ultra-froids, l'énergie cinétique des atomes est insuffisante pour faire passer les atomes de l'état $|f\rangle$ à l'état $|e\rangle$. Cependant, il peut se produire qu'un état lié du puits de potentiel V_e devienne quasi-résonnant avec l'énergie des atomes incidents. Dans ce cas, les atomes peuvent d'après les inégalités de Heisenberg passer un temps $\tau \sim \hbar/\Delta E$ dans cet état. Lorsqu'ils se trouvent dans l'état lié, les atomes sont localisés plus près l'un de l'autre ce qui augmente considérablement leur interaction. La théorie de la diffusion quantique montre que proche de la condition de résonance $\Delta E = 0$, la longueur de diffusion est donnée par $a \propto -1/\Delta E$ et diverge donc en changeant de signe lorsque ΔE s'annule : c'est la résonance de Feshbach.*

En pratique, la position relative des états $|f\rangle$ et $|e\rangle$ est modifiée par l'ajout d'un champ magnétique externe. En effet, dans le cas du lithium et d'autres atomes tels que le potassium, les moments magnétiques de l'état fondamental et de l'état excité sont différents ce qui permet de décaler magnétiquement les courbes V_e et V_f l'une par rapport à l'autre. Dans le cas de l'isotope fermionique ^6Li du lithium, la variation de la longueur de diffusion est représentée sur la figure et nous utilisons dans nos expériences la résonance de Feshbach localisée au voisinage de 0,083 T.

Une des propriétés frappantes de la résonance de Feshbach est l'existence, pour $\Delta E < 0$, d'un état lié du potentiel V_e énergétiquement plus stable *que des atomes libres dans l'état $|f\rangle$. En comparaison des molécules usuelles, ces dimères obtenus près d'une résonance de Feshbach ont une très grande extension spatiale et une très faible énergie. En effet, comme nous l'avons vu plus haut, la longueur de diffusion a caractérise complètement la physique de basse énergie. Au voisinage de la résonance de Feshbach où l'énergie de liaison ΔE est très faible, une analyse dimensionnelle simple nous indique que la taille de l'état moléculaire est de l'ordre de a et son énergie de liaison vaut $\Delta E \sim -\hbar^2/ma^2$. Pour une longueur de diffusion typique de 100 nm, ceci correspond à une énergie de 10^{-10} eV, à comparer aux énergies de liaisons chimiques habituelles de l'ordre d'une fraction d'électron volt.*

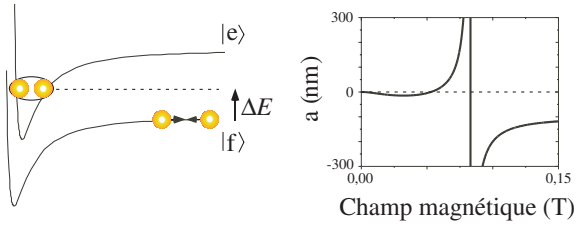

Figure - *A gauche : principe de la résonance de Feshbach. On déplace un état lié de l'état $|e\rangle$ à l'aide d'un champ magnétique. Lorsque l'énergie ΔE de cet état devient résonnante avec celle des atomes incidents, la longueur de diffusion diverge. A droite : longueur de diffusion entre deux atomes de ^6Li de spins opposés en fonction du champ magnétique. La résonance de Feshbach est localisée au voisinage de 0.0834 T.*

Au-delà de la différence de largeur due à la différence de longueur de diffusion des deux systèmes, les profils partagent deux caractéristiques prouvant l'observation de la condensation de Bose-Einstein des molécules : la double structure, somme des parties condensées et non condensées, et le profil elliptique signalant une expansion superfluide.

Pour explorer le régime fortement corrélé CBE-BCS, nous partons d'un condensat de molécules obtenu à un champ de 700 G. On augmente alors le champ magnétique jusqu'à une valeur B pour laquelle on image le nuage.

En mesurant le rayon du nuage après temps de vol, nous avons accès à une quantité baptisée « énergie relâchée ». En effet, lorsque l'on ouvre le piège, le nuage explose et une partie de l'énergie d'interaction entre particules est transformée en énergie cinétique. Ce transfert est très rapide et on estime qu'au bout d'une fraction de milliseconde, toute l'énergie est convertie sous forme cinétique. Plus l'énergie relâchée dans ces premiers instants sera grande, plus le nuage explosera vite. Après un temps de vol donné, on s'attend donc à ce que le nuage soit d'autant plus étendu que l'énergie sera grande.

Le graphe de l'énergie relâchée en fonction du champ magnétique est représentée sur la figure 5. On constate que, de même que pour les profils de densité, aucun accident ne semble marquer le passage à la résonance. On peut comparer ce graphe aux théories limites du condensat de molécules (ligne pleine) et du gaz de Fermi en interaction faible (ligne tiretée) pour lesquelles ont trouve un accord relativement bon. Dans le régime de condensation de molécules, la mesure de l'énergie relâchée nous donne accès à la longueur de diffusion a_{mm} associée aux collisions entre molécules. Expérimentalement, on trouve $a_{mm} \sim 0{,}6a$, ainsi que le prédisent les calculs réalisés par D. Petrov et G. Shlyapnikov.

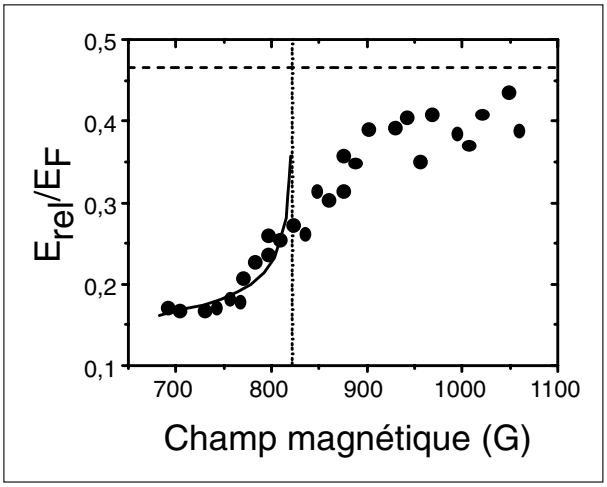

Figure 5 - *Energie relâchée dans la région de la transition CBE-BCS. Dans le domaine de condensation de molécules, les données expérimentales coïncident avec les prédictions de la théorie de la condensation de Bose-Einstein (ligne pleine). A grand champ, on approche le comportement d'un gaz de Fermi sans interaction (ligne tiretée). A la résonance (ligne pointillée) la valeur de E_{rel} donne accès au paramètre β caractérisant le comportement unitaire.*

A résonance, on peut montrer que si l'on suppose que les paires sont toutes brisées par l'ouverture du piège, l'énergie relâchée est donnée par $E_{rel} = \sqrt{1+\beta}E^0_{rel}$, où E^0_{rel} est l'énergie relâchée par un gaz de Fermi sans interaction et β est le paramètre sans dimension caractérisant le régime unitaire (cf. encadré 2). Nos données expérimentales nous donnent $\beta \sim -0.68 \pm 0.13$ ce qui est relativement proche de la valeur $\beta \sim -0.56$ prédite théoriquement.

Perpectives

Les résultats que nous avons présentés ici ne constituent qu'une facette des études effectuées ces derniers mois sur ces gaz de Fermi en interaction et d'autres données importantes ont été prises en Europe et aux USA. Les équipes de R. Grimm à l'université d'Innsbruck et de J. Thomas à Duke ont étudié les modes d'excitation des condensats de fermions dans la zone de transition CBE-BCS. Plus récemment, le groupe d'Innsbruck a réalisé l'observation de paires liées dans la région $a < 0$. Ces observations sont complétées par les résultats des équipes de D. Jin à JILA et W. Ketterle à MIT qui ont montré que la distributions de vitesse de ces paires étaient très piquées autour de $k = 0$, indiquant la présence d'un condensat de paires de fermions.

De l'ensemble de ces études il ressort aujourd'hui qu'une phase superfluide existe très probablement au voisinage de la résonance de Feshbach. L'étude de la région BCS achèverait de clore l'exploration du diagramme de phase proposé par T. Leggett, P. Nozières et S. Schmitt-Rink. L'étude de la superfluidité dans cette région se heurte cependant au fait que les paires de Cooper sont localisées sur une bande de largeur Δ autour de la surface de Fermi. Loin de la résonance, Δ tend vers 0 et le nombre de paires diminue. Le condensat BCS ressemble donc beaucoup à une mer de Fermi pour ce qui est de ses propriétés de volume, telles que l'énergie relâchée. Pour étudier directement la superfluidité du système, les propositions théoriques ne manquent pas. On peut songer à mettre en rotation le gaz de Fermi, une méthode qui s'est avérée très fructueuse pour produire des tourbillons quantifiés dans les condensats de bosons ou encore à étudier par des méthodes d'interférence l'ordre à longue portée existant dans l'échantillon.

Au-delà de ces études sur la superfluidité, les gaz de Fermi ouvrent un nouveau point de vue sur certains phénomènes observés en matière condensée. On peut ainsi citer l'étude des mélanges bosons-fermions dont on a vu un exemple avec le condensat de ^{7}Li immergé dans la mer de Fermi de ^{6}Li, qui est l'analogue microscopique des mélanges ^{3}He/ ^{4}He utilisés par exemple en cryogénie dans les réfrigérateurs à dilution. Une autre possibilité serait de placer ces fermions dans des réseaux optiques, des potentiels périodiques obtenus par piégeage dipolaire dans une figure d'interférence lumineuse. Cette configuration permettrait par exemple d'étudier les mécanismes de transition métal-isolant induite par le désordre ou les interactions dont certains aspects sont encore mal compris dans les systèmes bidimensionnels.

Pour en savoir plus

Aspect (A.), Salomon (C.), « Atomes refroidis par laser, vers le microKelvin », *Images de la Physique*, p. 74, (1990).

Courtois (J.Y.), Grynberg (G.), « Cristallisation d'atomes dans un réseau de lumière », *Images de la physique*, p. 88, (1994).

Dalibard (J.), « Les condensats de Bose-Einstein en phase gaseuse », *Images de la physique*, p. 22, (2000).

Bourdel (T.), Khaykovich (L.), Cubizolles (J.), Zhang (J.), Chevy (F.), Teichmann (M.), Tarruell (L.), Kokkelmans (S.), Salomon (C.), « Experimental Study of the BEC-BCS Crossover Region in Lithium 6 », Phys. Rev. Lett., 93, p. 050401, (2004).

Experimental Study of the BEC-BCS Crossover Region in Lithium 6

Experimental Study of the BEC-BCS Crossover Region in Lithium 6

T. Bourdel, L. Khaykovich, J. Cubizolles, J. Zhang, F. Chevy, M. Teichmann, L. Tarruell, S. J. J. M. F. Kokkelmans, and C. Salomon

Laboratoire Kastler-Brossel, ENS, 24 rue Lhomond, 75005 Paris

(Received 2 March 2004; revised manuscript received 14 April 2004; published 27 July 2004)

We report Bose-Einstein condensation of weakly bound $^6Li_2$ molecules in a crossed optical trap near a Feshbach resonance. We measure a molecule-molecule scattering length of 170^{+100}_{-60} nm at 770 G, in good agreement with theory. We study the 2D expansion of the cloud and show deviation from hydrodynamic behavior in the BEC-BCS crossover region.

DOI: 10.1103/PhysRevLett.93.050401 PACS numbers: 03.75.Ss, 05.30.Fk, 32.80.Pj, 34.50.–s

By applying a magnetic field to a gas of ultracold atoms, it is possible to tune the strength and the sign of the effective interaction between particles. This phenomenon, known as Feshbach resonance, offers in the case of fermions the unique possibility to study the crossover between situations governed by Bose-Einstein and Fermi-Dirac statistics. Indeed, when the scattering length a characterizing the 2-body interaction at low temperature is positive, the atoms are known to pair in a bound molecular state. When the temperature is low enough, these bosonic dimers can form a Bose-Einstein condensate (BEC) as observed very recently in ^{40}K [1] and ^{6}Li [2,3]. On the side of the resonance where a is negative, one expects the well-known Bardeen-Cooper-Schrieffer (BCS) model for superconductivity to be valid. However, this simple picture of a BEC phase on one side of the resonance and a BCS phase on the other is valid only for small atom density n. When $n|a|^3 \gtrsim 1$ the system enters a strongly interacting regime that represents a challenge for many-body theories [4–6] and that now begins to be accessible to experiments [7–9].

In this Letter, we report on Bose-Einstein condensation of ^{6}Li dimers in a crossed optical dipole trap and a study of the BEC-BCS crossover region. Unlike all previous observations of molecular BEC made in single beam dipole traps with very elongated geometries, our condensates are formed in nearly isotropic traps. Analyzing free expansions of pure condensates with up to 4×10^4 molecules, we measure the molecule-molecule scattering length $a_m = 170^{+100}_{-60}$ nm at a magnetic field of 770 G. This measurement is in good agreement with the value deduced from the resonance position [9] and the relation $a_m = 0.6\,a$ of Ref. [10]. Combined with tight confinement, these large scattering lengths lead to a regime of strong interactions where the chemical potential μ is on the order of $k_B T_C$ where $T_C \simeq 1.5\,\mu$K is the condensation temperature. As a consequence, we find an important modification of the thermal cloud time of flight expansion induced by the large condensate mean field. Moreover, the gas parameter $n_m a_m^3$ is no longer small but on the order of 0.3. In this regime, the validity of mean field theory becomes questionable [11–13]. We show, in particular, that the anisotropy and gas energy released during expansion varies monotonically across the Feshbach resonance.

Our experimental setup has been described previously [14,15]. A gas of ^{6}Li atoms is prepared in the absolute ground state $|1/2, 1/2\rangle$ in a Nd-doped yttrium aluminum garnet crossed beam optical dipole trap. The horizontal beam (respectively vertical) propagates along x (y), has a maximum power of $P_o^h = 2$ W ($P_o^v = 3.3$ W) and a waist of $\sim 25\,\mu$m ($\sim 40\,\mu$m). At full power, the ^{6}Li trap oscillation frequencies are $\omega_x/2\pi = 2.4(2)$, $\omega_y/2\pi = 5.0(3)$, and $\omega_z/2\pi = 5.5(4)$ kHz, as measured by parametric excitation, and the trap depth is $\sim 80\,\mu$K. After sweeping the magnetic field B from 5 to 1060 G, we drive the Zeeman transition between $|1/2, 1/2\rangle$ and $|1/2, -1/2\rangle$ with a 76 MHz rf field to prepare a balanced mixture of the two states. As measured very recently [9], the Feshbach resonance between these two states is peaked at 822(3) G, and for $B = 1060$ G, $a = -167$ nm. After 100 ms the coherence between the two states is lost and plain evaporation provides $N_\uparrow = N_\downarrow = N_{tot}/2 = 1.5 \times 10^5$ atoms at $10\,\mu\text{K} = 0.8 T_F$, where $k_B T_F = \hbar^2 k_F^2/2m = \hbar(3N_{tot}\omega_x\omega_y\omega_z)^{1/3} = \hbar\bar{\omega}(3N_{tot})^{1/3}$ is the Fermi energy. Lowering the intensity of the trapping laser to $0.1\,P_0$, the Fermi gas is evaporatively cooled to temperatures T at or below $0.2\,T_F$ and $N_{tot} \approx 7 \times 10^4$.

Then, sweeping the magnetic field to 770 G in 200 ms, the Feshbach resonance is slowly crossed. In this process atoms are reversibly transformed into cold molecules [14,16] near the BEC critical temperature as presented in Fig. 1(a). The onset of condensation is revealed by bimodal and anisotropic momentum distributions in time of flight expansions of the molecular gas. These images are recorded as follows. At a fixed magnetic field, the optical trap is first switched off. The cloud expands typically for 1 ms and then the magnetic field is increased by 100 G in 50 μs. This converts the molecules back into free atoms above resonance without releasing their binding energy [3]. Switching the field abruptly off in 10 μs, we detect free ^{6}Li atoms by light absorption near the D2 line. Using this method, expansion images are not altered by the adiabatic following of the molecular state to a

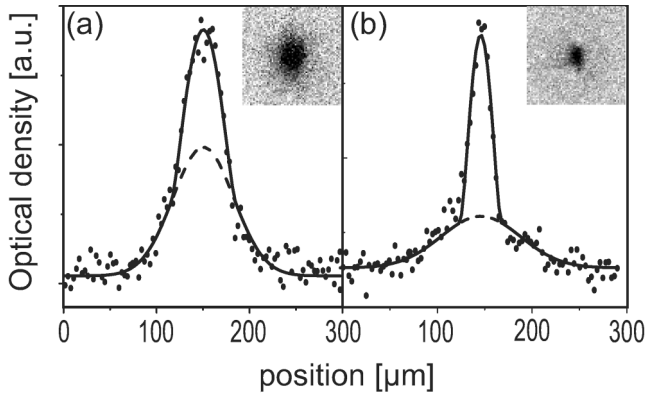

FIG. 1. Onset of Bose-Einstein condensation in a cloud of 2×10^4 ^{6}Li dimers at 770 G (a) and of 2×10^4 ^{7}Li atoms at 610 G (b) in the same optical trap. (a) 1.2 ms expansion profiles along the weak direction x of confinement. (b) 1.4 ms expansion. The different sizes of the condensates reflect the large difference in scattering length $a_m = 170$ nm for ^{6}Li dimers and $a_7 = 0.55$ nm for ^{7}Li. Solid line: Gaussian+Thomas-Fermi fit. Dashed line: Gaussian component. Condensate fractions are both 28%. $\omega_x/2\pi = 0.59(4)$ kHz, $\omega_y/2\pi = 1.6(1)$ kHz, and $\omega_z/2\pi = 1.7(1)$ kHz in (a). $\omega_x/2\pi = 0.55(4)$ kHz, $\omega_y/2\pi = 1.5(1)$ kHz, and $\omega_z/2\pi = 1.6(1)$ kHz in (b).

deeper bound state during switch-off as observed in our previous work [14]. Furthermore, we check that there are no unpaired atoms before expansion. In Fig. 1(b), a Bose-Einstein condensate of ^{7}Li atoms produced in the same optical trap is presented. The comparison between the condensate sizes after expansion reveals that the mean field interaction and scattering length are much larger for $^6Li_2$ dimers [Fig. 1(a)] than for ^{7}Li atoms [Fig. 1(b)].

To measure the molecule-molecule scattering length, we produce pure molecular condensates by taking advantage of our crossed dipole trap. We recompress the horizontal beam to full power while keeping the vertical beam at the low power of $0.035P_0^v$ corresponding to a trap depth for molecules $U = 5.6\,\mu$K. Temperature is then limited to $T \leq 0.9\,\mu$K assuming a conservative $\eta = U/k_BT = 6$, whereas the critical temperature increases with the mean oscillation frequency. Consequently, with an axial (respectively radial) trap frequency of 440 Hz (respectively 5 kHz), we obtain $T/T_C^0 \leq 0.3$, where $T_C^0 = \hbar\bar{\omega}(0.82N_{tot}/2)^{1/3} = 2.7\,\mu$K is the noninteracting BEC critical temperature. Thus, the condensate should be pure as confirmed by our images. After 1.2 ms of expansion, the radius of the condensate in the x (respectively y) direction is $R_x = 51\,\mu$m ($R_y = 103\,\mu$m). The resulting anisotropy $R_y/R_x = 2.0(1)$ is consistent with the value 1.98 [17] predicted the scaling equations [18,19]. Moreover, this set of equations leads to an *in-trap* radius $R_x^0 = 26\,\mu$m (respectively $R_y^0 = 2.75\,\mu$m). We then deduce the molecule-molecule scattering length from the Thomas-Fermi formula $R_{x,y}^0 = a_{ho}\bar{\omega}/\omega_{x,y}(15N_{tot}a_m/2a_{ho})^{1/5}$, with $a_{ho} = \sqrt{\hbar/2m\bar{\omega}}$. Averaging over several images, this yields $a_m = 170^{+100}_{-60}$ nm at 770 G. Here, the statistical uncertainty is negligible compared to the systematic uncertainty due to the calibration of our atom number. At this field, we calculate an atomic scattering length of $a = 306$ nm. Combined with the prediction $a_m = 0.6\,a$ of [10], we obtain $a_m = 183$ nm in good agreement with our measurement. For ^{7}Li, we obtain with the same analysis a much smaller scattering length of $a_7 = 0.65(10)$ nm at 610 G also in agreement with theory [20].

Such large values of a_m bring our molecular condensates into a novel regime where the gas parameter $n_m a_m^3$ is no longer very small. Indeed, $a_m = 170$ nm and $n_m = 6 \times 10^{13}$ cm^{-3} yield $n_m a_m^3 = 0.3$. As a first consequence, corrections due to beyond mean field effects [11,21] or to the underlying fermionic nature of atoms may play a role, since the average spacing between molecules is then of the order of the molecule size $\sim a/2$. Second, even in a mean field approach, thermodynamics is expected to be modified. For instance, in the conditions of Fig. 1(a), we expect a large shift of the BEC critical temperature [11–13]. The shift calculated to first order in $n^{1/3}a$ [12], $\Delta T_C/T_C^0 = -1.4$, is clearly inapplicable and a more refined approach is required [22]. Third, we observe that partially condensed cloud expansions are modified by interactions. Indeed, double structure fits lead to temperatures inconsistent with the presence of a condensate. In Fig. 1, we find $T = 1.6\,\mu$K, to be compared with $T_C^0 = 1.4\,\mu$K, whereas for the ^{7}Li condensate $T = 0.7\,\mu\text{K} = 0.6T_C^0$.

This inconsistency results from the large mean field interaction which modifies the thermal cloud expansion. To get a better estimate of the temperature, we rely on a release energy calculation. We calculate the Bose distribution of thermal atoms in a Mexican hat potential that is the sum of the external potential and the repulsive mean field potential created by the condensate. For simplicity we neglect the mean field resulting from the thermal component. The release energy is the sum of the thermal kinetic energy, condensate interaction energy, and Hartree-Fock interaction energy between the condensate and thermal cloud. The temperature and chemical potential are then adjusted to fit the measured atom number and release energy. For Fig. 1(a), we obtain a condensate fraction of 28% and $\mu = \hbar\bar{\omega}/2(15N_C a_m/2a_{ho})^{2/5} = 1.4\,\mu$K. The temperature $T = 0.9\,\mu$K is then found below $T_C^0 = 1.4\,\mu$K.

The condensate lifetime is typically $\sim$300 ms at 715 G ($a_m = 66$ nm) and $\sim 3\,s$ at 770 G ($a_m = 170$ nm), whereas for $a = -167$ nm at 1060 G, the lifetime exceeds 30 s. On the BEC side, the molecule-molecule loss rate constant is $G = 0.26^{+0.08}_{-0.06} \times 10^{-13}$ cm^3/s at 770 G and $G = 1.75^{+0.5}_{-0.4} \times 10^{-13}$ cm^3/s at 715 G with the fit procedure for condensates described in [23]. Combining similar results for four values of the magnetic field ranging from 700 to 770 G, we find $G \propto a^{-1.9\pm0.8}$. Our data are in

agreement with the theoretical prediction $G \propto a^{-2.55}$ of Ref. [10] and with previous measurements of G in a thermal gas at 690 G [14] or in a BEC at 764 G [8]. A similar power law was also found for ^{40}K [24].

We now present an investigation of the crossover from a Bose-Einstein condensate to an interacting Fermi gas (Figs. 2 and 3). We prepare a nearly pure condensate with 3.5×10^4 molecules at 770 G and recompress the trap to frequencies of $\omega_x = 2\pi \times 830$ Hz, $\omega_y = 2\pi \times 2.4$ kHz, and $\omega_z = 2\pi \times 2.5$ kHz. The magnetic field is then slowly swept at a rate of 2 G/ms to various values across the Feshbach resonance. The 2D momentum distribution after a time of flight expansion of 1.4 ms is then detected as previously.

Figure 2 presents the observed profiles (integrated over the orthogonal direction) for different values of the magnetic field. At the lowest field values $B \leq 750$ G, $n_m a_m^3 \ll 1$, condensates number are relatively low because of the limited molecule lifetime. As B increases, the condensate width gradually increases towards the width of a non-interacting Fermi gas, and nothing dramatic happens on resonance. At the highest fields ($B \geq 925$ G), where $k_F|a| \leq 3$, distributions are best fitted with zero temperature Fermi profiles. More quantitatively, Fig. 3(b) presents both the gas energy released after expansion E_{rel} and the anisotropy η across resonance. These are calculated from Gaussian fits to the density after time of flight: $E_{rel} = m(2\sigma_y^2 + \sigma_x^2)/2\tau^2$ and $\eta = \sigma_y/\sigma_x$, where σ_i is the rms width along i, and τ is the time of flight [17]. On the BEC side at 730 G, the measured anisotropy is $\eta \sim 1.6(1)$, in agreement with the hydrodynamic prediction, 1.75. It then decreases monotonically to 1.1 at 1060 G on the BCS side. On resonance, at zero temperature, superfluid hydrodynamic expansion is expected [25] corresponding to $\eta = 1.7$. We find, however, $\eta = 1.35(5)$, indicating a partially hydrodynamic behavior that could be due to a reduced superfluid fraction. On the $a < 0$ side, the decreasing anisotropy would indicate a further decrease of the superfluid fraction that could correspond to the reduction of the condensed fraction of fermionic atom pairs away from resonance observed in [7,9]. Interestingly, our results differ from that of Ref. [26] where hydrodynamic expansion was observed at 910 G in a more elongated trap for $T/T_F \simeq 0.1$.

In the BEC-BCS crossover regime, the gas energy released after expansion E_{rel} is also smooth [Fig. 3(c)]. E_{rel} presents a plateau for $B \leq 750$ G, and then increases monotonically towards that of a weakly interacting Fermi

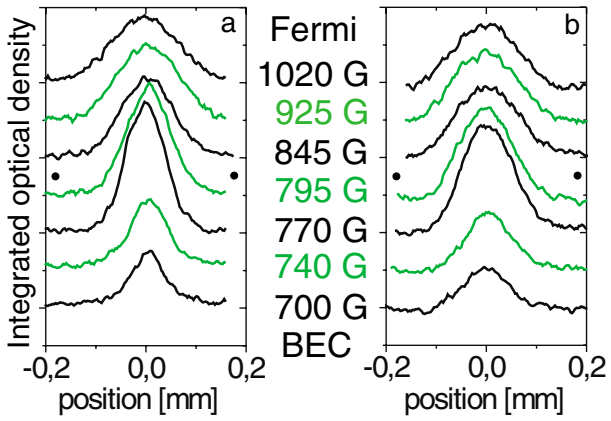

FIG. 2 (color online). Integrated density profiles across the BEC-BCS crossover region. 1.4 ms time of flight expansion in the axial (a) and radial (b) direction. The magnetic field is varied over the whole region of the Feshbach resonance from $a > 0$ ($B < 822$ G) to $a < 0$ ($B > 822$ G). ●: Feshbach resonance peak.

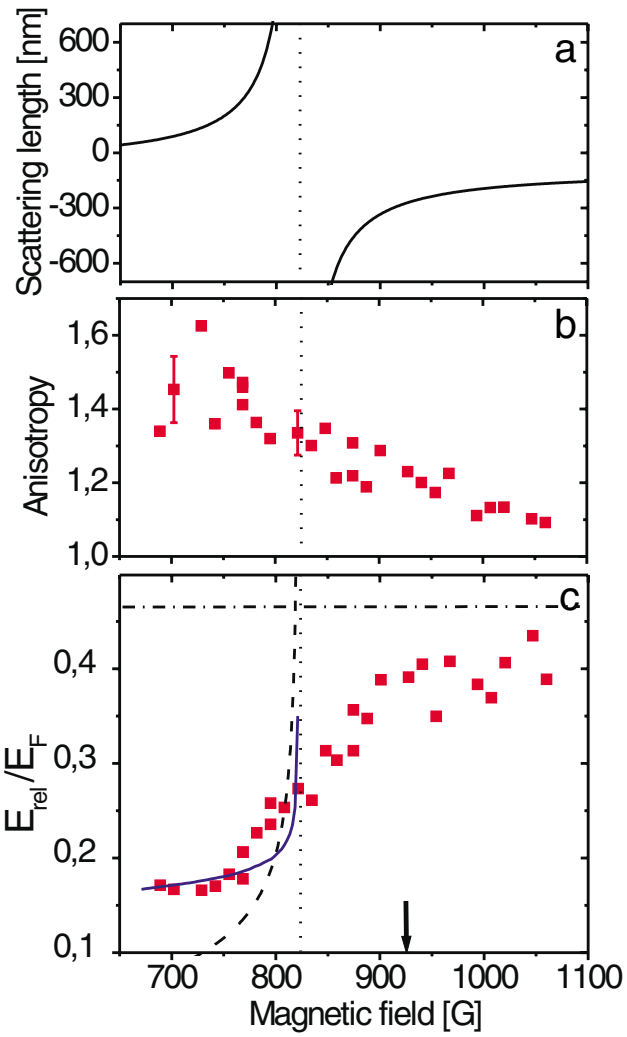

FIG. 3 (color online). (a) scattering length between the $|1/2, 1/2\rangle$ and $|1/2, -1/2\rangle$ ^{6}Li states. The Feshbach resonance peak is located at 822 G (dotted line). (b): anisotropy of the cloud, (c) release energy across the BEC-BCS crossover region. In (c), the dot-dashed line corresponds to a $T = 0$ ideal Fermi gas. The dashed curve is the release energy from a pure condensate in the Thomas-Fermi limit. The solid curve corresponds to a finite temperature mean field model described in the text with $T = 0.6\,T_C^0$. Arrow: $k_F|a| = 3$.

gas. The plateau is not reproduced by the mean field approach of a pure condensate (dashed line). This is a signature that the gas is not at $T = 0$. It can be understood with the mean field approach we used previously to describe the behavior of the thermal cloud. Since the magnetic field sweep is slow compared to the gas collision rate [14], we assume that this sweep is adiabatic and conserves entropy [27]. We then adjust this entropy to reproduce the release energy at a particular magnetic field, $B = 720$ G. The resulting curve as a function of B (solid line in Fig. 3(c)] agrees well with our data in the range 680 G $\leq B \leq$ 770 G, where the condensate fraction is 40%, and the temperature is $T \approx 0.6T_C^0 = 1.4\ \mu$K. This model is limited to $n_m a_m^3 \lesssim 1$. Near resonance the calculated release energy diverges and clearly departs from the data. On the BCS side, the release energy of a $T = 0$ ideal Fermi gas gives an upper bound for the data (dot-dashed curve), as expected from negative interaction energy and a very cold sample. This low temperature is supported by our measurements on the BEC side and the assumption of entropy conservation through resonance which predicts $T = 0.1\,T_F$ [27].

On resonance the gas is expected to reach a universal behavior, as the scattering length a is not a relevant parameter any more [5]. In this regime, the release energy scales as $E_{rel} = \sqrt{1+\beta}E_{rel}^0$, where E_{rel}^0 is the release energy of the noninteracting gas and β is a universal parameter. From our data at 820 G, we get $\beta = -0.64(15)$. This value is larger than the Duke result $\beta = -0.26 \pm 0.07$ at 910 G [26], but agrees with that of Innsbruck $\beta = -0.68^{+0.13}_{-0.10}$ at 850 G [8], and with the most recent theoretical prediction $\beta = -0.56$ [6]. Around 925 G, where $a = -270$ nm and $(k_F|a|)^{-1} = 0.35$, the release energy curve displays a change of slope. This is a signature of the transition between the strongly and weakly interacting regimes. It is also observed near the same field in [8] through *in situ* measurement of the trapped cloud size. Interestingly, the onset of resonance condensation of fermionic atom pairs observed in ^{40}K [7] and ^{6}Li [9], corresponds to a similar value of $k_F|a|$.

In summary, we have explored the whole region of the ^{6}Li Feshbach resonance, from a Bose-Einstein condensate of fermion dimers to an ultracold interacting Fermi gas. The extremely large scattering length between molecules that we have measured leads to novel BEC conditions. We have observed hydrodynamic expansions on the BEC side and nonhydrodynamic expansions at and above resonance. We suggest that this effect results from a reduction of the superfluid fraction and we point to the need of a better understanding of the dynamics of an expanding Fermi gas.

We are grateful to Y. Castin, C. Cohen-Tannoudji, R. Combescot, J. Dalibard, G. Shlyapnikov, and S. Stringari for fruitful discussions. This work was supported by CNRS, Collège de France, and Région Ile de France. S. Kokkelmans acknowledges a Marie Curie grant from the E.U. under Contract No. MCFI-2002-00968. Laboratoire Kastler-Brossel is Unité de recherche de l'Ecole Normale Supérieure et de l'Université Pierre et Marie Curie, associée au CNRS.

[1] M. Greiner, C. A. Regal, and D. S Jin, Nature (London) **426**, 537 (2003).
[2] S. Jochim *et al.*, Science **302**, 2101 (2003).
[3] M.W. Zwierlein *et al.*, Phys. Rev. Lett. **91**, 250401 (2003).
[4] A. J. Leggett, J. Phys. C (Paris) **41**, 7 (1980); P. Nozières and S. Schmitt-Rink, J. Low Temp. Phys. **59**, 195 (1985); C. Sá de Melo, M. Randeria, and J. Engelbrecht, Phys. Rev. Lett. **71**, 3202 (1993); M. Holland, S. Kokkelmans, M. Chiofalo, and R. Walser, Phys. Rev. Lett. **87**, 120406 (2001); Y. Ohashi and A. Griffin, Phys. Rev. Lett. **89**, 130402 (2002); J. N. Milstein, S. J. J. M. F. Kokkelmans, and M. J. Holland, Phys. Rev. A **66**, 043604 (2002); R. Combescot, Phys. Rev. Lett. **91**, 120401 (2003); G. M. Falco and H. T. C. Stoof, cond-mat/0402579.
[5] H. Heiselberg, Phys. Rev. A **63**, 043606 (2001).
[6] J. Carlson, S-Y Chang, V. R. Pandharipande, and K. E. Schmidt, Phys. Rev. Lett. **91**, 050401 (2003).
[7] C. A. Regal, M. Greiner, and D. S. Jin, Phys. Rev. Lett. **92**, 040403 (2004).
[8] M. Bartenstein *et al.*, Phys. Rev. Lett. **92**, 120401 (2004).
[9] M. Zwierlein *et al.*, Phys. Rev. Lett. **92**, 120403 (2004).
[10] D. S. Petrov, C. Salomon, and G.V. Shlyapnikov, cond-mat/0309010.
[11] G. Baym *et al.*, Eur. Phys. J. B **24**, 107 (2001).
[12] F. Dalfovo, S. Giorgini, L. P. Pitaevskii, and S. Stringari, Rev. Mod. Phys. **71**, 463 (1999).
[13] F. Gerbier *et al.*, Phys. Rev. Lett. **92**, 030405 (2004).
[14] J. Cubizolles *et al.*, Phys. Rev. Lett. **91**, 240401 (2003).
[15] T. Bourdel *et al.*, Phys. Rev. Lett. **91**, 020402 (2003).
[16] C. A. Regal, C. Ticknor, J. L. Bohn, and D. S. Jin, Nature (London) **424**, 47 (2003).
[17] We correct our data for the presence of a magnetic field curvature which leads to an antitrapping frequency of 100 Hz at 800 G along x.
[18] Yu. Kagan, E. L. Surkov, and G.V. Shlyapnikov, Phys. Rev. A **54**, 1753(R) (1996).
[19] Y. Castin and R. Dum, Phys. Rev. Lett. **77**, 5315 (1996).
[20] L. Khaykovich *et al.*, Science **296**, 1290 (2002).
[21] L. Pitaevskii and S. Stringari, Phys. Rev. Lett. **81**, 4541 (1998).
[22] A mean field self-consistent calculation of the molecular density profile in the trap at T_C leads to $T_C^{mf} = 0.58T_C^0 \approx 0.8\,\mu$K. S. Kokkelmans (to be published).
[23] J. Söding *et al.*, Appl. Phys. B **69**, 257 (1999).
[24] C. Regal, M. Greiner, and D. Jin, Phys. Rev. Lett. **92**, 083201 (2004).
[25] C. Menotti, P. Pedri, and S. Stringari, Phys. Rev. Lett. **89**, 250402 (2002).
[26] K. O'Hara *et al.*, Science **298**, 2179 (2002); M. Gehm *et al.*, Phys. Rev. A **68**, 011401 (2003).
[27] L. D. Carr, G.V. Shlyapnikov, and Y. Castin, Phys. Rev. Lett. **92**, 150404 (2004).

P-wave Feshbach resonances of ultracold ^{6}Li

PHYSICAL REVIEW A **70**, 030702(R) (2004)

P-wave Feshbach resonances of ultracold ^{6}Li

J. Zhang,[1,2] E. G. M. van Kempen,[3] T. Bourdel,[1] L. Khaykovich,[1,4] J. Cubizolles,[1] F. Chevy,[1] M. Teichmann,[1] L. Tarruell,[1] S. J. J. M. F. Kokkelmans,[1,3] and C. Salomon[1]

[1]*Laboratoire Kastler-Brossel, ENS, 24 rue Lhomond, 75005 Paris, France*

[2]*SKLQOQOD, Institute of Opto-Electronics, Shanxi University, Taiyuan 030006, People's Republic of China*

[3]*Eindhoven University of Technology, P.O. Box 513, 5600 MB Eindhoven, The Netherlands*

[4]*Department of Physics, Bar Ilan University, Ramat Gan 52900, Israel*

(Received 18 June 2004; published 30 September 2004)

We report the observation of three *p*-wave Feshbach resonances of ^{6}Li atoms in the lowest hyperfine state $f=1/2$. The positions of the resonances are in good agreement with theory. We study the lifetime of the cloud in the vicinity of the Feshbach resonances and show that, depending on the spin states, two- or three-body mechanisms are at play. In the case of dipolar losses, we observe a nontrivial temperature dependence that is well explained by a simple model.

DOI: 10.1103/PhysRevA.70.030702 PACS number(s): 34.50.−s, 03.75.Ss, 05.30.Fk, 32.80.Pj

In the presence of a magnetic field, it is possible to obtain a quasidegeneracy between the relative energy of two colliding atoms and that of a weakly bound molecular state. This effect, known as a Feshbach resonance, is usually associated with the divergence of the scattering length and is the key ingredient that led to the recent observation of superfluids from fermion atom pairs of ^{6}Li [1–4] and ^{40}K [5]. Up to now these pairs were formed in *s*-wave channels but it is known from condensed matter physics that fermionic superfluidity can arise through higher angular momentum pairing: *p*-wave Cooper pairs have been observed in ^{3}He [6] and *d*-wave cooper pairs in high-T_c superconductivity [7]. Although Feshbach resonances involving *p* or higher partial waves have been found in cold atom systems [8–10], *p*-wave atom pairs have never been directly observed.

In this paper we report the observation of three narrow *p*-wave Feshbach resonances of ^{6}Li in the lowest hyperfine state $f=1/2$. We measure the position of the resonance as well as the lifetime of the atomic sample for all combinations $|f=1/2,m_f\rangle+|f=1/2,m_f'\rangle$, henceforth denoted (m_f,m_f'). We show that the position of the resonances are in good agreement with theory. In the case of atoms polarized in the ground state $(1/2,1/2)$, the atom losses are due to three-body processes. We show that the temperature dependence of the losses at resonance cannot be described by the threshold law predicted by [11] on the basis of the symmetrization principle for identical particles. In the case of atoms polarized in $(-1/2,-1/2)$ or that of a mixture $(1/2,-1/2)$, the losses are mainly due to two-body dipolar losses. These losses show a nontrivial temperature dependence that can nevertheless be understood by a simple theoretical model with only one adjustable parameter. In the $(1/2,-1/2)$ channel, we take advantage of a sharp decrease of the two-body loss rate below the Feshbach resonance to present a first evidence for the generation of *p*-wave molecules.

The *p*-wave resonances described in this paper have their origin in the same singlet $(S=0)$ bound state that leads to the *s*-wave Feshbach resonances located at 543 G and ~830 G. The latter has been used to generate stable molecular Bose-Einstein condensates [1–4]. In order to discuss the origin of these resonances, it is useful to introduce the molecular basis quantum numbers S,I, and l, which correspond to the total electron spin $\boldsymbol{S}=\boldsymbol{s}_1+\boldsymbol{s}_2$, total nuclear spin $\boldsymbol{I}=\boldsymbol{i}_1+\boldsymbol{i}_2$, and orbital angular momentum $\boldsymbol{l}$. Furthermore, the quantum numbers must fulfill the selection rule

$$S+I+l=\text{even}, \tag{1}$$

which is a result of the symmetrization requirements of the two-body wave function. Since the atomic nuclear spin quantum numbers are $i_1=i_2=1$, and $S=0$, there are two possibilities for the total nuclear spin in combination with an *s*-wave $(l=0)$ collision: $I=0$ and $I=2$. These two states give rise to the two aforementioned *s*-wave Feshbach resonances. For *p*-wave $(l=1)$ collisions only $I=1$ is possible. This bound state may then give rise to the three *p*-wave Feshbach resonances of Fig. 1. This threshold state does not suffer from exchange decay, and is therefore relatively stable. Our predicted resonance field values B_F (Table I) result from an analysis which takes into account the most recent experimental data available for ^{6}Li. The calculation has been performed for all spin channels (m_f,m_f') and a typical collision energy

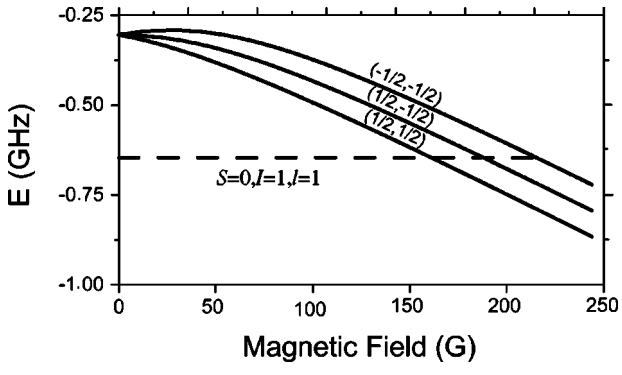

FIG. 1. Coupled channels calculation of *p*-wave binding energies, which give rise to Feshbach resonances at threshold. The two-atom states (full line) are indicated by their quantum number (m_{f_1},m_{f_2}), while the bound state (dashed line) is labeled by the molecular quantum numbers S,I, and l.

TABLE I. Theoretical and experimental values of the magnetic field B_F at the *p*-wave Feshbach resonance for ^{6}Li atoms in $|f_1=1/2,m_{f_1}\rangle$ and $|f_1=1/2,m_{f_2}\rangle$.

(m_{f_1},m_{f_2})	Theory (G)	Experiment (G)
$(1/2,1/2)$	159	160.2(6)
$(1/2,-1/2)$	185	186.2(6)
$(-1/2,-1/2)$	215	215.2(6)

of 15 μK. A more detailed analysis will be published elsewhere [12].

Experimentally, we probe these *p*-wave resonances using the setup described in previous papers [13,14]. After evaporative cooling in the magnetic trap, we transfer $\sim 5\times 10^5$ atoms of ^{6}Li in $|f=3/2, m_f=3/2\rangle$ in a far-detuned crossed optical trap at low magnetic field. The maximum power in each arm is $P_h^0=2$ W and $P_v^0=3.3$ W in the horizontal and vertical beam, respectively, and corresponds to a trap depth of ~ 80 μK. The oscillation frequencies measured by parametric excitation are, respectively, $\omega_x=2\pi\times 2.4(2)$ kHz, $\omega_y=2\pi\times 5.0(3)$ kHz, $\omega_z=2\pi\times 5.5(4)$ kHz, where the $x(y)$ direction is chosen along the horizontal (vertical) beam. A first radio-frequency (rf) sweep brings the atoms to $|f=1/2, m_f=1/2\rangle$ and, if necessary, we perform a second rf transfer to prepare the mixture $(1/2,-1/2)$ or the pure $(-1/2,-1/2)$. The variable magnetic field B is the sum of two independent fields B_0 and B_1. B_0 offers a wide range of magnetic field while B_1 can be switched off rapidly. After the radio-frequency transfer stage, we ramp the magnetic field to $B_0\sim 220$ G with $B_1\sim 8$ G in 100 ms. When needed, we reduce in 100 ms the power of the trapping beams to further cool the atoms. For the coldest samples, we obtain at the end of this evaporation sequence $N\sim 10^5$ atoms at a temperature ~ 5 μK. This corresponds to a ratio $T/T_F\sim 0.5$, where $k_BT_F=\hbar(6N\omega_x\omega_y\omega_z)^{1/3}$ is the Fermi energy of the system. To reach the Feshbach resonance, we reduce B_0 in 4 ms to its final value $B_{0,f}\sim B_F$, near the Feshbach resonance. At this stage, we abruptly switch off B_1 so that the total magnetic field is now close to resonance. After a waiting time in the trap $t_{\rm wait}=50$ ms, we switch off the trapping and the magnetic field and we measure the remaining atom number after a 0.35 ms time of flight.

We show in Fig. 2 the dependence of the atom number on the final value of $B_{0,f}$ in the case of the spin mixture $(1/2, -1/2)$ at a temperature $T\sim 14$ μK. As expected from theory, we observe a sharp drop of the atom number for values of the magnetic field close to 186 G. The other two *p*-wave Feshbach resonances have a similar loss signature and Table I shows that for all spin channels, the resonance positions are in good agreement with predictions. Note that in Table I the uncertainty is mainly due to the magnetic field calibration while the short term stability is $\lesssim 50$ mG.

To evaluate the possibility of keeping *p*-wave molecules in our trap, we have studied the lifetime of the gas sample at the three Feshbach resonances. We have measured the number N of atoms remaining in the trap after a variable time $t_{\rm wait}$. Accounting for two- and three-body processes only, N should follow the rate equation

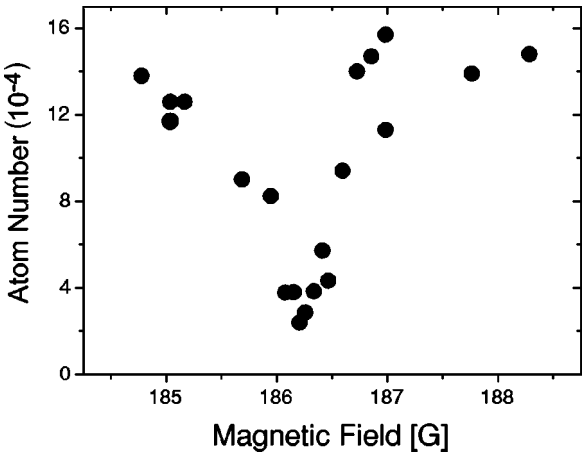

FIG. 2. Atom number vs magnetic field $B_{0,f}$ after a 50 ms wait for atoms in the spin mixture $(1/2,-1/2)$ at $T\sim 14$ μK. The sharp drop close to $B_0\sim 186$ G over a range $\simeq 0.5$ G is the signature of the *p*-wave Feshbach resonance predicted by theory.

$$\frac{\dot{N}}{N}=-G_2\langle n\rangle-L_3\langle n^2\rangle, \tag{2}$$

where n is the atom density and $\langle n^a\rangle=\int d^3r\, n^{a+1}/N$ $(a=1,2)$ is calculated from the classical Boltzman distribution. In this equation, we can safely omit one-body losses since the measured decay time is ~ 100 ms, much smaller than the one-body lifetime ~ 30 s.

In the $(1/2,1/2)$ channel, we find that three-body losses are dominant. The dependence of L_3 with temperature is very weak [Fig. 3(a)]. A theoretical calculation of the temperature dependence of three-body loss rate has been performed in [11] and it predicts that in the case of indistinguishable fermions L_3 should be proportional to T^λ, with $\lambda\geqslant 2$. Although this prediction seems in disagreement with our experimental

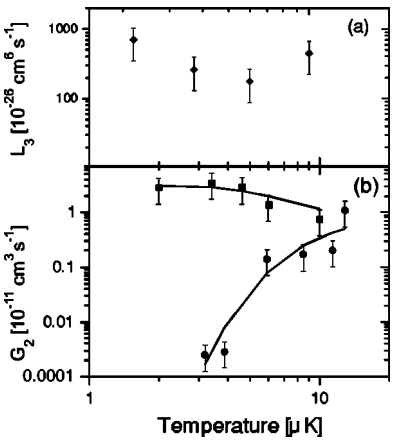

FIG. 3. Variations of (a) three-body and (b) two-body loss rates vs temperature at the Feshbach resonance. (a) ♦: atoms in the Zeeman ground state $|f=1/2,m_f=1/2\rangle$, $B_{0,f}\sim 159$ G. (b) ■: atoms polarized in $|f=1/2,m_f=-1/2\rangle$, $B_{0,f}\sim 215$ G. ●: the mixture $|f=1/2,m_f=1/2\rangle+|f=1/2,m_f=-1/2\rangle$, $B_{0,f}\sim 186$ G. In both cases, the full line is a fit to the data using the prediction of Eq. (4) with the magnetic field as the only fitting parameter.

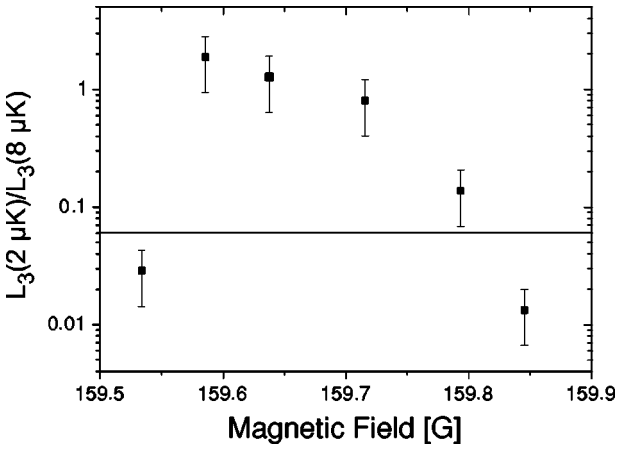

FIG. 4. Ratio $L_3(T=2\ \mu\text{K})/L_3(T=8\ \mu\text{K})$ of the three-body decay rate for two different temperatures for a gas of atoms polarized in $|f=1/2, m_f=1/2\rangle$. The full line is the threshold law $L_3 \sim T^2$.

results, the analysis of [11] relies on a Wigner threshold law, i.e., a perturbative calculation based on the Fermi golden rule. At the Feshbach resonance where the scattering cross section is expected to diverge, this simplified treatment is not sufficient. This suggests that three-body processes must be described by a more refined formalism, analogous to the unitary limited treatment of the *s*-wave elastic collisions [15]. To confirm this assumption, we have compared the loss rates at two given temperatures ($T=2\ \mu$K and $T=8\ \mu$K, respectively) for various values of the magnetic field (Fig. 4). If the threshold law is valid, then the ratio $L_3(2\ \mu\text{K})/L_3(8\ \mu\text{K})$ should always be smaller than $(2/8)^2 \sim 0.0625$ (full line of Fig. 4). As seen before, experimental data show no significant variation of L_3 with temperature near resonance. However, when the magnetic field is tuned out of resonance we recover a dependence in agreement with [11].

In contrast to *s*-wave Feshbach resonances where dipolar losses are forbidden in the $f=1/2$ manifold [16], the losses at resonance are found to be dominantly two body in the $(1/2,-1/2)$ and $(-1/2,-1/2)$ channels. The variations of the two-body loss rate with temperature are displayed in Fig. 3(b). The temperature dependence appears very different in the two cases. We show now that this is the consequence of a strong sensitivity to magnetic field detuning from resonance, rather than a specific property of the states involved. In an extension of the work presented in [17], we describe inelastic collisions by two noninteracting open channels coupled to a single *p*-wave molecular state [18]. This model leads to an algebra close to the one describing photoassociation phenomena [19] and the two-body loss rate at energy E is given by

$$g_2(E) = \frac{KE}{(E-\delta)^2 + \gamma^2/4}. \tag{3}$$

Here $\delta = \mu(B - B_F)$ is the detuning to the Feshbach resonance and K, μ, and γ are phenomenological constants, depending on the microscopic details of the potential [21]. For each channel, these parameters are estimated from our coupled-channel calculation (Table II). To compare with experimental

TABLE II. Parameters characterizing the two-body loss rates for $(1/2,-1/2)$ and $(-1/2,-1/2)$ spin channels.

(m_{f_1}, m_{f_2})	K ($\text{cm}^3\ \mu\text{K s}^{-1}$)	γ (μK)	μ ($\mu\text{K G}^{-1}$)
$(1/2,-1/2)$	1.21×10^{-13}	0.05	117
$(-1/2,-1/2)$	7.33×10^{-13}	0.08	111

data, Eq. (3) is averaged over a thermal distribution and for $\delta > 0$ and $\delta \gg \gamma$ we get

$$G_2 \sim 4\sqrt{\pi}\frac{K}{\gamma}\left(\frac{\delta}{k_B T}\right)^{3/2} e^{-\delta/k_B T}. \tag{4}$$

Equation (4) is used to fit the data of Fig. 3(b), with $B - B_F$ as the only fitting parameter. We get a fairly good agreement if we take $B - B_F = 0.04$ G (0.3 G) for the $(-1/2, -1/2)[(1/2,-1/2)]$ channel, illustrating the extreme sensitivity of G_2 to detuning and temperature. This feature was also qualitatively tested by measuring the variations of G_2 with magnetic field at constant temperature. Another interesting feature of Eq. (4) is that it predicts that the width δB of the Feshbach resonance, as measured by atom losses, should scale like $k_B T/\mu$. For a typical temperature $T \sim 15\ \mu$K, this yields $\delta B \sim 0.15$ G, in agreement with the resonance width shown in Fig. 2.

From Eq. (4) we see that G_2 nearly vanishes at $\delta = 0$. The thermal average of Eq. (4) for $\delta = 0$ yields $G_2(\delta=0) \propto K k_B T$. The ratio between the maximum two-body loss rate ($\delta = 3k_B T/2$) and that at $\delta = 0$ is then $\sim k_B T/\gamma$, $\sim 10^2$ for $\sim 10\ \mu$K. In the region $\delta < 0$ where we expect to form molecules, we benefit from a $1/\delta^2$ further reduction of the two-body losses [see Eq. (4)].

We have checked the production of molecules in $(1/2, -1/2)$ by using the scheme presented in [13,22]. We first generate molecules in $|S=0, I=1, l=1\rangle$ by ramping in 20 ms the magnetic field from 190 G $> B_F$ to $B_{\text{nuc}} = 185$ G $< B_F$. At this stage, we can follow two paths before detection (Fig. 5). Path 1 permits us to measure the number N_1 of free atoms: by ramping *down* in 2 ms the magnetic field from 185 G to 176 G, we convert the molecules into deeply bound molecu-

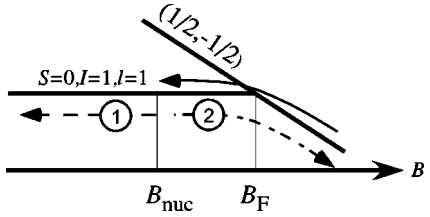

FIG. 5. Molecules are generated by ramping from a magnetic field higher than B_F to $B_{\text{nuc}} < B_F$. From there, two paths are used. In path 1 (dashed line), the magnetic field is decreased to create tightly bound molecules that will not appear on absorption images. In path 2 (dashed-dotted line), the magnetic field is ramped up across resonance to dissociate the molecules. The efficiency of the molecule production is simply given by $(1 - N_1/N_2)$, where N_i is the atom number measured after path i.

lar states that decay rapidly by two-body collisions. Path 2 gives access to the total atom number N_2 (free atoms + atoms bound in *p*-wave molecules). It consists of ramping *up* the magnetic field in 2 ms from B_{nuc} to 202 G$>B_F$ to convert the molecules back into atoms. Since the atoms involved in molecular states appear only in pictures taken in path 2, the number of molecules in the trap is $(N_2-N_1)/2$. In practice, both sequences are started immediately after reaching B_{nuc} and we average the data of 25 pictures to compensate for atom number fluctuations. We then get $N_1=7.1(5)\times10^4$ and $N_2=9.1(7)\times10^4$ which corresponds to a molecule fraction $1-N_1/N_2=0.2(1)$. Surprisingly, we failed to detect any molecule signal when applying the same method to $(1/2,1/2)$ atoms.

Since the dramatic reduction of inelastic losses close to a *s*-wave Feshbach resonance [23] was a key ingredient to the recent observation of fermionic superfluids, the formation of stable atom pairs requires a full understanding of the decay mechanisms at play close to a *p*-wave resonance. In this paper we have shown that in the particular case of two-body losses, the maximum losses take place when the detuning is positive. Since stable dimers are expected to be generated for negative detuning, dipolar losses should not present a major hindrance to further studies of *p*-wave molecules.

We thank Z. Hadzibabic for very helpful discussions. S.K. acknowledges support from the Netherlands Organization for Scientific Research (NWO). E.K. acknowledges support from the Stichting FOM, which is financially supported by NWO. This work was supported by CNRS, and Collège de France. Laboratoire Kastler Brossel is *Unité de recherche de l'École Normale Supérieure et de l'Université Pierre et Marie Curie, associée au CNRS*.

[1] S. Jochim *et al.*, Science **302**, 2101 (2003).
[2] M. W. Zwierlein *et al.*, Phys. Rev. Lett. **91**, 250401 (2003).
[3] T. Bourdel *et al.*, e-print cond-mat/0403091.
[4] J. Kinast *et al.*, Phys. Rev. Lett. **92**, 150402 (2004).
[5] M. Greiner, C. A. Regal, and D. S Jin, Nature (London) **426**, 537 (2003).
[6] D. M. Lee, Rev. Mod. Phys. **69**, 645 (1997).
[7] C. C Tsuei and J. R. Kirtley, Phys. Rev. Lett. **85**,182 (2000).
[8] C. Chin *et al.*, Phys. Rev. Lett. **85**, 2717 (2000).
[9] C. A. Regal *et al.*, Phys. Rev. Lett. **90**, 053201 (2003).
[10] T. Weber *et al.*, Phys. Rev. Lett. **91**, 123201 (2003).
[11] B. D. Esry, C. H. Greene, and H. Suno, Phys. Rev. A **65**, 010705 (2002).
[12] E. G. M. van Kempen *et al.*, e-print cond-mat/0406722.
[13] J. Cubizolles *et al.*, Phys. Rev. Lett. **91** 240401 (2003).
[14] T. Bourdel *et al.*, Phys. Rev. Lett. **91**, 020402 (2003).
[15] H. Suno, B. D. Esry, and C. H. Greene, Phys. Rev. Lett. **90**, 053202 (2003).
[16] K. Dieckmann *et al.*, Phys. Rev. Lett. **89**, 203201 (2002).
[17] M. Holland *et al.*, Phys. Rev. Lett. **87**, 120406 (2001).
[18] We also neglect the splitting between the different m_l predicted by [20].
[19] R. Napolitano *et al.*, Phys. Rev. Lett. **73**, 1352 (1994)
[20] C. Ticknor *et al.*, Phys. Rev. A **69**, 042712 (2004).
[21] Note that in our case μ is positive. This corresponds to molecular states stable at low field.
[22] C. A. Regal *et al.*, Nature (London) **424**, 47 (2003).
[23] D. S. Petrov, Phys. Rev. A **67**, 010703 (2003).

Resonant scattering properties close to a p-wave Feshbach resonance

Resonant scattering properties close to a *p*-wave Feshbach resonance

F. Chevy,[1] E. G. M. van Kempen,[2] T. Bourdel,[1] J. Zhang,[3] L. Khaykovich,[4] M. Teichmann,[1] L. Tarruell,[1] S. J. J. M. F. Kokkelmans,[2] and C. Salomon[1]

[1]*Laboratoire Kastler-Brossel, ENS, 24 rue Lhomond, 75005 Paris*

[2]*Eindhoven University of Technology, P. O. Box 513, 5600 MB Eindhoven, The Netherlands*

[3]*SKLQOQOD, Institute of Opto-Electronics, Shanxi University, Taiyuan 030006, People's Republic of China*

[4]*Department of Physics, Bar Ilan University, Ramat Gan 52900, Israel*

(Received 15 December 2004; published 22 June 2005)

We present a semianalytical treatment of both the elastic and inelastic collisional properties near a *p*-wave Feshbach resonance. Our model is based on a simple three-channel system that reproduces more elaborate coupled-channel calculations. We stress the main differences between *s*-wave and *p*-wave scattering. We show in particular that, for elastic and inelastic scattering close to a *p*-wave Feshbach resonance, resonant processes dominate over the low-energy behavior.

DOI: 10.1103/PhysRevA.71.062710 PACS number(s): 34.50.−s, 03.75.Ss, 05.30.Fk, 32.80.Pj

I. INTRODUCTION

The observation of molecular gaseous Bose-Einstein condensates (BECS) and the subsequent experimental study of the BEC-BCS crossover [1–5] were made possible by the possibility of tuning interatomic interactions using a magnetic field (the so-called Feshbach resonances). Although all these experiments were based on *s*-wave interatomic interactions, it is known from condensed matter physics that superfluidity of fermionic systems can also arise through higher-order partial waves. The most famous examples of this nonconventionnal superfluidity are ^{3}He [6], for which the Cooper pairs spawn from *p*-wave interactions, and high-T_c superconductivity, in which pairs are known to possess *d*-wave symmetry [7]. Recent interest in *p*-wave interactions in cold atom gases stemmed from these possibilities and resulted in the observation of *p*-wave Feshbach resonances in ^{40}K [8] and ^{6}Li [9,10], as well as theoretical studies on the superfluidity of cold atoms interacting through *p*-wave pairing [11,12].

The present paper is devoted to the study of *p*-wave interactions close to a Feshbach resonance and it derives some results presented in [9]. In a first part, we present the model we use to describe both elastic and inelastic processes that are discussed in the second part. We stress in particular the main qualitative differences between *p*-wave and *s*-wave physics and show that contrarily to the case of the *s* wave, which is dominated by low-energy physics, *p*-wave scattering is dominated by a resonance peak associated to the quasibound molecular state. Finally, we compare our analytical results to numerical coupled-channel calculations.

II. MODEL FOR *p*-WAVE INTERACTIONS

We consider the scattering of two identical particles of mass m. As usual when treating a two-body problem, we work in the center-of-mass frame and consider only the motion of a fictitious particle of mass $m/2$ interacting with a static potential. In order to study the *p*-wave Feshbach resonance, we use a model based on the separation of open and closed channels. In this framework, the Feshbach resonance arises in an open channel as a result of the coupling with a closed channel [13]. At resonance, scattering properties are dominated by resonant effects and we can neglect all "background" scattering (i.e., we assume there is no scattering far from resonance).

(1) We restrict ourselves to a three-channel system, labeled 1, 2, and 3, which correspond to the different two-body spin configurations (Fig. 1). Channels $|1\rangle$ and $|2\rangle$ are open channels. We focus on the situation where atoms are prepared initially in state $|1\rangle$. Atoms may be transferred to state $|2\rangle$ after an inelastic process. Channel $|3\rangle$ is closed and hosts the bound state leading to the Feshbach resonance.

Let us consider, for instance, the case of ^{6}Li atoms prepared in a mixture of $|F=1/2,m_F=1/2\rangle$ and $|F'=1/2,m'_F=-1/2\rangle$. In this system, the only two-body decay channel is associated with the flipping of an $m'_F=-1/2$ atom to $m'_F=1/2$. If we denote by (m_F,m'_F) the symmetrized linear combination of the states $|F=1/2,m_F\rangle$ and $|F'=1/2,m'_F\rangle$, then $|1\rangle=(1/2,-1/2)$ and $|2\rangle=(1/2,1/2)$.

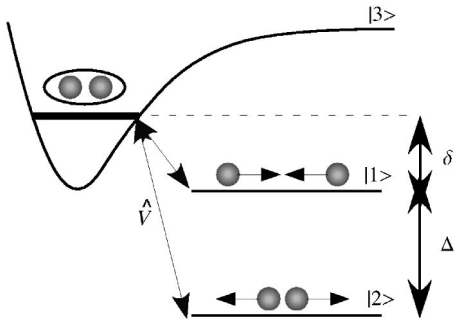

FIG. 1. The *p*-wave model: we consider three internal states, labeled $|1\rangle$, $|2\rangle$, and $|3\rangle$. States $|1\rangle$ and $|2\rangle$ are two open channels corresponding, respectively, to the incoming and decay channels. The released energy in an inelastic collision bringing an atom initially in $|1\rangle$ to $|2\rangle$ is denoted Δ. State $|3\rangle$ is a closed channel that possesses a *p*-wave bound state of energy δ nearly resonant with state $|1\rangle$. Finally, we assume that these three channels interact through a potential $\hat{V}$ acting only on the internal states and coupling the two open channels to the closed channel.

(2) The Feshbach resonances studied here are all located at values of the magnetic field where the Zeeman splitting is much larger than the hyperfine structure. In a first approximation we can therefore assume that the internal states are described by uncoupled electronic and nuclear spin states. In the absence of any dipolar or hyperfine coupling between the electronic singlet and triplet manifolds, we assume we have no direct interaction in channels 1 and 2 so that the eigenstates are plane waves characterized by their relative wave vector k and their energy $E_1(k)=\hbar^2k^2/m$ (channel 1) and $E_2(k)=-\Delta+\hbar^2k^2/m$ (channel 2). $\Delta>0$ is the energy released in an inelastic process leading from 1 to 2. Δ can be considered as independent of the magnetic field and is assumed to be much larger than any other energy scales (in the case relevant to our experiments, $\Delta/h\sim 80$ MHz is the hyperfine splitting of ^{6}Li at high field).

(3) In channel 3, we consider only a p-wave bound state nesting at an energy δ quasiresonant with channel 1. In the case of ^{6}Li atoms in the $F=1/2$ hyperfine state, $\delta=2\mu_B(B-B_0)$, where B is the magnetic field and B_0 is the position of the "bare" Feshbach resonance. If the projection of the angular momentum (in units of $\hbar$) is denoted by $m_{\mathbf{u}}$ for a quantization axis chosen along some vector $\mathbf{u}$, the eigenfunctions associated with this bound state can be written as $g(r)Y_1^{m_{\mathbf{u}}}(\theta,\phi)$, where (r,θ,ϕ) is the set of polar coordinates and the Y_l^m are the spherical harmonics.

(4) The coupling $\hat{V}$ between the various channels affects only the spin degrees of freedom. Therefore the orbital angular momentum is conserved during the scattering process and we restrict our analysis to the p-wave manifold. This is in contrast to the situation in heavy alkalimetals where incoming particles in the s wave can be coupled to molecular states of higher orbital angular momentum [14,15].

We assume also that the only nonvanishing matrix elements are between the closed and the open channels (i.e., $\langle 1,2|\hat{V}||3\rangle$ and $\langle 3|\hat{V}|1,2\rangle$).

Let us denote a state of the system by $|\alpha,\chi\rangle$, where $\alpha\in\{1,2,3\}$ and χ describe, respectively, the internal (spin) and the orbital degrees of freedom. According to assumption ((4)), the matrix element $\langle\alpha,\chi|\hat{V}|\alpha',\chi'\rangle$ is simply given by

$$\langle\alpha,\chi|\hat{V}|\alpha',\chi'\rangle=\langle\chi|\chi'\rangle\langle\alpha|\hat{V}|\alpha'\rangle, \tag{1}$$

and is therefore simply proportional to the overlap $\langle\chi|\chi'\rangle$ between the external states.

Let us now particularize to the case where $\alpha\in\{1,2\}$, and $|\chi\rangle=|\mathbf{k}\rangle$ is associated with a plane wave of relative momentum $\hbar\mathbf{k}$. According to hypothesis ((4)), this state is coupled only to the closed channel $|3\rangle$. Moreover, using the well-known formula $e^{ikz}=\Sigma_l i^l\sqrt{4\pi(2l+1)}j_l(kr)Y_l^0(\theta,\phi)$, where the j_l are the spherical Bessel functions, we see that $|\chi\rangle$ is coupled only to the state $|\alpha'=3,\mathbf{k}=\mathbf{0}\rangle$ describing the pair in the bound state $|\alpha'=3\rangle$ with zero angular momentum in the $\mathbf{k}$ direction. The matrix element then reads

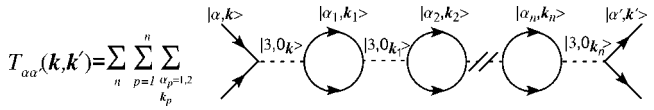

FIG. 2. Diagrammatic expansion of the T matrix. The full (dashed) lines represent free atoms (molecules). $|\alpha,\mathbf{k}\rangle$ is the scattering state of the two particles, in the internal state $\alpha=1,2$. $|3,0_{\mathbf{k}}\rangle$ represents the state of a p-wave molecule with orbital angular momentum component zero on the $\mathbf{k}$ direction.

$$\langle\alpha,\mathbf{k}|\hat{V}|3,m_{\mathbf{k}}\rangle=i\delta_{m_{\mathbf{k}},0}\sqrt{\frac{12\pi}{L^3}}\langle\alpha|\hat{V}|3\rangle\int g^*(r)j_1(kr)r^2dr, \tag{2}$$

where L^3 is a quantization volume. Since for small k we have $j_1(kr)\sim kr/3$, the matrix element $\langle\alpha,\mathbf{k}|\hat{V}|3,m_{\mathbf{k}}\rangle$ takes the general form

$$\langle\alpha,\mathbf{k}|\hat{V}|3,m_{\mathbf{k}}\rangle=\delta_{m_{\mathbf{k}},0}\frac{kF_\alpha(k)}{\sqrt{L^3}}, \tag{3}$$

where $F_\alpha(k)$ has a finite (in general nonzero) limit when k goes to zero.

Later on, we shall also need the coupling between $|\alpha,\mathbf{k}\rangle$ and $|3,m_{\mathbf{k}'}=0\rangle$ (that will be denoted by $|3,0_{\mathbf{k}'}\rangle$), where the momentum $\mathbf{k}$ and the direction of quantization $\mathbf{k}'$ are no longer parallel. The calculation presented above yields readily

$$\langle\alpha,\mathbf{k}|\hat{V}|3,0_{\mathbf{k}'}\rangle=\frac{kF_\alpha(k)}{\sqrt{L^3}}\langle 0_{\mathbf{k}}|0_{\mathbf{k}'}\rangle=\frac{kF_\alpha(k)}{\sqrt{L^3}}\cos(\widehat{\mathbf{k},\mathbf{k}'}), \tag{4}$$

where $(\widehat{\mathbf{k},\mathbf{k}'})$ is the angle between $\mathbf{k}$ and $\mathbf{k}'$ [16].

III. T MATRIX

From general quantum theory, it is known that the scattering properties of a system are given by the so-called T matrix $\hat{T}$. It can be shown in particular that $\hat{T}$ is given by the following expansion in powers of the coupling potential:

$$\hat{T}(E)=\hat{V}+\hat{V}\hat{G}_0(E)\hat{V}+\hat{V}\hat{G}_0(E)\hat{V}\hat{G}_0(E)\hat{V}+\cdots, \tag{5}$$

where $\hat{G}_0(E)=1/(E-\hat{H}_0)$ and $\hat{H}_0=\hat{H}-\hat{V}$ is the free Hamiltonian of the system.

Let us consider $|\alpha,\mathbf{k}\rangle$ and $|\alpha',\mathbf{k}'\rangle$, two states of the *open channels*, and let us set $T_{\alpha\alpha'}(\mathbf{k},\mathbf{k}',E)=\langle\alpha,\mathbf{k}|\hat{T}(E)|\alpha',\mathbf{k}'\rangle$. According to formula (5), this matrix element is the sum of terms that can be represented by the diagram of Fig. 2 and we get after a straightforward calculation

$$T_{\alpha\alpha'}(\mathbf{k},\mathbf{k}',E)=\frac{kk'}{L^3}F_\alpha(k)F^*_{\alpha'}(k')\sum_{n=0}^{\infty}R_n\Lambda(E)^nG_0^{(m)}(E)^{n+1}.$$

Here $G_0^{(m)}(E)=1/(E-\delta)$ is the free propagator for the molecule, $\Lambda=\Lambda_1+\Lambda_2$ with

$$\Lambda_\alpha(E) = \int \frac{q^4 dq}{(2\pi)^3} \frac{|F_\alpha(q)|^2}{E - E_\alpha(q)} \tag{6}$$

the results of the integration on the loops, and finally

$$R_n = \int d^2\Omega_1 \cdots d^2\Omega_n \cos(\widehat{\mathbf{k},\mathbf{k}_1}) \times \cos(\widehat{\mathbf{k}_1,\mathbf{k}_2}) \cdots \cos\widehat{\mathbf{k}_n,\mathbf{k}'},$$

where Ω_p is the solid angle associated with $\mathbf{k}_p$, arises from the pair-breaking vertices $|3,0_{\mathbf{k}_i}\rangle \rightarrow |\alpha_{i+1},\mathbf{k}_{i+1}\rangle$. This last integral can be calculated recursively and we get $R_n = (4\pi/3)^n \cos(\widehat{\mathbf{k},\mathbf{k}'})$, that is, for the T matrix

$$T_{\alpha\alpha'}(\mathbf{k},\mathbf{k}',E) = \frac{1}{L^3} \frac{kk' F_\alpha(k) F^*_{\alpha'}(k')}{E - \delta - \Sigma_1 - \Sigma_2} \cos(\widehat{\mathbf{k},\mathbf{k}'}),$$

with $\Sigma_\alpha = 4\pi\Lambda_\alpha/3$.

This expression can be further simplified since, according to Eq. (2), the width of $F_\alpha(q)$ is of the order of $1/R_e$, where R_e is the characteristic size of the resonant bound state. In the low-temperature limit, we can therefore expand Σ_α with the small parameter kR_e.

From Eq. (2), we see that replacing $F_\alpha(q)$ by its value at $q=0$ leads to a q^2 divergence. This divergence can be regularized by the use of counterterms in the integral, namely, by writing that

$$\Sigma_\alpha(E) = \int |F_\alpha(q)|^2 \left[\frac{q^4}{E - E_\alpha(q)} + \frac{mq^2}{\hbar^2} + \frac{m^2}{\hbar^4}[E - E_\alpha(0)] \right] \frac{dq}{6\pi^2} - \int |F_\alpha(q)|^2 \frac{mq^2}{\hbar^2} \frac{dq}{6\pi^2} - [E - E_\alpha(0)] \int |F_\alpha(q)|^2 \frac{m^2}{\hbar^4} \frac{dq}{6\pi^2},$$

where we have assumed that F_α was decreasing fast enough at large q to ensure the convergence of the integrals. $|F_\alpha(q)|^2$ can now be safely replaced by $\lambda_\alpha = |F_\alpha(0)|^2$ in the first integral and we finally get

$$\Sigma_\alpha = -i \frac{\lambda_\alpha}{6\pi} \frac{m}{\hbar^2} \left(\frac{m}{\hbar^2}[E - E_\alpha(0)] \right)^{3/2} - \delta_{0,\alpha} - \eta_\alpha [E - E_\alpha(0)],$$

with

$$\delta_0^{(\alpha)} = \int |F_\alpha(q)|^2 \frac{mq^2}{\hbar^2} \frac{dq}{6\pi^2},$$

$$\eta_\alpha = \int |F_\alpha(q)|^2 \frac{m^2}{\hbar^4} \frac{dq}{6\pi^2}.$$

If we assume that the release energy Δ is much larger than E and if we set $\delta_0 = \delta_0^{(1)} + \delta_0^{(2)}$ and $\eta = \eta_1 + \eta_2$, we get for the T matrix

$$T_{\alpha\alpha'}(\mathbf{k},\mathbf{k}',E) \simeq \frac{1}{L^3} \frac{kk' F_\alpha(0) F^*_{\alpha'}(0) \cos(\widehat{\mathbf{k},\mathbf{k}'})/(1+\eta)}{E - \tilde{\delta} + i\hbar\gamma(E)/2} \tag{7}$$

with

$$\hbar\gamma(E) = \left(\frac{m}{\hbar^2} \right)^{5/2} \frac{(\lambda_2 \Delta^{3/2} + \lambda_1 E^{3/2})}{3\pi(1+\eta)},$$

$$\tilde{\delta} = \frac{(\delta - \delta_0)}{1+\eta}.$$

We note that this expression for the T matrix is consistent with the general theory of multichannel scattering resonances [13], where resonantly enhanced transitions to other channels are readily included. In a similar context of two open channels and a Feshbach resonance, a recent experiment was analyzed [15] that involved the decay of a molecular state formed from a Bose-Einstein condensate.

IV. *s* WAVE VS *p* WAVE

This section is devoted to the discussion of the expression found for the T matrix. In addition to the scattering cross section, the study of the T matrix yields important information on the structure of the dressed molecular state underlying the Feshbach resonance and we will demonstrate important qualitative differences between the behaviors of *p*-wave and *s*-wave resonances.

A. Molecular state

The binding energy E_b of the molecule is given by the pole of T. In the limit $\delta \sim \delta_0$, it is therefore given by

$$E_b = \tilde{\delta} - i\hbar\gamma(\tilde{\delta})/2,$$

We see that the real part of E_b (the "physical" binding energy) is $\sim\tilde{\delta}$ and therefore scales linearly with the detuning $\delta - \delta_0$. This scaling is very different from what happens for *s*-wave processes where we expect a $(\delta - \delta_0)^2$ behavior. This difference is in practice very important: indeed, the molecules can be trapped after their formation only if their binding energy is smaller than the trap depth. The scaling we get for the *p*-wave molecules means that the binding energy increases much faster when we increase the detuning than what we obtain for *s*-wave molecules (this feature was already pointed out in [11]). Hence, *p*-wave molecules must be looked for only in the close vicinity of the Feshbach resonance—for instance, for $\eta \ll 1$ (relevant for ^{6}Li, as we show below) and a trap depth of 100 μK, the maximum detuning at which molecules can be trapped is $\simeq 0.1$ G.

This asymptotic behavior of the binding energy is closely related to the internal structure of the molecule. Indeed, the molecular wave function $|\psi_m(B)\rangle$ can be written as a sum $|\text{open}\rangle + |\text{closed}\rangle$ of its projections on the closed and open channels, which correspond, respectively, to short- and long-range molecular states. If we neglect decay processes by setting $\lambda_2 = 0$, we can define the magnetic moment of the molecule (relative to that of the free atom pair) by

$$\Delta\mu_{\rm eff}(B) = -\frac{\partial E_b}{\partial B} = -\frac{\partial \tilde{\delta}}{\partial B},$$

that is, in the case of ^{6}Li where $\delta = 2\mu_B(B - B_0)$,

$$\Delta\mu_{\rm eff}(B) = -\frac{2\mu_B}{1+\eta}. \tag{8}$$

On the other hand, we can also write $E_b = \langle\psi_m(B)|\hat{H}(B)|\psi_m(B)\rangle$. Since in the absence of any decay channel, the molecular state is the ground state of the two-body system, we can write using the Hellmann-Feynman relation

$$\Delta\mu_{\rm eff} = -\frac{\partial E_b}{\partial B} = -\langle\psi_m(B)|\frac{\partial \hat{H}(B)}{\partial B}|\psi_m(B)\rangle.$$

In our model, the only term of the Hamiltonian depending on the magnetic field is the energy $\delta = 2\mu_B(B - B_0)$ of the bare molecular state in the closed channel and we finally have

$$\Delta\mu_{\rm eff} = -2\mu_B\langle{\rm closed}|{\rm closed}\rangle. \tag{9}$$

If we compare Eqs. (8) and (9), we see that the probability $P_{\rm closed} = \langle{\rm closed}|{\rm closed}\rangle$ to be in the closed channel is given by

$$P_{\rm closed} = 1/(1+\eta).$$

In other words, unless $\eta = \infty$, there is always a finite fraction of the wave function in the tightly bound state. In practice, we will see that in the case of ^{6}Li, $\eta \ll 1$. This means that the molecular states that are nucleated close to a Feshbach resonance are essentially short-range molecules. On the contrary, for *s*-wave molecules, $E_b \propto (\delta - \delta_0)^2$ leads to $\Delta\mu_{\rm eff} = -2\mu_B\langle{\rm closed}|{\rm closed}\rangle \propto (\delta - \delta_0)$. This scaling leads to a zero probability of occupying the bare molecular state near an *s*-wave resonance.

We can illustrate these different behaviors in the simplified picture of Fig. 3. For small detunings around threshold, the *p*-wave potential barrier provides a large forbidden region, which confines the bound state behind this barrier. The bound-state wave function decays exponentially inside the barrier and the tunneling remains nearly negligible. Since there is no significant difference for the shape of the *p*-wave bound state for small positive and negative detunings, the linear dependence of the closed channel on magnetic field will be conserved for the bound state, and therefore the binding energy will also linearly approach the threshold. We note that the linear dependence close to threshold can also be found from the general Breit-Wigner expression for a resonance, in combination with the *p*-wave threshold behavior of the phase shift [13].

The imaginary part of E_b corresponds to the lifetime of the molecule. In the case of *s*-wave molecules for which two-body decay is forbidden [20,21], the only source of instability is the coupling with the continuum of the incoming channel that leads to a spontaneous decay when $\tilde{\delta} > 0$ [see Fig. 3(a)]. By contrast, we get a finite lifetime in the *p* wave even at $\tilde{\delta} < 0$: due to dipolar relaxation between its constituents, the molecule can indeed spontaneously decay toward

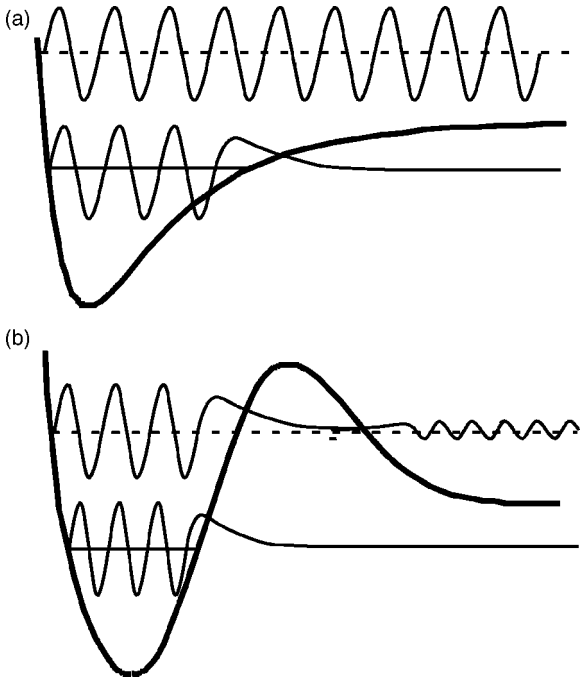

FIG. 3. Effect of the centrifugal barrier on the bound state in *p*-wave Feshbach resonances. (a) Case of *s*-wave scattering: the bare molecular state goes from $\delta < 0$ (full line) to $\delta > 0$ (dashed line). In the process, the molecular state becomes unstable and the wave function becomes unbounded. (b) In the case of a *p*-wave bound state, the presence of the centrifugal barrier smooths the transition from $\delta > 0$ to $\delta < 0$. Even for $\delta > 0$, the wave function stays located close to the bottom of the well.

state $|2\rangle$. For $\tilde{\delta} \sim 0$, the decay rate γ_0 associated with this process is given by

$$\gamma_0 = \gamma(0) = \frac{\lambda_2}{1+\eta}\frac{m}{3\pi\hbar^3}\left(\frac{m\Delta}{\hbar^2}\right)^{3/2}.$$

B. Elastic scattering

The scattering amplitude $f(\mathbf{k},\mathbf{k}')$ for atoms colliding in the channel 1 can be extracted from the *T* matrix using the relation

$$f(\mathbf{k},\mathbf{k}') = -\frac{mL^3}{4\pi\hbar^2}T_{11}(\mathbf{k},\mathbf{k}', E = \hbar^2k^2/m),$$

that is,

$$f(\mathbf{k},\mathbf{k}') = -\frac{m\lambda_1}{4\pi\hbar^2}\left(\frac{k^2\widehat{\cos(\mathbf{k},\mathbf{k}')}/(1+\eta)}{\hbar^2k^2/m - \tilde{\delta} - i\hbar\gamma/2}\right).$$

The $\widehat{\cos(\mathbf{k},\mathbf{k}')}$ dependence is characteristic of *p*-wave processes and, once again, this expression shows dramatic differences from the *s*-wave behavior. First, at low k, $f(\mathbf{k},\mathbf{k}')$ vanishes like k^2. If we introduce the so-called scattering volume V_s [13] defined by

$$f(\mathbf{k},\mathbf{k}') = -V_s k^2,$$

then we have

$$V_s = \frac{-m\lambda_1}{4\pi\hbar^2[\delta - \delta_0 + i(1+\eta)\hbar\gamma_0/2]} \sim \frac{-m\lambda_1}{2\pi\hbar^2(\delta-\delta_0)},$$

if we neglect the spontaneous decay of the molecule. We see that in this approximation, the binding energy E_b of the molecule is given by

$$E_b = -\frac{m\lambda_1}{2\pi\hbar^2(1+\eta)}\frac{1}{V_s}.$$

In *s*-wave processes, the binding energy and the scattering length are related through the universal formula $E_b = -\hbar^2/ma^2$. This relationship is of great importance since it allows one to describe both scattering properties and the molecular state with only one scattering length, without having to be concerned care with any other detail of the interatomic potential. In the case of the *p* wave, we see that no such universal relation exists between the scattering volume and E_b, a consequence of the fact that we have to deal with short-range molecular states, even at resonance. We therefore need two independent parameters to describe both the bound states and the scattering properties.

In the general case, the elastic cross section σ_{el} is proportional to $|f|^2$. According to our calculation, we can put σ_{el} under the general form

$$\sigma_{\mathrm{el}}(E) = \frac{CE^2}{(E-\tilde{\delta})^2 + \hbar^2\gamma^2/4}, \tag{10}$$

where $E=\hbar^2k^2/m$ is the kinetic energy of the relative motion and C is a constant depending on the microscopic details of the system. Noticeably, the energy dependence of the cross section exhibits a resonant behavior at $E=\tilde{\delta}$ as well as a plateau when $E\to\infty$, two features that were observed in the numerical coupled-channel calculations presented in [17]. Once again, this leads to physical processes very different from what is expected in *s*-wave scattering. Indeed, we know that in *s*-wave scattering, we have $f\sim -a$, as long as $ka \ll 1$. Since a is in general nonzero, the low-energy behavior gives a non-negligible contribution to the scattering processes. By contrast, we have just seen that in the case of the *p* wave, the low-energy contribution is vanishingly small ($\sigma_{\mathrm{el}}\sim E^2$) so that the scattering will be dominated by the resonant peak $E\sim\tilde{\delta}$.

C. Inelastic scattering.

For two particules colliding in channel 1 with an energy $E=\hbar^2k^2/m$, the probability to decay to channel 2 is proportional to $\rho_2(k')|T_{12}(\mathbf{k},\mathbf{k}',E)|^2$ where ρ_2 is the density of states in channel 2. Since k' is given by the energy conservation condition $\hbar^2k'^2/m-\Delta=E$, and in practice $\Delta \gg E$, we see that $k'\sim\sqrt{m\Delta/\hbar^2}$ is therefore a constant. Using this approximation, we can write the two-body loss rate $g_2(E)$ for particles of energy E as

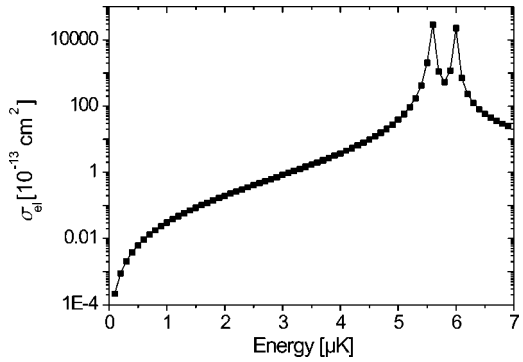

FIG. 4. Energy dependence of the elastic cross section. Dots: numerical closed-channel calculation. The left peak corresponds to $m_l=0$ and the right peak to $m_l=\pm1$. Full line: Fits using Eq. (11).

$$g_2(E) = \frac{DE}{(E-\tilde{\delta})^2 + \hbar^2\gamma^2/4},$$

where D is a constant encapsulating the microscopic details of the potential.

V. COMPARISON WITH COUPLED-CHANNEL CALCULATION

The quantities such as C, D, γ_0, etc., that were introduced in the previous section were only phenomenological parameters to which we need to attribute some value to be able to perform any comparison with the experiment. These data are provided by *ab initio* numerical calculations using the coupled-channel scheme described in [18]. The result of this calculation for the elastic scattering cross section is presented in Fig. 4. The most striking feature of this figure is that it displays two peaks instead of one, as predicted by Eq. (10). This difference can be easily understood by noting that the dipolar interaction that couples the molecular state to the outgoing channel provides a "spin-orbit" coupling that modifies the relative orbital angular momentum of the pair [17]. In other words, each resonance corresponds to a different value of the relative angular momentum m_l (the $m_l=+1$ and $m_l=-1$ resonances are superimposed because the frequency shift induced by the dipolar coupling is proportional to m_l^2, as noted in [17]).

As the spin-orbit coupling is not included in our simplified three-level model, we take the multiple peak-structure into account by fitting the data of Fig. 4 using a sum of three laws (10) with a different set of phenomenological parameters for each value of the angular momentum:

$$\sigma_{\mathrm{el}}(E) = \sum_{m_l=-1}^{+1} \frac{C_{m_l}E^2}{(E-\tilde{\delta}_{m_l})^2 + \hbar^2\gamma_{m_l}^2/4}, \tag{11}$$

where $\tilde{\delta}_{m_l}$ is related to the magnetic field through $\tilde{\delta}_{m_l}=\mu(B-B_{F,m_l})$ and $\gamma_{m_l}=\gamma_{0,m_l}+a_{m_l}E^{3/2}$. Using this law, we obtain a perfect fit to the elastic as well as inelastic data obtained from the coupled-channel calculations. The values obtained

TABLE I. Values of the phenomenological parameters obtained after a fit to the coupled-channel calculation data of Fig. 4. δB_F is the shift between the $m_l=\pm 1$ and $m_l=0$ resonances.

Channel	$(1/2,-1/2)$			$(-1/2,-1/2)$		
m_l	-1	0	1	-1	0	1
$C(10^{-13}\ \mathrm{cm}^2)$	0.22	0.22	0.22	0.87	0.88	0.87
$D(10^{-13}\ \mathrm{cm}^2\ \mu\mathrm{K/s})$	0.00002	0.59	0.56	3×10^{-5}	1.54	5.72
$\gamma_0(\mathrm{s}^{-1})$	$<10^{-2}$	110	110	<1	220	830
$a(\mu\mathrm{K}^{-1/2})$	0.0017	0.0017	0.0017	0.0024	0.0024	0.0024
η	0.22	0.22	0.22	0.23	0.23	0.23
$\delta B_F(\mathrm{G})$	-0.0036	0	-0.0036	-0.012	0	-0.012

for the different phenomenological parameters are presented on Table I.

From these data, we see first that the "elastic" properties are independent of m_l. This comes from the fact that the elastic scattering is mainly a consequence of the hyperfine coupling that does not act on the center-of-mass motion of the atoms. However, we see that both the inelastic collision rate constant D and the molecule lifetime γ_0 exhibit large variations with the relative angular momentum [22]. First, the spontaneous decay rate γ_0 of a molecule in $m_l=0,+1$ is always larger than $\sim 10^2\ \mathrm{s}^{-1}$, which corresponds to a maximum lifetime of about 10 ms. Second, we observe a strong reduction of the losses in the $m_l=-1$ channel, in which no significant spontaneous decay could be found. An estimate of γ_0 can nevertheless be obtained by noting that, since the elastic parameters are independent of m_l, the ratio D/γ_0 should not depend on m_l [this can be checked by comparing the ratios D/γ_0 for $m_l=0$ and $m_l=+1$ in the $(-1/2,-1/2)$ channel]. Using this assumption we find that $\gamma_0\sim 4\times10^{-3}\ \mathrm{s}^{-1}$ both in $(1/2,-1/2)$ and $(-1/2,-1/2)$. The reason for this strong increase of the lifetime of the molecules in $m_l=-1$ is probably because, due to angular momentum conservation, the outgoing pair is expected to occupy a state with $l=3$ after an inelastic process. Indeed, if we start in a two-body state (m_F,m_F') and if the dipolar relaxation flips the spin m_F', then the atom pair ends up in a state $(m_F,m_F'+1)$. This increase of the total spin of the pair must be compensated by a decrease of the relative angular momentum. Therefore, if the molecule was associated with a relative angular momentum m_l, it should end up with m_l-1. In the case of $m_l=-1$, this means that the final value of the relative angular momentum is $m_l=-2$, i.e., $l\geqslant 2$. But, according to selection rules associated with spin-spin coupling, the dipolar interaction can only change l by 0 or 2. Therefore, starting from a p-wave ($l=1$) compound, this can only lead to $l=3$. Let us now assume that the coupling between the molecular state and the outgoing channel is still proportional to the overlap between the two states [see Eq. (1)], even in the presence of a dipolar coupling: the argument above indicates that the ratio $\rho=\gamma_{0,m_l=-1}/\gamma_{0,m_l'\neq-1}$ between the decay rate of molecules in $m_l=-1$ and the one of molecules in $m_l'\neq 1$ is then of the order of

$$\rho\sim\left|\frac{\int g^*(r)j_3(kr)r^2dr}{\int g^*(r)j_1(kr)r^2dr}\right|^2,$$

where $k=\sqrt{m\Delta/\hbar^2}$ is the relative momentum of the atoms after the decay. For lithium, we have $R_e\sim 3$ Å [23] which yields $kR_e\sim 7\times10^{-2}$. This permits us to approximate the spherical Bessel functions j_l by their expansion at low k, $j_l(kr)\sim(kr)^l$, that is,

$$\rho\sim k^4\left|\frac{\int g^*(r)r^5dr}{\int g^*(r)r^3dr}\right|^2\sim(kR_e)^4.$$

With the numerical value obtained for kR_e, we get $\rho\sim 2\times10^{-5}$, which is, qualitatively, in agreement with the numerical coupled-channel calculations presented above.

VI. TEMPERATURE AVERAGING

In realistic conditions, the two-body loss rate G_2 needs to be averaged over the thermal distribution of atoms. G_2 is therefore simply given by

$$G_2(E)=\sqrt{\frac{\pi}{4(k_BT)^3}}\int_0^\infty g_2(E)e^{-E/k_BT}E^{1/2}dE.$$

The evolution of G_2 vs detuning is displayed in Fig. 5 and shows a strongly asymmetric profile that was already noticed in previous theoretical and experimental papers [8,10].

This feature can readily be explained by noting that in situations relevant to experiments, γ_0 is small with respect to temperature. We can therefore replace g_2 by a sum of Dirac functions centered on δ_{0,m_l}. When the δ_{0,m_l} are positive, G_2 takes the simplified form

$$G_2=4\sqrt{\pi}\sum_{m_l}\left(\frac{D_{m_l}}{\hbar\gamma_{m_l}(\tilde{\delta}_{m_l})}\right)\left(\frac{\tilde{\delta}_{m_l}}{k_BT}\right)^{3/2}e^{-\tilde{\delta}_{m_l}/k_BT}.$$

Moreover, if we neglect the lift of degeneracy due to the dipolar interaction coupling and we assume all the $\tilde{\delta}_{m_l}$ to be equal to some $\tilde{\delta}$, we get

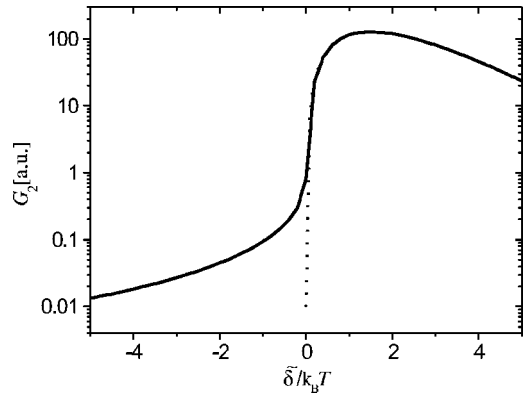

FIG. 5. Full line: numerical calculation of the loss rate for $T=10\ \mu$K. Dotted line: asymptotic expansion (12).

$$G_2 = 4\sqrt{\pi}\left(\frac{\overline{D}}{\hbar\,\overline{\gamma}(\tilde{\delta})}\right)\left(\frac{\tilde{\delta}}{k_BT}\right)^{3/2} e^{-\tilde{\delta}/k_BT}, \tag{12}$$

with $\overline{D}=\Sigma_{m_l} D_{m_l}$ and $\overline{D}/\overline{\gamma}=\Sigma_{m_l} D_{m_l}/\gamma_{m_l}$ [19].

For $\tilde{\delta}<0$ and $|\tilde{\delta}|\gg k_BT$, we can replace the denominator of g_2 by $\tilde{\delta}^2$ and we get the asymptotic form for G_2

$$G_2 = \frac{3}{2}k_BT\sum_{m_l}\frac{D_{m_l}}{\tilde{\delta}^2_{m_l}}. \tag{13}$$

Let us now comment on the two equations (12) and (13) .

(1) We note that the maximum value of G_2 is obtained for $\tilde{\delta}/k_BT=3/2$. It means that when tuning the magnetic field (i.e., $\tilde{\delta}$), the maximum losses are not obtained at the resonance $\tilde{\delta}=0$, but at a higher field, corresponding to $\tilde{\delta}=3k_BT/2$. For a typical experimental temperature $T=10\ \mu$K, this corresponds to a shift of about 0.1 G.

(2) Similarly, the width of $G_2(\tilde{\delta})$ scales like k_BT. Expressed in terms of magnetic field, this corresponds to $\sim$0.1 G for $T=10\ \mu$K. This width is a consequence of the resonance nature of the scattering in *p*-wave processes. As seen earlier, both elastic and inelastic collisions are more favorable when the relative energy $E=\tilde{\delta}$. When $\tilde{\delta}<0$, the resonance conditions cannot be satisfied, since there are no states in the incoming channel with negative energy. The scattering is then formally analogous to optical pumping or other second-order processes and yields the $1/\tilde{\delta}^2$ obtained in Eq. (13). When $\tilde{\delta}\gg k_BT$, the resonance condition is satisfied by states that are not populated (since for a thermal distribution, we populate states up to $E\sim k_BT$).

VII. CONCLUSION

In this paper, we have developed a simple model capturing the main scattering properties close to a *p*-wave Feshbach resonance. The analytical formulas we obtained show very good agreement with both numerical coupled-channel calculations and experimental measurements from our group [9] and from Chin and Grimm [24]. We have shown that the line shape of the resonance is very different from what is expected for an *s*-wave process: while *s*-wave scattering is mainly dominated by low-energy processes, *p*-wave scattering is rather dominated by collisions at energies equal to that of the molecular state. Regarding *p*-wave molecules, we have seen that at resonance their wave function was dominated by the short-range bare molecular state. Finally, the study of the spontaneous decay of these molecules has shown a very different lifetime depending on the relative angular momentum of its constituents, since molecules in $m_l=-1$ could live 10^4 times longer than those in $m_l=0,+1$. This very intriguing result might prove to be a valuable asset for the experimental study of *p*-wave molecules since it guarantees that $m_l=-1$ dimers are very stable against two-body losses in the absence of depolarizing collisions.

ACKNOWLEDGMENTS

We thank Z. Hadzibabic, J. Dalibard, and Y. Castin for very helpful discussions. S.K. acknowledges support from the Netherlands Organisation for Scientific Research (NWO) and E.U. Contract No. HPMF-CT-2002-02019. E.K. acknowledges support from the Stichting FOM, which is financially supported by NWO. M.T. acknowledges support from E.U. Contracts No. HPMT-2000-00102 and No. MEST-CT-2004-503847. This work was supported by CNRS, by the ACI photonique and nanosciences programs from the French Ministry of Research, and by Collège de France. Laboratoire Kastler Brossel is "Unité de recherche de l'École Normale Supèrieure et de l'Université Pierre et Marie Curie, associée au CNRS."

[1] S. Jochim, M. Bartenstein, A. Altmeyer, G. Hendl, S. Riedl, C. Chin, J. Hecker Denschlag, and R. Grimm, Science **302**, 2101 (2003).
[2] M. W. Zwierlein, C. A. Stan, C. H. Schunck, S. M. F. Raupach, S. Gupta, Z. Hadzibabic, and W. Ketterle, Phys. Rev. Lett. **91**, 250401 (2003).
[3] T. Bourdel, L. Khaykovich, J. Cubizolles, J. Zhang, F. Chevy, M. Teichmann, L. Tarruell, S. J. J. M. F. Kokkelmans, and C. Salomon, Phys. Rev. Lett. **93**, 050401 (2004).
[4] J. Kinast, S. L. Hemmer, M. E. Gehm, A. Turlapov, and J. E. Thomas, Phys. Rev. Lett. **92**, 150402 (2004).
[5] M. Greiner, C. A. Regal, and D. S. Jin, Nature (London) **426**, 537 (2003).
[6] D. M. Lee, Rev. Mod. Phys. **69**, 645 (1997).
[7] C. C. Tsuei and J. R. Kirtley, Phys. Rev. Lett. **85**, 182 (2000).
[8] C. A. Regal *et al.*, Phys. Rev. Lett. **90**, 053201 (2003).
[9] J. Zhang, E. G. M. van Kempen, T. Bourdel, L. Khaykovich, J. Cubizolles, F. Chevy, M. Teichmann, L. Tarruell, S. J. J. M. F. Kokkelmans, and C. Salomon, Phys. Rev. A **70**, 030702(R) (2004).

[10] C. H. Schunck, M. W. Zwierlein, C. A. Stan, S. M. F. Raupach, W. Ketterle, A. Simoni, E. Tiesinga, C. J. Williams, and P. S. Julienne, e-print cond-mat/0407373.
[11] T. L. Ho and N. Zahariev, e-print cond-mat/0408469; T. L. Ho and R. B. Diener, e-print cond-mat/0408468.
[12] Y. Ohashi, e-print cond-mat/0410516.
[13] J. R. Taylor, *Scattering Theory* (John Wiley, New York, 1972); H. Feshbach, *Theoretical Nuclear Physics* (John Wiley, New York, 1992).
[14] C. Chin, V. Vuletic, A. J. Kerman, and S. Chu, Phys. Rev. Lett. **85**, 2717 (2000); P. J. Leo, C. J. Williams, and P. S. Julienne, *ibid.* **85**, 2721 (2000).
[15] Thomas Volz, Stephan Drr, Niels Syassen, Gerhard Rempe, Eric van Kempen, and Servaas Kokkelmans, e-print cond-mat/0410083.
[16] A. R. Edmunds, *Angular Momentum in Quantum Mechanics* (Princeton University Princeton, NJ, Press, 1996).
[17] C. Ticknor, C. A. Regal, D. S. Jin, and J. L. Bohn, Phys. Rev. A **69**, 042712 (2004).
[18] E. G. M. van Kempen, B. Marcelis, and S. J. J. M. F. Kokkelmans, e-print cond-mat/0406722.
[19] For the sake of simplicity, these averaged parameters only were presented in [9].
[20] K. Dieckmann, C. A. Stan, S. Gupta, Z. Hadzibabic, C. H. Schunck, and W. Ketterle, Phys. Rev. Lett. **89**, 203201 (2002).
[21] H. T. C. Stoof, J. M. V. A. Koelman, and B. J. Verhaar, Phys. Rev. B **38**, 4688 (1988).
[22] Note that the different lifetimes calculated for the three m_l states do not violate any rotational symmetry. Indeed, the magnetic field used to reach the Feshbach resonance provides a preferred direction to the system.
[23] We evaluate R_e by identifying it with the relative distance r at which the total (centrifugal + long-range) potential $3\hbar^2/mr^2 - C_6/r^6 - C_8/r^8 - C_{10}/r^{10}$ cancels and we used the $C_{8,9,10}$ coefficients of [24]. Z.-C. Yan *et al.*, Phys. Rev. A **54**, 2824 (1996).
[24] C. Chin and R. Grimm (private communication).

Chapitre 3

Gaz de fermions déséquilibrés et impureté dans une mer de Fermi

noindent Nage nage
Ou tu bois le potage
Si tu bois le bouillon c'est bon
Mais si tu bois la tasse
Fais la brasse
Anne Sylvestre : Nage nage

3.1 Introduction

Le mécanisme BCS de superfluidité dans les systèmes fermioniques se fondant sur l'appariement de particules de spin opposés, il est tout naturel de se poser la question de la robustesse de l'ordre quantique à un éventuel déséquilibre des composantes de spins. Clogston et Chandrasekhar furent, dans les années 60, les premiers à offrir une réponse théorique à cette question : selon eux la superfluidité peut résister à un déséquilibre des potentiels chimiques $\mu_{\sigma=\uparrow,\downarrow}$ tant que la différence $\mu_\uparrow - \mu_\downarrow$ ne dépasse pas l'énergie de liasion des paires de Cooper [1, 2]. Au delà, l'état BCS devient instable selon un mécanisme qui n'est qu'encore partiellement élucidé. Dans le scénario le plus simple, les phases normales et superfluides se séparent spatialement selon une transition du premier ordre : dans la phase superfluide, les atomes minoritaires ($\downarrow$ pour fixer les idées)sont appariés avec un nombre identique d'atomes majoritaires, les atomes $\uparrow$ excédentaires se logeant dans une phase

normale par conséquent parfaitement polarisée. Des modèles plus raffinés ont par la suite été développés, notamment la théorie de Fulde, Ferrell, Larkin et Ovshinikov, qui ont proposé l'apparition d'une phase superfluide inhomogène (la phase FFLO) [3] ou bien la théorie de Sarma qui prédit au contraire qu'il pourrait exister une phase superfluide homogène caractérisée par une bande interdite dans la mer de Fermi des atomes majoritaires [4]. Expérimentalement, la réalisation de ces systèmes de spins déséquilibrés mit du temps à voir le jour, les candidats les plus évidents, les supraconducteurs, se prêtant mal à ce type de situation physique. En effet, pour polariser les électrons, il faut les immerger dans un champ magnétique intense, ce qui est interdit dans un supraconducteur qui se comporte comme un diamagnétique parfait (le fameux effet *Meissner*, responsable notamment de la lévitation d'un aimant au dessus d'un supraconducteur). Certaines analogies ont pu être trouvées entre ce problème et le comportement des mélanges boson/fermion d'^{4}He et d'^{3}He [5] : en effet, dans le régime de forte interaction, les paires de fermions responsables de la superfluidité sont des dimères bosoniques et un système de fermions déséquilibrés se comporte donc comme un mélange de bosons (les molécules) en présence d'atomes fermioniques excédentaires.

La réponse expérimentale aux interrogations de Clogston et Chandrasekar ne fut donnée qu'avec l'observation de la superfluidité des fermions ultra-froids, suite aux expériences réalisées indépendamment à Rice et MIT [6, 7]. Dans les systèmes atomiques, il est en effet très facile de contrôler le degré de polarisation des atomes par pompage optique ou transitions radiofréquences. Par ailleurs, le faible taux de collisions inélastiques résultant de l'extrême dilution de ces systèmes permet de conserver ces polarisations pendant toute la durée des séquences expérimentales. Ces deux expériences confirmèrent le résultat de Clogston et Chandrasekar concernant la rigidité de l'état superfluide : dans les deux cas, on put observer que des atomes de spins opposés restaient appariés au centre du nuage, dans une région où les densités des deux espèces étaient égales. La structure du nuage en dehors de ce cœur superfluide révéla cependant des surprises qui restent encore à élucider bien que d'importants pas vers leur compréhension aient déjà été faits. En effet, alors que le groupe de Rice observait une démixion complète dans laquelle tous les atomes minoritaires s'apparient avec les atomes majoritaires, laissant ainsi uniquement des atomes majoritaires dans la phase extérieur, le groupe de MIT mettait en évidence une phase intermédiaire supplémentaire dans laquelle coexistaient atomes minoritaires et majoritaires avec des densités différentes (Fig. 3.1).

Le chapitre qui suit est consacré à des travaux théoriques portant sur

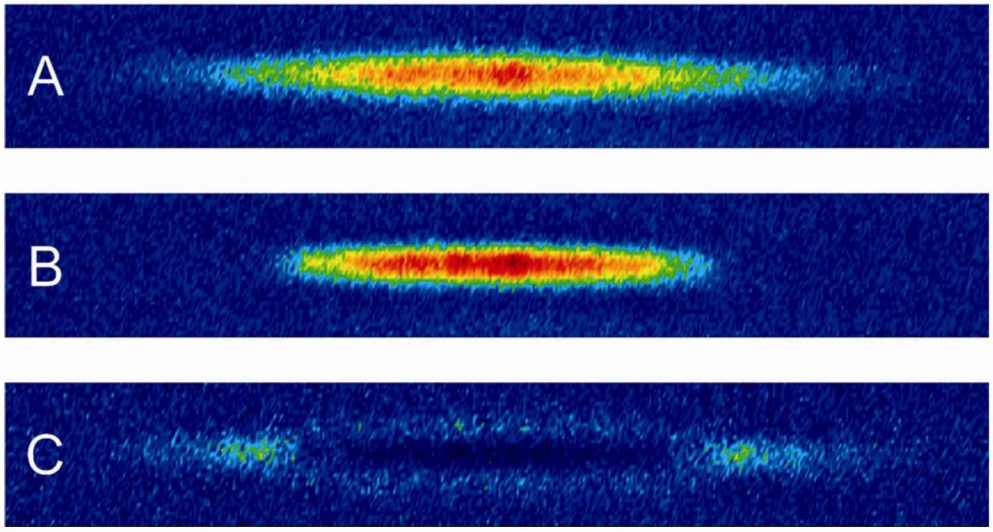

FIG. 3.1 – Profils de densités dans les expériences de Rice. (A) et (B) : profil de densité des espèces majoritaires et minoritaires. (C) Différence des deux précédents profils. On observe une démixion entre le cœur superfluide où les densités des deux espèces sont égales et la phase extérieure où ne subsiste que l'espèce majoritaire (données extraites de [6]). Dans des conditions similaires, le groupe de MIT observe une troisième phase s'intercalant entre les deux précédentes et contenant les deux espèces d'atomes avec des densités différentes.

l'analyse des données de Rice et MIT. Ces expériences étant réalisées à la résonance de Feshbach, nous avons utilisé les propriétés de lois d'échelles caractéristiques de la limite unitaire pour déterminer le nombre de phase d'un gaz de fermions déséquilibré et comparer aux résultats expérimentaux. Dans *Universal phase diagram of a strongly interacting Fermi gas with unbalanced spin populations*, nous avons montré que l'étude du problème dit à *N+1 corps* d'une impureté immergée dans une mer de Fermi permettait de discriminer entre un scénario à 2 ou 3 phases. Une étude variationnelle de ce problème à la limite unitaire nous a permis de déterminer une valeur approchée de l'énergie de l'état fondamental de l'impureté très proche de celle obtenue par les calculs Monte-Carlo, et d'en déduire la stabilité de la phase intermédiaire observée au MIT. Nous avons ensuite utilisé ce diagramme de phase pour analyser les données de Rice et MIT afin de tenter de saisir l'origine de leur désaccord.

3.2 Diagramme de phase d'un gaz de Fermi déséquilibré et problème à N+1 corps

Dans ce paragraphe, on cherche à établir l'allure générale du diagramme de phase d'un gaz de Fermi dont on déséquilibre les populations de spin. Comme signalé plus haut, cette étude a été motivée par les résultats des expériences de Rice et MIT, dans lesquelles les profils de densité semblaient indiquer l'existence de trois (MIT) ou deux (Rice) phases distinctes. La quasi-totalité des études théoriques tentant d'expliquer cette contradiction se fondent sur la théorie BCS, un modèle dont on sait qu'il ne fournit au mieux que des informations qualitatives dans le régime de forte interaction où sont réalisées les expériences. Nous avons donc cherché à contourner ce modèle trop simple afin de fournir une description aussi quantitative que possible des résultats expérimentaux.

Dans cette optique, nous avons pu montrer que de nombreuses propriétés physiques de ce problème complexe peuvent être déduites du problème à N+1 corps, autrement dit un système déséquilibré à l'extrême où l'on ajoute à une mer de Fermi de N spin $\uparrow$ une unique impureté de spin $\downarrow$. Considérons en effet un scénario de transition de phase impliquant trois phases distinctes : un superfluide complètement apparié dans lequel les densités des deux espèces sont égales, un gaz de fermions totalement polarisé ne contenant que des particules d'une espèce et enfin une phase intermédiaire (normale ou superfluide) contenant des particules des deux espèces en proportions différentes. Les équations d'état des phases totalement polarisées et totalement appariées sont connues : dans le premier cas il s'agit simplement d'un gaz parfait de fermions (puisque le principe de Pauli interdit les interactions entres fermions polarisés dans un même état de spin), et dans le second cas, l'équation d'état du superfluide fermionique a pu être établie à l'aide de simulations Monte-Carlo [8]. L'existence, la nature et la stabilité d'une éventuelle phase normale intermédiaire a longtemps fait débat. Parmi les nombreuses phases scénarios proposés, notons que le modèle BCS prédit que cette phase intermédiaire n'existe que dans le régime BCS ($a < 0$) et proche de l'unitarité. Dans le domaine BEC, cette phase intermédiaire est instable et on s'attend à une démixion totale des dimères bosoniques et des fermions excédentaires.

Afin de simplifier le problème, nous nous sommes dans un premier temps restreints au cas d'un système homogène de volume V dans le régime unitaire, où la divergence de la longueur de diffusion aboutit à des lois d'échelle simples. Ayant en tête une application ultérieure aux gaz piégés, nous avons

étudié le problème dans l'ensemble grand-canonique où les potentiels chimiques μ_σ sont fixés. Dans ce cas, la phase la plus stable est celle dont le grand potentiel Ω est le plus bas, ou, en vertu de l'identité thermodynamique $\Omega = -PV$, celle où la pression est la plus haute. En notant P_0 la pression d'un gaz parfait d'atomes majoritaires de potentiel chimique $\mu_\uparrow$, nous avons schématiquement représenté l'allure de P/P_0 en fonction de $\eta = \mu_\downarrow/\mu_\uparrow$ pour les trois phases sur la figure 3.2. Les valeurs η_c et η_β marquant respectivement les frontières des phases superfluides et intermédiaires avec la phase totalement polarisée déterminent la stabilité de la phase intermédiaire : en effet, on constate graphiquement que cette dernière ne sera stable que lorsque $\eta_\beta < \eta_\alpha$. η_c peut à la limite unitaire être calculé à partir du paramètre ξ introduit au chapitre précédent par la relation $\eta_c = (2\xi)^{3/5} - 1 \sim -0.09$. Le point η_β étant par ailleurs donné par la disparition de la dernière particule de spin minoritaire $\downarrow$, on voit que le problème est ramené à celui de l'étude d'une unique impureté immergée dans une mer de Fermi de particules majoritaires. Bien que considérablement simplifié par rapport au problème initial, ce problème à $N+1$ corps ne possède pour le moment pas de solution exacte, et nous nous sommes rabattus sur une résolution variationnelle du problème[1]. Les détails de ce calculs sont présentés dans *Universal phase diagram of a strongly interacting Fermi gas with unbalanced spin populations*. Pour résumer, on fait l'hypothèse que l'effet de l'impureté est faible sur la mer de Fermi environnante, et que l'on peut se limiter à la création d'une seule paire particule-trou. Tout calcul fait, on obtient la borne supérieure $\eta_\beta < -0.6$. Puisque $\eta_c > -0.6$, on en déduit donc la stabilité de la phase intermédiaire à l'unitarité.

En parallèle de ces calculs, les groupes de Trento et Amherst ont engagé une simulation Monte-Carlo de ce même problème [9, 10] et obtinrent un résultat identique à celui du calcul analytique présenté ci-dessus, prouvant que la borne supérieure du calcul variationnel était en réalité très proche du résultat exact. La raison de cet accord peut être comprise en évaluant la probabilité de créer une paire particule-trou à l'unitarité : bien que la longueur de diffusion soit infinie, la probabilité donnée par le calcul variationnel n'est que de 20%. Une évaluation naïve de la probabilité de former deux paires particules trou est donc de seulement 4%, ce qui justifie *a posteriori* l'ansatz choisi. Cette argument a par la suite était raffiné par le groupe de R. Combescot par un développement diagrammatique en puissance de k_F [11]. Le calcul Monte-Carlo ne s'arrête pas au problème à $N+1$ corps puis-

[1] La discussion de la stabilité de la phase intermédiaire ne nécessite en effet qu'une borne supérieure de η_β.

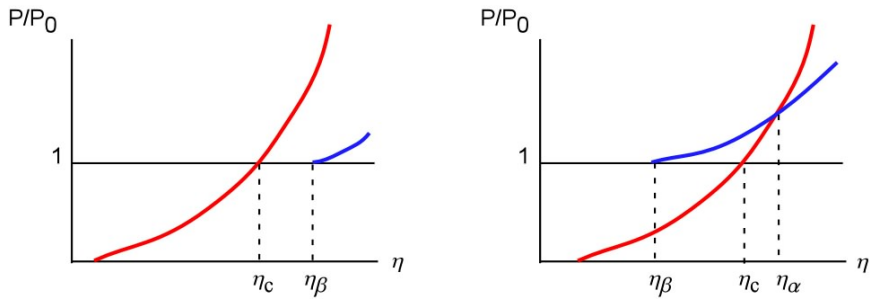

FIG. 3.2 – Pression P des différentes phases entrant en jeu dans les systèmes déséquilibrés, normalisée à la pression P_0 du gaz totalement polarisé. La ligne noire $P/P_0 = 1$ correspond au gaz parfaitement polarisé. La ligne rouge est le superfluide totalement apparié et la ligne bleu une éventuelle phase intermédiaire. Pour chaque valeur $\eta = \mu_\downarrow/\mu_\uparrow$ des rapports des potentiels chimiques, la phase la plus stable est celle dont la pression est la plus forte. À gauche, $\eta_\beta > \eta_c$ et la phase intermédiaire n'est jamais stable. À droite $\eta_\beta < \eta_c$ et la phase intermédiaire est stable entre η_α et η_β.

qu'il fournit également l'équation d'état de toute la phase intermédiaire : il montre qu'à basse densité d'impuretés, celles-ci se comporte comme un gaz parfait de particules fermioniques possédant la même masse effective $m^* \sim 1.197m$ que celle prédite par notre calcul variationnel. À plus haute densité, il montre que la transition entre la phase superfluide et ce mélange normal se produit pour $\eta_\alpha \sim 0.1$.

3.3 Application aux gaz piégés : les expériences de Rice et MIT

Les études précédentes sont faites dans le cadre de systèmes homogènes. Pour les étendre à des situations réalistes d'atomes piégés, une approximation couramment utilisées est l'approximation de densité locale dans laquelle on fait l'hypothèse que les potentiels chimiques locaux se mettent sous la forme $\mu_\sigma(\boldsymbol{r}) = \mu_\sigma^0 - V(\boldsymbol{r})$, où μ_σ^0 désigne le potentiel chimique global et V est le potentiel de piégeage. Dans le cas des expériences de MIT, l'accord entre théorie et expérience est remarquable, et ce malgré l'absence de paramètre ajustable dans le modèle (Fig. 3.3). Ainsi, les profils de densité sont parfaitement reproduits et l'observation à l'unitarité d'une polarisation critique $P_c = (N_\uparrow - N_\downarrow)/(N_\uparrow + N_\downarrow)$ de 0.76 au delà de laquelle le cœur du nuage n'est

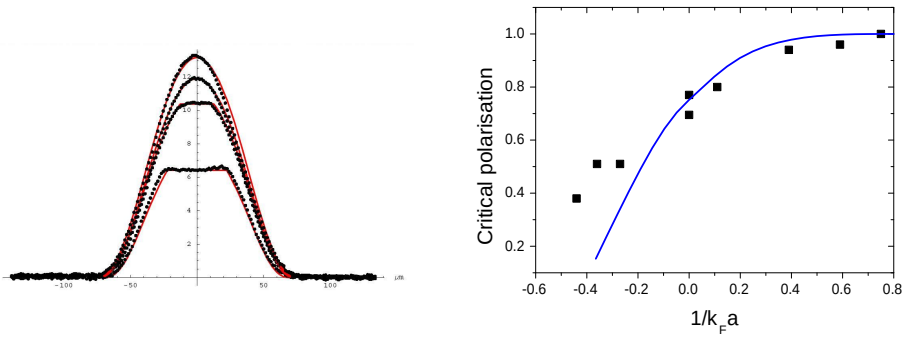

FIG. 3.3 – Gauche : Différence de densité intégrée dans deux dimensions d'un gaz de fermions à la limite unitaire (points : données de MIT, courbe : modèle variationnel). Les différentes courbes correspondent, de bas en haut, aux valeurs de polarisation P =58%, 73%, 80% et 92%. Le plateau de densité est une signature de la phase superfluide complètement appariée [13]. On note qu'au delà de la polarisation critique $P_c = 76\%$ ce plateau disparaît (Figure extraite de [12]). Droite : Évolution en fonction du paramètre $1/k_F a$ de la polarisation critique P_c au-delà de laquelle la phase superfluide disparaît. Les carrés correspondent aux données de MIT et la courbe en trait plein au modèle sans paramètre ajustable de gaz parfait de quasi-particules fermioniques habillées de paire particules trous.

plus superfluide est confirmée par les calculs précédents (Fig. 3.3). Lorsque $1/k_F a$ devient supérieure à 0.44, on constate expérimentalement que la polarisation critique devient égale à 1, et que la superfluidité résiste donc à tout déséquilibre. Devant l'étonnante réussite du calcul variationnel, nous avons poussé son application au-delà de la limite unitaire (*Normal State of Highly Polarized Fermi Gases : Simple Many-Body Approaches*) : dans le régime BCS, cette approche se ramène à un calcul perturbatif et coïncide avec celui-ci jusqu'à l'ordre deux inclus en perturbation, ce qui est confirmé par les calculs Monte-Carlo. Dans la région BEC, on retrouve pour $a \to 0^+$ l'énergie de liaison d'un dimère $E_b = -\hbar^2/ma^2$. Afin de tester la validité de notre approche, nous avons calculé la polarisation critique de disparition de la phase superfluide. Le résultat de ce calcul, ainsi que sa comparaison aux données expérimentales, est présenté sur la figure 3.3. On constate que pour $1/k_F a > 0.44$, le cœur du nuage est toujours superfluide, et qu'en dessous, la théorie reproduit bien l'expérience, sans paramètre ajustable.

Le modèle théorique élaboré aux paragraphes précédent reproduisant parfaitement les données expérimentales, on est alors naturellement amené à se poser la question du désaccord observé entre les résultats de Rice et MIT : d'une part la phase intermédiaire est absente des données de Rice et d'autre part on a pu y observer d'importantes déviations à l'approximation de densité locale. On pourrait être tenté d'accuser un artefact expérimental dans les données de Rice : pourtant, ces données sont parfaitement compatibles avec le scénario simple dans lequel on n'utilise que les phases superfluides et totalement polarisées, en introduisant une tension de surface entre ces deux phases afin de décrire les effets de violation de l'approximation de la densité locale (*Density Profile of a Trapped Strongly Interacting Fermi Gas with Unbalanced Spin Populations*) et [13]. On a pendant un certain temps cru que ces effets de tension de surface, amplifiés dans l'expérience de Rice du fait d'un plus petit nombre d'atomes et d'une plus grande anisotropie du piège, pouvaient être responsables de cette différence de comportement. Cependant, il s'est avéré que la tension de surface devait jouer en sens opposé et défavoriser un scénario à deux phases. Des expériences complémentaires menées à MIT ont d'ailleurs montré qu'en augmentant l'anisotropie de leur piège, ils ne reproduisaient toujours pas le résultat de Rice. Cette première explication étant invalidée, la polémique se poursuit. Une seconde possibilité pourrait provenir de la dynamique de refroidissement des nuages dans les deux expériences : à Rice, les atomes sont évaporés loin dans le régime BEC, dans un régime où la phase intermédiaire est instable. Les transitions mises en jeu étant du premier ordre, on sait qu'elles peuvent donner lieu à des phénomènes de métastabilité, éventuellement amplifiés par la tension

de surface comme dans les transitions liquide-vapeur plus classiques. Cette tentative d'explication est pour le moment purement spéculative et devra être confirmée ou infirmée par des expériences ultérieures.

3.4 Conclusion

Malgré ses succès évidents, l'étude théorique présentée dans ce chapitre est loin d'être close. En sus des mystères posés par les expériences de Rice, il faut noter que toute l'analyse se fonde sur une hypothèse de température nulle. Lorsque l'on se place à température finie, on s'attend à ce que le diagramme de phase s'enrichisse. Ainsi, on attend une phase de Sarma superfluide, mais non totalement appariés, ainsi qu'un point tricritique au niveau duquel la transition normal-superfluide passe du premier ordre au second ordre, comme cela avait déjà été brièvement envisagé dans *Density Profile of a Trapped Strongly Interacting Fermi Gas with Unbalanced Spin Populations* [5, 14].

Par ailleurs, ces études statiques doivent être complétées par la caractérisation du comportement dynamique du système : les modes de vibration étudiés jusqu'à présent étaient des modes d'"onde de densité" pour lesquels les deux espèces de spin oscillent avec la même phase. Les gaz polarisés autorisent à présent l'étude de modes d'"ondes de spin" pour lesquels les deux espèces oscillent avec des phases différentes. Partant de l'équation d'état de la phase intermédiaire, le groupe de Trento a ainsi pu établir le spectre du mode dipôlaire d'un gaz unitaire et quadrupolaire dans le régime normal [15, 12].

Bibliographie

[1] A. M. Clogston, Phys. Rev. Lett. **9**, 266 (1962)

[2] B. S. Chandrasekhar, Appl. Phys. Lett. **1**, 7 (1962) ;

[3] P. Fulde and R. A. Ferrell, Phys. Rev. **135**, A550 (1964) ; J. Larkin and Y. N. Ovchinnikov, Sov. Phys. JETP **20**, 762 (1965).

[4] G. Sarma, J. Phys. Chem. Solids **24**, 1029 (1963) ;

[5] M. M. Parish, F. M. Marchetti, A. Lamacraft et B. D. Simons Nature Physics **3**, 124 (2007).

[6] G. B. Partridge, W. Li, R. I. Kamar, Y. Liao, and R. G. Hulet, Science **311**, 503 (2006)

[7] M.W. Zwierlein, A. Schirotzek, C. H. Schunck, and W. Ketterle, Science **311**, 492 (2006) ;

[8] G. E. Astrakharchik, J. Boronat, J. Casulleras, and S. Giorgini, Phys. Rev. Lett. **93**, 200404 (2004).

[9] C. Lobo, A. Recati, S. Giorgini, and S. Stringari, Phys. Rev. Lett. **97**, 200403 (2006).

[10] N. Prokof'ev et B. Svistunov, Phys. Rev. B **77**, 020408(R) (2008).

[11] R. Combescot et S. Giraud, Phys. Rev. Lett. **101**, 050404 (2008).

[12] A. Recati, C. Lobo et S. Stringari, arXiv :0803.4419.

[13] T. N. De Silva and E. J. Mueller, Phys. Rev. Lett. **97**, 070402 (2006).

[14] K. B. Gubbels et H. T. Stoof, Phys. Rev. Lett. **100**, 140407 (2008).

[15] I. Bausmerth, A. Recati et S. Stringari, arXiv :0806.1885.

Density Profile of a Trapped Strongly Interacting Fermi Gas with Unbalanced Spin Populations

Density Profile of a Trapped Strongly Interacting Fermi Gas with Unbalanced Spin Populations

F. Chevy
Laboratoire Kastler Brossel, École Normale Supérieure, Paris, France
(Received 6 January 2006; published 4 April 2006)

We present a theoretical study of the density profile of a trapped strongly interacting Fermi gas with unbalanced spin populations. Making the assumption of the existence of a first order phase transition between an unpolarized superfluid phase and a fully polarized normal phase, we show good agreement with a recent experiment presented by Partridge *et al.*

DOI: 10.1103/PhysRevLett.96.130401 PACS numbers: 03.75.Hh, 03.75.Ss

In the Bardeen-Cooper-Schrieffer (BCS) mechanism, the onset of superfluidity is associated with pairing between two fermionic species with matched Fermi levels. This scheme is relevant to systems like metal superconductors, superfluid ^{3}He, or ultracold gases, as observed in recent ground breaking experiments [1–6]. However, other physical systems, like magnetized superconductors or neutron stars, require the understanding of fermionic superfluidity in the presence of mismatched chemical potentials. The nature of superfluidity in these systems has been the subject of long-standing debate [7–9], which has been renewed by the opportunity to address this topic experimentally using gaseous samples. Various mechanisms were proposed to describe the ground state of an ensemble of fermions with mismatched Fermi levels: deformed Fermi surface [10], Fulde-Ferrell-Larkin-Ovshinnikov (FFLO) states, where Cooper pairs acquire finite momentum, and their generalization to trapped systems [11–13], interior gap superfluidity [14], or phase separation between a normal and a superfluid state through a first order phase transition [15–18]. When the strength of the interactions is varied, a complicated phase diagram mixing several of these scenarios is expected [19–21].

Extending the seminal observation of fermionic superfluidity in ultracold atom systems, two recent experiments [22,23] have started probing the regime of mismatched Fermi levels by cooling samples containing different atom numbers in each spin state. In this Letter we focus on the results presented in Ref. [23] where the authors studied the density profile of a gas of fermionic lithium when varying, in the regime of strong interactions, the population imbalance between the two trapped spin states. One of the most striking results is displayed in Fig. 1. It shows that the radius of the minority component is strongly reduced with respect to that of noninteracting gas with the same atom number. In this Letter, we propose an interpretation of this result on the basis of the existence of first order phase separation between the normal and superfluid components and the use of universality in the strong interaction regime. We show that these two ingredients are sufficient to provide a good quantitative agreement with experimental data. It is therefore complementary to recent studies of Refs. [24–27], who address the same topics using a more complicated formalism.

Our analysis is based on the assumption of the existence of a zero temperature first order phase transition between a fully polarized normal phase containing a single spin species and an ''unpolarized'' superfluid state composed of a balanced mixture of the two species. The existence of this phase transition was suggested by previous theoretical studies [15–17] and is based on the following qualitative argument: In the grand canonical ensemble, the chemical potentials μ_i of the two species are fixed. In the ground state, the system minimizes the grand-potential $\Xi = H - \sum_i \mu_i N_i$, where H is the Hamiltonian of the system and N_i is the population of species i. Let us now consider a situation where the chemical potentials are mismatched, with $\delta\mu = \mu_1 - \mu_2 > 0$. Promoting a particle from state 2 to state 1 decreases the grand potential by $\delta\mu$ but implies the breaking of a pair, hence increases the energy by the

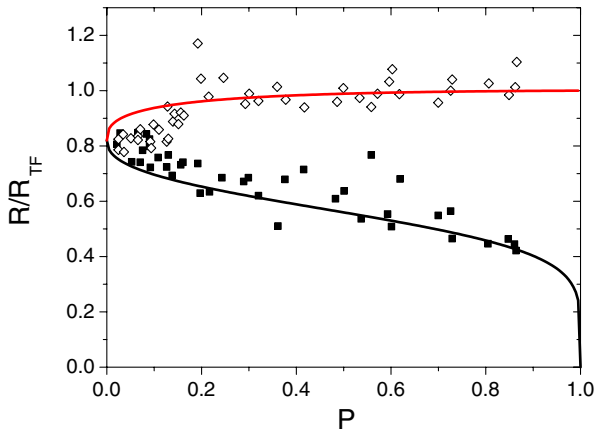

FIG. 1 (color online). Comparison between experimental data of Ref. [23] and the model presented here. $P = (N_1 - N_2)/(N_1 + N_2)$ is the imbalance between the two spin populations. The radius R of each component is normalized to the radius R_{TF} of the ideal Fermi gas containing the same atom number. Squares and diamonds correspond to experimental measurements of the radii of the minority and majority components, respectively. The full lines are the predictions of the first order transition model.

superfluid gap Δ. When $\delta\mu \lesssim \Delta$ we therefore expect the system to be unpolarized, while above this threshold a fully polarized system is obtained.

At zero temperature, the actual position of the phase transition can be found analytically in the case of a homogeneous unitary gas by matching chemical potentials and pressures in the two phases [17]. Indeed, we can write in the unpolarized phase $n_1 = n_2 = f(\mu_1, \mu_2)$. Using the thermodynamical identity $\partial_{\mu_1} n_2 = \partial_{\mu_2} n_1$, we deduce that f can actually be expressed as a function of $\mu = (\mu_1 + \mu_2)/2$ only. To obtain the exact expression for f, we then consider the case of matched Fermi surfaces, $\mu_1 = \mu_2 = \mu$. In this latter case, universality at the unitary limit allows one to write $\mu = \xi E_F$, where $E_F = \hbar^2(6\pi^2 n)^{2/3}/2m$ is the Fermi energy of a noninteracting gas of density $n = n_{1,2}$ and ξ is a universal parameter whose determination has attracted a lot of attention from both theoretical [17,28–30] and experimental groups [4,23,31–33] and is now thought to be $\xi \sim 0.45$. Using this expression for the chemical potential, we then deduce that

$$n_1 = n_2 = \frac{1}{6\pi^2}\left(\frac{m}{\xi\hbar^2}(\mu_1 + \mu_2)\right)^{3/2}. \tag{1}$$

The Gibbs-Duhem identity $dP_S = n_1 d\mu_1 + n_2 d\mu_2$ finally yields for the pressure in the superfluid phase

$$P_{\mathrm{S}} = \frac{1}{15\pi^2}\left(\frac{m}{\xi\hbar^2}\right)^{3/2}(\mu_1 + \mu_2)^{5/2}. \tag{2}$$

In the normal phase, we assume only the majority component is present. We have then an ideal gas constituted of particles of type 1 with chemical potential μ_1, thus giving

$$P_{\mathrm{N}} = \frac{1}{15\pi^2}\left(\frac{2m}{\hbar^2}\right)^{3/2}\mu_1^{5/2}. \tag{3}$$

Equating P_{N} and P_{S} [34], we see that the two phases coexist only if μ_1 and μ_2 satisfy the condition $\mu_2/\mu_1 = \eta_{\mathrm{c}}$ with

$$\eta_{\mathrm{c}} = (2\xi)^{3/5} - 1 \sim -0.061, \tag{4}$$

a relation already found in Refs. [17,18]. In a trap, the chemical potential depends on position.

To compare with experiments, we now consider the case of a cloud of atoms trapped in a harmonic potential $V(\boldsymbol{r}) = m\sum_i \omega_i^2 x_i^2/2$. Without loss of generality, we will restrict our analysis to the case of a isotropic trap with frequency $\bar{\omega} = (\omega_x\omega_y\omega_z)^{1/3}$. We can indeed always recover the more general anisotropic case by making the scaling transform $x_i \to \omega_i x_i/\bar{\omega}$.

To calculate the density profile of the cloud, we make use of the local density approximation, where we assume that the chemical potential of species i depends on position as $\mu_i(\boldsymbol{r}) = \mu_i^0 - V(\boldsymbol{r})$.

If we assume component 1 is the most populated, the inner superfluid region is defined by the condition $\mu_2(\boldsymbol{r})/\mu_1(\boldsymbol{r}) < \eta_c$ and is bounded by the radius R_2 defined by

$$R_2^2 = \frac{2}{m\bar{\omega}^2}\left(\frac{\mu_2^0 - \eta_{\mathrm{c}}\mu_1^0}{1 - \eta_{\mathrm{c}}}\right). \tag{5}$$

Atoms of the minority species are located in the paired superfluid phase only. We thus have

$$N_2 = \int_{r<R_2} n_2(\boldsymbol{r}) d^3\boldsymbol{r} = \frac{2}{3\pi\xi^{3/2}}\left(\frac{\mu_1^0 + \mu_2^0}{\hbar\bar{\omega}}\right)^3 g(R_2/\bar{R}), \tag{6}$$

where $\bar{R}^2 = (\mu_1^0 + \mu_2^0)/m\bar{\omega}^2$ and

$$g(x) = \frac{x\sqrt{1-x^2}(-3 + 14x^2 - 8x^4) + 3\arcsin(x)}{48}. \tag{7}$$

Excess atoms of the majority species are located between $r = R_2$ and $r = R_1$ such that $m\bar{\omega}^2 R_1^2/2 = \mu_1^0$. The number of excess atoms is therefore $N_1 - N_2 = \int_{R_2}^{R_1} n_1(\boldsymbol{r}) d^3\boldsymbol{r}$, hence

$$N_1 - N_2 = \frac{2}{3\pi}\left(\frac{2\mu_1^0}{\hbar\bar{\omega}}\right)^3 [g(1) - g(R_2/R_1)]. \tag{8}$$

Dividing (8) by (6) yields the implicit equation for $\eta_0 = \mu_2^0/\mu_1^0$ as a function of N_1/N_2

$$\frac{N_1}{N_2} = 1 + \xi^{3/2}\frac{8}{(1+\eta_0)^3}\frac{g(1) - g(R_2/R_1)}{g(R_2/\bar{R})}. \tag{9}$$

Equation (9) is solved numerically and the value obtained for η_0 is then used to calculate the radii R_1 and R_2. The predicted evolution of the R_i versus the population imbalance $P = (N_1 - N_2)/(N_1 + N_2)$ is shown in Fig. 1. To follow Ref. [23], we have normalized each R_i to the Thomas-Fermi radius R_{TF} associated with an ideal gas containing N_i atoms. The agreement with the experimental data is quite good as soon as $P \gtrsim 0.1$, a remarkable result, since the model presented here contains no adjustable parameter, as soon as the value of ξ is known.

For weak population unbalance, experimental variations of the radii are flatter than predicted by the first order transition model. As proposed in Ref. [23], this suggests that the phase separation does not happen exactly at $P = 0$, but above some threshold $P_{\mathrm{c}} \sim 0.1$. This point is strengthened when one compares the theoretical and experimental density profiles. As in Ref. [23], we have represented in Fig. 2 the integrated column density $\tilde{n}_i(x) = \int dy n_i(x, y, 0)$ for $P = 0.57$ (as in Fig. 2.D of Ref. [23]). We immediately see in this figure that the transition between the two phases is very sharp, by contrast to what is observed experimentally. Finite temperature might explain this discrepancy. Indeed, for low population imbalance, the superfluid phase extends nearly throughout all the cloud, and, in particular, in regions where the density, hence the Fermi energy, is

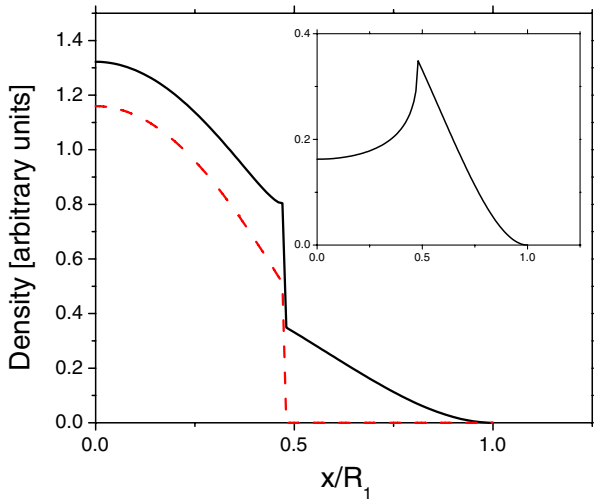

FIG. 2 (color online). Integrated column density of the majority (full line) and minority components (dashed line) for a population imbalance $P = 0.57$. Inset: excess column density $\tilde{n}_1 - \tilde{n}_2$. By contrast with the experimental results, the boundary between the two phases is here very sharp.

very low. In the unitary regime, the critical temperature for the superfluid-normal transition is given by the scaling $k_B T_c = \alpha E_F$, with $\alpha \sim 0.2$ [35]. It may then happen that near the cloud edge, the temperature T of the sample becomes locally larger than T_c. If this condition is satisfied at a radius R_c smaller than the demixing radius R_2, then the first order transition to the fully unpaired state will not happen. If we introduce the Fermi temperature $T_F = \hbar\bar{\omega}(6N_1)^{1/6}/k_B$ associated with a number of atoms N_1, the superfluid-normal and paired-unpaired transitions will happen at the same position if T/T_F satisfies the condition

$$\frac{T}{T_F} = \frac{\alpha}{2\xi}\left(\frac{R_1}{R_{TF}}\right)^2\left[1 + \eta_0 - 2\left(\frac{R_2}{R_1}\right)^2\right]. \qquad (10)$$

In Fig. 3, we have plotted as a function of temperature the evolution of the critical imbalance under which no demixing is expected. Experimentally, demixing only happens in the conditions of Ref. [23] for $P \gtrsim 0.1$, which, according to Eq. (10), corresponds to $T/T_F \lesssim 0.1$, a value compatible with experimental data. Despite a semiqualitative agreement, this finite temperature argument needs to be clarified by a more careful analysis, following, for instance, the work presented in Ref. [25]. Other scenarios can also be envisioned to explain the smooth crossover between the two phases, such as the existence of an intermediate phase—e.g., a gapless or FFLO phase as proposed in Ref. [20]—or a breakdown of the local density approximation due to the fast variation of the density profile. Nevertheless, the good agreement between theory and experiment for the data presented in Fig. 1 suggests that the crossover region between paired and unpaired phases should remain relatively narrow.

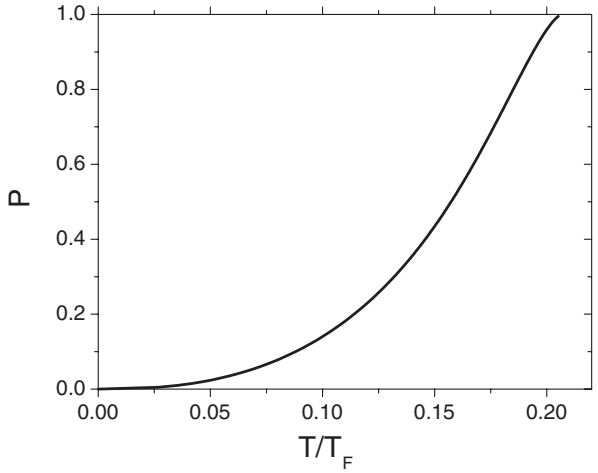

FIG. 3. Critical population imbalance under which finite temperature effects overrule demixing. The observed experimental threshold $P \sim 0.1$ corresponds to a temperature $T/T_F \lesssim 0.1$.

From the analysis presented here, it appears that the observations of Ref. [23] are consistent with a scenario of a transition between a fully paired and a fully polarized phase separated by a narrow crossover region probably related to finite temperature effects breaking the superfluid phase before demixing may occur. Interestingly, if this thermal scenario were confirmed the measurement of the critical population unbalance under which no phase separation happens could provide a useful tool for fermion thermometry. Another issue not addressed here is related to the superfluid character of the system when the population imbalanced is varied. This is especially important if one wishes to understand the results presented in Ref. [22] where it is shown that a mismatch of the Fermi surfaces by about 50% leads to a breakdown of superfluidity.

The author wishes to thank C. Mora and C. Salomon as well as the cold atom group for helpful discussions. This work is partially supported by CNRS, Collège de France, ACI nanoscience, and Région Ile de France (IFRAF). Laboratoire Kastler Brossel is Unité de recherche de l'École Normale Supérieure et de l'Université Pierre et Marie Curie, associée au CNRS.

[1] S. Jochim, M. Bartenstein, A. Altmeyer, G. Hendl, S. Riedl, C. Chin, J. Hecker Denschlag, and R. Grimm, Science **302**, 2101 (2003).
[2] M. Greiner, C. A. Regal, and D. S. Jin, Nature (London) **426**, 537 (2003).
[3] M. W. Zwierlein, C. A. Stan, C. H. Schunck, S. M. F. Raupach, S. Gupta, Z. Hadzibabic, and W. Ketterle, Phys. Rev. Lett. **91**, 250401 (2003).
[4] T. Bourdel, L. Khaykovich, J Cubizolles, J. Zhang, F. Chevy, M. Teichmann, L. Tarruell, S. J. J. M. F. Kokkelmans, and C. Salomon, Phys. Rev. Lett. **93**, 050401 (2004).

[5] J. Kinast, S. L. Hemmer, M. E. Gehm, A. Turlapov, and J. E. Thomas, Phys. Rev. Lett. **92**, 150402 (2004).
[6] G. B. Partridge, K. E. Strecker, R. I. Kamar, M. W. Jack, and R. G. Hulet, Phys. Rev. Lett. **95**, 020404 (2005).
[7] G. Sarma, J. Phys. Chem. Solids **24**, 1029 (1963).
[8] P. Fulde and R. A. Ferrell, Phys. Rev. **135**, A550 (1964).
[9] J. Larkin and Y. N. Ovchinnikov, Sov. Phys. JETP **20**, 762 (1965).
[10] A. Sedrakian, J. Mur-Petit, A. Polls, and H. Müther, Phys. Rev. A **72**, 013613 (2005).
[11] R. Combescot, Europhys. Lett. **55**, 150 (2001).
[12] C. Mora and R. Combescot, Phys. Rev. B **71**, 214504 (2005).
[13] P. Castorina, M. Grasso, M. Oertel, M. Urban, and D. Zappalà, Phys. Rev. A **72**, 025601 (2005).
[14] W. V. Liu and F. Wilczek, Phys. Rev. Lett. **90**, 047002 (2003).
[15] P. F. Bedaque, H. Caldas, and G. Rupak, Phys. Rev. Lett. **91**, 247002 (2003).
[16] H. Caldas, Phys. Rev. A **69**, 063602 (2004).
[17] J. Carlson and S. Reddy, Phys. Rev. Lett. **95**, 060401 (2005).
[18] T. D. Cohen, Phys. Rev. Lett. **95**, 120403 (2005).
[19] C. H. Pao, Shin-Tza Wu , and S.-K. Yip, cond-mat/0506437 [Phys. Rev. B (to be published)].
[20] D. T. Son and M. A. Stephanov, cond-mat/0507586.
[21] D. E. Sheehy and L. Radzihovsky, Phys. Rev. Lett. **96**, 060401 (2006).
[22] M. W. Zwierlein, A. Schirotzek, C. H. Schunck, and W. Ketterle, Science **311**, 492 (2006).
[23] G. B. Partridge, W. Li, R. I. Kamar, Y.-A. Liao, and R. G. Hulet, Science **311**, 503 (2006).
[24] P. Pieri and G. C. Strinati, cond-mat/0512354.
[25] W. Yi and L.-M. Duan, cond-mat/0601006 [Phys. Rev. A (to be published)].
[26] T. N. De Silva, and E. J. Mueller, cond-mat/0601314.
[27] M. Haque and H. T. C. Stoof, cond-mat/0601321.
[28] A. Perali, P. Pieri, and G. C. Strinati, Phys. Rev. Lett. **93**, 100404 (2004).
[29] J. Carlson, S.-Y. Chang, V. R. Pandharipande, and K. E. Schmidt, Phys. Rev. Lett. **91**, 050401 (2003).
[30] G. E. Astrakharchik, J. Boronat, J. Casulleras, and S. Giorgini, Phys. Rev. Lett. **93**, 200404 (2004).
[31] K. M. O'Hara, S. L. Hemmer, M. E. Gehm, S. R. Granade, and J. E. Thomas, Science **298**, 2179 (2002).
[32] M. Bartenstein, A. Altmeyer, S. Riedl, S. Jochim, C. Chin, J. H. Denschlag, and R. Grimm, Phys. Rev. Lett. **92**, 120401 (2004).
[33] J. Kinast *et al.*, Science **307**, 1296 (2005).
[34] The equality between the pressures in the two phases is actually not rigorous when trapping is taken into account. Indeed, in a trap the interface between the two phases is curved and surface tension will provoke a pressure jump given by Laplace's law $\Delta P \sim \sigma/R$, where σ is the surface tension constant. However, using a universality argument, one expects that $\sigma \sim P_F/k_F$, where P_F and k_F are, respectively, the Fermi pressure and the Fermi wave vector of the uniform system. Hence $\Delta P/P_F \sim (k_F R)^{-1/3} \ll 1$ in the Thomas-Fermi limit. Surface tension effects will have to be taken into account only in the limit of strongly curved interfaces, i.e., when the minority component is vanishingly small and forms a tiny drop of radius $R \sim k_F^{-1}$ at the center of the trap.
[35] A. Bulgac, J. E. Drut, and P. Magierski, Phys. Rev. Lett. **96**, 090404 (2006).

Universal phase diagram of a strongly interacting Fermi gas with unbalanced spin populations

Universal phase diagram of a strongly interacting Fermi gas with unbalanced spin populations

F. Chevy
Laboratoire Kastler Brossel, École Normale supérieure, Paris, France
(Received 31 May 2006; published 29 December 2006)

We present a theoretical interpretation of a recent experiment presented by Zwierlein *et al.* [Nature (London) **442**, 54 (2006)] on the density profile of Fermi gases with unbalanced spin populations. We show that in the regime of strong interaction, the boundaries of the three phases observed by Zwierlein *et al.* can be characterized by two dimensionless numbers η_α and η_β. Using a combination of a variational treatment and a study of the experimental results, we infer rather precise bounds for these two parameters.

DOI: 10.1103/PhysRevA.74.063628 PACS number(s): 03.75.Hh, 05.30.Fk, 03.75.Ss, 32.80.Pj

I. INTRODUCTION

In fermionic systems, superfluidity arises from the pairing of two particles with opposite spin states, a scenario first pointed out by Bardeen, Cooper, and Schrieffer (BCS) to explain the onset of superconductivity in metals. For this mechanism to be efficient, the Fermi surfaces associated with each spin component need be matched, and soon after the seminal BCS work the question of the effect of a population imbalance between the two states was raised. At the time, it was understood that pairing and superfluidity could sustain a certain amount of mismatch, above which the system would undergo a quantum phase transition toward a normal state [1]. The original work of Fulde, Ferrel, Larkin, and Ovchinnikov, who proposed the existence of Cooper pairing at finite momentum, was later generalized to trapped systems [2]. Alternative scenarios were also proposed, including deformed Fermi surfaces [3], interior gap superfluidity [4], phase separation between a normal and a superfluid state through a first-order phase transition [5], BCS quasiparticle interactions [7] or onset of *p*-wave pairing [8]. When the strength of the interactions is varied, a complicated phase diagram mixing several of these scenarios is expected [9].

However, due to the absence of experimental evidence, these scenarios could never be tested experimentally until the subject was revived by the possibility of reaching superfluidity in ultracold fermionic gaseous systems [10,11]. Contrary to usual condensed matter systems, spin relaxation is very weak in cold atoms, and this allows one to keep spin-polarized samples for long times. This unique possibility led to the first experimental studies of imbalanced Fermi gases at MIT and Rice University [12–14]. These results triggered a host of theoretical work aimed at explaining the various results observed by the two groups [15,16].

One remarkable feature of Ref. [14] is the observation of three different phases in the cloud. At the center, the authors observe a superfluid core, where the densities of the two spin states are equal, then an intermediate normal shell where the two states coexist, and finally an outer rim of the majority component. In the present paper, we show that, though performed in a trap, the observations of MIT can offer valuable information on the phase diagram of a strongly interacting Fermi gas with unbalanced populations. In the first part, we will present a brief overview of the simplest free-space scenario for transition from a paired superfluid to a pure normal state, through a mixed phase. Focusing on the disappearance of the minority component, we will present a variational study of the problem of a single minority particle embedded in the Fermi sea of majority atoms. Finally, we will show that the comparison with experiments allows for a rather precise determination of the transition thresholds. One of the key point is that, contrary to previous works, we rely on universal thermodynamics [17] as well as "exact" experimental or Monte Carlo results, without the need of the mean-field BCS ansatz often used in other publications, an approach similar to that of [18].

II. HOMOGENEOUS SYSTEM

Before addressing the case of trapped fermions, let us first discuss their free-space phase diagram. We consider zero-temperature fermions of mass m with two internal states labeled 1 and 2. Within a quantization volume V and in the limit of short-range interactions, we can write the Hamiltonian of the system as

$$\hat{H} = \sum_{k,\sigma} \epsilon_k \hat{a}^\dagger_{k,\sigma} \hat{a}_{k,\sigma} + \frac{g_b}{V} \sum_{k,k',q} \hat{a}^\dagger_{k+q,1} \hat{a}^\dagger_{k'-q,2} \hat{a}_{k',2} \hat{a}_{k,1}. \quad (1)$$

Here, $\epsilon_k = \hbar^2 k^2/2m$, $\hat{a}_{k,\sigma}$ is the annihilation operator of a species σ particle with momentum $\boldsymbol{k}$, and g_b is the bare coupling constant characterizing interparticle interactions. It is related to the *s*-wave scattering length of the system a by the Lippmann-Schwinger equation,

$$\frac{1}{g_b} = \frac{m}{4\pi\hbar^2 a} - \frac{1}{V}\sum_k \frac{1}{2\epsilon_k}. \quad (2)$$

We note that only interactions between particles of opposite spins are taken into account due to the Pauli principle, which forbids *s*-wave scattering of atoms with identical spin. In this paper, we assume we are working at the unitary limit where $|a| = \infty$, and, using the grand canonical ensemble, we wish to find the ground state of the grand potential $\hat{\Xi} = \hat{H} - \mu_1 \hat{N}_1 - \mu_2 \hat{N}_2$. Here, $\hat{N}_i$ is the particle number operator for species i and μ_i is the associated chemical potential (we take species 1 as majority, hence $\mu_1 > \mu_2$). The grand potential can be expressed as the function of the volume V and pressure P of the ensemble according to $\langle \hat{\Xi} \rangle = -PV$. In other words, searching the ground state of the system is equivalent

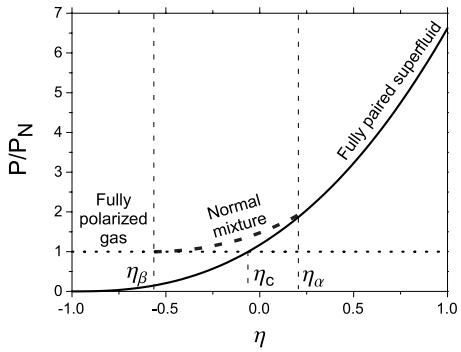

FIG. 1. Comparison of the pressure of the various phases, normalized by the pressure P_N of the fully polarized ideal Fermi gas, as a function of the chemical potential mismatch $\eta=\mu_2/\mu_1$. Dotted line: fully polarized phase. Full line: fully paired superfluid phase. The fully paired and fully polarized states meet for $\eta_c\sim-0.099$. Dashed line: sketch of the intermediate normal phase. η_α and η_β designate the universal chemical potential thresholds for this phase.

to searching the phase with the highest pressure P.

To start our analysis, we note first that two exact eigenstates of $\hat{\Xi}$ can be found quite easily. First, when the gas is fully polarized, we recover the case of an ideal Fermi gas for which we know that

$$P_N=\frac{1}{15\pi^2}\left(\frac{2m}{\hbar^2}\right)^{3/2}\mu_1^{5/2}.$$

Second, let us now consider the exact ground state $|\mathrm{SF}\rangle_\mu$ of the balanced grand potential $\hat{\Xi}'=\hat{H}-\mu(\hat{N}_1+\hat{N}_2)$, describing a superfluid with chemical potential μ. This potential commutes with the number operators, hence the ground state can be searched as an eigenstate for both $\hat{N}_1$ and $\hat{N}_2$, with $\hat{N}_1|\mathrm{SF}\rangle_\mu=\hat{N}_2|\mathrm{SF}\rangle_\mu$. We check readily that $|\mathrm{SF}\rangle_{\bar{\mu}}$, with $\bar{\mu}=(\mu_1+\mu_2)/2$, is still an eigenstate of the unbalanced $\hat{\Xi}$, by noting that $\hat{\Xi}=\hat{\Xi}'+(\mu_1-\mu_2)(\hat{N}_1-\hat{N}_2)/2$. At unitarity, the pressure of a balanced Fermi gas reads $P_S=2(2m/\xi\hbar^2)^{3/2}\mu^{5/2}/15\pi^2$, where $\xi\sim0.42$ is a universal parameter whose determination has attracted the interest of both theoreticians [6,19–21] and experimentalists [11,22]. In the case of mismatched chemical potentials, the pressure of this fully paired superfluid state is therefore

$$P_S=\frac{1}{15\pi^2}\left(\frac{m}{\xi\hbar^2}\right)^{3/2}(\mu_1+\mu_2)^{5/2}.$$

The evolution of P_N and P_S is presented in Fig. 1 as a function of $\eta=\mu_2/\mu_1$. We see that they cross for $\eta_c=(2\xi)^{3/5}-1\sim-0.10$, marking the instability of the superfluid against large population imbalances [16]. However, since we only compare the energy of the fully paired state to the one of the fully polarized ideal gas, the real breakdown of superfluidity could very well happen for some η larger than η_c. We know this is actually the case, since in Ref. [14] the authors observed an intermediate normal phase, containing atoms of both species. From universality at unitarity, the phase transition from the fully paired to the intermediate phase, and then from the intermediate to the fully polarized normal phase, are given by the conditions $\mu_2/\mu_1=\eta_\alpha$ and $\mu_2/\mu_1=\eta_\beta$, where η_α and η_β are two universal parameters we would like to determine as precisely as possible.

Noting that the transition from the fully paired state to the intermediate one must happen before the transition to the fully polarized phase, we see graphically that we have necessarily $\eta_\alpha>\eta_c$, and, similarly, $\eta_\beta<\eta_c$. The upper bound on η_β can be further improved by noting that at the threshold between the normal mixture and the fully polarized ideal gas, there are only a few atoms of the minority species. In principle, the value of η_β should then be found by studying the $(N+1)$-body problem of a Fermi sea of N particles 1, in the presence of a single minority atom. To address this problem, we use here a variational method inspired from first-order perturbation theory, where we expect the ground state of the system to take the form

$$|\psi\rangle=\phi_0|\mathrm{FS}\rangle+\sum_{\boldsymbol{k},\boldsymbol{q}}\phi_{\boldsymbol{k},\boldsymbol{q}}|\boldsymbol{k},\boldsymbol{q}\rangle,$$

where $|\mathrm{FS}\rangle$ is a noninteracting majority Fermi sea plus a minority atom with momentum, and $|\boldsymbol{k},\boldsymbol{q}\rangle$ is the perturbed Fermi sea with a majority atom with momentum $\boldsymbol{q}$ (with q lower than k_F) excited to momentum $\boldsymbol{k}$ (with $k>k_F$). To satisfy momentum conservation, the minority atom acquires a momentum $\boldsymbol{q}-\boldsymbol{k}$. The energy of this state with respect to the noninteracting ground state is $\langle\hat{\Delta}H\rangle=\langle\hat{H}_0\rangle+\langle\hat{V}\rangle$, with

$$\langle\hat{H}_0\rangle=\sum_{\boldsymbol{k},\boldsymbol{q}}|\phi_{\boldsymbol{k},\boldsymbol{q}}|^2(\epsilon_{\boldsymbol{k}}+\epsilon_{\boldsymbol{q}-\boldsymbol{k}}-\epsilon_{\boldsymbol{q}})$$

and

$$\langle\hat{V}\rangle=\frac{g_b}{V}\left(\sum_{\boldsymbol{q}}|\phi_0|^2+\sum_{\boldsymbol{k},\boldsymbol{k}',\boldsymbol{q}}\phi_{\boldsymbol{k}',\boldsymbol{q}}\phi^*_{\boldsymbol{k},\boldsymbol{q}}+\sum_{\boldsymbol{k},\boldsymbol{q},\boldsymbol{q}'}\phi_{\boldsymbol{k},\boldsymbol{q}}\phi^*_{\boldsymbol{k},\boldsymbol{q}'}+\sum_{\boldsymbol{q},\boldsymbol{k}}(\phi_0^*\phi_{\boldsymbol{k},\boldsymbol{q}}+\phi_0\phi^*_{\boldsymbol{k},\boldsymbol{q}})\right),$$

where the sums on q and k are implicitly limited to $q<k_F$ and $k>k_F$. As we will check later [see below, Eq. (3)], $\phi_{\boldsymbol{k},\boldsymbol{q}}\sim1/k^2$ for large momenta, in order to satisfy the short-range behavior $1/r$ of the pair wave function in real space. This means that most of the sums on $\boldsymbol{k}$ diverge for $k\to\infty$. This singular behavior is regularized by the renormalization of the coupling constant using the Lippman-Schwinger formula, thus yielding a vanishing g_B. As a consequence, since the third sum in $\langle\hat{V}\rangle$ is convergent, it gives a zero contribution to the final energy when multiplied by g_B, and can therefore be omitted in the rest of the calculation.

The minimization of $\langle\hat{H}\rangle$ with respect to ϕ_0 and $\phi_{\boldsymbol{k},\boldsymbol{q}}$ is straightforward and yields the following set of equations:

$$(\epsilon_{\boldsymbol{k}}+\epsilon_{\boldsymbol{q}-\boldsymbol{k}}-\epsilon_{\boldsymbol{q}})\phi_{\boldsymbol{k},\boldsymbol{q}}+\frac{g_b}{V}\sum_{\boldsymbol{k}'}\phi_{\boldsymbol{k}',\boldsymbol{q}}+\frac{g_b}{V}\phi_0=E\phi_{\boldsymbol{k},\boldsymbol{q}},$$

$$\frac{g_b}{V}\sum_{\boldsymbol{q}}\phi_0+\frac{g_b}{V}\sum_{\boldsymbol{q},\boldsymbol{k}}\phi_{\boldsymbol{k},\boldsymbol{q}}=E\phi_0,$$

where E is the Lagrange multiplier associated with the normalization of $|\psi\rangle$, and can also be identified with the trial energy. These equations can be solved self-consistently by introducing an auxiliary function $\chi(\boldsymbol{q})=\phi_0+\Sigma_{\boldsymbol{k}}\phi_{\boldsymbol{k},\boldsymbol{q}}$, and we obtain

$$\phi_{\boldsymbol{k},\boldsymbol{q}}=\frac{g_B\chi(\boldsymbol{q})/V}{E-(\epsilon_{\boldsymbol{k}}+\epsilon_{\boldsymbol{q}-\boldsymbol{k}}-\epsilon_{\boldsymbol{q}})}. \tag{3}$$

After a straightforward calculation, this yields

$$E=\sum_{q<k_F}\frac{1}{\sum_{k>k_F}\left(\frac{1}{\epsilon_{\boldsymbol{k}}+\epsilon_{\boldsymbol{q}-\boldsymbol{k}}-\epsilon_{\boldsymbol{q}}-E}-\frac{1}{2\epsilon_{\boldsymbol{k}}}\right)-\sum_{k<k_F}\frac{1}{2\epsilon_{\boldsymbol{k}}}},$$

where we got rid of the bare coupling constant g_B by using the Lippman-Schwinger equation (2). This equation can be solved numerically and yields $E=-0.3\hbar^2k_F^2/m$, i.e., $\eta_\beta<-0.6$ [26]. Note that the same analytical result was obtained independently in [27].

III. TRAPPED SYSTEM AND COMPARISON WITH EXPERIMENTS

In the rest of the paper, we would like to show how experimental data from Ref. [14] permits us to improve the determination of the parameters $\eta_{\alpha,\beta}$. In this pursuit, we use the local-density approximation (LDA) to calculate the density profile of the cloud in a harmonic trap, which for simplicity we assume is isotropic. In this case, the chemical potentials $\mu_{1,2}$ of each species depend on position according to the law $\mu_{1,2}(\boldsymbol{r})=\mu_{1,2}^0-m\omega^2r^2/2$, where ω is the trap frequency.

Using this assumption, the transition between the various phases will happen at radii R_α and R_β given by $\mu_2(R_{\alpha,\beta})/\mu_1(R_{\alpha,\beta})=\eta_{\alpha,\beta}$. When these two equations are associated with the condition giving the radius R_1 of the majority component, $\mu_1(R_1)=0$, we can eliminate both μ_1^0 and μ_2^0 from the equations, yielding the following close formula relating the radii R_α, R_β, and R_1:

$$\frac{R_\alpha}{R_1}=\sqrt{\frac{(R_\beta/R_1)^2-q}{1-q}}. \tag{4}$$

Here, $q=(\eta_\alpha-\eta_\beta)/(1-\eta_\beta)$ corresponds to the value of the R_β^2/R_1^2 at which R_α vanishes, i.e., at which the superfluid fraction disappears. In Fig. 2, we compare the prediction of Eq. (4) with the experimental finding of Ref. [14], taking $q=0.32$ to match the superfluidity thresholds. We see that close to the threshold, the agreement between the two graphs is quite good. However, they depart from each other for $R_\beta/R_1\gtrsim0.7$, corresponding to low population imbalance. One explanation for this discrepancy might involve finite-temperature effects. Indeed, it was already noted in Fig. 4 of Ref. [12] that, although the superfluid fraction was very sensitive to temperature at small imbalances, the value of the critical population imbalance was more robust.

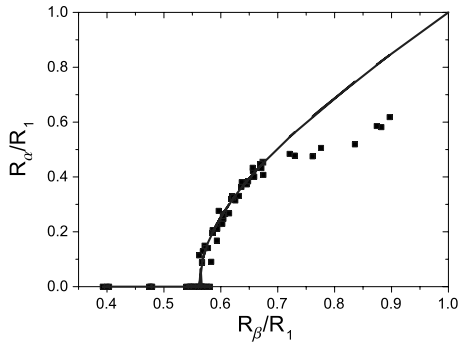

FIG. 2. Comparison between experimental data of Ref. [14] (squares) and Eq. (4) (full line). R_α, R_β, and R_1 are, respectively, the radii of the superfluid, minority, and majority components. The condensate vanishes for $R_\alpha=0$ at $q=R_\beta^2/R_1^2\sim0.32$.

The superfluid phase disappears when R_α vanishes. From Eq. (4), we see this happens for a ratio $R_\beta^2/R_1^2=q$. As seen in Fig. 2, q can be extracted from the experimental data of Ref. [14], which yield $q\sim0.32$ and therefore constrain the possible values of η_α and η_β. Indeed, using this determination of q, as well as the rough upper and lower values for $\eta_{\alpha,\beta}$, one obtains

$$-0.10<\eta_\alpha<-0.088, \tag{5}$$

$$-0.62<\eta_\beta<-0.60. \tag{6}$$

.

These bounds can be compared to the values deduced by BCS theory, predicting $\eta_\alpha\sim0.1$ and $\eta_\beta=0$. Our calculation excludes these values and explains why the width of the mixed normal state predicted by BCS theory is much narrower than observed in experiments.

IV. CONCLUSION

In conclusion, we have presented an analysis of the experimental data of Ref. [14] providing stringent bounds on the values of the thresholds for quantum phase transitions in uniform unbalanced fermi gases. Since they were obtained using minimal assumptions (mainly zero temperature and LDA), these bounds are fairly robust. In particular, they do not depend precisely on the superfluid nature of the intermediate phase. Our results suggest interesting follow-ups. First, the full understanding of the system, and in particular of the density profile of the cloud, requires knowledge of the state equation of the intermediate phase, whose exact nature then needs to be clarified. Second, the comparison with the data of Ref. [13] suggests an intriguing issue. Indeed, although the superfluidity threshold was not directly measured in this paper, the parameter q can be inferred from the critical imbalance 0.7 measured by MIT. Rice's experimental data yield at this value $q\sim0.16$. Not only is this value very far from the one obtained here from the analysis of MIT's experiments, but it also contradicts the theoretical bounds $\eta_\alpha>-0.10$ and $\eta_\beta<-0.60$, which imply $q>0.31$. As suggested in Ref. [23], this discrepancy may arise from surface tension effects pro-

voked by the strong anisotropy of Rice's trap. Another interpretation might be the onset of the intermediate phase due to finite-temperature effects, as suggested by some mean-field scenarios. Finally, the $\eta_{\alpha,\beta}$ parameters can be evaluated experimentally using the value of q associated with the measurement of the density discontinuity $\Delta n_{1,2}$ at $r=R_\alpha$, given by $\Delta n_1/\Delta n_2=-\eta_\alpha$ [24]. The preliminary data presented in Fig. 2.b of Ref. [25] suggest that the discontinuity Δn_1 is very weak, hence indicating a small value of η_α, in agreement with the bounds obtained here.

ACKNOWLEDGMENTS

The author wishes to thank M. Zwierlein, M. McNeil-Forbes, A. Bulgac, C. Salomon, F. Werner, L. Tarruell, J. McKeever, and the ENS cold atom group for fruitful discussions. This work is partially supported by CNRS, Collège de France, ACI Nanoscience, and Région Ile de France (IFRAF). Laboratoire Kastler Brossel is Unité de Recherche de l'École Normale Supérieure et de l'Université Pierre et Marie Curie, associée au CNRS.

[1] B. S. Chandrasekhar, Appl. Phys. Lett. **1**, 7 (1962); A. M. Clogston, Phys. Rev. Lett. **9**, 266 (1962); G. Sarma, J. Phys. Chem. Solids **24**, 1029 (1963); P. Fulde and R. A. Ferrell, Phys. Rev. **135**, A550 (1964); J. Larkin and Y. N. Ovchinnikov, Sov. Phys. JETP **20**, 762 (1965).

[2] R. Combescot, Europhys. Lett. **55**, 150 (2001); C. Mora and R. Combescot, Phys. Rev. B **71**, 214504 (2005); P. Castorina, M. Grasso, M. Oertel, M. Urban, and D. Zappalà, Phys. Rev. A **72**, 025601 (2005); T. Mizushima, K. Machida, and M. Ichioka, Phys. Rev. Lett. **94**, 060404 (2005); T. Mizushima, K. Machida, and M. Ichioka, *ibid.* **95**, 117003 (2005); K. Machida, T. Mizushima, and M. Ichioka, *ibid.* **97**, 120407 (2006).

[3] A. Sedrakian, J. Mur-Petit, A. Polls, and H. Müther, Phys. Rev. A **72**, 013613 (2005).

[4] W. V. Liu and F. Wilczek, Phys. Rev. Lett. **90**, 047002 (2003).

[5] P. F. Bedaque, H. Caldas, and G. Rupak, Phys. Rev. Lett. **91**, 247002 (2003); H. Caldas, Phys. Rev. A **69**, 063602 (2004); T. D. Cohen, Phys. Rev. Lett. **95**, 120403 (2005).

[6] J. Carlson and S. Reddy, Phys. Rev. Lett. **95**, 060401 (2005).

[7] T.-L. Ho and H. Zai, e-print cond-mat/0602568.

[8] A. Bulgac, M. McNeil Forbes, and A. Schwenk, Phys. Rev. Lett. **97**, 020402 (2006).

[9] C. H. Pao, Shin-Tza Wu, and S.-K. Yip, Phys. Rev. B **73**, 132506 (2006); D. T Son and M. A. Stephanov, Phys. Rev. A **74**, 013614 (2006); D. E. Sheehy and L. Radzihovsky, Phys. Rev. Lett. **96**, 060401 (2006).

[10] S. Jochim, M. Bartenstein, A. Altmeyer, G. Hendl, S. Riedl, C. Chin, J. H. Denschlag, and R. Grimm, Science **302**, 2101 (2003); M. W. Zwierlein, C. A. Stan, C. H. Schunck, S. M. F. Raupach, S. Gupta, Z. Hadzibabic, and W. Ketterle, Phys. Rev. Lett. **91**, 250401 (2003); M. Greiner, C. A. Regal, and D. S. Jin, Nature (London) **426**, 537 (2003); J. Kinast, S. L. Hemmer, M. E. Gehm, A. Turlapov, and J. E. Thomas, Phys. Rev. Lett. **92**, 150402 (2004); G. B. Partridge, K. E. Strecker, R. I. Kamar, M. W. Jack, and R. G. Hulet, *ibid.* **95**, 020404 (2005).

[11] T. Bourdel, L. Khaykovich, J. Cubizolles, J. Zhang, F. Chevy, M. Teichmann, L. Tarruell, S. J. J. M. F. Kokkelmans, and C. Salomon, Phys. Rev. Lett. **93**, 050401 (2004).

[12] M. W. Zwierlein, A. Schirotzek, C. H. Schunck, and W. Ketterle, Science **311**, 492 (2006).

[13] G. B. Partridge, W. Li, R. I. Kamar, Y. Liao, and R. G. Hulet, Science **311**, 503 (2006).

[14] M. W. Zwierlein, C. H. Schunck, A. Schirotzek, and W. Ketterle, Nature (London) **442**, 54 (2006).

[15] P. Pieri and G. C. Strinati, Phys. Rev. Lett. **96**, 150404 (2006); W. Yi and L.-M. Duan, Phys. Rev. A **73**, 031604(R) (2006); T. N. De Silva and E. J. Mueller, *ibid.* **73**, 051602(R) (2006); M. Haque and H. T. C. Stoof, *ibid.* **74**, 011602 (2006); H. Hu and X.-J. Liu, *ibid.* **73**, 051603(R) (2006).

[16] F. Chevy, Phys. Rev. Lett. **96**, 130401 (2006).

[17] T. L. Ho, Phys. Rev. Lett. **92**, 090402 (2004).

[18] A. Bulgac and M. McNeil Forbes, e-print cond-mat/0606043.

[19] J. Carlson, S.-Y. Chang, V. R. Pandharipande, and K. E. Schmidt, Phys. Rev. Lett. **91**, 050401 (2003).

[20] G. E. Astrakharchik, J. Boronat, J. Casulleras, and S. Giorgini, Phys. Rev. Lett. **93**, 200404 (2004).

[21] A. Perali, P. Pieri, and G. C. Strinati, Phys. Rev. Lett. **93**, 100404 (2004).

[22] K. M. O'Hara, S. L. Hemmer, M. E. Gehm, S. R. Granade, and J. E. Thomas, Science **298**, 2179 (2002); M. Bartenstein, A. Altmeyer, S. Riedl, S. Jochim, C. Chin, J. H. Denschlag, and R. Grimm, Phys. Rev. Lett. **92**, 120401 (2004); J. Kinast, A. Turlapov, J. E. Thomas, Q. Chen, J. Stajic, and K. Levin, Science **307**, 1296 (2005).

[23] T. N. De Silva and E. J. Mueller, Phys. Rev. Lett. **97**, 070402 (2006).

[24] This result is obtained by assuming the universal form $P=P_N f(\eta)$, with $n_i=\partial P/\partial \mu_i$, and using the continuity of pressure and chemical potentials at the transition.

[25] M. W. Zwierlein and W. Ketterle, e-print cond-mat/0603489.

[26] We note that the upper bound found here is very close to the result of recent Monte Carlo simulations presented in C. Lobo, A. Recati, S. Giorgini, and S. Stringari, e-print cond-mat/0607730.

[27] R. Combescot (private communication).

Normal State of Highly Polarized Fermi Gases : Simple Many-Body Approaches

Normal State of Highly Polarized Fermi Gases: Simple Many-Body Approaches

R. Combescot
Laboratoire de Physique Statistique, Ecole Normale Supérieure, 24 rue Lhomond, 75231 Paris Cedex 05, France

A. Recati and C. Lobo
Dipartimento di Fisica, Università di Trento and CNR-INFM BEC Center, I-38050 Povo, Trento, Italy

F. Chevy
Laboratoire Kastler Brossel, Ecole Normale Supérieure, 24 rue Lhomond, 75231 Paris Cedex 05, France
(Received 16 February 2007; published 1 May 2007)

We consider the problem of a single ↓ atom in the presence of a Fermi sea of ↑ atoms, in the vicinity of a Feshbach resonance. We calculate the chemical potential and the effective mass of the ↓ atom using two simple approaches: a many-body variational wave function and a T-matrix approximation. These two methods lead to the same results and are in good agreement with existing quantum Monte Carlo calculations performed at unitarity and, in one dimension, with the known exact solution. Surprisingly, our results suggest that, even at unitarity, the effect of interactions is fairly weak and can be accurately described using single particle-hole excitations. We also consider the case of unequal masses.

DOI: 10.1103/PhysRevLett.98.180402 PACS numbers: 05.30.Fk, 03.75.Ss, 71.10.Ca, 74.72.−h

The investigation of ultracold Fermi gases with two unbalanced hyperfine states (which we shall denote as ↑ and ↓) has been through an impressive expansion last year. This subfield is of great interest both on practical and on theoretical grounds. Indeed, on one hand, it is related to other fields of physics, namely, superconductivity, astrophysics, and high-energy physics, where similar situations arise [1]. On the other hand, the additional parameter provided by the population imbalance should provide a tool to deepen our understanding of the Bose-Einstein condensation (BEC)-BCS crossover in these systems and contribute to improving our control of many-body theory. This recent activity has been started by striking experimental results [2] which have given rise to a considerable number of theoretical works [3]. Experiments performed on trapped systems have observed equal density superfluid states as well as partially and fully polarized regions.

The analysis of the $T = 0$ phase separation requires the knowledge of the properties of both the superfluid and the partially polarized normal phase [4–6]. This has been developed in the recent work of Lobo *et al.* [6], where, at unitarity, the properties of the partially polarized phase have been obtained by calculating through a quantum Monte Carlo (QMC) approach the parameters which characterize a single ↓ atom immersed in a Fermi sea of ↑ atoms, with density $n_\uparrow = k_F^3/(6\pi^2)$. In this way, they were able to obtain very good agreement with experimental results.

Here we consider the general problem of a single ↓ atom in a completely polarized ↑ atom Fermi sea. The ↑-↓ interaction is characterized by an s-wave scattering length a, whose value can be tuned via a Feshbach resonance from the BEC ($1/k_F a \gg 1$) to the BCS ($1/k_F a \ll -1$) limits. The Fermi gas is ideal due to the suppression of higher angular momentum scattering at low temperatures. This problem is a much simpler one than the case of two equal spin populations in the BEC-BCS crossover, although still quite nontrivial due to the absence of a small parameter in the strongly interacting regime. It is the simplest realization of the moving impurity problem, and it bears a strong similarity with other old, famous, and notoriously difficult condensed matter problems, such as the Kondo problem, the x-ray singularity in metals [7], and the mobility of ions [8] and ^{4}He atoms [9] in ^{3}He. This gives to the present atomic system a much wider significance beyond the context of polarized Fermi gases. We may hope to have a full control and understanding of this system and to obtain further physical insight in these kinds of problems.

In this Letter, in addition to considering a general scattering length a, we will extend the parameter range by treating the general case where the masses $m_\uparrow$ and $m_\downarrow$ are different, although they have been the same in experiments up to now. This can be accomplished by using atoms belonging to different elements. The limit $m_\downarrow/m_\uparrow \to \infty$ is then compared to the fully solvable problem of a fixed impurity in a Fermi sea.

Here we are interested in the two physical quantities which have been calculated by Lobo *et al.* [6], namely, the chemical potential $\mu_\downarrow$ of the ↓ atom and its effective mass m^*. We have addressed this problem by two different and complementary many-body methods. The first one is a natural extension of the many-body trial wave function used by Chevy [5] to obtain the effective mass. The second one is a T-matrix approximation, whose basic ingredient, ladder diagrams, appears in more elaborate schemes. This approximation has already been used in a wide range of physical systems, including high T_c superconductors [10] and the BEC-BCS crossover [11,12], and it is known to give reasonable results. The variational method has the advantage of providing a rigorous upper bound to the energy, while the T matrix can be easily extended to

include more sophisticated approximations. As we will see, these two methods lead exactly to the same results and, moreover, are in surprisingly good agreement with QMC calculations [6,13].

The trial wave function $|\psi\rangle$ we consider, for a system of total momentum $\mathbf{p}$, is the following momentum eigenstate (we set $\hbar = 1$ throughout the Letter):

$$|\psi\rangle = \phi_0 |\mathbf{p}\rangle_\downarrow |0\rangle_\uparrow + \sum_{q<k_F}^{k>k_F} \phi_{\mathbf{qk}} |\mathbf{p}+\mathbf{q}-\mathbf{k}\rangle_\downarrow c^\dagger_{\mathbf{k}_\uparrow} c_{\mathbf{q}_\uparrow} |0\rangle_\uparrow, \quad (1)$$

where $c_{\mathbf{k}_\uparrow}$ and $c^\dagger_{\mathbf{k}_\uparrow}$ are annihilation and creation operators, respectively. In the first term, the $\uparrow$ -spin free Fermi sea is in its ground state $|0\rangle_\uparrow = \prod_{k<k_F} c^\dagger_{\mathbf{k}_\uparrow} |\mathrm{vac}\rangle$, and the $\downarrow$ -spin atom is in the plane-wave state $|\mathbf{p}\rangle_\downarrow$, while in the second term it is in excited states corresponding to the creation of a particle-hole pair in the Fermi sea with momentum $\mathbf{k}$ and $\mathbf{q}$, respectively, the $\downarrow$ -spin atom carrying the rest of the momentum. The coefficients ϕ_0 and $\phi_{\mathbf{qk}}$ are found by minimizing the total energy. This wave function is by construction suitable to reproduce the molecule in the BEC limit as well as the perturbative mean-field limit. We follow the procedure of Ref. [5], in particular, with respect to the zero range interaction and the regularization in terms of the scattering length. We obtain for the change in energy E due to the addition of the $\downarrow$ -spin atom:

$$E = \epsilon_{\downarrow p} + \sum_{q<k_F} \Bigg[\frac{m_r}{2\pi a} - \sum_k \frac{2m_r}{k^2} + \sum_{k>k_F} \frac{1}{\epsilon_{\uparrow k} + \epsilon_{\downarrow \mathbf{p}+\mathbf{q}-\mathbf{k}} - \epsilon_{\uparrow q} - E} \Bigg]^{-1}, \quad (2)$$

where $\epsilon_{\uparrow,\downarrow k} = k^2/2m_{\uparrow,\downarrow}$ is the kinetic energy of the $\uparrow$ and $\downarrow$ atoms, and $m_r = m_\uparrow m_\downarrow/(m_\uparrow + m_\downarrow)$ is the reduced mass. For $\mathbf{p} = \mathbf{0}$, we have $E = \mu_\downarrow$, while the variation of E for small $\mathbf{p}$ gives the effective mass.

These results can be obtained exactly from the knowledge of the self-energy $\Sigma(p, \omega)$ of the $\downarrow$ atom. Indeed, the pole of the $\downarrow$ Green's function $G_\downarrow(p, \omega) = [\omega - \epsilon_{\downarrow p} + \mu_\downarrow - \Sigma(p, \omega)]^{-1}$, giving the dispersion relation of the $\downarrow$ quasiparticle, satisfies

$$\omega - \epsilon_{\downarrow p} + \mu_\downarrow - \Sigma(p, \omega) = 0. \quad (3)$$

Since ω is the energy measured from the chemical potential, and physically the chemical potential corresponds to the addition of a particle with zero momentum $p = 0$, the chemical potential is given by

$$\mu_\downarrow = \Sigma(0, 0). \quad (4)$$

Moreover, the effective mass, giving the dispersion relation of the $\downarrow$ quasiparticle, is obtained from the small p behavior of the dispersion relation and is given by

$$\frac{m^*}{m_\downarrow} = \frac{1 - \frac{\partial \Sigma}{\partial \omega}}{1 + \frac{\partial \Sigma}{\partial (p^2/2m_\downarrow)}}, \quad (5)$$

where the derivatives of the self-energy are taken for $p = \omega = 0$ (Σ is real in the situations we deal with below).

The self-energy itself is obtained [14] from the unknown two-particle vertex Γ, the only very important simplifying feature of our problem being that the $\uparrow$ -atom Green's function is exactly the bare one, namely, $G_{0\uparrow}(k, \omega) = [\omega - \epsilon_{\uparrow k} + \mu_\uparrow]^{-1}$, where $\mu_\uparrow = k_F^2/2m_\uparrow$, since the single $\downarrow$ atom does not perturb in the thermodynamic limit the free Fermi sea of $\uparrow$ atoms. To obtain actual answers, we proceed to take the simplest approximation for this vertex, namely, the T-matrix approximation, where the $\downarrow$ atom interacts only with a single $\uparrow$ atom. This implies, in particular, that the only excited states of the $\uparrow$ Fermi sea coming in this problem are the single particle-hole excitations, just as in Eq. (1). In this approximation, the $\downarrow$ and the $\uparrow$ atoms scatter any number of times through the bare potential, just as in any two-body problem solved exactly by perturbation theory, which leads to the well-known series of "ladder" diagrams. When there is a single $\uparrow$ atom, the problem reduces to the full scattering of the $\downarrow$ and $\uparrow$ atoms, and the solution can be expressed in terms of the scattering amplitude. When this problem is compared to the one in the presence of the Fermi sea of $\uparrow$ atoms, the bare interaction V can be eliminated in favor of the scattering properties. In our approximation, the vertex Γ depends only on the total momentum $\mathbf{K}$ and the total energy Ω of incoming particles. After performing the above steps, we find [12,14]

$$\Gamma^{-1}(K, \Omega) = \frac{m_r}{2\pi a} - \int \frac{d\mathbf{k}}{(2\pi)^3} \Bigg[\frac{2m_r}{k^2} + G_\downarrow(k, \Omega + \mu_\uparrow - \epsilon_{\uparrow \mathbf{K}-\mathbf{k}}) \theta(\epsilon_{\uparrow \mathbf{K}-\mathbf{k}} - \mu_\uparrow) \Bigg], \quad (6)$$

where $\theta(x)$ is the Heaviside function. In obtaining this result, we have made explicit use of the fact that we will find $\mu_\downarrow < 0$ as it is obvious physically.

In our approximation, the self-energy is given by

$$\Sigma(p, \omega) = \frac{1}{2i\pi} \int \frac{d\mathbf{K}}{(2\pi)^3} \int_C d\Omega \Gamma(K, \Omega) G_{0\uparrow}(\mathbf{K} - \mathbf{p}, \Omega - \omega), \quad (7)$$

where, as mentioned above, using $G_{0\uparrow}$ as the $\uparrow$ -atom Green's function does not imply any approximation. Contour C goes anticlockwise around the left-hand side part $\mathrm{Re}\omega < 0$ of the ω complex plane. We deform it to enclose only the singularities of the integrand. Physically, the singularities of $\Gamma(K, \Omega)$ correspond to the continuous spectrum of the scattering states of the $\uparrow$ and $\downarrow$ atom and possibly to a bound state of these atoms. On the other hand, $G_{0\uparrow}(k, \omega)$ has just, for fixed k, a pole at $\omega = \epsilon_{\uparrow k} - \mu_\uparrow$. Since we work at $T = 0$, the particle-particle continuous spectrum does not contribute as it is physically obvious. Indeed, from Eq. (6), the corresponding singularities are at $\Omega > 0$ and are outside contour C. On the other hand, we will restrict ourselves mainly to the case where there are no bound states between the $\uparrow$ and the $\downarrow$ atoms. Such a bound

state exists clearly in the BEC limit $1/k_F a \to +\infty$, where molecules will be present. While, as we shall shortly show, our simple approach recovers also this limiting behavior, the effect of a bound state in the intermediate regime will be investigated in further work. This leaves us only with the contribution of the pole of $G_{0\uparrow}$:

$$\Sigma(p,\omega) = \int \frac{d\mathbf{K}}{(2\pi)^3}\theta(\mu_\uparrow - \epsilon_{\uparrow\mathbf{K}-\mathbf{p}})\Gamma(K,\omega+\epsilon_{\uparrow\mathbf{K}-\mathbf{p}}-\mu_\uparrow) = \frac{1}{2\pi^2}\int_0^{k_F} dK K^2 \langle \Gamma(\mathbf{K}+\mathbf{p},\omega+\epsilon_{\uparrow K}-\mu_\uparrow)\rangle, \quad (8)$$

where the bracket is for the angular average over the direction of $\mathbf{K}$.

At this stage, it is interesting to consider the weak coupling limit $a \to 0_-$, in which case the first term dominates in the right-hand side of Eq. (6). This gives $\Gamma(K,\Omega) = 2\pi a/m_r$ and $\Sigma(p,\omega) = \Sigma(0,0) = \mu_\downarrow = k_F^3 a/(3\pi m_r) = 2\pi n_\uparrow a/m_r$. Hence, we recover the expected result for the mean-field interaction energy with a short-range interaction $V(\mathbf{r}) = (2\pi a/m_r)\delta(\mathbf{r})$. We can view the more general result Eq. (8) as having a similar physical interpretation but with the effective interaction having now a wave vector and energy dependence.

In the general case, Eq. (8) together with Eq. (6) provide an integral equation for $\Sigma(p,\omega)$. We leave the exact solution of this equation for further work, whereas in the present Letter we will proceed to a further approximation. We will just stop at the first step of an iteration loop which would provide the full answer; that is, we will set $\Sigma(p,\omega) = 0$ in the expression of $G_\downarrow(p,\omega)$. In this case, we can check that Eqs. (2) and (3) are identical, provided E is identified with $\omega + \mu_\downarrow$.

For the case of the $\downarrow$ atom chemical potential, we are just left with solving numerically an equation for $\mu_\downarrow$. At unitarity, $1/k_F a = 0$, and for $m_\downarrow = m_\uparrow$ this gives $\mu_\downarrow = -0.6066\mu_\uparrow$, in remarkable agreement with the QMC [5,6] result $\mu_\downarrow = -(3/5)(0.97 \pm 0.02)\mu_\uparrow = -0.58 \pm 0.01\mu_\uparrow$. This surprising agreement suggests that the effect of interactions is weak even at unitarity.

It is interesting to investigate the regime where the ratio $\rho = |\mu_\downarrow|/\mu_\uparrow$ becomes large. In this case, the expression of $\Gamma(K,\Omega)$ becomes quite simple. We find to dominant order $\Gamma(K,\Omega) = [2\pi/(m_r k_F)]\{1/k_F a - [\rho r/(1+r)]^{1/2}\}^{-1}$, with $r = m_\downarrow/m_\uparrow$. Since Γ does not depend on K and Ω, the situation is completely analogous to the one found above in the weak coupling limit: $\mu_\downarrow = \Sigma(0,0)$ is easily calculated, and the resulting relation between ρ and $1/k_F a$ can be written as

$$\frac{1}{k_F a} = \sqrt{\frac{\rho r}{1+r}} - \frac{2}{3\pi}\frac{1+r}{\rho r}. \quad (9)$$

In the case of equal masses $m_\uparrow = m_\downarrow$, this is plotted for comparison in Fig. 1 and is seen to give a quite good agreement with the numerical value [15]. In the weak coupling regime $a \to 0_-$, we recover the mean-field result given above, while the asymptotic behavior for large ρ is $\rho = (1 + 1/r)(1/k_F a)^2$, which is the two-body bound state energy. This formula can be seen as an interpolation between these two extremes. At unitarity, it gives $\rho = (1 + 1/r)(2/3\pi)^{2/3}$. For equal masses, we get $\rho \approx 0.71$, which is fairly near the numerical result.

In the inset in Fig. 1, we present the results of our model at unitarity as a function of the mass ratio $r = m_\downarrow/m_\uparrow$. Again the interpolation equation (9), i.e., $\rho = (2/3\pi)^{2/3} \times (1 + 1/r)$, is in quite reasonable agreement with numerical results. For small r, the chemical potential $\mu_\downarrow$ goes to $-\infty$, as can be seen easily from Eq. (8). In the other limit $m_\downarrow \to \infty$, this ratio is seen to saturate.

Assuming that the thermodynamic and infinite mass limits commute, the problem reduces to that of an impurity interacting with a free Fermi sea, which is well known in solid state physics [16]. It can be solved exactly in the following way. The Fermi sea is enclosed in a large sphere of radius R, with $R \to \infty$ in the thermodynamic limit and the impurity at the center. Since the s-wave functions have to be zero at the sphere, the allowed wave vectors k_p are given by $k_p R + \delta_0(k_p) = p\pi$, with integer $p \le n$ and $k_F R = n\pi$. For low energy atoms, the phase shift is given by $\tan\delta_0(k) = -ka$. The energy of all of the atoms of the Fermi sea is $E = \sum_p k_p^2/2m_\uparrow$. The calculation is conveniently performed by finding the change in energy due to a change in the scattering length. In this limiting case, the change in total energy of the Fermi sea is identified with the $\downarrow$ atom chemical potential. We find in this way

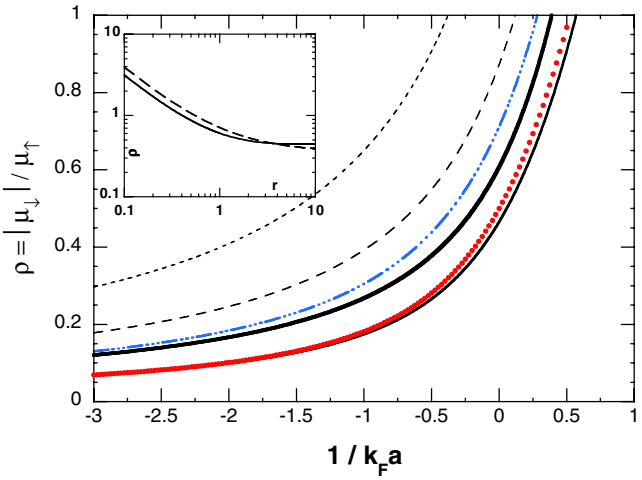

FIG. 1 (color online). Reduced $\downarrow$ atom chemical potential $|\mu_\downarrow|$ as a function of $1/k_F a$ for various mass ratios $r = m_\downarrow/m_\uparrow$. Black curves from top to bottom: Numerical results for $r = 0.25, 0.5, 1$ (solid thick line), and ∞ (lower solid line). The dashed–triple-dotted blue line above the $r = 1$ line is the corresponding interpolating approximation Eq. (9). The dotted red line just above the $r = \infty$ line is the exact result Eq. (10). The inset compares, at unitarity, the approximation equation (9) (dashed line) with the numerical results (solid line) as a function of the mass ratio r.

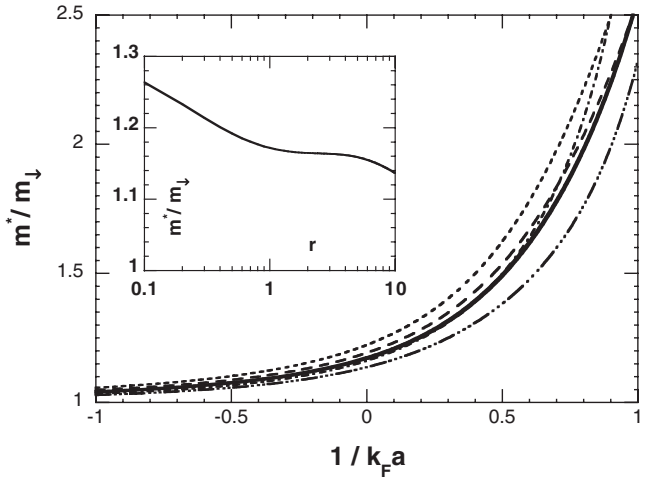

FIG. 2. Relative effective mass $m^*/m_\downarrow$ as a function of $1/k_F a$ for various mass ratios $r = m_\downarrow/m_\uparrow$. Same conventions as in Fig. 1 for $r = 0.25$, 0.5, and 1. The dashed-dotted line is $r = 4$, and the dashed–triple-dotted line is $r = 10$. The inset shows $m^*/m_\downarrow$ as a function of r at unitarity.

$$\frac{|\mu_\downarrow|}{\mu_\uparrow} = \frac{1}{\pi}\left[(1+y^2)\left(\frac{\pi}{2} + \arctan y\right) + y\right], \qquad (10)$$

where $y = 1/k_F a$. The result is plotted in Fig. 1 and is seen to be in excellent agreement with the variational and T-matrix results. In particular, we find $\rho = 0.5$ at unitarity, to be compared to the approximate value 0.465.

Finally, the relative effective mass $m^*/m_\downarrow$ is displayed in Fig. 2 for various mass ratios. The first striking feature is that the mass enhancement is quite small around unitarity, whereas we might have expected a much stronger effect around resonance. Naturally, when we go further to the BEC side, $m^*/m_\downarrow$ increases rapidly. Quantitatively, our result $m^*/m_\downarrow = 1.17$ for equal masses at unitarity is in quite reasonable agreement with the QMC result 1.04(3), taking into account that effective mass is more sensitive to approximations than energy. The other noticeable feature of Fig. 2 is the weak dependence of $m^*/m_\downarrow$ on the mass ratio r, as can be seen in the inset at unitarity. We note that, within our approximation, no bound state appears in the plotted range. We have to keep in mind that, in improved approximations, the location for the appearance of a bound state might be somewhat changed.

To further check the reliability of our approach, we have done the calculations in one dimension. In this case, we can compare our results with the exact solution for equal masses [17]. We find very good agreement along the whole crossover, from BCS-like state to the molecular Tonks state, for the energy, while the mass is more sensitive to our approximations precisely when the two-body bound state plays a major role.

In conclusion, we have found that the physical properties of a single $\downarrow$ atom in the presence of a Fermi sea of $\uparrow$ atoms can be described fairly accurately by the simple inclusion of single particle-hole excitations. Two equivalent schemes based, respectively, on a many-body trial wave function and a simple T-matrix approach were developed and give very good agreement with known QMC results for $m_\uparrow = m_\downarrow$ at unitarity.

We are grateful to S. Giorgini, M. Yu. Kagan, X. Leyronas, and S. Stringari for stimulating discussions. The Laboratoire de Physique Statistique and Laboratoire Kastler Brossel are Laboratoires associés au Centre National de la Recherche Scientifique et aux Universités Paris 6 et Paris 7. C. L. and A. R. acknowledge support by the Ministero dell'Istruzione, dell'Università e della Ricerca (MIUR). F. C. acknowledges support from Region Ile de France (IFRAF).

[1] R. Casalbuoni and G. Nardulli, Rev. Mod. Phys. **76**, 263 (2004).
[2] M. W. Zwierlein, A. Schirotzek, C. H. Schunck, and W. Ketterle, Science **311**, 492 (2006); G. B. Partridge, W. Li, R. I. Kamar, Y. Liao, and R. G. Hulet, Science **311**, 503 (2006); Y. Shin, M. W. Zwierlein, C. H. Schunck, A. Schirotzek, and W. Ketterle, Phys. Rev. Lett. **97**, 030401 (2006); C. H. Schunk, Y. Shin, A. Schirotzek, M. W. Zwierlein, and W. Ketterle, cond-mat/0702066.
[3] See, for example, D. E. Sheehy and L. Radzihovsky, cond-mat/0607803 [Ann. Phys. (N.Y.) (to be published)], and references therein.
[4] A. Bulgac and M. M. Forbes, Phys. Rev. A **75**, 031605(R) (2007).
[5] F. Chevy, Phys. Rev. A **74**, 063628 (2006).
[6] C. Lobo, A. Recati, S. Giorgini, and S. Stringari, Phys. Rev. Lett. **97**, 200403 (2006).
[7] G. D. Mahan, *Many-Particle Physics* (Kluwer Academic, Dordrecht, 2000).
[8] N. V. Prokof'ev, Phys. Rev. Lett. **74**, 2748 (1995), and references therein.
[9] F. Arias de Saavedra, J. Boronat, A. Polls, and A. Fabrocini, Phys. Rev. B **50**, 4248 (1994), and references therein.
[10] M. Yu. Kagan, R. Frésard, M. Capezzali, and H. Beck, Phys. Rev. B **57**, 5995 (1998), and references therein.
[11] P. Pieri and G. C. Strinati, Phys. Rev. B **61**, 15 370 (2000), and references therein.
[12] R. Combescot, X. Leyronas, and M. Yu. Kagan, Phys. Rev. A **73**, 023618 (2006), and references therein.
[13] S. Pilati and S. Giorgini (unpublished).
[14] For an introduction to many-body techniques, see, for example, A. A. Abrikosov, L. P. Gorkov, and I. E. Dzyaloshinkski, *Methods of Quantum Field Theory in Statistical Physics* (Dover, New York, 1963).
[15] Reference [13] has calculated ρ on the $a < 0$ side for equal masses, and the results are in excellent agreement with ours. The agreement is not as good for the effective mass but still within 10% in the worst case.
[16] J. Friedel, Philos. Mag. **43**, 153 (1952); F. G. Fumi, Philos. Mag. **46**, 1007 (1955).
[17] J. B. McGuire, J. Math. Phys. (N.Y.) **7**, 123 (1966).

Conclusion

Une des conclusions que l'on peut tirer des résultats présentés dans ce manuscrit est l'étonnante vitalité de deux "vieilles dames" de la physique que sont les théories de la thermodynamique et de la mécanique des fluides qui ont toutes deux vues le jour au XIX^{e} siècle. En effet, même si il est parfois nécessaire de faire des détours par des modèles microscopique (cf. le problème à N+1 corps)les concepts tirés de ces deux théories macroscopiques sont capables d'expliquer des phénomènes aussi divers que le rebond sur des surfaces super-hydrophobes, la dynamique des vortex dans un superfluide ou la séparation de phase dans un gaz de fermions déséquilibrés. Qui plus est, les thèmes abordés sont toujours en plein développement. Les perspectives prometteuses offertes par les propriétés remarquables des matériaux superhydrophobes se heurtent encore à des difficultés pratiques. Mathilde Reyssat a ainsi étudié durant sa thèse dans le groupe de David Quéré les limites du non mouillage sur des surfaces modèles constituées de réseau de plot micromètriques : à quel condition les gouttes les gouttes s'empalent-elles sur les plots au lieu de rebondir dessus ? Comment les propriétés de super-hydrophobies sont-elles modifiées par le vieillissement de la surface, notamment par la pollution par des huiles ? D'un point de vue plus fondamental, nous avons déjà mentionné les questions ouvertes concernant la dynamique des gouttes dans le régime de faible vitesse dans lequel la description en terme linéaire (le modèle du "ressort liquide") semble ne plus être valable et sur lequel nous poursuivons nos études.

Comme nous l'avons déjà mentionné dans les chapitres précédents, le domaine des atomes ultra-froids en général, et des gaz de fermions dégénérés en particulier, voit fleurir une nouvelle génération d'expériences tentant de pousser encore plus loin les techniques et les résultats déjà impressionnants des générations précédentes. Dans le cadre du projet ERC FERLODIM (Fermions in Low Dimensions), nous allons mettre à profit les deux expériences de fermions ultra-froids de l'ENS pour étudier les systèmes quantiques fortement corrélés dans des situations de dimension réduite (une ou deux di-

mensions). Comme on le constate sur la représentation schématique de la la figure 3.4, les systèmes de dimensions réduites offrent une grande flexibilité dans les situations physiques accessible :

1. Dans les expériences de physique atomique où l'on image des échantillons tridimensionnels, l'imagerie par absorption ne fournit qu'une information partielle, car celui-ci est automatiquement moyenné dans la direction d'observation. Observer un unique plan atomique permet naturellement de contourner cette difficulté et donne ainsi accès à toute l'information présente dans le profil de densité. Par ailleurs, le développement d'un dispositif d'imagerie à très haute résolution permettra de sonder les corrélations quantiques dans les systèmes à N-corps au niveau de l'atome unique.
2. Une lame de phase peut être utilisé pour projeter un potentiel lumineux de forme et de topologie quasi-arbitraire sur les atomes. Ici aussi, la dimensionalité réduite est un atout, car il n'est alors pas nécessaire de générer des profils tridimensionnels plus compliqués à réaliser.
3. De nouvelles techniques de refroidissement dans les réseaux optiques sont en cours de développement pour atteindre les températures extrêmes requises par l'observation de l'antiferromagnétisme, en particulier le refroidissement entropique dans lequel on modifie lentement le profil du piège de façon à isoler les régions où l'entropie du système est la plus faible.

De manière général, les systèmes de basse dimensionalité sont plus sensibles aux corrélations. À 1D, l'ansatz de Bethe permet d'obtenir des résultats analytique qui pourront être comparés aux données tirées de nos expériences. Dans les systèmes antiferromagnétiques, la transition entre 1D et 2D est particulièrement intéressante puisque l'on passe de d'excitations de type magnons (spin 1, à 2D) à des spinons (spin 1/2 à 1D) correspondant à des nombres quantiques fractionnaires. Les systèmes antiferromagnétiques bidimensionnels sont enfin particulièrement importants car les scénarios les plus crédibles de mécanisme d'appariement dans les supraconducteurs à haute température critique semblent suggérer que le modèle de Hubbard bidimensionnel pourrait être suffisant pour expliquer la supraconductivité dans ces systèmes dont l'explication résiste encore à l'analyse théorique.

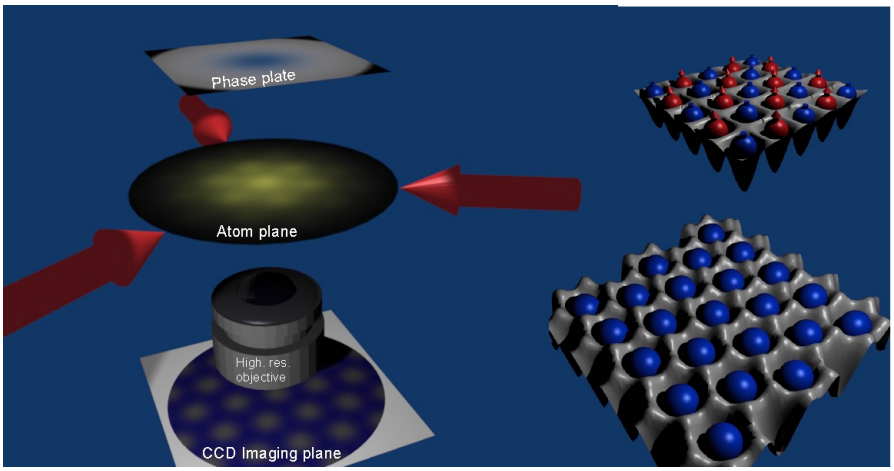

FIG. 3.4 – Principe d'une expérience d'une expérience d'atomes froids de nouvelle génération : les atomes sont piégés dans un potentiel périodique par l'interférence de plusieurs faisceaux laser. La lame de phase permet de projeter des murs raides confinant les atomes transversalement et un système d'imagerie de haute résolution permet d'observer les atomes à l'échelle d'un site unique du réseau optique.